frontiers | Research Topics

Biologically-informed approaches to design processes and applications

Edited by
Mark A. Elgar, Cecilia Laschi, Devi Stuart-Fox, Alberto Pugnale and Ahu Gumrah Dumanli-Parry

Published in
Frontiers in Ecology and Evolution
Frontiers in Built Environment
Frontiers in Bioengineering and Biotechnology

ISSN 1664-8714
ISBN 978-2-83251-868-7
DOI 10.3389/978-2-83251-868-7

About Frontiers

Frontiers is more than just an open access publisher of scholarly articles: it is a pioneering approach to the world of academia, radically improving the way scholarly research is managed. The grand vision of Frontiers is a world where all people have an equal opportunity to seek, share and generate knowledge. Frontiers provides immediate and permanent online open access to all its publications, but this alone is not enough to realize our grand goals.

Frontiers journal series

The Frontiers journal series is a multi-tier and interdisciplinary set of open-access, online journals, promising a paradigm shift from the current review, selection and dissemination processes in academic publishing. All Frontiers journals are driven by researchers for researchers; therefore, they constitute a service to the scholarly community. At the same time, the *Frontiers journal series* operates on a revolutionary invention, the tiered publishing system, initially addressing specific communities of scholars, and gradually climbing up to broader public understanding, thus serving the interests of the lay society, too.

Dedication to quality

Each Frontiers article is a landmark of the highest quality, thanks to genuinely collaborative interactions between authors and review editors, who include some of the world's best academicians. Research must be certified by peers before entering a stream of knowledge that may eventually reach the public - and shape society; therefore, Frontiers only applies the most rigorous and unbiased reviews. Frontiers revolutionizes research publishing by freely delivering the most outstanding research, evaluated with no bias from both the academic and social point of view. By applying the most advanced information technologies, Frontiers is catapulting scholarly publishing into a new generation.

What are Frontiers Research Topics?

Frontiers Research Topics are very popular trademarks of the *Frontiers journals series*: they are collections of at least ten articles, all centered on a particular subject. With their unique mix of varied contributions from Original Research to Review Articles, Frontiers Research Topics unify the most influential researchers, the latest key findings and historical advances in a hot research area.

Find out more on how to host your own Frontiers Research Topic or contribute to one as an author by contacting the Frontiers editorial office: frontiersin.org/about/contact

Biologically-informed approaches to design processes and applications

Topic editors

Mark A. Elgar — The University of Melbourne, Australia
Cecilia Laschi — National University of Singapore, Singapore
Devi Stuart-Fox — The University of Melbourne, Australia
Alberto Pugnale — The University of Melbourne, Australia
Ahu Gumrah Dumanli-Parry — The University of Manchester, United Kingdom

Citation

Elgar, M. A., Laschi, C., Stuart-Fox, D., Pugnale, A., Dumanli-Parry, A. G., eds. (2023). *Biologically-informed approaches to design processes and applications*. Lausanne: Frontiers Media SA. doi: 10.3389/978-2-83251-868-7

Table of contents

04 Editorial: Biologically-informed approaches to design processes and applications
Alberto Pugnale, Devi Stuart-Fox, Mark A. Elgar, Cecilia Laschi and Ahu Gumrah Dumanli

07 Cortex Thickness Is Key for the Colors of Iridescent Starling Feather Barbules With a Single, Organized Melanosome Layer
Pascal Freyer, Bodo D. Wilts and Doekele G. Stavenga

20 Distribution of Biominerals and Mineral-Organic Composites in Plant Trichomes
Hans-Jürgen Ensikat and Maximilian Weigend

32 From Bioinspired to Bioinformed: Benefits of Greater Engagement From Biologists
Leslie Ng, Mark A. Elgar and Devi Stuart-Fox

41 An Artificial Intelligence Agent That Synthesises Visual Abstractions of Natural Forms to Support the Design of Human-Made Habitat Structures
Gabriele Mirra, Alexander Holland, Stanislav Roudavski, Jasper S. Wijnands and Alberto Pugnale

62 Numerosity Categorization by Parity in an Insect and Simple Neural Network
Scarlett R. Howard, Julian Greentree, Aurore Avarguès-Weber, Jair E. Garcia, Andrew D. Greentree and Adrian G. Dyer

77 Aerodynamic Performance of a Dragonfly-Inspired Tandem Wing System for a Biomimetic Micro Air Vehicle
Erfan Salami, Elham Montazer, Thomas A Ward, Nik Nazri Nik Ghazali and Irfan Anjum Badruddin

89 Tangled Tales of Mycelium and Architecture: Learning From Failure
Janet McGaw, Alex Andrianopoulos and Alessandro Liuti

97 Producing non-steady-state gaits (starting, stopping, and turning) in a biologically realistic quadrupedal simulation
William Irvin Sellers, Charlotte Francesca Cross, Akira Fukuhara, Akio Ishiguro and Eishi Hirasaki

frontiers | Frontiers in Ecology and Evolution

TYPE Editorial
PUBLISHED 29 November 2022
DOI 10.3389/fevo.2022.1090859

OPEN ACCESS

EDITED AND REVIEWED BY
Elise Huchard,
UMR5554 Institut des Sciences de l'Evolution de Montpellier (ISEM), France

*CORRESPONDENCE
Devi Stuart-Fox
d.stuart-fox@unimelb.edu.au

SPECIALTY SECTION
This article was submitted to Behavioral and Evolutionary Ecology, a section of the journal Frontiers in Ecology and Evolution

RECEIVED 06 November 2022
ACCEPTED 11 November 2022
PUBLISHED 29 November 2022

CITATION
Pugnale A, Stuart-Fox D, Elgar MA, Laschi C and Dumanli AG (2022) Editorial: Biologically-informed approaches to design processes and applications.
Front. Ecol. Evol. 10:1090859.
doi: 10.3389/fevo.2022.1090859

Editorial: Biologically-informed approaches to design processes and applications

Alberto Pugnale[1], Devi Stuart-Fox[2]*, Mark A. Elgar[2], Cecilia Laschi[3] and Ahu Gumrah Dumanli[4]

[1]Faculty of Architecture, Building and Planning, The University of Melbourne, Melbourne, VIC, Australia, [2]School of BioSciences, The University of Melbourne, Melbourne, VIC, Australia, [3]Department of Mechanical Engineering, National University of Singapore, Singapore, Singapore, [4]Department of Materials, The University of Manchester, Manchester, United Kingdom

KEYWORDS

biomimetic, bioinspiration, robotics, architectural design, materials, biophotonics

Editorial on the Research Topic
Biologically-informed approaches to design processes and applications

Practitioners across domains—from architectural design (Zari, 2010; Ha and Lu, 2020), medical interventions (Chen et al., 2021), and robotics (Coyle et al., 2018; Ahmed et al., 2022) to materials science (Wegst et al., 2015)—are increasingly drawing inspiration from biology to address a wide range of challenges. This is perhaps unsurprising because life on earth represents over 3.8 billion years of evolution, whereby natural selection ruthlessly purges design failures. Despite the growth and promise of biomimetic and bioinspired approaches, the analogy to biological form or function is often superficial or largely figurative. This Research Topic was born from the topic editors' shared belief that to capitalize on insights from biology, we need to move beyond figurative referencing toward functional analogy informed by accurate biological knowledge. For this reason, we advocate a biologically-informed (or bio-informed) approach that captures key properties of living organisms and systems, such as sustainability, multifunctionality and self-assembly.

The articles collected in this interdisciplinary Research Topic illustrate the strengths of a bio-informed approach to design processes and applications. Ultimately, the goal is to demonstrate how simple concepts can be abstracted from highly complex and inter-connected biological materials, structures and processes to be applied or manufactured at scale.

A bio-informed approach requires deep collaboration between biologists and practitioners in other fields. To gauge the current extent of engagement with biologists in biomimetic and bioinspired research, Ng et al. surveyed the literature over 30 years (1990–2020) to reveal that only 41% of research papers published in the field included an author affiliated to a biology-related department, and most of them focus on a limited range of popular model species. The authors show the value of capitalizing on biological

diversity and understanding the ecological and evolutionary context of the biological models. They also highlight that interdisciplinary engagement is a two-way street—for example, application of engineering approaches can improve biological understanding just as biology can offer new engineering solutions.

Several of the articles in this Research Topic focused on expanding biological knowledge for bio-informed applications. Ensikat and Weigend explored the diversity and distribution of biominerals (organic/inorganic composite materials) that comprise the "hairs" (trichomes) on leaf surfaces of many plants. Biomineralization is an area of considerable interest for biomedical applications and plant trichomes provide a more tractable model to enable *in-vivo* study of complex composite materials comprising different minerals and organic compounds.

Turning from plants to animals, Freyer et al. compared the structures responsible for different types of iridescent plumage in two bird species. Their study shows how adjusting the thickness of one layer in the complex feather microstructure can tune the iridescence from blue-purple in the European starling to blue-green in the Cape starling. This discovery has potential applications in bioinspired materials that tune color through a single sensing layer.

Two studies in this Research Topic provided elegant demonstrations of how complex biological processes can be simulated, simultaneously enhancing biological understanding and paving the way for future applications. Howard et al. showed that honeybees are able to process and categorize odd and even numbers of elements and that this learning task can be simulated with a simple neural network comprising 5 neurons. On one hand, this study suggests that complex cognitive-like behaviors can be seen in honeybees and other assumed simple biological systems. On the other hand, it demonstrates that it is possible to design computing solutions with very simplified mechanisms that resemble simple animal brains.

Sellers et al. also simulated a biological process, namely locomotion, borrowing from robotics to improve our understanding of animal biomechanics. Rather than typical steady state locomotion such as walking or running at constant speed, the study focused on non-steady-state movements such as starting, stopping and turning. The study shows how gait controllers used in robotics can be used to realistically simulate non-steady-state gaits of a chimpanzee.

Turning to applications, Salami et al. used a bio-informed approach to design a novel tandem flapping wing mechanism based on dragonflies, which achieve remarkable flying agility with four wings arranged in a tandem configuration. The tandem flapping mechanism enabled the team to study the aerodynamic forces and demonstrate how tandem wings can generate higher lift and improve stability compared with a single pair of wings. The mechanism could be used for the design of a future biomimetic micro air vehicle.

A bio-informed approach to the design process is exemplified by the article by Mirra et al. The authors implement a novel artificial intelligence (AI) agent to design 3D tree forms with complexity and features that are attractive to arboreal wildlife. Although the generated artificial designs deviate from natural structural forms, they are easy to build, and their form preserves those visual features that are meaningful to birds and other wildlife.

Finally, a bio-informed approach encompasses not only artificial materials and technologies, but also natural materials. Mycelium—the vegetative body of a mushroom or fungus—is one of the most promising natural materials for a wide range of applications. Like polystyrene, it is light weight with excellent thermal insulation and fire retardance, but unlike polystyrene, it is sustainable and biodegradable. McGaw et al. argue that the slow uptake of mycelium-based materials is due to psychological, aesthetic and economic barriers, rather than technical challenges. McGaw et al. show the importance of considering social, cultural and economic factors in the design of bioinspired sustainable materials, and identify opportunities for future zero-waste mycelium-based products.

Concluding remarks

The articles in this Research Topic span an extraordinary breadth of biological systems and disciplines. They showcase the utility of a biologically informed approach to enhance not only design processes and applications, but also biological understanding and sustainability. The focus of the articles ranges from expanding biological knowledge and simulating complex biological processes for bioinspired applications, designing new technologies and human-made habitat structures, to exploring the social and economic context for the uptake of products based on novel biomaterials. We hope that this collection of articles inspires new ideas and helps to foster deeper collaboration between biologists, physical and social scientists, engineers and designers to solve the significant challenges of our time.

Author contributions

AP and DS-F wrote the first draft. All authors edited and contributed intellectually to the work and approved it for publication.

Acknowledgments

The Research Topic was conceived through the Bioinspiration Hallmark Research Initiative at the University of Melbourne.

Conflict of interest

The authors declare that the research was conducted in the absence of any commercial or financial relationships that could be construed as a potential conflict of interest.

Publisher's note

All claims expressed in this article are solely those of the authors and do not necessarily represent those of their affiliated organizations, or those of the publisher, the editors and the reviewers. Any product that may be evaluated in this article, or claim that may be made by its manufacturer, is not guaranteed or endorsed by the publisher.

References

Ahmed, F., Waqas, M., Jawed, B., Soomro, A. M., Kumar, S., Hina, A., et al. (2022). Decade of bio-inspired soft robots: a review. *Smart Mater. Struct.* 31, 073002. doi: 10.1088/1361-665X/ac6e15

Chen, H., Zhang, Y., Zhang, L., Ding, X., and Zhang, D. (2021). Applications of bioinspired approaches and challenges in medical devices. *Bio-Design Manuf.* 4, 146–148. doi: 10.1007/s42242-020-00103-6

Coyle, S., Majidi, C., LeDuc, P., and Hsia, K. J. (2018). Bio-inspired soft robotics: material selection, actuation, and design. *Extreme Mech. Lett.* 22, 51–59. doi: 10.1016/j.eml.2018.05.003

Ha, N. S., and Lu, G. (2020). A review of recent research on bio-inspired structures and materials for energy absorption applications. *Compos. Part B: Eng.* 181, 107496. doi: 10.1016/j.compositesb.2019.107496

Wegst, U. G. K., Bai, H., Saiz, E., Tomsia, A. P., and Ritchie, R. O. (2015). Bioinspired structural materials. *Nat. Mater.* 14, 23–36. doi: 10.1038/nmat4089

Zari, M. P. (2010). Biomimetic design for climate change adaptation and mitigation. *Architect. Sci. Rev.* 53, 172–183. doi: 10.3763/asre.2008.0065

frontiers in Ecology and Evolution

ORIGINAL RESEARCH
published: 19 November 2021
doi: 10.3389/fevo.2021.746254

Cortex Thickness Is Key for the Colors of Iridescent Starling Feather Barbules With a Single, Organized Melanosome Layer

Pascal Freyer[1†], Bodo D. Wilts[2†] and Doekele G. Stavenga[1†]*

[1] Zernike Institute for Advanced Materials, University of Groningen, Groningen, Netherlands, [2] Adolphe Merkle Institute, University of Fribourg, Fribourg, Switzerland

OPEN ACCESS

Edited by:
Ahu Gumrah Dumanli-Parry,
The University of Manchester,
United Kingdom

Reviewed by:
Hugo Gruson,
University of London, United Kingdom
Rox Middleton,
University of Bristol, United Kingdom

***Correspondence:**
Doekele G. Stavenga
D.G.Stavenga@rug.nl

†ORCID:
Pascal Freyer
orcid.org/0000-0002-9581-4693
Bodo D. Wilts
orcid.org/0000-0002-2727-7128
Doekele G. Stavenga
orcid.org/0000-0002-2518-6177

Specialty section:
This article was submitted to Behavioral and Evolutionary Ecology, a section of the journal Frontiers in Ecology and Evolution

Received: 23 July 2021
Accepted: 26 October 2021
Published: 19 November 2021

Citation:
Freyer P, Wilts BD and Stavenga DG (2021) Cortex Thickness Is Key for the Colors of Iridescent Starling Feather Barbules With a Single, Organized Melanosome Layer. Front. Ecol. Evol. 9:746254. doi: 10.3389/fevo.2021.746254

The iridescent plumage of many birds is structurally colored due to an orderly arrangement of melanosomes in their feather barbules. Here, we investigated the blue- to purple-colored feathers of the European starling (*Sturnus vulgaris*) and the blue and green feathers of the Cape starling (*Lamprotornis nitens*). In both cases, the barbules contain essentially a single layer of melanosomes, but in *S. vulgaris* they are solid and rod-shaped, and in *L. nitens* they are hollow and rod- as well as platelet-shaped. We analyzed the coloration of the feathers by applying imaging scatterometry, bifurcated-probe- and micro-spectrophotometry. The reflectance spectra of the feathers of the European starling showed multiple peaks and a distinct, single peak for the Cape starling feathers. Assuming that the barbules of the two starling species contain a simple multilayer, consisting locally only of a cortex plus a single layer of melanosomes, we interpret the experimental data by applying effective-medium-multilayer modeling. The optical modeling provides quantitative insight into the function of the keratin cortex thickness, being the principal factor to determine the peak wavelength of the reflectance bands; the melanosome layer only plays a minor role. The air cavity in the hollow melanosomes of the Cape starling creates a strongly enhanced refractive index contrast, thus very effectively causing a high reflectance.

Keywords: refractive index, effective medium approach, multilayer modeling, keratin, melanin, directional reflectance

INTRODUCTION

Many bird species feature a brightly colored plumage due to wavelength-selective absorbing pigments and/or more or less orderly arranged nano-scale structures (Durrer, 1977; Hill and McGraw, 2006; Kinoshita, 2008). A frequently occurring pigment in organisms is melanin, which causes, for example, the black feather colors of numerous bird species (McGraw, 2006) and has recently also attracted attention in bio-inspired materials (Xiao et al., 2020). In feathers of passerines that are colored by carotenoids, or parrot feathers colored by psittacofulvins, melanin functions to enhance color contrast by absorbing stray light that would otherwise desaturate the coloration (Tinbergen et al., 2013). Melanin has a similar contrast-enhancing function in feather barbs that

are structural colored due to nano-sized, spongy keratin structures (Prum, 2006; D'Alba et al., 2012; Tinbergen et al., 2013; Shawkey and D'Alba, 2017).

Remarkably, however, instead of being an effective absorber of light, melanised organelles (the melanosomes) can function as reflectors, because melanin has a relatively high refractive index (∼1.75) with respect to the bulk feather material, keratin (∼1.55; Mason, 1923; Durrer, 1977; Stavenga et al., 2015). When the melanosomes are contiguously packed in layers that alternate with keratin layers, they form optical multilayers in the barbules that highly reflect incident light within a restricted wavelength-range (Kinoshita, 2008). Striking examples where multilayers of solid melanin rodlets create bright reflectors include the feathers of birds-of-paradise (Durrer, 1977; Stavenga et al., 2011), common bronzewing pigeons (Xiao et al., 2014), and ducks (Eliason and Shawkey, 2012; Stavenga et al., 2017).

Air has a much lower refractive index than keratin, which causes a means to increase the refractive index contrast in a reflecting structure in feathers and therefore offers an attractive way to enhance their reflectance. For example, barbules with hollow melanin rodlets arranged in multilayers occur in turkey, magpie, and trogons (Durrer and Villiger, 1966; Eliason et al., 2013; Stavenga et al., 2018). Similarly, barbules with stacks of melanosomes that resemble hollow platelets generate the bright colors in many hummingbird feathers (Greenewalt et al., 1960; Durrer, 1977; Giraldo et al., 2018; Gruson et al., 2019; Eliason et al., 2020). In the unique case of peacock feathers, rectangular lattices of melanin rodlets and air channels embedded in the keratin matrix create highly reflecting barbules (Durrer, 1986). The rainbow of different colors of peacock feathers is realized by small variations in the dimensions of the lattice of air channels and melanin rodlets (Durrer, 1965; Zi et al., 2003; Freyer et al., 2019).

In the course of our studies on peacock feathers, we found that a crucial element of the peacock's photonic structures is the keratin cortex, a superficial layer of keratin overlying the layer of melanosomes. When the number of melanin and air channel layers is high, the cortex thickness has a minor effect on the reflectance spectrum of the barbules, but when the number of layers decreases, the cortex thickness becomes increasingly important (Freyer and Stavenga, 2020). We therefore decided to study the role of the cortex in greater detail in the limiting case where only a single layer of melanosomes exists. This is realized in the barbules of the colored feathers that are interspersed in the general blackish plumage of the European or Common starling, *Sturnus vulgaris*. Its melanin granules are solid rodlets (Durrer and Villiger, 1970). In the feather barbules of the Cape starling, *Lamprotornis nitens*, because of its exceptionally directional appearance also called the Cape glossy starling, a single layer of hollow, platelet-shaped melanosomes exists below a keratin cortex (Durrer and Villiger, 1970).

Here we investigate the effect of the different melanosome monolayers on the feather reflection properties of the two starling species. We calculate the reflectance spectra with an effective-medium-multilayer model based on realistic anatomical data and compare the results with optical measurements. We conclude that, for feather barbules with a single layer of melanosomes, the thickness of the cortex is the most important parameter that determines the feather color and that the characteristics of the melanosome layer are of secondary importance. The air cavity in the melanosomes of the Cape starling considerably enhances the reflectance and thus the feather coloration.

MATERIALS AND METHODS

Starling Feather Samples and Images

Feathers were collected from dead specimens of *S. vulgaris* (in the Netherlands, near Groningen) and *L. nitens* (in Namibia, near Windhoek). Photomacrographs were made with a Canon EOS 30D camera. Micrographs of single barbules were made with a Zeiss Universal microscope (Zeiss AG, Oberkochen, Germany) equipped with a Zeiss Epiplan 40 × /0.85 objective and a ScopeTek DCM510 camera. A Zeiss 100 × /1.3 oil immersion objective was used for visualizing the melanosomes.

Anatomy

Transmission electron microscopy (TEM) studies showed that the melanosomes of *S. vulgaris* are solid rodlets with a length of 1.2–1.7 μm and diameter of 0.250–0.254 μm (Durrer and Villiger, 1970). The hollow and platelet-shaped melanosomes found in the feather barbules of *Lamprotornis* species have a diameter of about 1.0 μm by 0.8 μm and a thickness of about 210–240 nm, because of two melanin layers of 70 nm and an intermittent air layer of 73–98 nm [as provided by Durrer and Villiger (1970); see also **Supplementary Tables 1, 2**]. We compared these values with data deduced from epi-illumination micrographs of barbules immersed in oil as well as with scanning electron micrographs (SEM) of the barbules (**Figures 2C**, **6C**). We measured >30 of the *S. vulgaris* melanosome rodlet widths from six different barbule cells from different barbs of a feather.

For SEM, small feather pieces were deposited on an aluminum SEM stub (Plano-EM, Wetzlar, Germany) covered with conductive carbon tape and subsequently sputter-coated with a 5 nm thick layer of gold, using a Cressington 208 HR sputter coater (Cressington Scientific Instruments, Watford, England). Additionally, silver paste was added to part of the feather piece to increase the conductivity of the sample, limit charging effects and provide a protecting envelope to limit curtaining effects when cutting the barbule. Electron microscope images were taken using a Thermo Scientific Scios 2 (FEI, Eindhoven, Netherlands) focused ion-beam scanning electron microscope (FIB-SEM). On-view images were recorded using the built-in Everhart-Thornley detector (ETD) with an electron beam current of 5 kV. To image the cross-section of the barbules, barbules embedded in silver paste were milled with the Ga-ion beam with 30 kV acceleration voltage and 1 nA beam current. Tilt-corrected images were acquired using the ETD and a beam current of 2 kV.

Multilayer Modeling

The starling barbules were treated as a simple multilayer in air consisting of a keratin cortex and a melanosome layer embedded in keratin. We calculated reflectance spectra for

normal illumination using a transfer matrix program, written in Matlab code, based on classical optical multilayer theory (Yeh, 2005; Stavenga, 2014). An effective medium approach was chosen as these are often more intuitive and computationally accessible than full wave simulations, as performed below. The effective refractive index of the layer with melanosomes was obtained by:

$$\tilde{n}_{\text{eff}} = (f_{\text{k}} n_{\text{k}}^{w} + f_{\text{m}} \tilde{n}_{\text{m}}^{w} + f_{\text{a}} n_{\text{a}}^{w})^{1/w} \quad (1)$$

where f_{k}, f_{m}, and f_{a}, are the volume fractions of the keratin, melanin, and air components, with $f_{\text{k}} + f_{\text{m}} + f_{\text{a}} = 1$; w is a weighting factor. The implemented refractive index of keratin was assumed to be pure dielectric with $n_{\text{k}} = A_{\text{k}} + B_{\text{k}}\lambda^{-2}$ with $A_{\text{k}} = 1.532$ and $B_{\text{k}} = 5890$ nm^2, as keratin absorption in the visible is negligible (Leertouwer et al., 2011). The applied refractive index of melanin was complex: $\tilde{n}_{\text{m}} = n_{\text{m}} - ik_{\text{m}}$ where $n_{\text{m}} = A_{\text{m}} + B_{\text{m}}\lambda^{-2}$ and $k_{\text{m}} = a_{\text{m}} \exp(-\lambda/b_{\text{m}})$, with $A_{\text{m}} = 1.648$, $B_{\text{m}} = 23700$ nm^2, $a_{\text{m}} = 0.56$, and $b_{\text{m}} = 270$ nm (Stavenga et al., 2015); the refractive index of air is wavelength-independent, with $n_{\text{a}} = 1$. In the case of solid melanosomes (*S. vulgaris*), the effective refractive index of the melanosome layer was calculated with $f_{\text{a}} = 0$. In a previous study on magpie feather barbules with stacked hollow melanosomes, a weighting factor w varying between −2.0 and 2.0 was found to have distinct effects on the calculated reflectance spectra (Stavenga et al., 2018; similar effects occur in peacock barbules, see Freyer et al., 2019). However, in the present cases of barbules with a single melanosome layer, the reflectance spectra calculated for various values of w were very similar, and therefore all results presented here were obtained with a weighting factor $w = 1$.

To ascertain the validity of the effective medium approach, we furthermore performed for a few cases FDTD modeling, using Ansys Lumerical R2021.1 (see **Supplementary Figures 1, 2**). For these simulations, an idealized structured multilayer of keratin and melanin was placed in a 2D simulation box with a length of 2 μm and a width determined by the modeled melanosome with periodic boundary conditions along the structure dimensions and perfectly matched layers (PMLs) in the direction of light illumination. The illumination was a linearly polarized, broadband light source (300–900 nm). A reflection monitor placed behind the light source measured the reflectance.

Imaging Scatterometry

The spatial reflection of the barbules was visualized by imaging scatterometry (ISM). An isolated barbule was glued to the tip of a glass micropipette (Stavenga et al., 2009; Wilts et al., 2009). A narrow-aperture (< 5°) white-light beam was focused on a small circular area (diameter 13 μm) of a single barbule cell and the spatial distribution of the far-field scattered light was then monitored. The exposure times were adjusted to obtain a sufficiently clear image without overexposure.

Spectrophotometry

Reflectance spectra of different areas of the starling feathers, about 2 mm in diameter, were measured with a bifurcated reflection probe (Avantes FCR-7UV200), using a CCD detector array spectrometer (Avantes AvaSpec-2048, Apeldoorn, Netherlands). The light source was a deuterium-halogen lamp (Avantes AvaLight-D(H)-S), and the reference was a white diffusely scattering reflection tile (Avantes WS-2). Reflectance spectra of small barbule areas were measured with a microspectrophotometer (MSP). The MSP was a Leitz Ortholux microscope (Leitz, Wetzlar, Germany) with a LUCPlanFL 20 × /0.45 objective (Olympus, Tokyo, Japan) and a xenon arc light source. The area measured with the MSP was a square (edge length ∼5 μm) that was determined by a diaphragm in the microscope's image plane. The latter was imaged at the entrance of an optical fiber connected to the detector array spectrometer. Due to the glass optics inside the microscope, the MSP spectra were limited to wavelengths > 360 nm. However, this limitation is compensated by the bifurcated reflection probe measurements that yield a reliable signal between 250–900 nm. Note that the probe and MSP collect light from a limited aperture, and therefore the measured reflectance depends on the spatial reflection properties of the object, for instance its local flatness. All optical measurements were conducted with illumination at normal incidence.

RESULTS

The European Starling, *Sturnus vulgaris*

Feathers, Barbules and Melanosomes

The plumage of the European starling (*S. vulgaris*) is gray-black with whitish spots, but it can prominently feature metallic blue, green or purple feather areas (**Figure 1A**). Epi-illumination light microscopy demonstrated that the colors originate from the feather barbules, which branch from either side of the barbs and partly overlap each other (**Figures 1B,C**). The barbules consist of a row of more or less flat cells, each exposing a surface with size ∼30 × 60 μm^2. The hue can differ between neighboring cells, but within a cell the hue varies only slightly, which indicates that the anatomical variation within a single barbule cell is small (**Figures 1D,E**).

As shown by electron microscopy, the barbule cell border is marked by a layer of melanosomes below a keratin cortex layer (**Figures 2A,B**). Numerous melanosomes exist in the barbule's central area, but they are randomly distributed (**Figures 2A,B**). The TEM data from previous literature yielded virtually identical values for the melanosome diameters of the green and purple barbules: $D_{\text{m}} = 250$ nm and $D_{\text{m}} = 254$ nm, respectively, (Durrer and Villiger, 1970). Our SEM images of cross-sectioned barbules (**Figure 2B**) also yielded similar, but slightly larger mean diameters of 273 ± 20 nm and 271 ± 25 nm for the green and purple barbules, respectively. The cortex thickness of the green and purple barbules varies over the width of the barbule and was estimated to be 275 ± 30 nm and 336 ± 27 nm, respectively.

To visualize the melanosomes of the starling's feather barbules *in situ*, we applied epi-illumination microscopy on barbules immersed in oil (**Figure 2C**). The micrographs show ∼1.5 μm long, rod-shaped melanosomes, arranged in clusters that are generally oriented parallel to the barbule axis (**Figures 2C,D**; **Figure 2C** shows an example of a melanosome cluster with a deviant orientation). The micrographs yielded an interdistance

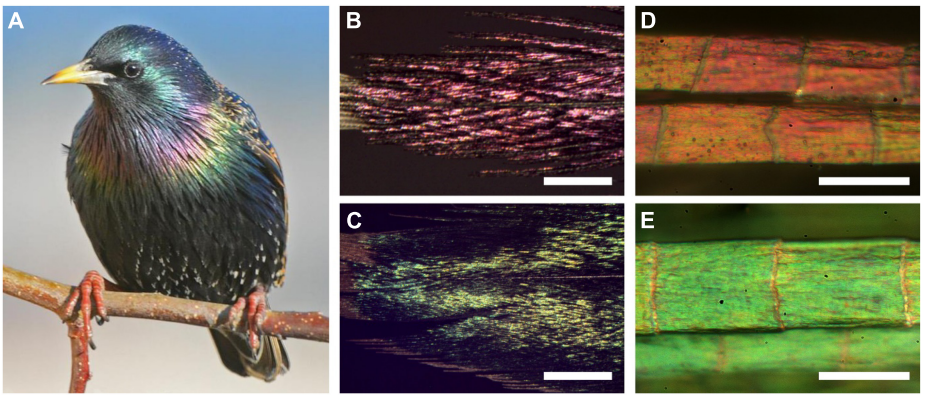

FIGURE 1 | The European starling, *Sturnus vulgaris*, and its structural colors. **(A)** A starling with colorful throat and breast feathers (photograph by Nathan deBoer). **(B-E)** Epi-illumination light microscopy images of **(B)** a throat feather, **(C)** a breast feather, **(D)** throat barbules, and **(E)** breast barbules. Scale bars: **(B,C)** 1 mm; **(D,E)** 50 μm.

of the melanosome rodlets in the green barbules of 349 ± 25 nm and for the purple barbules 351 ± 22 nm, meaning that the melanosomes are on average spaced apart by D_i = ∼80 nm.

The anatomy suggests that the barbule's cortex and melanosome layer form a simple layer-based interference reflector that causes the structural coloration. We tested this hypothesis by applying imaging scatterometry (**Figure 2F**). Local illumination of a purple barbule by a narrow aperture light beam indeed produced a scatterogram with a very restricted light spot. This signature of a very directional reflection validates the assumption. We note, however, that frequently the local scatterogram patterns deviated from an ideal, single spot. Clearly, the barbule is not flat throughout its width, as also evident from the anatomical data (**Figures 2A,B**).

Multilayer Modeling

We calculated the barbule's reflectance spectra with an effective-medium-multilayer model (**Figure 3**). We treated the barbule structure as a multilayer, consisting of a keratin cortex (thickness c, facing air) and a single layer of rodlet-shaped melanosomes (diameter D_m, interdistance D_i) in a keratin matrix (see inset of **Figure 3A**). The colored feathers differ in the thickness of the barbule cortex, as for blue-green and red-violet feathers c = 290 nm and c = 330 nm, respectively (**Figure 2** and Durrer and Villiger, 1970). For our initial calculations, we took for the cortex thickness c = 310 nm together with a melanosome diameter D_m = 250 nm as a starting point, as these values should produce reflectance values in the visible wavelength range. We used these values and the refractive indices of keratin and melanin in Eq. 1 to calculate the real and imaginary effective refractive index profiles, Re ($\tilde{n}_{eff}$) and Im($\tilde{n}_{eff}$), along the coordinate perpendicular to the barbule surface. We then investigated the influence of varying parameters within a realistic parameter range chosen to be slightly larger than the derived values.

At first, we investigated three cases, where the melanosome interdistance is D_i = 0, 50, and 100 nm. By applying a transfer matrix-based calculation procedure, we then obtained the reflectance and transmittance spectra (**Figures 3B,C**). The reflectance spectra of **Figure 3B** show two distinct bands, peaking in the UV, at ∼340 nm, and in the green, at ∼510 nm. The reflectance amplitude slightly decreases with an increasing melanosome separation (**Figure 3B**), together with a slight increase of the transmittance (**Figure 3C**), but the spectral shapes hardly depend on D_i. To check the effective medium results, we performed FDTD calculations for the case D_m = 250 nm, D_i = 0 nm, and c = 310 nm, for both TE- and TM- polarized light, yielding reflectance spectra that are virtually identical to those of **Figure 3B** (**Supplementary Figure 1**).

The transmittance increases with increasing wavelength, which is immediately recognized as the hallmark of melanin absorption. To assess the possible effect of absorption on the reflectance, we assumed that the melanin refractive index is real instead of complex. The reflectance spectrum then obtained, for the case D_i = 0 (**Figure 3B**, green curve), has a slightly higher amplitude than the spectrum resulting with the complex refractive index, and its peak wavelength is a few nm shifted, but overall the effect of melanin absorption on the reflectance spectrum can be considered to be minor. When fully neglecting melanin absorption, given a reflectance of at most a few percent (**Figure 3B**), the transmittance becomes almost 100%, as expected (**Figure 3C**, green curve).

In studies of the structural coloration by melanosomes, the layers are often assumed to create discrete, stepwise changes in refractive index (see, e.g., Doucet et al., 2006). In our effective medium approach, we implemented more realistic, gradual changes in the refractive index by interpolation and thresholding with a very fine mesh. We investigated the difference between gradual and stepwise changes of the refractive index by comparing an array of contiguous solid rodlets, diameter D_m = 250 nm and D_i = 0 nm, with a few discrete layers, homogeneously filled with the same total amount of melanin (**Figures 3D–F**). **Figure 3D** shows the real and imaginary effective refractive index profiles for four cases: (i) the rodlets with gradually changing melanin fraction f_m with averaged melanin content $(\pi {D_m}^2/4)/D_m = \pi D_m/4$; (ii) a discrete layer with pure melanin, f_m = 1 and thickness $\pi D_m/4$; (iii) a discrete layer

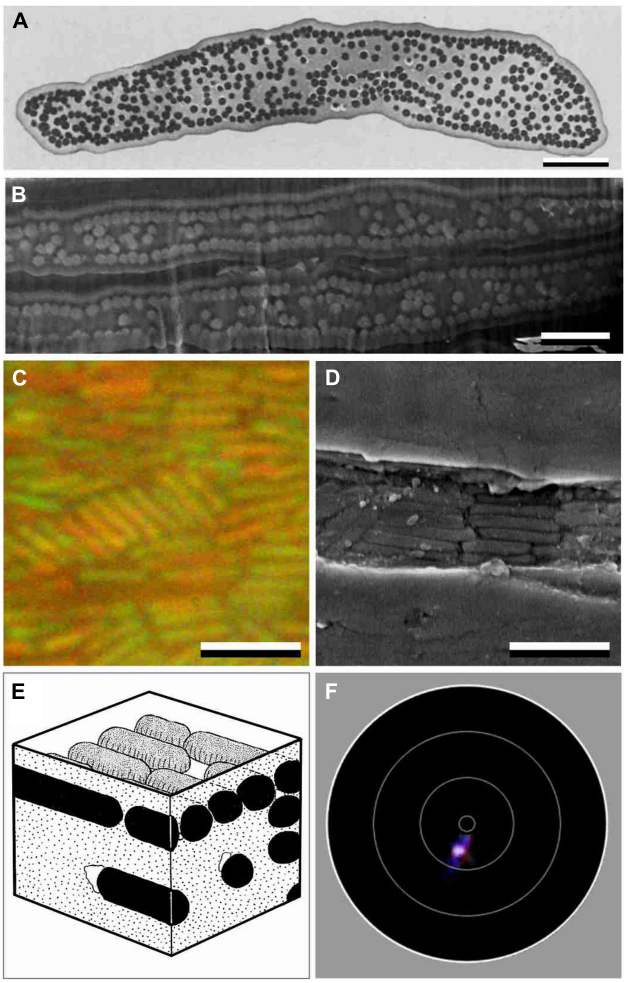

FIGURE 2 | Anatomy and scatterometry of starling barbules with solid melanosomes. **(A)** Transmission electron micrograph of a barbule cross section of the Sulawesi myna starling, *Basilornis celebensis* [modified after Durrer (1977)]. **(B)** FIB-SEM of a cross-section of two adjacent barbules of a *S. vulgaris* feather. **(C)** Epi-illumination micrographs of a green barbule of *S. vulgaris* in oil immersion. **(D)** FIB-SEM on-view of a *S. vulgaris* barbule where the cortex was accidently absent. **(E)** Diagram of a *S. vulgaris* barbule with melanosome rodlets in a keratin matrix [from Durrer (1977)]. **(F)** Imaging scatterogram of a purple barbule of *S. vulgaris*. The white circles in the diagrams indicate polar angles of 5°, 30°, 60° and 90°. Scale bars: **(A–D)** 2 μm.

with reduced melanin, $f_m = \sqrt{\pi}/2$ and thickness $D_m\sqrt{\pi}/2$; (iv) a discrete layer with even less melanin, $f_m = \pi/4$, and thickness D_m. In all cases, the location of the center of the melanosome layers was identical (**Figure 3D**). The reflectance spectra calculated for the four cases have similar shapes and peak wavelengths (∼510 nm) in the visible wavelength range, but the reflectance magnitudes of the extrema differ slightly (**Figure 3E**). As expected, the transmittance spectra are virtually identical, because the total melanin content is identical (**Figure 3F**).

The total melanin content is not constant when varying the diameter of the melanin rodlets (**Figures 3G–I**). We considered three cases of the melanosome diameter: D_m = 250, 300, and 350 nm, with interdistance D_i = 0 nm, keeping a constant cortex thickness c = 310 nm. Again, the detailed shape of the resulting reflectance spectra varies, but the spectral location of the UV stays about the same and the band in the green wavelength range (up to about 630 nm) varies only in its detailed shape (**Figure 3H**). In the long wavelength range, the reflectance peak moves bathochromic (to longer wavelengths) due to the increased optical pathlength resulting from the thicker melanin layer. Also, with an increasing rodlet diameter, the melanin content increases, causing a decrease in the transmittance (**Figure 3I**).

We finally investigated the effect of the cortex thickness. In addition to the values c = 290 and 330 nm informed by EM measurements of **Figure 2B** and literature (Durrer and Villiger, 1970), we also applied slightly smaller c = 250 nm and larger thicknesses c = 370 nm to investigate the effect on the color response. For all cases, D_m = 250 nm and D_i = 0 nm are kept constant (**Figures 3J–L**). The resulting reflectance spectra have all obtained approximately the same shape, but the peak wavelengths of the four cases, 455, 496, 536, and 577 nm, respectively, are shifted ∼40 nm with respect to each other along the wavelength abscissa (**Figure 3K**). The transmittance spectra are virtually identical again (**Figure 3L**). We can conclude from the various parameter values that the cortex thickness is the most sensitive parameter that determines the barbule's reflectance spectrum and thereby its color.

Comparison of Measured and Modeled Reflectance Spectra

We measured reflectance spectra in single cells of various colored feather barbules of *S. vulgaris* using a microspectrophotometer (MSP). **Figures 4A,B** show MSP spectra from barbule cells of a green and purple feather, respectively. Although the shape of the different spectra is similar, they are shifted with respect to each other by several tens of nm, and also the amplitude varies quite noticeably. The latter may be a consequence of the measurement procedure, because the objective of the microspectrophotometer projects a light beam with a considerable aperture onto the barbule. Since the barbule and its multilayer reflector is not perfectly flat, part of the reflected light will not be captured by the objective. In other words, even when the local cortex thickness and melanosome layer remain constant and the spectral shape thus stays the same, the amplitude of the measured reflectance will vary with the shape of the barbule surface.

In order to estimate the local cortex thicknesses, we compared two examples of measured spectra with spectra calculated with the above model. To obtain a close fit, we adjusted the parameters. Taking again D_m = 250 nm, satisfactory fits for the case of a blue-green and a purple barbule were obtained with c = 300 nm and c = 390 nm, respectively, (**Figure 4C**).

Whereas the reflectance spectra measured locally from within a single barbule cell area vary (**Figures 4A,B**), the coloration observed visually will be the sum of local reflection spectra. This can be illustrated by measuring the reflectance with a bifurcated probe, which integrates the reflections from an area on the order of 1 mm^2. The different colored feather areas then yield clearly distinct reflectance spectra (**Figure 4D**).

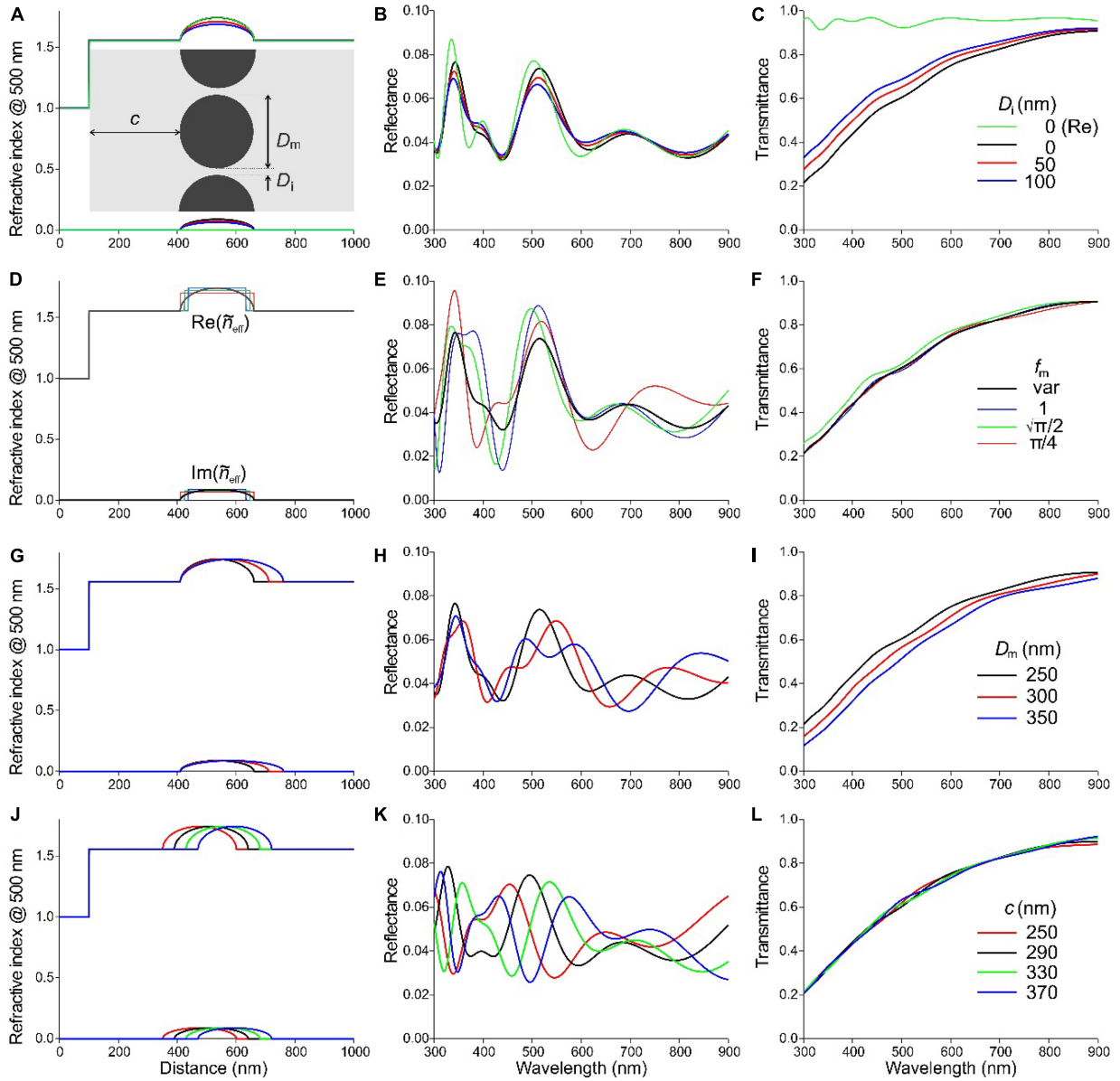

FIGURE 3 | Effective-medium-multilayer modeling of a *S. vulgaris* barbule. **(A–C)** Rodlet melanosomes with diameter D_m = 250 nm and interdistance D_i = 0, 50, and 100 nm embedded in a keratin barbule at a distance c = 310 nm from the border. In the legend of **(C)**, (Re) concerns the case where the refractive index is real, i.e., the melanin is absorptionless. **(D–F)** The case of a layer of rodlet melanosomes with varying melanin fraction (f_m var) compared with discrete melanin layers of different melanin fraction and layer thickness (see text for details). **(G–I)** Melanosomes with diameter D_m = 250, 300, and 350 nm. **(J–L)** Layer of melanosomes, diameter D_m = 250 nm, interdistance D_i = 0 nm, with cortex thickness c = 250, 290, 330, and 370 nm. **(A,D,G,J)** Profiles of the real and imaginary refractive index at 500 nm. The barbule (and cortex) surface is at abscissa (distance) value 100 nm. **(B,E,H,K)** Reflectance spectra. **(C,F,I,L)** Transmittance spectra.

Feathers of the Cape Starling, *Lamprotornis nitens*

Feathers, Barbules and Melanosomes

Compared to the European starling, the Cape starling (*L. nitens*) has a much more impressive coloration, with striking metallic colors throughout its entire iridescent plumage (**Figure 5A**). The head, body and wing feathers are colored variously blue-green (**Figure 5B**), while the tail is uniformly blue (**Figure 5C**). Micrographs show that individual barbule cells are again rather uniformly colored, but the color of adjacent cells can differ substantially (**Figures 5D,E**).

The Cape starling has hollow melanosomes (Craig and Hartley, 1985; Maia et al., 2013). A transmission electron micrograph of a barbule cross-section of a related glossy starling, the Superb starling *Lamprotornis superbus*, shows a single layer of hollow melanosomes, which line the entire barbule perimeter like the melanosomes of *S. vulgaris* barbules; in the barbule interior some randomly arranged hollow melanosomes are seen

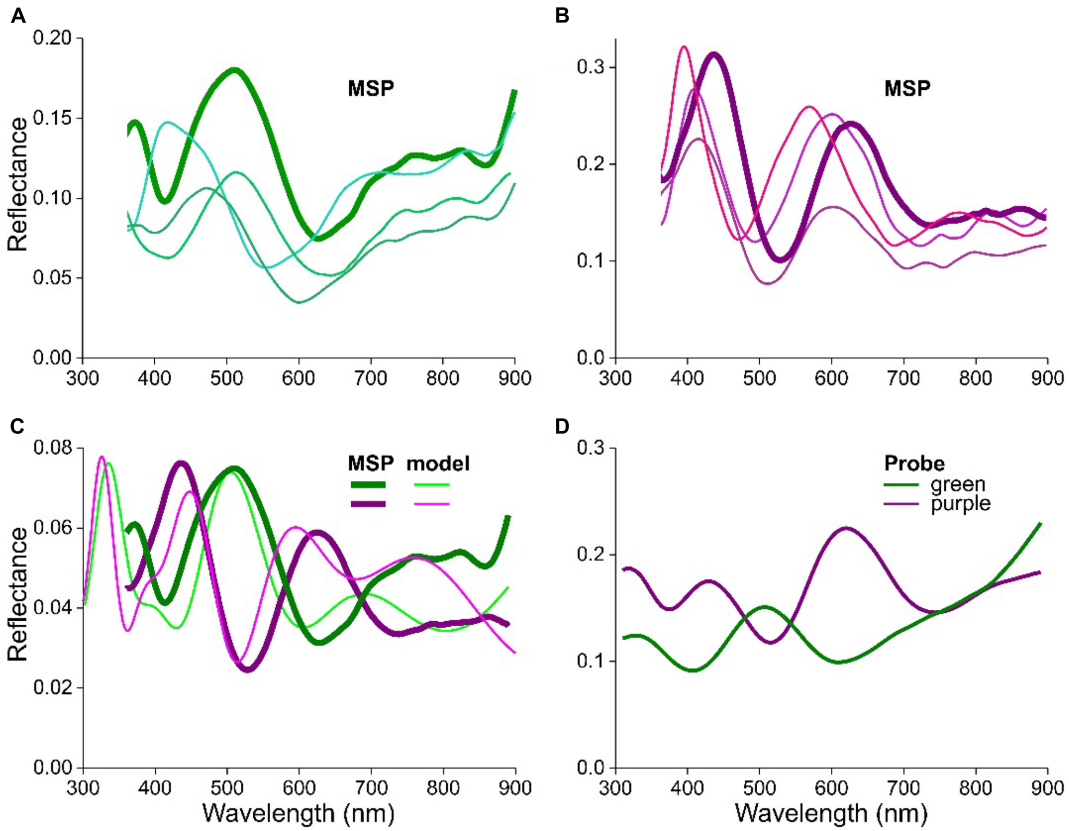

FIGURE 4 | Reflectance spectra of feathers and barbules of *S. vulgaris*. **(A)** Spectra from local areas of a green breast barbule measured with a microspectrophotometer (MSP). **(B)** Spectra from local areas of a purple throat barbule measured with the MSP. **(C)** The bold MSP spectra of **(A,B)** compared with modeled (model) spectra for cortex thicknesses of 300 nm (green) and 390 nm (purple). **(D)** Reflectance spectra measured with a bifurcated reflection probe of a green and purple wing area.

FIGURE 5 | The Cape starling (*L. nitens*) and its structural colors. **(A)** A starling with its main blue and some green feathers (photograph by T. Schoch). **(B,C)** Photographs of a **(B)** green secondary feather and **(C)** a blue tail feather. **(D,E)** Epi-illumination light microscope images of **(D)** a secondary feather barbule and **(E)** a tail feather barbule. Scale bars: **(B,C)** 2 cm, **(D,E)** 20 μm.

[**Figure 6A**; from Durrer and Villiger (1970)]. Scanning electron micrographs of cross-sections of the investigated *L. nitens* barbules show essentially the same organization (**Figure 6B**) and gives a cortex thickness of about 118 ± 25 and 185 ± 31 nm for the blue and the green barbule, respectively.

Durrer and Villiger described the melanosomes of four *Lamprotornis* species as platelet-shaped, with a compact melanin sheet that envelopes a honeycomb-like air-filled space (Durrer and Villiger, 1970). Epi-illumination microscopy on feather barbules of *L. nitens* immersed in oil visualized the melanosomes (**Figure 6C**). The resulting images differed remarkably from those of the European starling in that they show a distribution of different melanosome shapes with a majority of doughnut-like shapes intermingled with small bars. These different shapes were

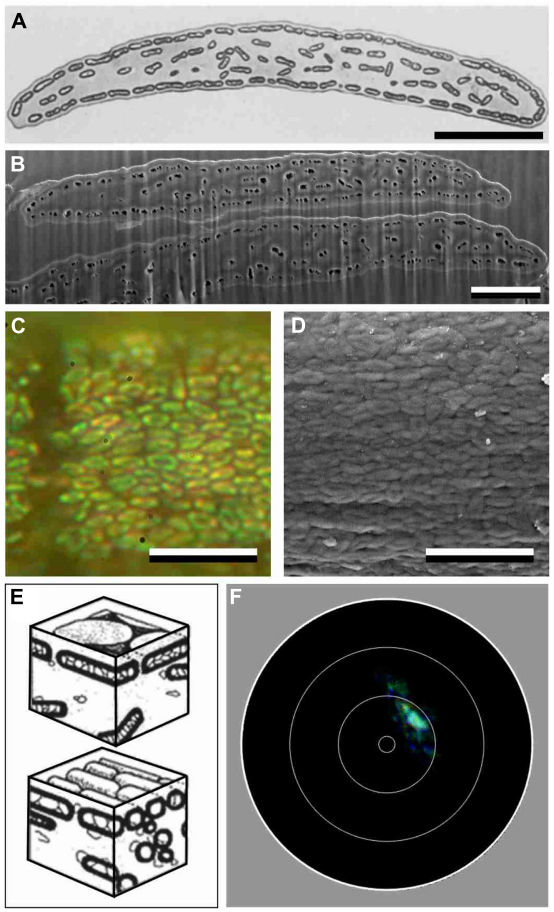

FIGURE 6 | Anatomy and scatterometry of a barbule of *L. nitens*. **(A)** Transmission electron micrograph (TEM) of a barbule cross-section of the Superb starling, *Lamprotornis superbus* [modified after Durrer (1977)]. **(B)** Scanning electron micrograph (SEM) of a cross- section of two overlapping barbules of *L. nitens*. Note that the contrast between TEM and SEM is reversed: melanin is dark in **(A)**, but it is light in **(B)**, while the air holes of the melanosomes are light in **(A)** and dark in **(B)**. **(C)** Epi-illumination micrographs of a blue barbule of *L. nitens* in oil immersion. **(D)** Scanning electron micrograph of the surface of a *L. nitens* feather barbule. **(E)** Diagrams of the two types of hollow melanosomes encountered in *Lamprotornis* starlings [from Durrer (1977)]. **(F)** Imaging scatterogram of a green barbule of *L. nitens*. Scale bars: **(A–D)** 5 μm.

also visible in scanning electron micrographs of the surface of an *L. nitens* feather barbule (**Figure 6D**).

The immersion images suggest that the melanosomes are less uniform in size and shape than the melanosomes of *S. vulgaris*. The images show the appearance of bars and doughnut-like shapes in **Figures 6C,D**, which might either suggest a mixture of melanosome shapes ranging between rodlets and platelets (**Figure 6E**), or a disordered arrangement of platelets alone. An extensive comparative study on the melanosomes of African starlings demonstrated that the melanin granules of *Lamprotornis* may be short and thick as well as slender and elongated (Craig and Hartley, 1985). Evolutionary transitions between rodlets and platelets have been recently suggested for starlings (Maia et al., 2013; Rubenstein et al., 2021). Furthermore, the interior of the melanosomes is presumably not fully hollow as TEM studies showed the existence of minor cross-linking elements (**Figure 6E**).

Whatever the fine structure, the single layer of melanosomes together with the keratin cortex will create a multilayer reflector. We investigated this by mounting a blue feather piece in the imaging scatterometer. Narrow beam illumination of a small barbule area yielded a quite discrete spot, demonstrating that locally the barbule indeed approximates an ideal reflector (**Figure 6F**). Similar as with the European starling, we often obtained scatterograms with more distributed patterns, indicating a varying flatness of the barbules' multilayers.

Multilayer Modeling

For the modeling of the reflectance spectra, we used anatomical data of the feathers of the Lesser blue-eared glossy-starling, *L. chloropterus*, as it is closely related to *L. nitens* and similarly colored (Durrer and Villiger, 1970; Craig and Hartley, 1985; Maia et al., 2013) in addition to the EM data of the investigated cross-sections. **Figure 7A** presents a diagram of a barbule with cortex thickness c and cylindrical, hollow melanosomes, membrane thickness d_m, air cavity thickness d_a, and width W_m, separated from each other by a distance W_i. For the modeling we used d_m = 70 nm and d_a = 85 nm (**Figure 6**; Durrer and Villiger, 1970). We first investigated the effect on the reflectance of an incomplete filling of the melanosome layer. For our initial calculations we took for the cortex thickness c = 160 nm, and we assumed, based on the electron micrographs, that the honeycomb of thin melanin membranes within the air cavities take up 10% of the volume, so that the inside air fraction is 0.9. The keratin filling factor of the melanosome layer $g = W_i/W_m$ has the value g = 0 when the melanosomes touch each other. With an increase of the filling factor to g = 0.1 and g = 0.2, the refractive index contrast of the melanosome layer decreases, as shown in the refractive index profiles (**Figure 7B**). The calculated reflectance spectra show that this causes a decrease of the reflectance amplitude, but the peak wavelength remains virtually the same (**Figure 7C**).

We subsequently considered a change in the air cavity thickness from 75 to 95 nm (well sampling the range reported for various *Lamprotornis* species of 73 to 98 nm; Durrer and Villiger, 1970). This causes slight changes in both the amplitude and peak wavelength of the reflectance spectra (λ_{max}), but their shape remains about the same (**Figure 7D**). For d_a = 75, 85, 95 nm, λ_{max} = 472, 479, and 486 nm, respectively, i.e., a 10 nm increase of the air cavity thickness causes a 7 nm peak wavelength shift (**Figure 7D**).

To underscore the effective medium results, we performed FDTD calculations for the case d_m = 70 nm, d_a = 85 nm, and c = 160 nm, for both TE- and TM-polarized light (**Supplementary Figure 2**). The calculated TE- and TM-reflectance spectra slightly differ in amplitude, demonstrating the effect of anisotropy of the melanosomes. Nevertheless, the reflectance spectra obtained for different filling factors with effective-medium-multilayer modeling and FDTD were virtually identical (**Figure 7C** and **Supplementary Figure 2**).

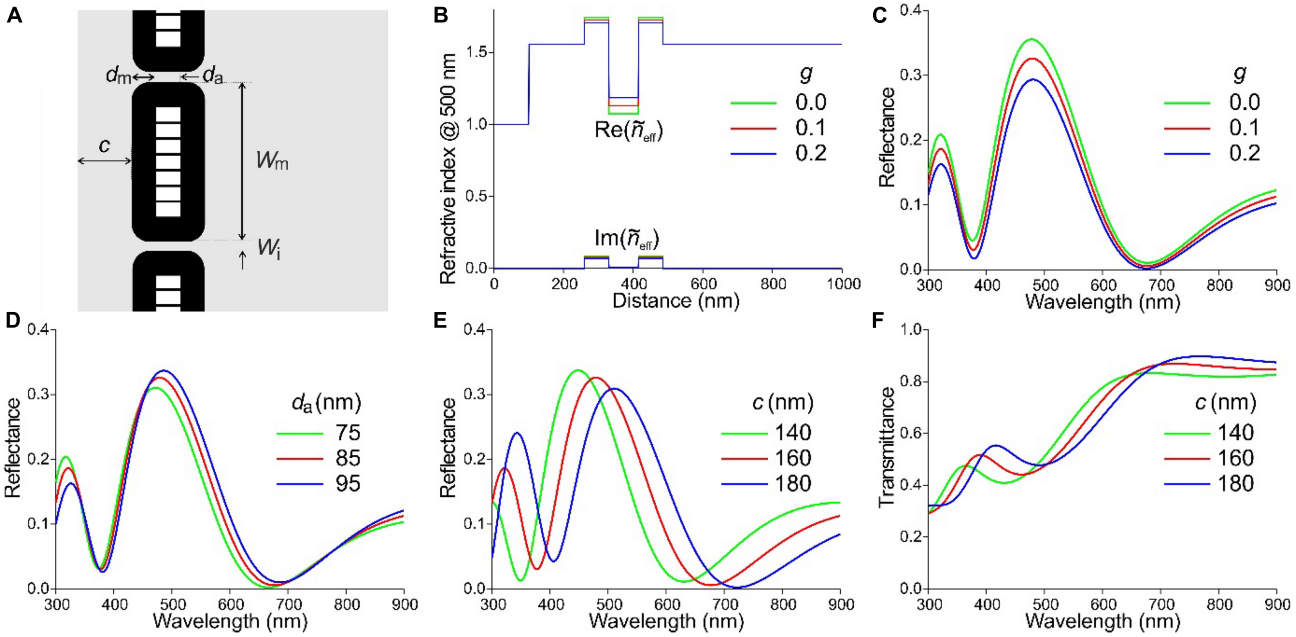

FIGURE 7 | Effective-medium-multilayer model of the *L. nitens* barbule anatomy. **(A)** Diagram of a barbule with cortex thickness c and hollow melanosomes with membrane thickness d_m, air cavity thickness d_a, width W_m, separated from each other by a distance W_i. **(B)** Real and imaginary refractive index profiles following from **(A)**; for parameter values, see text. **(C)** Reflectance spectra resulting for a few values of the keratin filling factor of the melanosome layer, g. **(D)** Reflectance spectra resulting for a few values of the air cavity thickness. **(E)** Reflectance spectra resulting for a few values of the cortex thickness. **(F)** Transmittance spectra corresponding to **(E)**.

Changes in the cortex thickness again have a substantial effect on the reflectance spectra (**Figure 7E**). For c = 140, 160 and 180 nm, the peak wavelength is λ_{max} = 449, 480, and 511 nm, respectively, i.e., an increase of the cortex thickness by 20 nm causes a 31 nm peak wavelength shift. **Figure 7F** shows the related transmittance spectra, where the melanin absorption spectrum is still well recognizable, but the transmittance in the blue-green wavelength range is reduced due to the higher reflectance in this band.

Comparison of Measured and Modeled Reflectance Spectra

We measured reflectance spectra of the variously colored feather barbules of *L. nitens* with a microspectrophotometer (MSP) on local areas of single barbule cells. **Figures 8A,B** show MSP spectra from single barbule cells of a blue and green feather, respectively. As in the case of the European starling, the shape of the various spectra is similar, but their spectral location somewhat differs, and even more their amplitudes. This will again be due to the dependence on the local barbule shape as well as the multilayer dimensions.

We compared two of the measured spectra with spectra following from optical modeling. Satisfactory fits were obtained for the tail feather barbules using a cortex thickness c = 135 nm and for the covert feather barbules c = 188 nm (**Figure 8C**). Nearly identical fits to the different color spectra of *L. nitens* could also be obtained by changing the melanosome air cavity thickness and/or the melanin membrane thickness, but the necessary parameter variation was larger for the air cavity thickness and the melanin membrane thickness than the 53 nm change that was necessary in cortex thickness variation. This would be beyond the range reported in the literature. We furthermore measured reflectance spectra of the tail and covert feathers of *L. nitens* with a bifurcated reflection probe (**Figure 8D**). The spectra are representative for the observed colors and closely resemble the averaged reflectance spectra of **Figures 8A,B**.

DISCUSSION

Here we performed a study on two starling species that combines optical modeling and direct optical and ultrastructural measurements on the barbules of starling feathers that contain a single layer of melanosomes. The experimentally obtained reflectance spectra could be interpreted well with effective-medium-multilayer modeling (**Figures 4C**, **8C**). In the optical modeling, we treated the barbules as containing a cortex with a single melanosome layer. However, the barbule interior contains randomly located melanosomes, which will contribute to the reflectance, because they will scatter light transmitted by the cortex-melanosome layers.

The transmittance calculations show that already a single melanosome layer considerably reduces the transmittance throughout the visible wavelength range. Consequently, the melanosomes of the barbule interior may somewhat enhance the reflectance in the longer wavelength range but they will also further reduce the transmittance at all wavelengths. A further

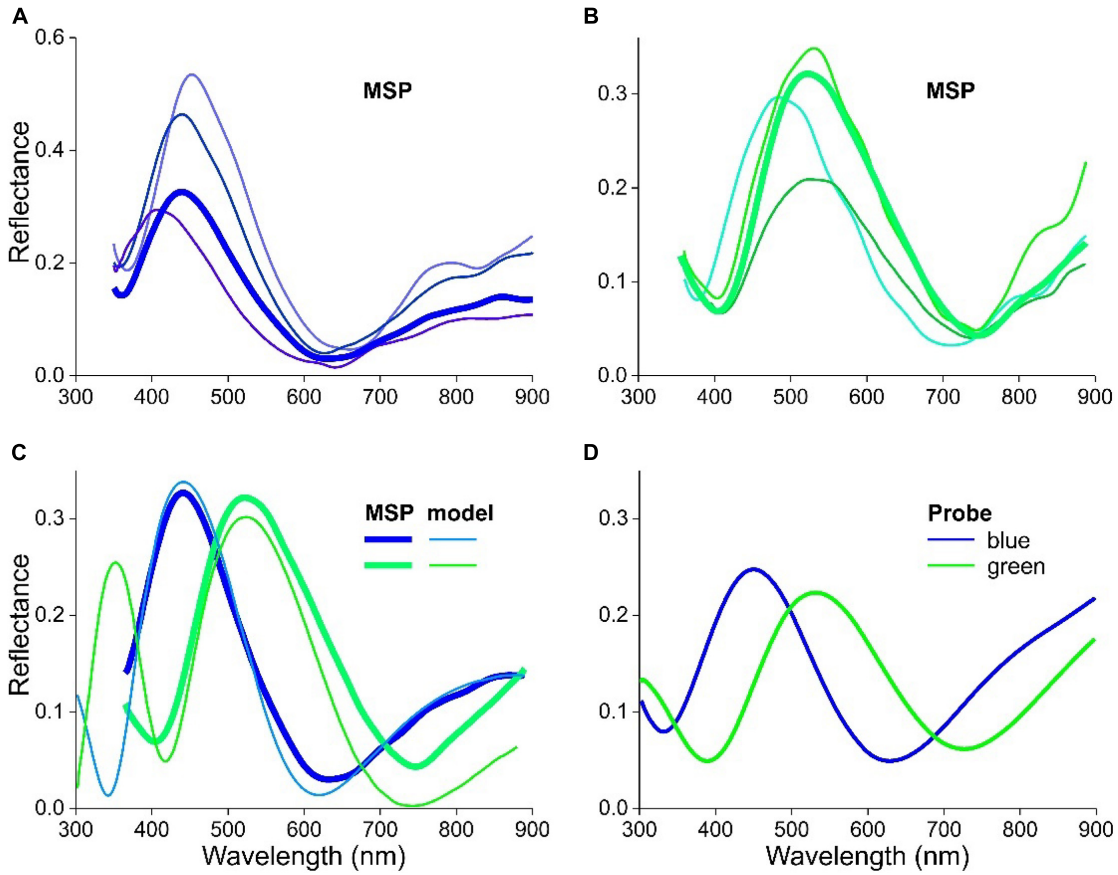

FIGURE 8 | Reflectance spectra of feathers and barbules of *L. nitens*. **(A)** Spectra of a tail feather measured with a microspectrophotometer. **(B)** Spectra of a covert feather measured with a microspectrophotometer. **(C)** An MSP spectrum of (A) compared with a modeled spectrum for a barbule with cortex thickness c = 135 nm (blue) and an MSP spectrum of **(B)** compared with a modeled spectrum for a barbule with cortex thickness c = 188 nm (green). **(D)** Spectra of a tail (blue) and covert (green) feather measured with a bifurcated probe.

contribution to the barbule reflectance could originate from the melanosome layer and cortex at the barbule's underside. However, the fraction of the light flux that is transmitted by the upper multilayer, passes through the interior and then is reflected (firstly) at the lower multilayer layers and (secondly) at the barbule's underside will be very minor. In other words, already with a monolayer of melanosomes near the barbule boundary, the reflectance is set by the layer on the illuminated side. Similarly, previous studies on mallard and magpie feathers, which have barbules with several layers of melanosomes on both sides of the barbules, demonstrated that the upper stack determines the barbule reflectance (Stavenga et al., 2017, 2018).

In a thin-film modeling study on blue-black grassquit feather barbules, where a keratin layer overlies a single melanin layer, Maia et al. (2009) similarly, concluded that a keratin layer above a melanin layer mainly determines the reflectance spectrum. Furthermore, a study on tree swallow barbules indicated that humidity-induced reflectance changes resulted from a modified cortex thickness (Eliason and Shawkey, 2010). Also, in a comparative study on a large number of bird species with matte and glossy plumage, Maia and colleagues emphasized the role of the keratin layer when the feather barbules have a single layer of melanosomes. Using thin film modeling, the authors concluded that a keratinous cortex thickness of 110–180 nm together with a melanosome layer with thickness greater than 115 nm causes glossy feathers (Maia et al., 2011). In these previous studies on bird feather coloration, the refractive indices of keratin and melanin were assumed to be wavelength-independent, and the real part of the refractive index of melanin of 2.0 was used. In the present study, we implemented the recently measured wavelength-dependent refractive index values of the different feather components, where the real part decreases from 1.8 to 1.7 for melanin (Leertouwer et al., 2011; Stavenga et al., 2015). The excessively high melanin refractive index used in the previous studies hence has not gravely affected the results for a single melanin layer, but will have larger implications for the optical function of more complex photonic multilayer structures (Wilts et al., 2014).

A high refractive index contrast is caused by the air compartments in the hollow melanosomes of *L. nitens*, which thus realizes a much higher barbule reflectance compared to

S. vulgaris. Hollow melanosomes therefore might have been selected in *L. nitens* due to the intensely directional appearance they generate. Since the exact dimensions of the melanosomes are again less relevant than the cortex thickness (**Figures 7C,D**), the keratin cortex most effectively determines the location of the spectral peaks (**Figure 7E**).

Our present measurements as well as modeling were only performed for normally incident light. The feather colors will depend on the angle of illumination or observation, due to the layered structure of the feathers, which causes iridescence. A hypsochromic shift of the reflectance spectra will occur with increasing angle of light incidence, as is amply shown in related papers (see, e.g., Eliason and Shawkey, 2012; Stavenga, 2014; Xiao et al., 2014). Accordingly, illumination with a wide-aperture light source, which was the case in the experiments with an oil immersion objective (**Figures 2C**, **6C**), will cause a strongly broadened reflectance spectrum and thus a color strongly differing from that seen with a low power objective (**Figures 1**, **5**).

Sturnus vulgaris has iridescent feathers containing solid melanosomes in a small part of the modestly shiny plumage, but *L. nitens* has barbules with hollow melanosomes in most feathers, which likely causes its strikingly glossy, iridescent plumage. Whether and how local irregularities will influence the iridescence will need to be further investigated. This will entail the assembly of quantitative anatomical data of the cortex and melanosome dimensions, but we expect that this data will not essentially change our insight into the principal function of the keratin cortex in determining the peak wavelength of the reflectance bands.

Whereas the plumage of the European starling is modestly colored and speckled, the plumage of the Cape starling is uniformly colored and strikingly directional. The iridescent plumage coloration can have various biological functions, for instance as a display for conspecifics or as camouflage against predators. It is therefore interesting to compare the starling colors with the spectral sensitivities of their photoreceptors. The four classes of photoreceptors of *S. vulgaris*, UVS, SWS, MWS, and LWS, are known to have sensitivity peak wavelengths at 369, 453, 545, and 607 nm, respectively, (Hart and Vorobyev, 2005). The reflectance spectra of the blue and green feathers of the Cape starling (**Figure 8D**) correspond to the sensitivity spectra of the SWS and MWS photoreceptors, but a similar correspondence is not immediately apparent for the European starling feathers. In fact, the spectra of **Figure 4D** are two examples of a broad continuum, as can also be seen from the variously colored feathers of the starling shown in **Figure 1A**.

The starlings, Sturnidae, constitute a large family of passerine birds that have structural-colored feathers, employing a remarkably wide variety of melanosomes that are arranged in diverse ways. This includes solid and hollow rodlets as well as solid and hollow platelets, which are mostly arranged in a single layer but also in a multilayer stack (Durrer and Villiger, 1970; Craig and Hartley, 1985; Maia et al., 2013). In the case of a large stack of melanosomes, the stack periodicity is responsible for the peak wavelength and the shape of the reflectance spectra (Eliason et al., 2013). Durrer and Villiger (1970) assumed that a single melanosome layer determines the feather color, particularly for structures with hollow melanosomes. We find in our modeling that the cortex thickness is a key factor in determining the feather colors. While the diameter of the solid melanosomes in the *S. vulgaris* seems to be unimportant, the hollow melanosomes in *L. nitens* crucially cause the high reflectance amplitude. Our findings can have implications also for the design of novel bio-inspired materials, e.g., by informing bio-inspired approaches to tune color with the use of a single sensing layer (Isapour and Lattuada, 2018).

Even in the presence of a large stack of melanosomes that form a multilayer, the keratin cortex can play a special role. This is for instance the case in the breast feathers of the bird of paradise *Parotia lawesii*. Their barbules contain a multilayer of solid melanin rodlets that creates a golden reflection. The layers are arranged skew to the enveloping cortex, and as a consequence the light beams reflected by the cortex and the multilayer become separated. For the light reflected by the cortex, the melanin rodlets then act together as a high refractive index medium as well as a strong absorber, and the cortex here acts as an independent blue-reflecting thin film (Stavenga et al., 2011; Wilts et al., 2014). Furthermore, in hummingbird feathers, where the barbules have large stacks of hollow platelet melanosomes, the cortex appears to importantly modulate the feather reflectance spectra (Eliason et al., 2020); for similar effects in the jewel beetle, see Yoshioka et al. (2012).

In conclusion, the two starling species, with a single layer of melanosomes in their feather barbules, demonstrate that the spectral position of the reflectance bands can be simply tuned by adjusting the cortex thickness. In both studied species, the variously colored feathers appeared to have an identical arrangement of melanosomes, but when the melanosomes are hollow, the reflectance is greatly enhanced. The wide variety of arrangements of solid or hollow melanosomes, embedded in the keratin matrix of bird feather barbules, demonstrates the large flexibility birds have in realizing their subdued or extravagant structural colors.

DATA AVAILABILITY STATEMENT

The raw data supporting the conclusions of this article will be made available by the authors, without undue reservation.

AUTHOR CONTRIBUTIONS

All authors performed the measurements and modeling and wrote the manuscript.

FUNDING

This study was financially supported by the Ph.D. scholarship programme of the University of Groningen and the Advanced Materials research program of the Zernike National Research Centre under the Bonus Incentive Scheme of the Dutch Ministry for Education, Culture and Science (to PF), by the Swiss National Science Foundation through the National Center of Competence in Research Bio-Inspired Materials and the Ambizione Programme (168223 to BW), and the Air Force Office of Scientific Research/European Office of Aerospace Research and Development AFOSR/EOARD (grant FA9550-15-1-0068 to DS).

ACKNOWLEDGMENTS

We thank H. L. Leertouwer for providing excellent technical support and C. J. van der Kooi and the reviewers for critical reading of the manuscript.

SUPPLEMENTARY MATERIAL

The Supplementary Material for this article can be found online at: https://www.frontiersin.org/articles/10.3389/fevo.2021.746254/full#supplementary-material

REFERENCES

Craig, A. J., and Hartley, A. H. (1985). The arrangement and structure of feather melanin granules as a taxonomic character in African starlings (Sturnidae). *Auk* 102, 629–632.

D'Alba, L., Kieffer, L., and Shawkey, M. D. (2012). Relative contributions of pigments and biophotonic nanostructures to natural color production: a case study in budgerigar (*Melopsittacus undulatus*) feathers. *J. Exp. Biol.* 215, 1272–1277. doi: 10.1242/jeb.064907

Doucet, S. M., Shawkey, M. D., Hill, G. E., and Montgomerie, R. (2006). Iridescent plumage in satin bowerbirds: structure, mechanisms and nanostructural predictors of individual variation in colour. *J. Exp. Biol.* 209, 380–390. doi: 10.1242/jeb.01988

Durrer, H. (1965). Bau und Bildung der Augfeder des Pfaus *Pavo cristatus* L. *Rev. Suisse Zool* 72, 264–411.

Durrer, H. (1977). Schillerfarben der Vogelfeder als Evolutionsproblem. *Denkschr. Schweiz. Naturforsch. Ges.* 91, 1–126.

Durrer, H. (1986). "Colouration," in *Biology of the Integument*, eds J. Bereiter-Hahn, A. G. Matoltsky, and K. Richards (Berlin: Springer), 239–247.

Durrer, H., and Villiger, W. (1966). Schillerfarben der Trogoniden. *J. Ornithol.* 107, 1–26. doi: 10.1007/bf01671870

Durrer, H., and Villiger, W. (1970). Schillerfarben der Stare (Sturnidae). *J. Ornithol.* 111, 133–153.

Eliason, C. M., and Shawkey, M. D. (2010). Rapid, reversible response of iridescent feather color to ambient humidity. *Opt. Express* 18, 21284–21292. doi: 10.1364/OE.18.021284

Eliason, C. M., and Shawkey, M. D. (2012). A photonic heterostructure produces diverse iridescent colours in duck wing patches. *J. R. Soc. Interface* 9, 2279–2289. doi: 10.1098/rsif.2012.0118

Eliason, C. M., Bitton, P. P., and Shawkey, M. D. (2013). How hollow melanosomes affect iridescent colour production in birds. *Proc. R. Soc. B* 280:20131505. doi: 10.1098/rspb.2013.1505

Eliason, C. M., Maia, R., Parra, J. L., and Shawkey, M. D. (2020). Signal evolution and morphological complexity in hummingbirds (Aves: Trochilidae). *Evolution* 74, 447–458. doi: 10.1111/evo.13893

Freyer, P., and Stavenga, D. G. (2020). Biophotonics of diversely coloured peacock tail feathers. *Faraday Discuss.* 223, 49–62. doi: 10.1039/d0fd00033g

Freyer, P., Wilts, B. D., and Stavenga, D. G. (2019). Reflections on iridescent neck and breast feathers of the peacock, *Pavo cristatus*. *Interface Focus* 9:20180043. doi: 10.1098/rsfs.2018.0043

Giraldo, M. A., Parra, J. L., and Stavenga, D. G. (2018). Iridescent colouration of male Anna's hummingbird (*Calypte anna*) caused by multilayered barbules. *J. Comp. Physiol. A* 204, 965–975. doi: 10.1007/s00359-018-1295-8

Greenewalt, C. H., Brandt, W., and Friel, D. D. (1960). Iridescent colors of hummingbird feathers. *J. Opt. Soc. Am.* 50, 1005–1013. doi: 10.1364/josa.50.001005

Gruson, H., Elias, M., Andraud, C., Djediat, C., Berthier, S., Doutrelant, C., et al. (2019). Hummingbird iridescence: an unsuspected structural diversity influences colouration at multiple scales. *bioRxiv* [Preprint] doi: 10.1101/699744

Hart, N. S., and Vorobyev, M. (2005). Modelling oil droplet absorption spectra and spectral sensitivities of bird cone photoreceptors. *J. Comp. Physiol. A* 191, 381–392.

Hill, G. E., and McGraw, K. J. (2006). *Bird Coloration. Vol. 1: Mechanisms and Measurements*. Cambridge, MA: Harvard University Press.

Isapour, G., and Lattuada, M. (2018). Bioinspired stimuli-responsive color-changing systems. *Adv. Mat.* 30:1707069. doi: 10.1002/adma.201707069

Kinoshita, S. (2008). *Structural Colors in the Realm Of Nature*. Singapore: World Scientific.

Leertouwer, H. L., Wilts, B. D., and Stavenga, D. G. (2011). Refractive index and dispersion of butterfly scale chitin and bird feather keratin measured by interference microscopy. *Opt. Express* 19, 24061–24066. doi: 10.1364/OE.19.024061

Maia, R., Caetano, J. V. O., Bao, S. N., and Macedo, R. H. (2009). Iridescent structural colour production in male blue-black grassquit feather barbules: the role of keratin and melanin. *J. R. Soc. Interface* 6, S203–S211. doi: 10.1098/rsif.2008.0460.focus

Maia, R., D'Alba, L., and Shawkey, M. D. (2011). What makes a feather shine? A nanostructural basis for glossy black colours in feathers. *Proc. R. Soc. B* 278, 1973–1980. doi: 10.1098/rspb.2010.1637

Maia, R., Rubenstein, D. R., and Shawkey, M. D. (2013). Key ornamental innovations facilitate diversification in an avian radiation. *Proc. Natl. Acad. Sci. U.S.A.* 110, 10687–10692. doi: 10.1073/pnas.1220784110

Mason, C. W. (1923). Structural colors in feathers. *J. Phys. Chem.* 27, 401–447. doi: 10.1021/j150230a001

McGraw, K. J. (2006). "Mechanics of uncommon colors: pterins, porphyrins and psittacofulvins," in *Bird Coloration, Vol. 1, Mechanisms and Measurements*, eds G. E. Hill and K. J. McGraw (Cambridge, MA: Harvard University Press), 354–398.

Prum, R. O. (2006). "Anatomy, physics, and evolution of avian structural colors," in *Bird Coloration, Vol. I, Mechanisms and Measurements*, eds G. E. Hill and K. J. McGraw (Cambridge, MA: Harvard University Press), 295–353.

Rubenstein, D. R., Corvelo, A., MacManes, M. D., Maia, R., Narzisi, G., Rousaki, A., et al. (2021). Feather gene expression elucidates the developmental basis of plumage iridescence in African starlings. *J. Hered.* 112, 417–429. doi: 10.1093/jhered/esab014

Shawkey, M. D., and D'Alba, L. (2017). Interactions between colour-producing mechanisms and their effects on the integumentary colour palette. *Phil. Trans. R. Soc. B* 372, 20160536. doi: 10.1098/rstb.2016.0536

Stavenga, D. G. (2014). Thin film and multilayer optics cause structural colors of many insects and birds. *Mat. Today Proc.* 1, 109–121. doi: 10.1016/j.matpr.2014.09.007

Stavenga, D. G., Leertouwer, H. L., Pirih, P., and Wehling, M. F. (2009). Imaging scatterometry of butterfly wing scales. *Opt. Express* 17, 193–202.

Stavenga, D. G., Leertouwer, H. L., Marshall, N. J., and Osorio, D. C. (2011). Dramatic colour changes in a bird of paradise caused by uniquely structured breast feather barbules. *Proc. R. Soc. B* 278, 2098–2104. doi: 10.1098/rspb.2010.2293

Stavenga, D. G., Leertouwer, H. L., Osorio, D. C., and Wilts, B. D. (2015). High refractive index of melanin in shiny occipital feathers of a bird of paradise. *Light Sci. Appl.* 4:e243. doi: 10.1038/lsa.2015.16

Stavenga, D. G., Leertouwer, H. L., and Wilts, B. D. (2018). Magnificent magpie colours by feathers with layers of hollow melanosomes. *J. Exp. Biol.* 221:174656. doi: 10.1242/jeb.174656

Stavenga, D. G., van der Kooi, C. J., and Wilts, B. D. (2017). Structural coloured feathers of mallards act by simple multilayer photonics. *J. R. Soc. Interface* 14, 10.1098. doi: 10.1098/rsif.2017.0407

Tinbergen, J., Wilts, B. D., and Stavenga, D. G. (2013). Spectral tuning of Amazon parrot feather coloration by psittacofulvin pigments and spongy structures. *J. Exp. Biol.* 216, 4358–4364. doi: 10.1242/jeb.091561

Wilts, B. D., Leertouwer, H. L., and Stavenga, D. G. (2009). Imaging scatterometry and microspectrophotometry of lycaenid butterfly wing scales with perforated multilayers. *J. R. Soc. Interface* 6, S185–S192. doi: 10.1098/rsif.2008.0299.focus

Wilts, B. D., Michielsen, K., De Raedt, H., and Stavenga, D. G. (2014). Sparkling feather reflections of a bird-of-paradise explained by finite-difference time-domain modeling. *Proc. Natl. Acad. Sci. U.S.A.* 111, 4363–4368. doi: 10.1073/pnas.1323611111

Xiao, M., Dhinojwala, A., and Shawkey, M. (2014). Nanostructural basis of rainbow-like iridescence in common bronzewing Phaps chalcoptera feathers. *Opt. Express* 22, 14625–14636. doi: 10.1364/OE.22.014625

Xiao, M., Shawkey, M. D., and Dhinojwala, A. (2020). Bioinspired melanin-based optically active materials. *Adv. Opt. Mat.* 8:2000932. doi: 10.3390/nano10112276

Yeh, P. (2005). *Optical Waves in Layered Media*. Hoboken NJ: Wiley-Interscience.

Yoshioka, S., Kinoshita, S., Iida, H., and Hariyama, T. (2012). Phase-adjusting layers in the multilayer reflector of a jewel beetle. *J. Phys. Soc. Jpn.* 81:054801.

Zi, J., Yu, X. D., Li, Y. Z., Hu, X. H., Xu, C., Wang, X. J., et al. (2003). Coloration strategies in peacock feathers. *Proc. Natl. Acad. Sci. U.S.A.* 100, 12576–12578.

Conflict of Interest: The authors declare that the research was conducted in the absence of any commercial or financial relationships that could be construed as a potential conflict of interest.

Publisher's Note: All claims expressed in this article are solely those of the authors and do not necessarily represent those of their affiliated organizations, or those of the publisher, the editors and the reviewers. Any product that may be evaluated in this article, or claim that may be made by its manufacturer, is not guaranteed or endorsed by the publisher.

frontiers in Bioengineering and Biotechnology

ORIGINAL RESEARCH
published: 19 November 2021
doi: 10.3389/fbioe.2021.763690

Distribution of Biominerals and Mineral-Organic Composites in Plant Trichomes

*Hans-Jürgen Ensikat and Maximilian Weigend**

University of Bonn, Bonn, Germany

Biomineralization is a common phenomenon in plants and has been shown to be chemically, functionally and topologically diverse. Silica and calcium carbonate have long been known as structural plant biominerals and calcium phosphate (apatite)–long known from animals–has recently been reported. Strikingly, up to three different biominerals may occur in a single trichome in, e.g., Urticaceae and Loasaceae, and in combination with organic compounds, can form organic/inorganic composite materials. This article presents an extension of previous studies on the distribution of these biominerals in Loasaceae trichomes with a focus on their spatial (three-dimensional) distribution and co-localization with organic substances. Light microscopy and scanning electron microscopy with high-resolution EDX element analyses of sample surfaces and sections illustrate the differential distribution and composition of the different biomineral phases across cell surfaces and cell walls. Raman spectroscopy additionally permits the identification of organic and inorganic compounds side by side. All three biominerals may be found in a nearly pure inorganic phase, e.g., on the plant surfaces and in the barbs of the glochidiate trichomes, or in combination with a larger proportion of organic compounds (cellulose, pectin). The cell lumen may be additionally filled with amorphous mineral deposits. Water-solubility of the mineral fractions differs considerably. Plant trichomes provide an exciting model system for biomineralization and enable the *in-vivo* study of the formation of complex composite materials with different biomineral and organic compounds involved.

Keywords: biomineralization, calcium carbonate, calcium phosphate, cell walls, loasaceae, Raman spectroscopy, scanning electron microscopy, trichomes

OPEN ACCESS

Edited by:
Devi Stuart-Fox,
University of Melbourne, Australia

Reviewed by:
Ling-Long Kuo-Huang,
National Taiwan University, Taiwan
Rand Evett,
University of California, Berkeley, United States

****Correspondence:***
Maximilian Weigend
mweigend@uni-bonn.de

Specialty section:
This article was submitted to Bionics and Biomimetics, a section of the journal Frontiers in Bioengineering and Biotechnology

Received: *24 August 2021*
Accepted: *25 October 2021*
Published: *19 November 2021*

Citation:
Ensikat H-J and Weigend M (2021) Distribution of Biominerals and Mineral-Organic Composites in Plant Trichomes. Front. Bioeng. Biotechnol. 9:763690. doi: 10.3389/fbioe.2021.763690

INTRODUCTION

Biomineralization is a well-known phenomenon in plants and animals (Skinner and Jahren, 2003). In plants, biomineralization is usually found at the level of individual cells, either in epidermal cell walls or as intracellular structures such as cystoliths. Plant biomineralization shows surprising structural and compositional diversity. Calcium oxalate is generally found as intracellular biomineral whereas calcium carbonate is both found as intracellular cystoliths and in the cell walls of trichomes and stinging hairs (Franceschi and Horner, 1980; Lanning and Eleuterius, 1989; He et al., 2014). Silica is the hardest biomineral and widely reported in the form of deposits in the outer cell walls of the epidermis and trichomes, but also as intracellular phytoliths (Nawaz et al., 2019; Gallaher et al., 2020). Abrasive grainy cell wall inclusions and mineralized sharp tips of trichomes, as well as a dense cover of stiff mineralized hairs forming a physical barrier, are assumed to provide protection against grazing animals (**Figure 1**).

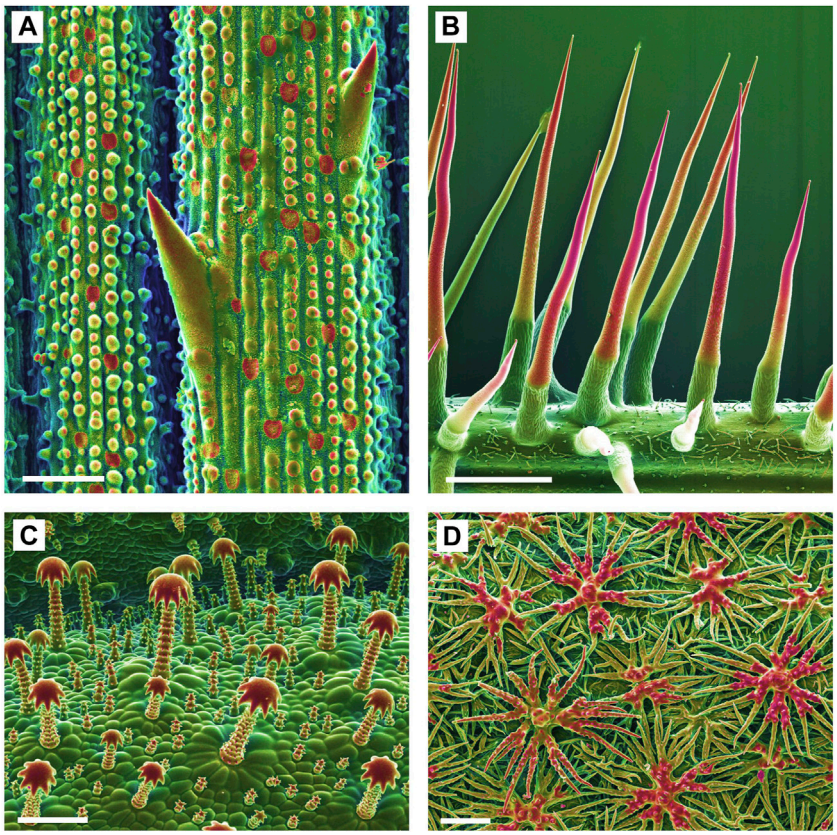

FIGURE 1 | Biomineralized plant surface structures. Combined topographic (SE) and compositional (BSE) contrast SEM images showing mineralized structures in red color. **(A)**: Sharp tips and abrasive epidermis inclusions in a grass (*Spartina pectinata*). **(B)**: Stinging hairs of stinging nettles (*Urtica mairei*). **(C)**: Complex glochidiate trichomes of *Blumenbachia insignis*. **(D)**: A dense cover of the leaf surface with stiff peltate, branched trichomes on Brassicaceae (*Phyllolepidum cyclocarpum*). Scale bars: A = 50 µm; B = 1 mm; C, D = 100 µm.

The diversity of structural plant biominerals has recently been expanded by the discovery of calcium phosphate-based structures in plants (Ensikat et al., 2016; Ensikat et al., 2017; Weigend et al., 2018). Our SEM studies on the complex plant trichomes of Loasaceae ("Rock nettles," Cornales) revealed the presence of calcium phosphate in high concentrations at specific sites in the cell wall, such as trichome tips, while the bulk of the trichome wall is typically mineralized with calcium carbonate. Additional studies have demonstrated its wide distribution across a range of plant families including Urticaceae, Boraginaceae, and Brassicaceae since the first discovery of calcium phosphate as a structural plant biomineral in Loasaceae (Mustafa et al., 2018a; Mustafa et al., 2018b; Weigend et al., 2018). Loasaceae are known for morphologically remarkably diverse trichome cover consisting of stinging hairs, much smaller barbed glochidiate trichomes, and scabrid trichomes with sharp tips (Weigend, 2003; **Figure 2**). Light microscopic (LM) images of Loasaceae trichomes (**Figures 2B–G**) illustrate the thickness of the walls and whether the trichomes are hollow or massive. Stinging hairs (**Figure 2B**) are essentially hollow, whereas the small glochidiate and scabrid trichomes are initially hollow, but later become massive (**Figures 2C–G**). Similar filling of small trichomes occurs in numerous species, such as *Urtica dioica* and *Galium aparine* (**Figures 2H,I**).

Detailed ontogenetic studies demonstrated that mineralization is initiated at the apex and in the trichome hooks and proceeds towards the trichome base; younger, partially mineralized trichomes still may have a non-mineralized base (Mustafa et al., 2017).

The three biominerals reported in plant trichomes are also found in the animal kingdom. Calcium phosphate and calcium carbonate, and to a lesser degree silica, play a major role in medicine, such as in bone formation. This and other applications are the basis for a rapidly growing body of studies on biomimetic materials based on apatite (calcium phosphate) (e.g., Vandecandelaere et al., 2012; Cazalbou et al., 2015; Haider et al., 2017; Nesseri et al., 2020; Bertolotti et al., 2021), calcium carbonate (Sommerdijk and de With, 2008; Wu and Wang 2013) and silica (Knecht and Wright, 2003; Jackson et al., 2015; Piletska et al., 2017). Despite this broad range of studies, very few focus on the exact localization, formation, composition and properties of plant biominerals. Trichome biomineralization is particularly useful for functional and physiological studies because the process of biomineralization can be studied more or less directly with suitable techniques. Previous studies examined the trichome surfaces for their elemental composition with various SEM-techniques, but we have little knowledge of the chemical composition of the cell walls below

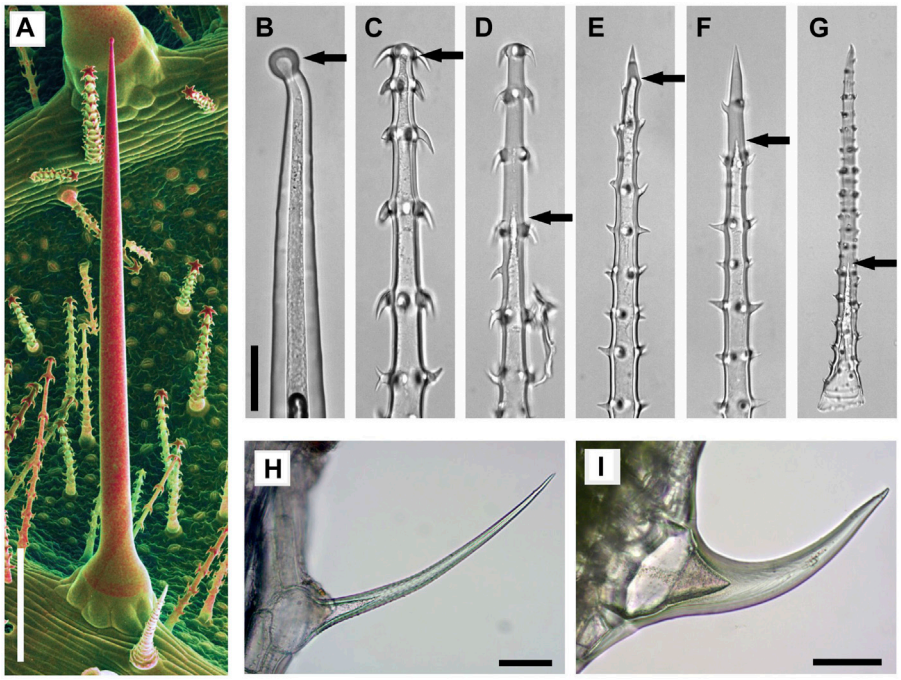

FIGURE 2 | Mineralized trichomes of *Loasa pallida* **(A–G)**, *Urtica dioica* **(H)**, and *Galium aparine* **(I)**. **(A)** SEM image of leaf underside with stinging hair and small glochidiate trichomes. Combined topographic and compositional contrast images showing mineralized structures in red color. Light microscopic (LM) images of a stinging hair **(B)**, glochidiate trichomes **(C–D)** and scabrid trichomes **(E–G)**. Stinging hairs and young stages of scabrid-glochidiate trichomes are hollow; they later become massive by fillings with mineral deposits **(C**, **E**, **F)**. Arrows indicate the end of hollow lumen. Small trichomes of *U*. *dioica* **(H)** and *G*. *aparine* **(I)** which are almost completely massive. Scale bars: A = 500 µm; B-G = 50 µm; H-I = 100 µm.

the surface, even though this likely plays a major role in functionality. Transmission electron microscopic (TEM) studies of thin sections and light microscopy of stained sections revealed the stratification of silicified and calcified cell wall structures of stinging hairs, and the different composition of stinging hair walls in Loasaceae, Euphorbiaceae, and Urticaceae have been known for a long time (Thurston, 1969; Thurston and Lersten, 1969), but the analytical capabilities in TEM were very limited at that time. Recently, Hughes et al. (2017) studied mineral deposits and stratification of biominerals in *Urtica* stinging hairs, while recently published detailed analyses of element distribution in stinging hairs, particularly of the genus *Nasa*, demonstrate complex deposition patterns of silica and calcium phosphate in trichome apices (Mustafa et al., 2017; Mustafa et al., 2018b). Raman spectroscopy as an analytical method with light microscopy resolution provides compositional data about organic and inorganic components of the samples with the possibility of analysing living trichomes, if they are kept immersed in water to avoid heat problems (Ensikat and Weigend, 2019).

We focus on species with triple biomineralization, i.e., containing SiO_2, $CaCO_3$, and Ca-phosphate (Ensikat et al., 2017) including the differential distribution of organic substances. Patterns of biomineralization at the micro-scale are investigated by sectioning and SEM block-face imaging of embedded samples. Complementary data from Raman spectroscopy are provided to understand both the inorganic compounds in trichome walls and their associated organic matrix substances. Our study strives to advance our knowledge of plant biomineralization and provide the basis for further exploration with sophisticated and high-resolution techniques and the tools of molecular physiology.

MATERIALS AND METHODS

Plant Material

For the study of trichome mineralization we used species of three Loasaceae genera (*Blumenbachia*, *Caiophora*, *Loasa*) that are known for complex biomineralization, and for the purposes of comparison, *Urtica dioica*. All plants used in this work were cultivated in the Botanical Gardens of the University Bonn, Germany. The following species appear in this study: *Blumenbachia insignis* (accession 36150, Herbarium T. Jossberger 1210); *Caiophora clavata* (accession 33612, T. Jossberger 548); *Loasa pallida* (accession 36565, T. Jossberger 666). Fully developed leaves of adult plants were used; however, mineralization patterns may vary due to seasonal changes as trichomes undergo distinctly individual development (Mustafa et al., 2017).

Microscopy

Scanning electron microscopy was performed with a Stereoscan S 200 SEM (Cambridge Instruments, Cambridge, United Kingdom) and a LEO 1450 SEM (Cambridge

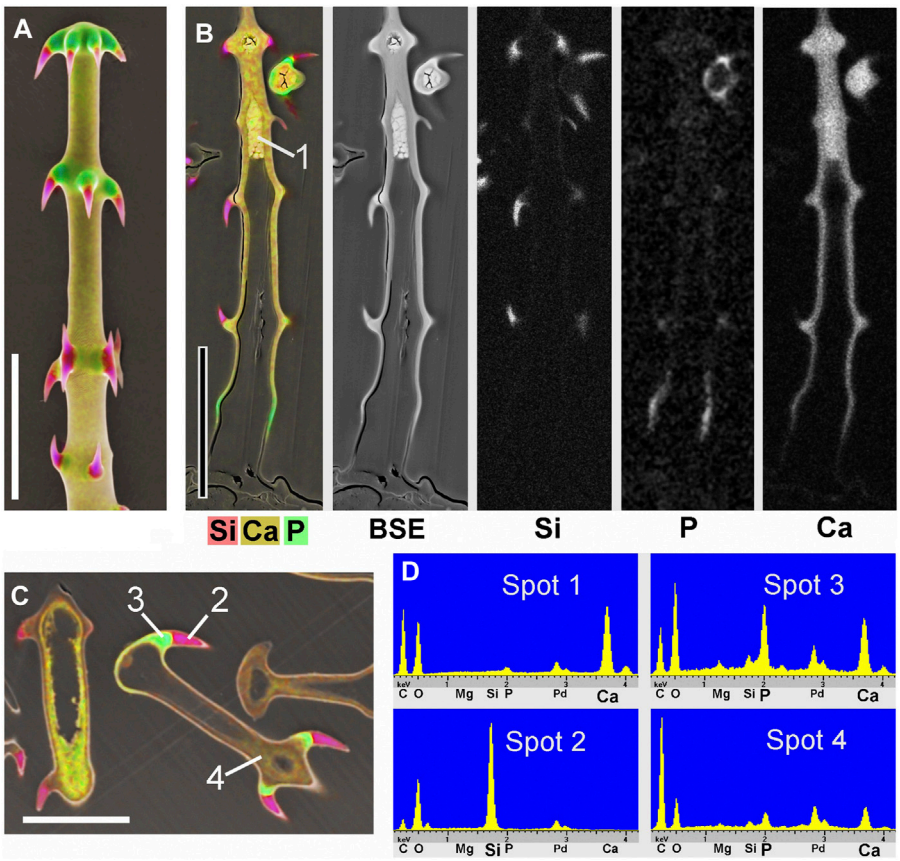

FIGURE 3 | *Caiophora clavata* glochidiate trichomes with three biominerals; element-mapping SEM images and EDX spectra of selected spots. Colours characterize different elements: red = Si; yellow to brown = Ca; green = Ca + P. **(A)** surface view; **(B–C)** longitudinal sections through embedded trichomes treated with different preparation methods: **(B)** Freeze substitution; grayscale mapping images of elements show lower concentrations. **(C)** conventional formaldehyde fixation. **(D)** EDX spectra from four locations indicated in **(B)** and **(C)** indicate different biominerals: calcium carbonate (Spot 1); silica (Spot 2); calcium phosphate (Spot 3); but only low Ca concentration in cell lumen after formaldehyde fixation (Spot 4). The freeze substitution-prepared sample **(B)** shows well-preserved Ca-minerals in cell wall and lumen, silica in barbs, and P in basal cell wall. Conventional preparation **(C)** caused irregular deposits in cell lumen and loss of Ca in walls, but silica and calcium phosphate structures in barbs appeared well preserved. Scale bars: A-B = 50 µm; C = 30 µm.

Instruments), equipped with secondary electron (SE) and backscattered electron (BSE) detectors and an energy-dispersive X-ray (EDX) element analysis system (Oxford Instruments, Oxford, United Kingdom) in conventional high-vacuum mode. Light microscopy was done with a Zeiss Axio Scope (Carl Zeiss GmbH, Oberkochen, Germany).

Sample Preparation for Scanning Electron Microscopy

Various preparation methods were applied because previous studies had shown that a conventional fixation with formaldehyde solutions could cause artefacts such as the dislocation of calcium compounds, even though silica and calcium phosphate deposits usually appeared unaltered. Alternatives such as freeze substitution for leaf pieces or rapid dehydration of isolated trichomes could avoid such artefacts. Surface images were taken from critical-point (CP)-dried leaf pieces or isolated trichomes. Block-face imaging of resin-embedded samples was used for the analysis of sections. Light microscopy (LM) was performed on isolated trichomes.

Conventional Ethanol-Formaldehyde Fixation

Leaf pieces of 5–10 mm size were fixed in 70% ethanol +4% formaldehyde for ca. 24 h, dehydrated with ethanol and acetone, followed by critical-point (CP) drying or embedding in "Agar Low viscosity resin" (Plano GmbH, Wetzlar, Germany) for sectioning, according to the product instructions.

Rapid Dehydration of Isolated Trichomes

Leaves were frozen in liquid nitrogen and the trichomes were scraped off the leaves with a knife blade. Then the trichomes were collected and washed in ethanol and subsequently in acetone. Trichome samples for immediate SEM-imaging were air-dried. For sectioning, trichomes were embedded in resin.

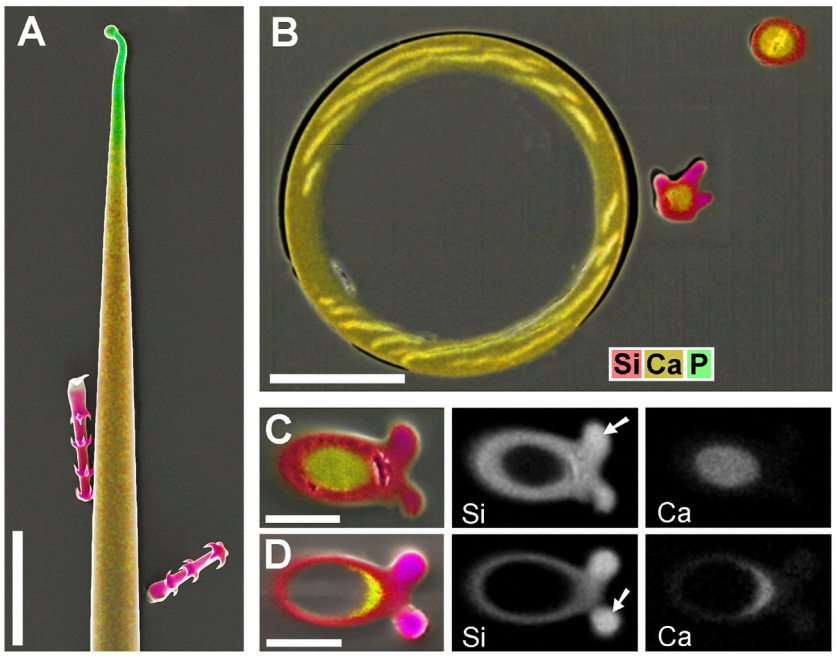

FIGURE 4 | *Blumenbachia insignis*, combined topographic and element-mapping images of stinging hair and glochidiate trichomes. Colors: Si shown in red, Ca in yellow, and P in green. **(A)** Surface view of part of a stinging hair (yellow, green) and two glochidiate trichomes (red, indicating Si). **(B)** Section through a similar arrangement of trichomes shows that stinging hair wall is mineralized with Ca compounds across entire thickness. Glochidiate trichomes have a silicified regular wall, very high Si concentration in barbs (arrows), and Ca in deposits in cell lumen. **(C–D)** Cross sections through massive and hollow regions of glochidiate trichomes including barbs; combined colour images and separate element maps of the Si and Ca distribution. Scale bars: A = 100 µm; B = 30 µm; C-D = 10 µm.

Freeze-Substitution

Small pieces of fresh leaves were rapidly immersed in cold acetone at its freezing temperature (−95°C), then stored for 3 days at −80°C and further 3 days at −30°C in acetone. After applying fresh acetone at room temperature, the samples were either CP-dried or embedded in resin for sectioning. The use of osmium tetroxide was omitted as osmium would interfere with the EDX detection of elements such as phosphorus and silicon. Prior to SEM imaging, the samples were sputter-coated with a thin layer of palladium (Pd) which, in contrast to gold, does not compromise EDX detection of the elements of interest.

Sectioning was done with an ultra-microtome (Reichert OM U3, Reichert AG, Wien, Austria) using a diamond knife.

Raman Spectroscopy

For Raman spectroscopy isolated trichomes were carefully washed to remove any remnants of cell plasma, dehydrated with acetone and air-dried. Raman spectra were collected with a confocal Horiba Scientific LabRam HR800 Raman spectrometer (Horiba Europe GmbH, Oberursel, Germany) at the Institute of Geosciences of the University of Bonn, Germany. The Raman spectra were excited with a 2 W frequency-doubled solid state Nd:YAG laser (532 nm); the laser power was adjusted to less than 20 mW at the sample surface. The scattered Raman light was dispersed by a grating with 600 grooves/mm and detected by an electron multiplier charged-coupled device (EM-CCD). A ×50 long-distance objective with a numerical aperture of N.A. = 0.5 was used for all measurements.

Image Processing

Colorized SEM images were rendered with standard image processing software "Corel Paint Shop Pro X9©." The images from different detectors were combined with the software function "Combine HSL". In combined SE-BSE images, the SE image was used for the lightness (L) channel, and the BSE signal was used to render a color shift so that mineralized structures appear red. Element mapping images were used to determine color saturation (S) and hue (H), so that the silicon signal causes a color shift towards red and the phosphorus signal shifts the color towards green.

RESULTS

Scanning electron microscopy (SEM) with integrated energy-dispersive X-ray spectroscopy (EDX) for element analysis is an excellent tool for identification of biominerals. However, surface analyses provide only an incomplete picture when mineralization extends into the volume of the sample. In such cases, sections or transmission views with LM, including Raman spectroscopy, are suitable to comprehensively characterize the sample composition.

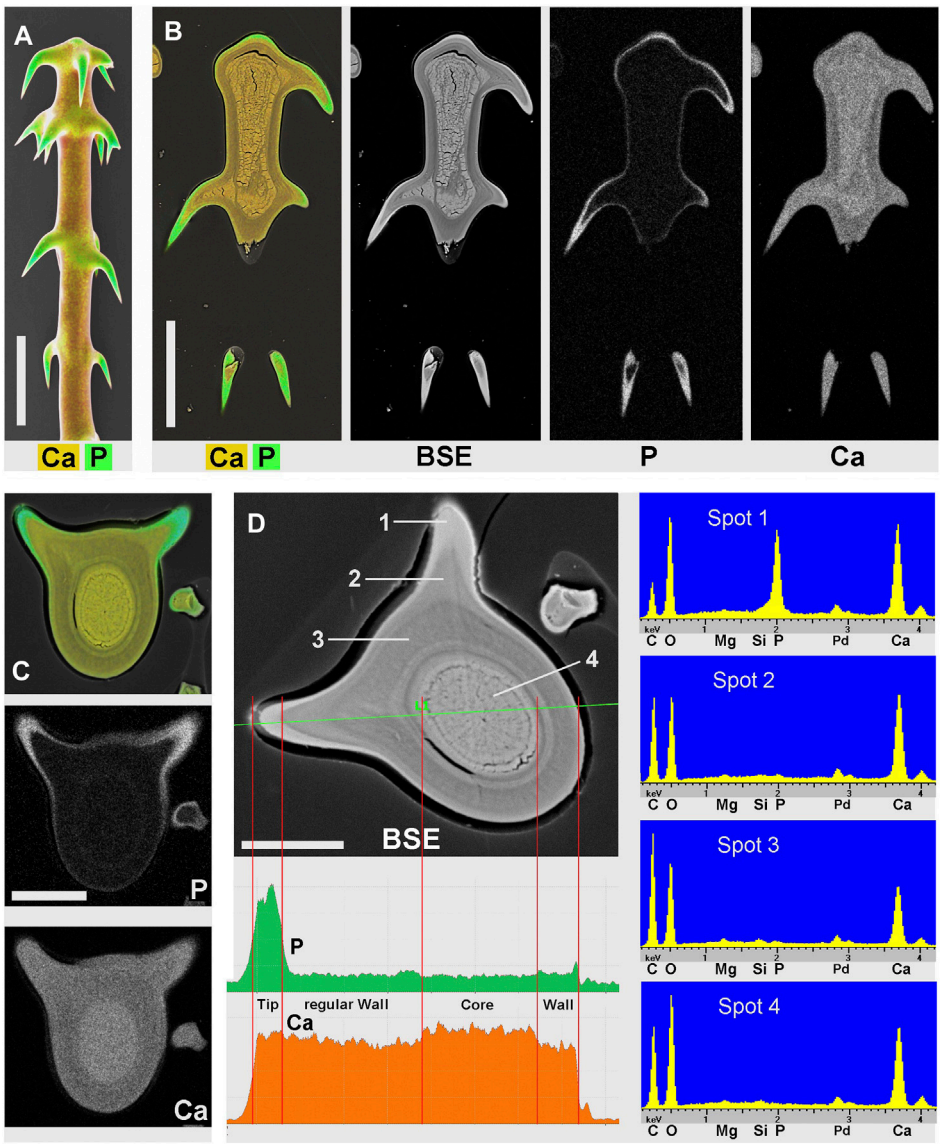

FIGURE 5 | *Loasa pallida*; element-mapping images and analyses of glochidiate trichomes. Colors indicate Ca in yellow to brown, P in green (together with Ca). **(A)** surface view; **(B)** longitudinal section through upper part of an embedded trichome. BSE image illustrates total mineral concentration with better resolution than EDX element mapping. P is found in the barb tips, as an apical cap, and as a thin surface coating, Ca concentrations are highest in barbs and inner deposits and slightly lower in the wall of the shaft. **(C–D)** Analysis of a single trichome cross section shows Ca and P distribution in the element-mapping images **(C)**, whereas a BSE compositional contrast image **(D)** shows different mineral concentrations and stratification due to higher resolution. EDX spectra of selected spots and a line-scan show different Ca concentrations quantitatively. (Spots: 1 = barb tip; 2 = barb shoulder; 3 = regular wall; 4 = core.) Note the low carbon concentration in spectrum of Spot 1 from calcium phosphate-rich barb tip. Scale bars: A-B = 50 µm; C-D = 20 µm.

Loasaceae Trichomes

For the present study we investigated three taxa of Loasaceae (*Blumenbachia*, *Caiophora*, *Loasa*) with trichomes, each having quite similar morphologies, but remarkable differences in biomineralization. All three species have three different types of mineralized trichomes (**Figure 2**): stinging hairs with length of 2–4 mm, which resemble the stinging hairs of Urticaceae (Stinging Nettles) (**Figures 2A,B**); glochidiate trichomes with a blunt apex and numerous basiscopic barbs and a length of typically 0.1–0.4 mm (**Figures 2A,C,D**); and scabrid trichomes with sharp tips and a length of 0.5–1 mm (**Figures 2E–G**). Biomineralization in all trichome types is highly site-specific for all three elements (Si, P, and Ca) examined.

Three Biominerals in Single-Celled Trichomes

Figure 3 shows images of glochidiate trichomes of *Caiophora clavata*. The coloured SEM images combine topography and element-mapping images, to highlight the elements in

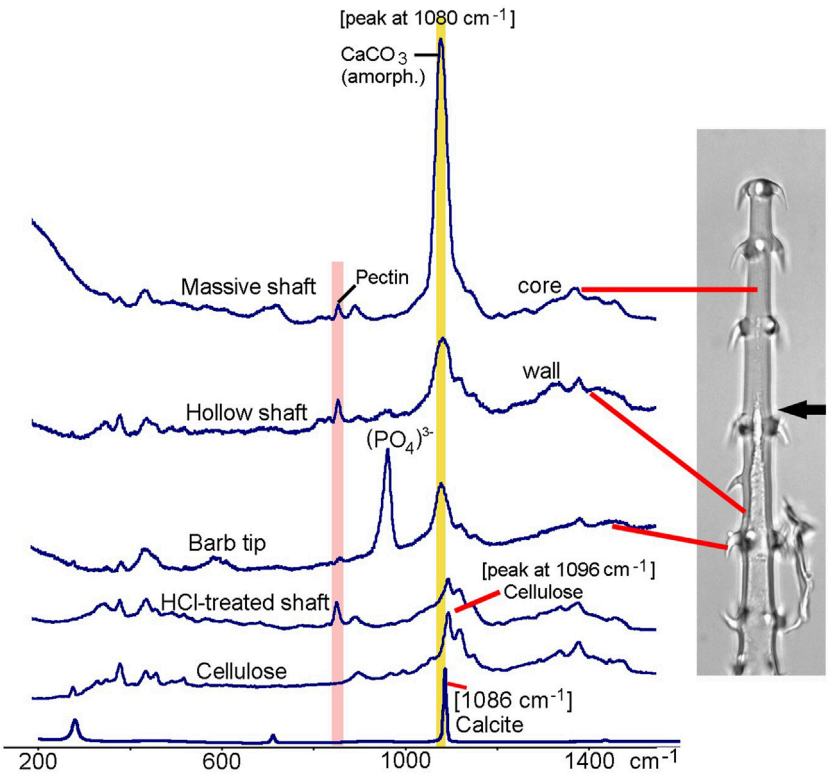

FIGURE 6 | *Loasa pallida*, Raman spectroscopy analyses of glochidiate trichomes. Raman spectra of core of massive shaft, wall of hollow shaft, a barb tip, and for comparison spectra from a demineralized, HCl-treated trichome and from cellulose and calcite. The broad carbonate peak at 1080 cm^{-1}, which overlaps with the main Raman band of cellulose at 1096 cm^{-1}, indicates amorphous or disordered calcium carbonate, with high concentration particularly in the core. A peak at 856 cm^{-1} indicates Pectin which is present in trichome walls even after HCl treatment. Barb tips show an intense phosphate peak at 958 cm^{-1} and smaller carbonate peak at 1080 cm^{-1}. HCl-treated trichomes show Raman bands typical for carbohydrates such as cellulose and pectin.

different colours: Si in red, Ca in yellow to brown, P (together with Ca) in green. SEM surface images show the composition of the outermost layer of the cell wall close to the surface, depending on the penetration depth of the electron beam (typically a few micrometers). **Figure 3B** shows longitudinal sections in combined colour images and separate grayscale mapping images for each mineral element; a surface image of a similar trichome is shown for comparison (**Figure 3A**). A detailed image of the barbs (**Figure 3C**) shows Si in the barb tips and strong signals of P and Ca in the barb shoulders. A comparison of **Figures 3B,C** illustrates differences in quality between two different preparation methods. The sample in **Figure 3B** was prepared by "freeze substitution," which preserves the calcium carbonate-based minerals particularly well. Location "1" shows the Ca-rich core in the cell lumen, which appears well preserved, as well as the calcium content of the cell wall, in contrast to the conventionally prepared trichome in **Figure 3C** with irregular deposits in the cell lumen and a loss of minerals in the walls. Silica in the barb tips and calcium phosphate in barb shoulders appear well preserved in both samples. Ca-phosphate is also found in the base of the trichome in **Figure 3B**. EDX spectra of selected spots (**Figure 3D**) indicate high concentrations of calcium carbonate (Spot 1), silica (Spot 2), calcium phosphate (Spot 3), and only low concentrations of Ca and P in the form of an irregular precipitation in Spot 4.

Silica in Barbs and in the Entire Shaft Wall

Blumenbachia insignis has a unique mineralization pattern (Ensikat et al., 2017): the cell walls of glochidiate trichomes are entirely silicified whereas the stinging hairs contain calcium compounds only. **Figure 4** A is a surface view; **Figure 4B** shows a cross section through a similar assembly of glochidiate trichomes and a shaft of a stinging hair. The stinging hair wall is homogeneously mineralized with calcium compounds (presumably carbonate, yellow). Cell walls of glochidiate trichomes are mineralized with silica, including the barbs. The lumen of massive trichomes is filled with calcium carbonate. Sections through a massive and a hollow glochidiate trichome are shown in **Figures 4C,D**. The silicon distribution map shows the highest Si concentration in the barbs (arrows).

Calcium Phosphate/Calcium Carbonate Distribution

Most *Loasa* species lack silica in their trichomes. Instead, stinging hair tips and glochidiate trichome barbs are mineralized with

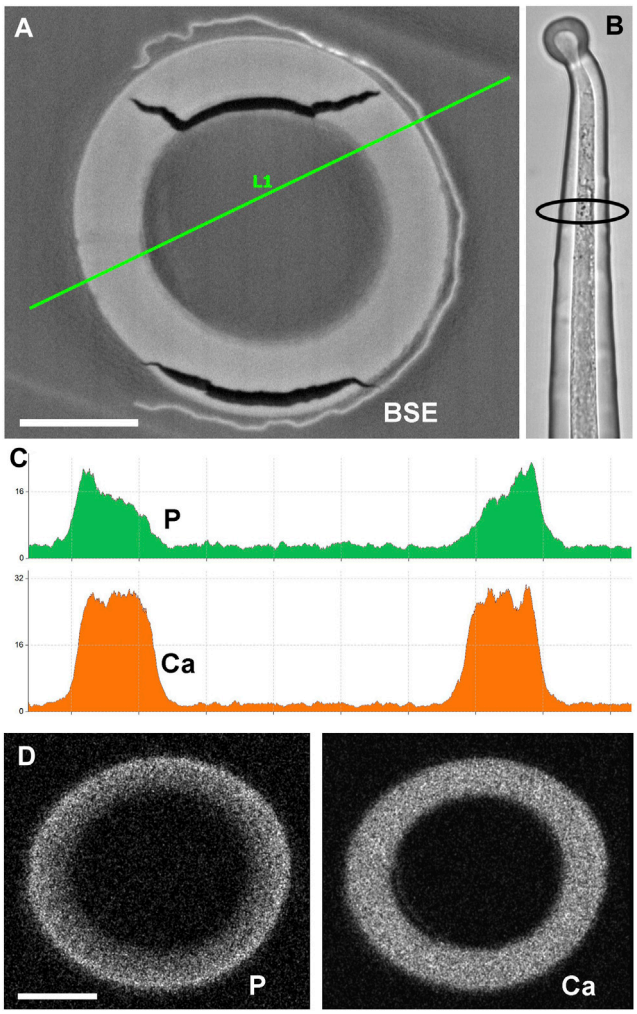

FIGURE 7 | Cross section of embedded stinging hair of *Loasa pallida* and analysis of P and Ca distribution. **(A)** BSE image with EDX linescan **(C)**; the LM image **(B)** illustrates the position of the section close to the apex. The line-scan concentration profiles and element mapping images **(D)** across the cell walls show a continuous decrease in P concentration from outside to inside, contrasting with a constant Ca concentration across the wall. Scale bars: 10 µm.

calcium phosphate. **Figure 5A,B** show the distal part of a glochidiate trichome of *Loasa pallida* in surface view and as longitudinal section. Element mapping images show the distribution of P and Ca. The barb tips and a thin layer on the apical cap contain calcium phosphate (P and Ca). The lumen is filled with calcium; the higher brightness indicates a slightly higher Ca concentration than in the wall of the shaft, which is also mineralized with calcium. A cross section of a glochidiate trichome (**Figures 5C,D**) was analysed by element mapping, spot spectra of selected locations, a BSE image, and an EDX line-scan that shows a concentration profile. The phosphorus map (**Figure 5C**) shows high concentrations in the barbs and a thin outer layer. The BSE image (**Figure 5D**) shows this phosphate layer with better resolution as a separate zone sharply delimited from the calcified wall. The EDX spectrum of this region (Spot 1) shows high P-to-Ca ratios and low carbon concentrations. The barb base (Spot 2) and the cell wall (Spot 3) contain Ca, but almost no P. The lumen filling (core, Spot 4) has a high Ca concentration. The Ca concentration in the wall is slightly lower than in the barb shoulder and core.

In addition to EDX, we used Raman spectroscopy to further characterize the minerals and the organic components of trichome walls. **Figure 6** shows Raman spectra from the massive and hollow regions of a glochidiate trichome, from a barb tip, and for comparison the spectra of a demineralized (HCl-treated) trichome and of cellulose and crystalline calcium carbonate (calcite). A strong carbonate peak can be identified in the massive, distal portion of the trichome; the hollow trichome wall shows a much smaller carbonate peak. The width of the carbonate band and the peak position at 1080 cm^{-1} are indications for amorphous calcium carbonate, whereas crystalline calcite is characterised by a sharp Raman peak at 1086 cm^{-1}. Most of the other minor peaks can be assigned to cellulose, except for the 856 cm^{-1} pectin peak (Chylinska et al., 2014). The barb tip spectrum is dominated by a phosphate peak which indicates calcium phosphate, and a smaller carbonate peak at 1080 cm^{-1}.

The stratification of different calcium phosphate and carbonate phases shown in **Figure 4** is in remarkable contrast to previous analyses of stinging hair sections of *Loasa pallida*, where we had found a continuous change in the phosphorus concentration from the inner to the outer side of the wall (Ensikat et al., 2016). Thus, we prepared new cross sections of stinging hairs in order to check the previous findings (**Figure 7**). Indeed, the phosphate concentration decreases gradually from the outside of the wall towards the inside of the wall. No separate layers of calcium phosphate and calcium carbonate are formed; calcium phosphate on the outside grades into calcium carbonate on the inside.

Raman spectroscopy enables the analysis and detection of organic and inorganic components in trichomes walls in living plants, requiring immersion in water to avoid heat damages. We acquired Raman spectra from the tips of very young stinging hairs of *Nasa amaluzensis* in the process of developing a calcium phosphate tip, and *Urtica dioica* with a silicified tip (**Figure 8**). The spectrum of *Nasa* clearly shows the Raman bands of cellulose, pectin, phosphate, and a small carbonate peak. Several sharp peaks indicated crystalline wax components, which occur commonly on young, untreated plant surfaces. In contrast, the spectrum of *Urtica* showed only traces of the wax and cellulose peaks; amorphous silica produces no detectable peaks in this region.

Solubility of Calcium-Based Biominerals in Water

Figure 9 shows blockface images of sectioned embedded trichomes of *Loasa pallida* treated with water (H_2O) for different intervals demonstrating a striking progression of demineralization: Trichomes without water treatment (A) show massive mineralization mainly with calcium carbonate, both in the cell walls and in the core. After 12 min of water treatment (B-D), the filling of amorphous calcium carbonate in the lumen is largely dissolved up to a depth of approximately 10 µm (arrows); the walls still contain some Ca, indicated by the yellow colour (Ca) or green color (Ca + P). After 2 h of water

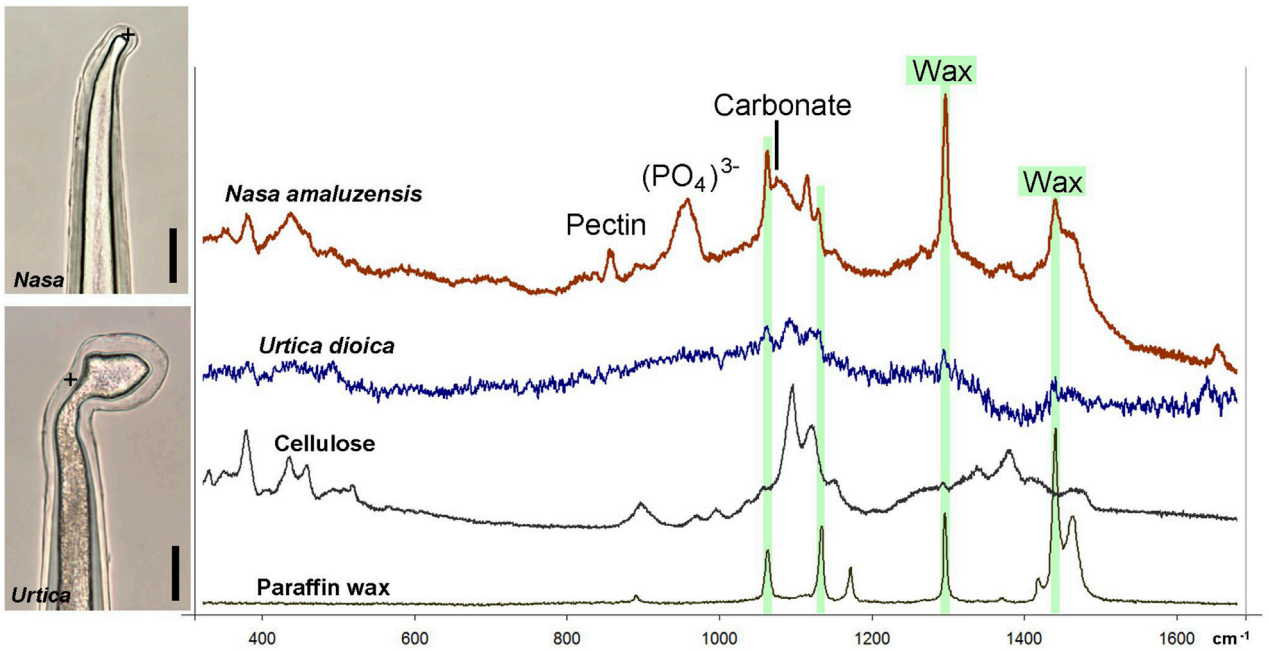

FIGURE 8 | Raman spectra of apices of living stinging hairs of *Nasa amaluzensis* and *Urtica dioica*. Spectra of cellulose and paraffin wax are shown for comparison. Leaf stalks with stinging hairs were immersed in water. Spectrum for the *Nasa* stinging hair tip clearly shows Raman bands of cellulose, pectin, phosphate, and a small carbonate peak which overlaps with the cellulose peak. Several sharp peaks indicate crystalline wax (highlighted in green). The spectrum of *Urtica* shows only traces of cellulose and wax bands. Scale bars: 10 μm.

treatment (E), the trichome is largely demineralized, only the calcium phosphate in the barbs appears to be largely untouched. **Figure 9F** illustrates the process of calcium carbonate mobilization and precipitation in a batch of isolated trichomes of *Loasa pallida* in water under a light microscope. Calcium carbonate dissolves from the cell lumen and cell walls, forming calcite crystals in the vicinity of the trichomes.

DISCUSSION

Loasaceae trichomes have previously been shown to display complex patterns of biomineralization (Ensikat et al., 2017). The present study is an extension of these studies to provide a three-dimensional view of biomineralization and a first look at the organic phase in inorganic/organic composites within trichome cells. The most striking result is the extreme zonation of mineral deposition across the cell walls and wall protuberances (barbs), with different minerals deposited with pinpoint precision. Similar complexity of cell wall structures are known from non-mineralized plant tissues. Plant cell walls are, unlike membranes of animal tissues, prominent structures contributing to the mechanical stability. Different cell wall composition, including hydrophilic carbohydrates (mainly cellulose) and hydrophobic components such as lignin, cutin and waxes, determine the permeability for water and ions. Tracheids or the cells of the Casparian strip are two examples, where the functional divergence in different wall portions is mediated by different types and quantities of organic compounds. Our observation of differentially mineralized trichome walls expands this phenomenon to the outer plant surface, where chemical heterogeneity at the micrometre level is expressed with the presence of up to three different mineral components in combination with different organic compounds.

The mineralization patterns in plant trichomes appear to reflect a range of functions, including plant defence. The tips and hooks of the trichomes are rendered particularly hard and sharp by the inclusion of either silica or calcium phosphate, enabling them to damage skin, mucous membranes and/or the exoskeleton of insects and other herbivores. Conversely, stinging hairs retain a certain degree of brittleness, so that the apex can break off and the caustic stinging substances injected into the attacker from the hollow interior of the mineralized trichome cell, functioning as hypodermic syringe (Thurston and Lersten, 1969; Tuberville et al., 1996). In trichomes containing both calcium carbonate and calcium phosphate there tends to be a trend towards phosphate "coatings," i.e., the part of the trichome exposed to the elements is "varnished" with calcium phosphate, possibly to make use of its lower water solubility, as shown by the leaching experiments. Defensive trichomes in other plant species may be functionally very similar to those of Loasaceae without being mineralized: Stinging hairs of Cnidoscolus are morphologically very similar to those of Loasaceae or Urticaceae, but are entirely made up of organic polymers (Mustafa et al., 2018b). Overall, biomineralization of the cell wall shows extraordinary diversity: Different parts of the cell wall are incrusted with different mineral components

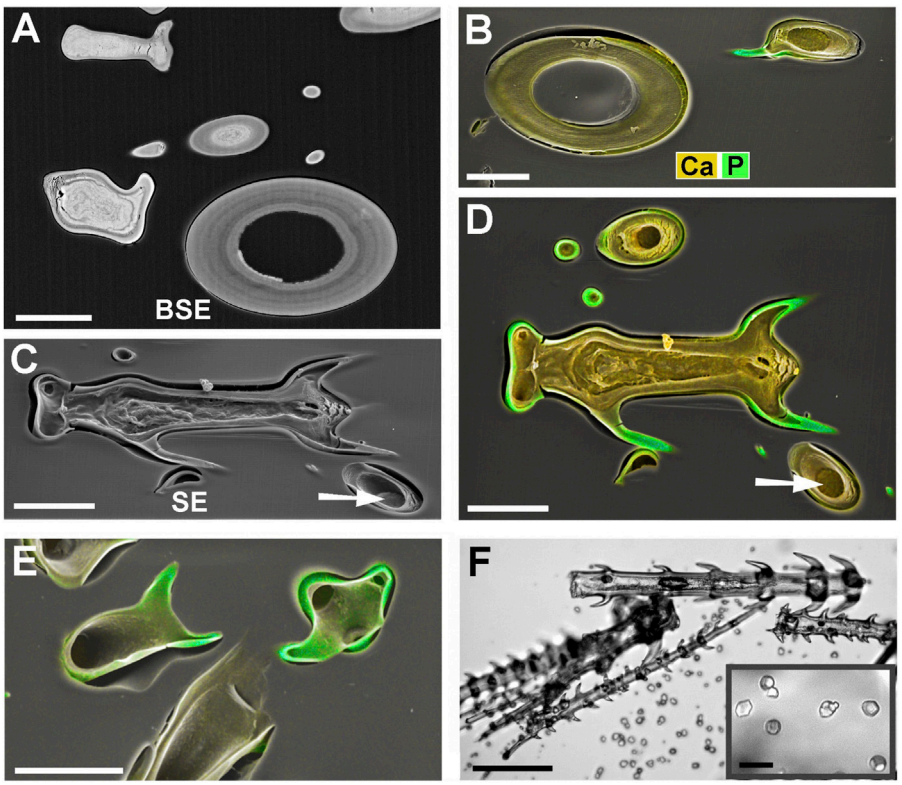

FIGURE 9 | SEM block-face images and LM image of *Loasa pallida* trichomes illustrating solubility of biominerals in water. **(A)** BSE image of sections through glochidiate trichomes and a stinging hair without H_2O treatment (control). High mineral concentrations appear bright. **(B–E)** Combined SE and element-mapping images of embedded trichomes after 12 min in water (at 29°C) **(B–D)**, and after 2 h in water **(E)**. **(B–D)** After 12 min H_2O treatment, Ca-carbonate of the core is dissolved to a depth of ca 10 µm. Remaining Ca-carbonate can be seen at the bottom of the holes (arrow). Ca-phosphate in the barb tips is still present (green). Cell walls still contain Ca (yellow) and show slight shrinkage. **(C)** SE image of tilted sample provides a better impression of depth of voids after mineral dissolution. **(E)** After 2 h of H_2O treatment, the calcium carbonate core has been dissolved completely. The regular cell walls still exist, but have lost most of their mineral content; Calcium phosphate is still present in barb tips and adjacent outer layers (green). **(F)** LM image of a batch of isolated glochidiate trichomes in water after 45 min of immersion. The amorphous $CaCO_3$ in the trichomes dissolves and calcite crystals start growing in the vicinity of dense trichome batches. The inset shows growing crystals in detail. Scale bars: A-E = 30 µm; *F* = 100 µm; inset in *F* = 20 µm.

(calcium carbonate, calcium phosphate, silica), in different structural contexts and relative concentrations, with varying amounts of an organic matrix. The distal and apical parts, where "rigidity" is of paramount importance, are nearly completely mineralized with minute organic admixtures. Other parts of the trichome, especially the shaft, have a higher proportion of cellulose and/or pectin, as shown by Raman spectroscopy, likely creating a composite material with higher strength and flexibility. In addition to the biomineralization of wall structures, we also find an amorphous "filling" of calcium carbonate in glochidiate trichomes, progressing basiscopically with trichome age. Both the amorphous filling and the calcium carbonate mineralization of the cell walls may be easily mobilized upon contact with water. Solubility of calcium-based biominerals in water has long been known as a problem in preparations for TEM investigations. It has been reported that during the ultramicrotomy of bone tissue sections floating on a water surface lose part of their mineral content; dry sectioning is required to avoid this artefact (Boothroyd, 1964; Thorogood and Gray, 1975; Studer et al., 2011).

Crystallinity is not necessarily an attribute of biominerals. Biogenic silica, for example, is generally amorphous. Biogenic plant calcium carbonate has been found as crystalline calcite in the seed coat (pericarp) of Lithospermum (Hilger et al., 1993; own data, not shown), whereas analyses of trichomes by Raman spectroscopy and X-ray powder diffraction always indicates amorphous material. Admixtures of various additives, such as phosphoproteins or inorganic phosphate, may stabilise amorphous $CaCO_3$ (Bentov et al., 2010; Gal et al., 2010).

The biomineral silica widely occurs as nearly pure substance in very hard structures or surface coatings. Thus, its integration into the wall of glochidiate trichome shafts of *Blumenbachia* is a remarkable novelty. In several species of other plant families, e.g., *Urtica mairei* and *Urera baccifera*, cell walls of trichomes are mainly mineralized with calcium phosphate instead of carbonate (Mustafa et al., 2018b). Thus, all three biominerals calcium carbonate, calcium phosphate, and silica can occur in concentrated form (in trichome tips or fillings in the cell lumen) or as composites with cellulose and pectin in the cell

walls. Biomineralization in plants, particularly the formation of calcium carbonate and phosphate, has received little attention in the past, even though calcium phosphate biomineralization is of considerable interest in medicine and for comparatives studies of the process of biomineralization in animals such as vertebrates (Dorozhkin and Epple, 2002; Dillon et al., 2019). Exploration of the physicochemical properties of biominerals is a promising field of research for biomedical applications (Al-Kattan et al., 2012; Credou and Berthelot, 2015; Haider et al., 2017; Konovalova et al., 2017; Markov et al., 2017; Hickey and Pelling, 2019; Nesseri et al., 2020; Tschon et al., 2020) and may get a novel stimulus by the expansion into carbohydrate-based biomineral composites.

Recent research focusses on the chemical and physical properties of plant biominerals and the physiological pathways leading to their formation (Kumar et al., 2021). The accessibility of plant trichomes for *in vivo* studies and analysis by light microscopy and Raman spectroscopy renders them highly suitable subjects for such studies.

DATA AVAILABILITY STATEMENT

The original contributions presented in the study are included in the article/Supplementary Material, further inquiries can be directed to the corresponding author.

AUTHOR CONTRIBUTIONS

The article was designed and written jointly, including experimental design and editing. The data and images were generated by HE.

ACKNOWLEDGMENTS

We thank Thorsten Geisler-Wierwille and Martina Menneken at the Institute of Geosciences, University of Bonn, for their assistance for Raman spectroscopy.

REFERENCES

Al-Kattan, A., Girod-Fullana, S., Charvillat, C., Ternet-Fontebasso, H., Dufour, P., Dexpert-Ghys, J., et al. (2012). Biomimetic Nanocrystalline Apatites: Emerging Perspectives in Cancer Diagnosis and Treatment. *Int. J. Pharm.* 423, 26–36. doi:10.1016/j.ijpharm.2011.07.005

Bentov, S., Weil, S., Glazer, L., Sagi, A., and Berman, A. (2010). Stabilization of Amorphous Calcium Carbonate by Phosphate Rich Organic Matrix Proteins and by Single Phosphoamino Acids. *J. Struct. Biol.* 171, 207–215. doi:10.1016/j.jsb.2010.04.007

Bertolotti, F., Carmona, F. J., Dal Sasso, G., Ramírez-Rodríguez, G. B., Delgado-López, J. M., Pedersen, J. S., et al. (2021). On the Amorphous Layer in Bone mineral and Biomimetic Apatite: A Combined Small- and Wide-Angle X-ray Scattering Analysis. *Acta Biomater.* 120, 167–180. doi:10.1016/j.actbio.2020.04.026

Boothroyd, B. (1964). The Problem of Demineralisation in Thin Sections of Fully Calcified Bone. *J. Cel Biol.* 20, 165–173. doi:10.1083/jcb.20.1.165

Cazalbou, S., Bertrand, G., and Drouet, C. (2015). Tetracycline-loaded Biomimetic Apatite: an Adsorption Study. *J. Phys. Chem. B* 119, 3014–3024. doi:10.1021/jp5116756

Chylinska, M., Szymanska-Chargot, M., and Zdunek, A. (2014). Imaging of Polysaccharides in the Tomato Cell wall with Raman Microspectroscopy. *Plant Methods* 10, 14. doi:10.1186/1746-4811-10-14

Credou, J., and Berthelot, T. (2014). Cellulose: from Biocompatible to Bioactive Material. *J. Mater. Chem. B* 2, 4767–4788. doi:10.1039/c4tb00431k

Dillon, S., Staines, K. A., Millán, J. L., and Farquharson, C. (2019). How to Build a Bone: PHOSPHO1, Biomineralization, and beyond. *JBMR Plus* 3 (7), e10202. doi:10.1002/jbm4.10202

Dorozhkin, S. V., and Epple, M. (2002). Die biologische und medizinische Bedeutung von Calciumphosphaten. *Angew. Chem.* 114, 3260–3277. doi:10.1002/1521-3757(20020902)114:17<3260:aid-ange3260>3.0.co;2-s

Ensikat, H.-J., Geisler, T., and Weigend, M. (2016). A First Report of Hydroxylated Apatite as Structural Biomineral in Loasaceae - Plants' Teeth against Herbivores. *Sci. Rep.* 6, 26073. doi:10.1038/srep26073

Ensikat, H.-J., Mustafa, A., and Weigend, M. (2017). Complex Patterns of Multiple Biomineralization in Single-Celled Plant Trichomes of the Loasaceae. *Am. J. Bot.* 104, 195–206. doi:10.3732/ajb.1600331

Ensikat, H. J., and Weigend, M. (2019). EDX and Raman Spectroscopy Reveal the Unexpected Complexity of Plant Biomineralisation. *Microsc. Anal.* 45, 20–23.

Franceschi, V. R., and Horner, H. T. (1980). Calcium Oxalate Crystals in Plants. *Bot. Rev.* 46, 361–427. doi:10.1007/bf02860532

Gal, A., Weiner, S., and Addadi, L. (2010). The Stabilizing Effect of Silicate on Biogenic and Synthetic Amorphous Calcium Carbonate. *J. Am. Chem. Soc.* 132, 13208–13211. doi:10.1021/ja106883c

Gallaher, T. J., Akbar, S. Z., Klahs, P. C., Marvet, C. R., Senske, A. M., Clark, L. G., et al. (2020). 3D Shape Analysis of Grass Silica Short Cell Phytoliths: a New Method for Fossil Classification and Analysis of Shape Evolution. *New Phytol.* 228, 376–392. doi:10.1111/nph.16677

Haider, A., Haider, S., Han, S. S., and Kang, I.-K. (2017). Recent Advances in the Synthesis, Functionalization and Biomedical Applications of Hydroxyapatite: a Review. *RSC Adv.* 7, 7442–7458. doi:10.1039/c6ra26124h

He, H., Veneklaas, E. J., Kuo, J., and Lambers, H. (2014). Physiological and Ecological Significance of Biomineralization in Plants. *Trends Plant Sci.* 19, 166–174. doi:10.1016/j.tplants.2013.11.002

Hickey, R. J., and Pelling, A. E. (2019). Cellulose Biomaterials for Tissue Engineering. *Front. Bioeng. Biotechnol.* 7, 45. doi:10.3389/fbioe.2019.00045

Hilger, H. H., Hoppe, J. R., and Hofmann, M. (1993). Energiedispersive Röntgenmikroanalyse (EDX) von Boraginaceae subfam. Boraginoideae - Klausenoberflächen. *Flora* 188, 387–398. doi:10.1016/s0367-2530(17)32289-2

Hughes, N. P., Perry, C. C., Williams, R. J. P., Watt, F., and Grime, G. W. (2017). "A Scanning Proton Microprobe Study of Stinging Emergences from the Leaf of the Common Stinging Nettle Urtica Dioica," in *Nuclear Instruments and Methods in Physics Research. Section B: Beam Interactions with Materials and Atoms.* Editors M. Breese, L.E. Rehn, C. Trautmann, and I. C. Vickridge (Amsterdam, Netherlands: Elsevier), 383–387.

Jackson, E., Ferrari, M., Cuestas-Ayllon, C., Fernández-Pacheco, R., Perez-Carvajal, J., de la Fuente, J. M., et al. (2015). Protein-templated Biomimetic Silica Nanoparticles. *Langmuir* 31, 3687–3695. doi:10.1021/la504978r

Knecht, M. R., and Wright, D. W. (2003). Functional Analysis of the Biomimetic Silica Precipitating Activity of the R5 Peptide from Cylindrotheca fusiformisElectronic Supplementary Information (ESI) Available: HPLC and MALDI of Peptides (11 Pgs); EMs of Silica Particles (4 Pgs); IR Data (3 Pgs); DLS Data (1 Pg) and Mechanistic Detail (1 Pg). *Chem. Commun.* 24, 3038–3039. Available at: http://www.rsc.org/suppdata/cc/b3/b309074d/. doi:10.1039/b309074d

Konovalova, M. V., Markov, P. A., Durnev, E. A., Kurek, D. V., Popov, S. V., and Varlamov, V. P. (2017). Preparation and Biocompatibility Evaluation of Pectin and Chitosan Cryogels for Biomedical Application. *J. Biomed. Mater. Res.* 105, 547–556. doi:10.1002/jbm.a.35936

Kumar, S., Natalio, F., and Elbaum, R. (2021). Protein-driven Biomineralization: Comparing Silica Formation in Grass Silica Cells to Other Biomineralization Processes. *J. Struct. Biol.* 213, 107665. doi:10.1016/j.jsb.2020.107665

Lanning, F. C., and Eleuterius, L. N. (1989). Silica Deposition in Some C3 and C4 Species of Grasses, Sedges and Composites in the USA. *Ann. Bot.* 64, 395–410. doi:10.1093/oxfordjournals.aob.a087858

Markov, P. A., Krachkovsky, N. S., Durnev, E. A., Martinson, E. A., Litvinets, S. G., and Popov, S. V. (2017). Mechanical Properties, Structure, Bioadhesion, and

Biocompatibility of Pectin Hydrogels. *J. Biomed. Mater. Res.* 105, 2572–2581. doi:10.1002/jbm.a.36116

Mustafa, A., Ensikat, H.-J., and Weigend, M. (2018a). Mineralized Trichomes in Boraginales: Complex Microscale Heterogeneity and Simple Phylogenetic Patterns. *Ann. Bot.* 121, 741–751. doi:10.1093/aob/mcx191

Mustafa, A., Ensikat, H.-J., and Weigend, M. (2017). Ontogeny and the Process of Biomineralization in the Trichomes of Loasaceae. *Am. J. Bot.* 104, 367–378. doi:10.3732/ajb.1600417

Mustafa, A., Ensikat, H.-J., and Weigend, M. (2018b). Stinging Hair Morphology and wall Biomineralization across Five Plant Families: Conserved Morphology versus Divergent Cell wall Composition. *Am. J. Bot.* 105 (7), 1109–1122. doi:10.1002/ajb2.1136

Nawaz, M. A., Zakharenko, A. M., Zemchenko, I. V., Haider, M. S., Ali, M. A., Imtiaz, M., et al. (2019). Phytolith Formation in Plants: From Soil to Cell. *Plants* 8, 249. doi:10.3390/plants8080249

Nesseri, E., Boyatzis, S. C., Boukos, N., and Panagiaris, G. (2020). Optimizing the Biomimetic Synthesis of Hydroxyapatite for the Consolidation of Bone Using Diammonium Phosphate, Simulated Body Fluid, and Gelatin. *SN Appl. Sci.* 2, 1892. doi:10.1007/s42452-020-03547-8

Piletska, E., Yawer, H., Canfarotta, F., Moczko, E., Smolinska-Kempisty, K., Piletsky, S. S., et al. (2017). Biomimetic Silica Nanoparticles Prepared by a Combination of Solid-phase Imprinting and Ostwald Ripening. *Sci. Rep.* 7, 11537. doi:10.1038/s41598-017-12007-0

Skinner, H. C. W., and Jahren, A. H. (2003). "Biomineralization," in *Treatise on Geochemistry*. Editor W. H. Schlesinger (Amsterdam, Netherlands: Elsevier).

Sommerdijk, N. A. J. M., and With, G. d. (2008). Biomimetic CaCO3 Mineralization Using Designer Molecules and Interfaces. *Chem. Rev.* 108, 4499–4550. doi:10.1021/cr078259o

Studer, D., Hillmann-Marti, T., Huffman, N. T., and Gorski, J. P. (2011). Eliminating Exposure to Aqueous Solvents Is Necessary for the Early Detection and Ultrastructural Elemental Analysis of Sites of Calcium and Phosphorus Enrichment in Mineralizing UMR106-01 Osteoblastic Cultures. *Cells Tissues Organs* 194, 138–145. doi:10.1159/000324252

Thorogood, P. V., and Craig Gray, J. (1975). Demineralization of Bone Matrix: Observations from Electron Microscope and Electron-Probe Analysis. *Calc. Tis Res.* 19, 17–26. doi:10.1007/bf02563987

Thurston, E. L. (1969). An Anatomical and fine Structure Study of Stinging Hairs in Some Members of the Urticaceae, Euphorbiaceae and Loasaceae. Retrospective Theses and Dissertations. USA: Iowa State University. Paper 3790.

Thurston, E. L., and Lersten, N. R. (1969). The Morphology and Toxicology of Plant Stinging Hairs. *Bot. Rev.* 35, 393–412. doi:10.1007/bf02858878

Tschon, M., Brogini, S., Parrilli, A., Bertoldi, S., Silini, A., Parolini, O., et al. (2020). Assessment of the *In Vivo* Biofunctionality of a Biomimetic Hybrid Scaffold for Osteochondral Tissue Regeneration. *Biotechnol. Bioeng.* 118, 465–480. doi:10.1002/bit.27584

Tuberville, T. D., Dudley, P. G., and Pollard, A. J. (1996). Responses of Invertebrate Herbivores to Stinging Trichomes of Urtica Dioica and Laportea canadensis. *Oikos* 75, 83–88. doi:10.2307/3546324

Vandecandelaere, N., Rey, C., and Drouet, C. (2012). Biomimetic Apatite-Based Biomaterials: on the Critical Impact of Synthesis and post-synthesis Parameters. *J. Mater. Sci. Mater. Med.* 23, 2593–2606. doi:10.1007/s10856-012-4719-y

Weigend, M. (2003). "Loasaceae," in *The Families and Genera of Vascular Plants*. Editors K. Kubitzki and C. Bayer (Berlin, Germany: Springer), Vol. 6, 239–254.

Weigend, M., Mustafa, A., and Ensikat, H.-J. (2018). Calcium Phosphate in Plant Trichomes: the Overlooked Biomineral. *Planta* 247, 277–285. doi:10.1007/s00425-017-2826-1

Wu, X., and Wang, S. (2013). Biomimetic Calcium Carbonate Concentric Microgrooves with Tunable Widths for Promoting MC3T3-E1 Cell Functions. *Adv. Healthc. Mater.* 2, 326–333. doi:10.1002/adhm.201200205

Conflict of Interest: The authors declare that the research was conducted in the absence of any commercial or financial relationships that could be construed as a potential conflict of interest.

Publisher's Note: All claims expressed in this article are solely those of the authors and do not necessarily represent those of their affiliated organizations, or those of the publisher, the editors and the reviewers. Any product that may be evaluated in this article, or claim that may be made by its manufacturer, is not guaranteed or endorsed by the publisher.

frontiers in Ecology and Evolution

PERSPECTIVE
published: 09 December 2021
doi: 10.3389/fevo.2021.790270

From Bioinspired to Bioinformed: Benefits of Greater Engagement From Biologists

Leslie Ng, Mark A. Elgar† and Devi Stuart-Fox†*

School of BioSciences, University of Melbourne, Melbourne, VIC, Australia

Bioinspiration and biomimetics is a rapidly growing field where insights from biology are used to solve current design challenges. Nature provides an abundance of inspiration to draw upon, yet biological information is under-exploited due to a concerning lack of engagement from biologists. To assess the extent of this problem, we surveyed the current state of the field using the Web of Science database and found that only 41% of publications on bioinspired or biomimetic research included an author affiliated with a biology-related department or organisation. In addition, most publications focus exclusively on a limited range of popular model species. Considering these findings, we highlight key reasons why greater engagement from biologists will enable new and significant insights from natural selection and the diversity of life. Likewise, biologists are missing unique opportunities to study biological phenomena from the perspective of other disciplines, particularly engineering. We discuss the importance of striving toward a bioinformed approach, as current limitations in the field can only be overcome with a greater understanding of the ecological and evolutionary contexts behind each bioinspired/biomimetic solution.

Keywords: bioinspiration, biomimetic, collaboration, ecology, evolution, adaptation, natural selection, interdisciplinary

OPEN ACCESS

Edited by:
Isabel Marques, University of Lisbon, Portugal

Reviewed by:
Hermann Ehrlich, Freiberg University of Mining and Technology, Germany
Sang-im Lee, Daegu Gyeongbuk Institute of Science and Technology (DGIST), South Korea

****Correspondence:***
Leslie Ng
tszn1@student.unimelb.edu.au

†These authors share senior authorship

Specialty section:
This article was submitted to Behavioral and Evolutionary Ecology, a section of the journal Frontiers in Ecology and Evolution

Received: *06 October 2021*
Accepted: *19 November 2021*
Published: *09 December 2021*

Citation:
Ng L, Elgar MA and Stuart-Fox D (2021) From Bioinspired to Bioinformed: Benefits of Greater Engagement From Biologists. Front. Ecol. Evol. 9:790270. doi: 10.3389/fevo.2021.790270

INTRODUCTION

The natural world has inspired creative minds throughout time, from Da Vinci's flying machines to Gaudi's Sagrada Familia, but only in the mid-20th century did this design philosophy become popular within the academy. Indeed, the term biomimetics was first coined in 1957 by Otto Herbert Schmitt and refers to the transfer of knowledge or principles from biological systems to engineering or design (ISO/TC266, 2015). Biomimetics has since further diversified into related terms such as "bioinspiration", a creative approach where design concepts are inspired from biology (ISO/TC266, 2015). These terms are sometimes used synonymously and other times as similar but separate approaches, and their broadly ambiguous use has resulted in many cases where the bioinspiration or knowledge transfer is trivial. For example, the behaviour of an animal (e.g., the flapping of wings or proboscis extension in butterflies) can be replicated using soft robotics without reference to the underlying biological mechanisms (Lin and Liu, 2019; Yu et al., 2021).

A superficial approach is not necessarily unwelcome, as some applications may depend on the broader biological concepts only (Cutkosky, 2015; Whitesides, 2015). However, we contend that

there are substantial opportunity costs in having only a shallow understanding of the biological system, and that effective inspiration or mimicry requires being truly "bioinformed". In other words, a bioinformed approach reflects an understanding of the mechanisms and processes underlying the biological system that is inspiring the innovative design. For example, early attempts at human flight were certainly inspired by nature but poorly informed by the actual biomechanics of bird flight – with sometimes fatal consequences. In contrast, a classic success story of a bioinformed design is the bullet-shaped nose of the Shinkansen train, which resembles the beak of the kingfisher. Although the inspiration may not be obvious at first glance, it is far from superficial – the shape of the kingfisher's beak allows it to forage for aquatic prey by diving into water at great speed, moving rapidly from mediums of low (air) to high (water) density without pushing the beak into the back of its head, and with barely a splash. Mimicking this structure allows a Shinkansen train to similarly "pierce" the compression waves that build up in front of the train as it enters a tunnel. The choice of bird species as a source of inspiration or mimicry is critical – the beak of crows would not work, and even the beak of certain kingfishers, such as kookaburras, may not work as these birds are rarely faced with the same problem as the Shinkansen train. On the other hand, further improvements to the Shinkansen design might come from investigations of sea birds, such as terns, which similarly forage by diving at speed into the sea. Understanding the selection pressures favouring the biological structure or processes is key, and biologists are well placed to provide these insights to facilitate bioinformed innovation.

In this perspective we make a case for greater engagement from biologists in projects that draw on biological systems as inspiration for resolving technological and design problems. We see a parallel between the design paradox – success through failure (Petroski, 2006), and the process of natural selection, in which optimum designs are achieved as natural selection ruthlessly weeds out design failures, thereby resulting in incremental improvements. Indeed, natural selection has, over a 3.8-billion-year time span, refined biological forms, functions and processes according to extraordinarily different biological and physical environments. We argue that by combining an *understanding* of the biological system with design and engineering ingenuity, we can use nature to solve many problems – from the nanoscale to the global. We first consider the current state of the field by asking three questions: (i) what is the growth in bioinspired research; (ii) what is the level of engagement from biologists to this research; (iii) to what extent is research in this area utilising biological diversity? Finally, we highlight three major areas in which biologists can participate and facilitate the advancement of bioinspired or biomimetic research.

What is the Growth and Where are the Biologists?

There has been a remarkable growth in interest in bioinspiration and biomimetics, but to what extent are biologists engaged with this research? We address this question by using publications as a measure of research engagement. We searched the Web of Science (WoS) database (Clarivate, 2021) for peer-reviewed articles and reviews from 1990 to 2020 that mention bioinspiration (bioinsp*) or biomimicry (biomim*) as key terms. We then searched the author addresses of these articles and calculated the proportion of research involving an author affiliated with a bio-related department (author address with the search string "bio" e.g., Biology, Biological Sciences, BioSciences, or Biochemistry; or string of "Ecol or Environ or Evol or Zool or Botan" e.g., Ecology, Evolution, Environmental Sciences, Zoology, and Botany).

Our findings confirmed that research in bioinspiration and biomimetics has grown exponentially over the past 30 years (**Supplementary Figure 1**), with an accumulation of 35265 papers since 1990. Indeed, we also found a similar growth rate in articles and reviews published in materials science, to which bioinspiration has contributed. However, very few biologists appear to have participated in the bioinspired research output – our survey revealed that less than half of papers included an author from a biology related department or organisation. Specifically, only 41% of papers included an author affiliated with a biology related department. These findings are relatively consistent with Snell-Rood (2016) who found that less than 8% of biologists were involved in biomimetics research, albeit using a stricter search criterion on a subset of 300 papers. Altogether, these findings are surprising given the assumed inter- and multi-disciplinary nature of bioinspired research and suggests that either biologists are not engaging in this research and/or that biological inspiration comes from relatively few model species.

What is the Taxonomic Diversity in Bioinspiration/Biomimetics Research?

The number of formally described species is currently 2.12 million (IUCN, 2021), which is widely acknowledged to be a gross underestimate of actual global biodiversity. The number of extant eukaryotic species is estimated at 5 ± 3 million (Costello et al., 2013), as well as an estimated 1 trillion microbial species (Locey and Lennon, 2016). This represents an extraordinary diversity of solutions to environmental challenges; but is research in bioinspiration taking advantage of this diversity? We addressed this question from the perspective of both research species and exemplar design challenges.

Research Species

We arbitrarily chose two groups of animals that commonly contribute to bioinspired research in materials: butterflies, whose wing characteristics have informed the development of technologies such as electronic displays and solar cells; and spiders, whose silk characteristics have wide applications as a sturdy yet light-weight biomaterial. We searched the WoS database for peer-reviewed research articles using bioinspiration, biomimetics, and butterflies or spiders as key search terms and screened each article for relevant taxonomic information. Specifically, we identified the species that each study was

primarily based upon, as well as studies involving multiple focal species. Using a systematic search protocol involving the filtering of irrelevant papers (e.g., articles with no mention of species) and the retrieval of relevant papers from reference lists (e.g., articles using specific terms such as the names of common genera e.g., *Morpho* for butterflies, *Trichonephila* or *Nephila* for spiders), we arrived at 173 research articles for butterflies and 218 for spiders (**Supplementary Information**).

A similar pattern can be observed in both butterfly and spider inspired research papers: the representation of focal species in this literature is unevenly distributed and focussed on a fraction of the described biodiversity (**Figure 1**). For example, while the 173 articles that drew inspiration from butterflies included species from 35 genera (**Supplementary Table 1**), 64% of these species belonged to the family *Nymphalidae*, and 44% focussed on a single genus, namely *Morpho*. Clearly, we have explored only the tip of the existing butterfly biodiversity, given the 18,000 formally described species across 125 families (Heppner, 2008; Espeland et al., 2018). A similar pattern emerges for spiders, where 33% of 218 articles focussed on the genus *Trichonephila* (golden orb-weaving spiders previously a subgenus of *Nephila*) from a total of 29 represented genera (**Supplementary Table 2**). In addition, 78% of the articles that drew inspiration from spiders belonged to the superfamily Araneoidea, of which 94% belonged to the family Araneidae (orb-weaving spiders). Nevertheless, the pattern for spiders is perhaps even more alarming than that of butterflies, since spiders are arguably a broader taxonomic group (Araneae), with approximately 49,500 described species from 4033 genera and 113 families (Selden, 2017; World Spider Catalog, 2021). Further, only 12% of butterfly- and 14% of spider-inspired research drew inspiration from multiple focal species.

Design Challenges

We arbitrarily chose two design challenges, which have attracted a great deal of bioinspired attention – drag reduction and surface adhesion. Engineers have often looked to nature for ways to improve the hydrodynamic performance of ships and aircrafts; similarly, animals have evolved countless solutions for interfacing with complex natural surfaces, inspiring the development of adhesive tapes and glues. Here, we used the same systematic protocol for research species but instead searched for peer-reviewed research articles with either drag reduction or surface adhesion as key terms. We arrived at 156 papers for drag reduction and 272 papers for surface adhesion (**Supplementary Figure 2**).

Again, we see a remarkably similar pattern – solutions to both design challenges are primarily drawn from a few model species (**Figure 2** and **Supplementary Tables 3, 4**). In particular, the Tokay gecko (*Gecko gecko*) is dominant in the surface adhesion literature despite being an unusually large gecko species. We also found that 3% of surface adhesion papers and 10% of drag reduction papers involved species from multiple taxonomic classes, showing that researchers do not usually consider more than one species. This problem of representation was further exacerbated by the lax reporting of taxonomy, especially in the context of popular models. For example, studies involving gecko-based adhesion often simply use the generalised term "gecko" without specifying further details.

Embracing Biodiversity

The taxonomically narrow approach to research species selection is problematic because significant insights can be overlooked by focusing on only a single genus or family. For example, it was recently discovered that the nanostructures of butterflies facilitates heat dissipation, allowing their thin wings to remain cool despite their large size (Tsai et al., 2020). This insight was made possible by using a multi-species comparative approach to understand processes common to all butterflies, rather than focussing on a single species. Tsai et al. (2020) found key commonalities among the 50 species studied: all had structures that enhanced radiative cooling of the thermally sensitive living parts of the wings (scent patches, scent pads, and wing veins). Differences between species were just as informative: different species used varying combinations of adaptations including cuticle thickness, specialised scale nanostructures, contrasting dorsal and ventral wing coloration, and finely-tuned behavioural reactions to enable temperature to be exquisitely tailored to environmental conditions. Due to the specific combination of traits, butterflies in tropical and temperate environments can bask longer to warm up their bodies while reducing the risk of overheating the wings: whereas butterflies at high latitudes or altitudes can warm up their wings efficiently. This example highlights that comparison of multiple species can reveal how different traits can vary and be combined to suit a wide range of environmental conditions.

Studying multiple species can also highlight the variation in the uses or properties of an adaptation. For example, all spiders produce at least one of seven types of silk that are used in conjunction with different activities, including attracting conspecific mates, forming a cocoon that protects vulnerable eggs, dispersing very considerable distances through ballooning, or capturing prey (Blamires et al., 2017). Yet our knowledge of the properties of spider silk is mostly confined to silks used for foraging, and in particular the dragline silk produced by orb-weaving spiders, the latter informed by a handful of species. Of course, there are excellent reasons for focussing on this type of silk, since it combines two seemingly incompatible properties – strength and elasticity, necessary to absorb the energy of insects arrested at speed. Nevertheless, orb-weaving spiders (Araneidae) are a large and diverse taxonomic group comprising over 3000 species in 177 genera. This taxonomic breadth incorporates remarkable diversity in their foraging ecology, which likely influences the properties of the dragline silk used to support the foraging webs: spiders in the genus *Plebs* and *Leucage* build small, delicate and easily broken webs, while the dragline silk that supports the orb-webs of Darwin's bark spider *Caerostris darwini* extends tens of meters across rivers (Agnarsson et al., 2010) and is twice as strong as that produced by other orb-weaving spiders (Garb et al., 2019). While differences in dragline silk mechanical properties are also reported among similarly-sized, closely related species (Kerr et al., 2018), the properties of other types of spider silk have been largely ignored. For example, the potential diversity of

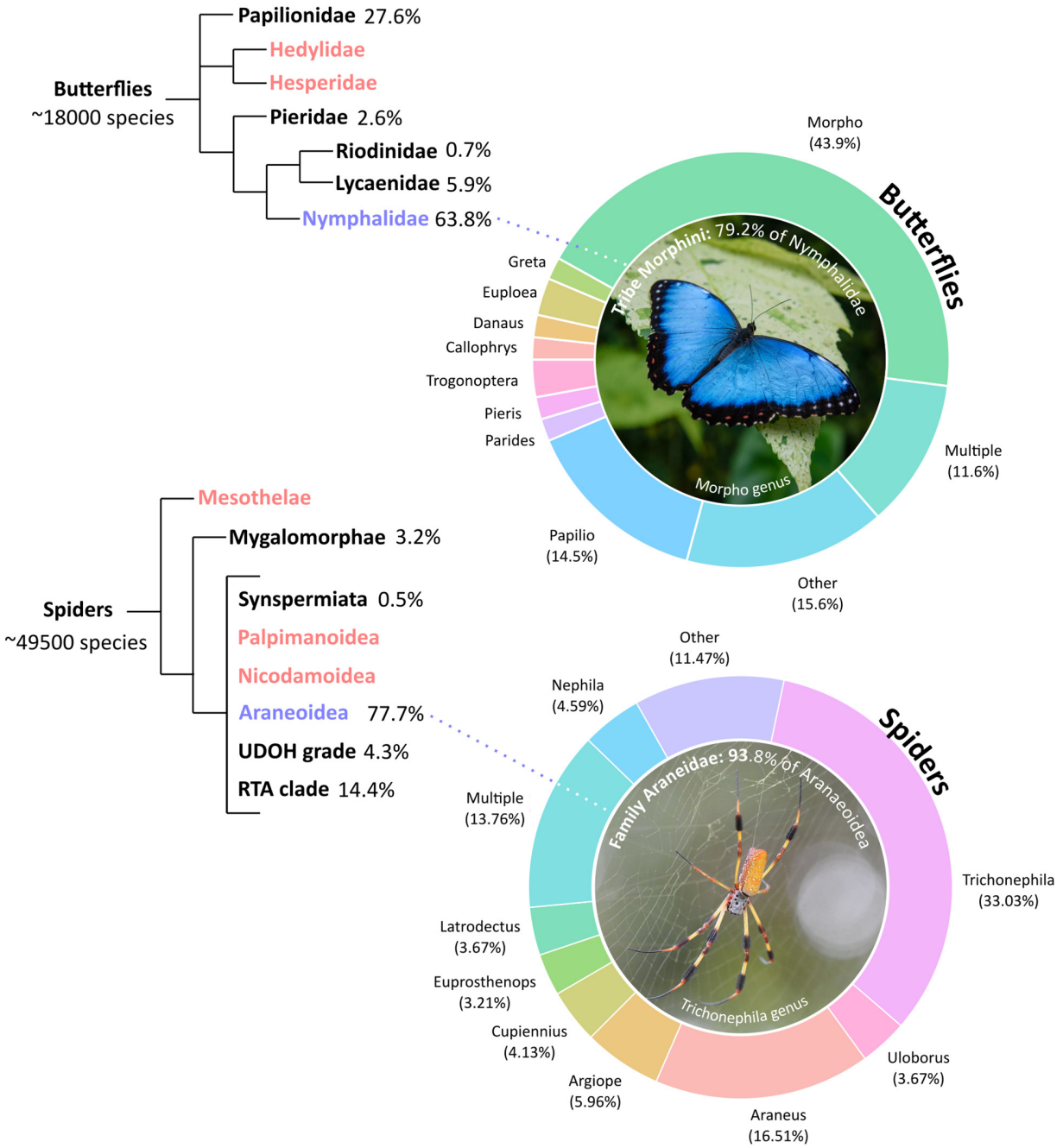

FIGURE 1 | Taxonomic distribution of butterfly and spider bioinspiration/biomimetic research. Donut charts represent the distribution of genera for each taxonomic group, based on 173 papers on butterflies and 218 papers on spiders. Percentages are the percentage of the identified papers focusing on each taxon. "Multiple" indicates research including multiple focal species, while "Other" indicates the sum of genera with less than 3% representation. Tree diagrams show the representation of major phylogenetic groups within butterflies (Rhopalocera) and spiders (Araneae). Red indicates groups with no representation, and blue represents the group with the most representation. Most species within both animal groups belong to a select few genera, and are largely represented by two phylogenetic groups only. Original photos by Michal Mrozek (butterfly) and Tom Earnhardt (spider).

the tubuliform and aciniform silk used to construct egg cases is poorly understood, but the remarkably rigid, free-standing foraging web of the thomisid spider *Saccodomus formivorus* also appears to comprise these silks, which could inspire rigid thread designs for tissue engineering (Haynl et al., 2020).

This approach of embracing biodiversity can also be expanded to organisms that live in unusual or hostile habitats. These environments are, by definition, difficult to access and study, and so organisms within them are likely to reveal novel solutions to specific environmental challenges. Notably, this perspective

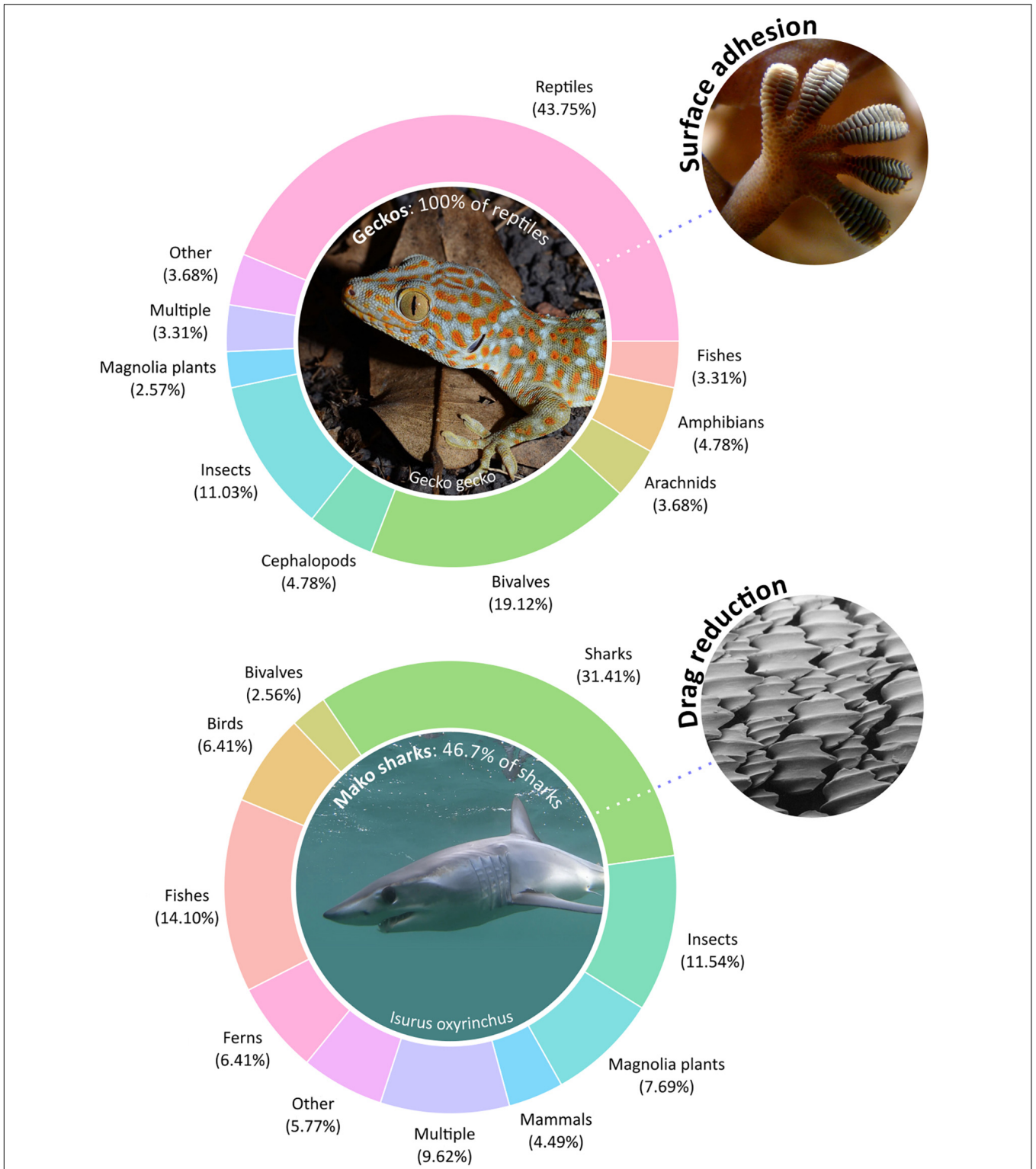

FIGURE 2 | Taxonomic distribution of surface adhesion and drag reduction research. We identified 156 papers for drag reduction and 272 papers for surface adhesion. Percentages are the percentage of the identified papers focusing on each taxon. "Multiple" indicates research including multiple focal species, while "Other" indicates the sum of genera with less than 4% representation. Most of the research is concentrated in a select few model species despite the biological diversity from which insights can be potentially drawn. Only few studies involve multiple species and instead focus on a single model. Original photos by Patrick Randall (gecko), Bjørn Tørrissen (gecko foot), Elaine Brewer (shark), and Pascal Deynat (shark skin).

has led to the emergence of "extreme biomimetics", defined by its focus on bioinspired solutions informed from biologically extreme conditions that are well outside the human comfort zone (Ehrlich, 2017; Petrenko et al., 2019). For example, the skeletal structure of fauna endemic to hydrothermal vents have inspired the study of biopolymers that are thermally stable and high-pressure tolerant under such conditions (Unterlass, 2017). Recent advances in this field have focused on the development of inorganic-organic hybrid materials using chitin or spongin scaffolds exposed to hydrothermal treatments (Ehrlich et al., 2013; Petrenko et al., 2019). This biomaterial fabrication strategy was only made possible by investigating chitin, collagen, and spongin skeletal structures across taxa, eventually settling on sponges (Porifera) as an ideal and renewable source of thermal and pressure tolerant biopolymers (Ehrlich, 2017). Hydrothermal vents are only one example of an extreme environment, and there is obvious value in drawing inspiration from organisms that live in habitats that reflect the extremities of other dimensions, such as oxygen concentration, humidity or cold temperatures. For example, the rapidly growing developments in bioinspired anti-freeze proteins from polar fish and freeze-tolerant insects have promising future biomedical applications (Xiang et al., 2020).

Clearly, there is untapped potential in shifting attention outside of obvious model species, especially as they may not always represent the optimal solution in every context. For example, shark skin is famous for its drag reducing properties, but is by no means the most effective material; other solutions include dolphin skin, penguin-inspired micro-bubbles, and lotus leaf surface structures (Yu et al., 2020). Notably, these species belong to very different phylogenetic groups and their adaptations reflect solutions from different evolutionary perspectives. Similarly, additional insights into surface adhesion may come from insect solutions (Zhou et al., 2014). In short, an optimal bioinspired/biomimetic design can be achieved by understanding, comparing, and even combining insights from nature's diversity of solutions.

KEY REASONS FOR ENGAGEMENT FROM BIOLOGISTS

Bioinspired design and engineering have had some impressive success stories, but our analysis suggests that we are barely scratching the surface of biological insights. Below, we highlight three key reasons that greater engagement from biologists is crucial for effective bioinspired or biomimetic design:

Understanding Evolution

The near infinite functional traits found in nature have been forged by natural selection; this evolutionary design process has quietly progressed for many millions of years. Therefore, by studying living organisms that have survived nature's optimisation algorithm (Maynard Smith, 1978), we can reap the rewards while skipping our own iterative and time-consuming design processes. This is one of the main appeals of bioinspiration/biomimetics, and biologists are well placed to fully appreciate these systems. However, effective bioinspiration/biomimetics is more complicated than simply selecting a species and replicating the desired adaptation; it can be difficult to identify the most functionally relevant traits to abstract into a design. One solution is to study the evolution of the trait in question using comparative methods, observing whether it appears in related species exhibiting the desired function, and whether it was lost in those without (Adriaens, 2019). Such a comparative approach enables insights into how traits are associated with specific environmental conditions. Again, such an approach requires an appreciation for evolutionary history to take advantage of insights from natural selection (Wolff et al., 2017).

In addition, non-biologists are often unaware of the limitations of natural selection as a design inspiration. While evolution has analogies to the design process, it is not exactly the same and suffers from different constraints. Engineers are often interested in designs that can optimally achieve a single function, however, biological traits are the product of balancing multiple functions and do not represent the objectively optimal solution for one specific function. For example, butterfly wings have inspired the production of structurally coloured materials (Schroeder et al., 2018), yet light manipulation is not their only function. The wings must also be hydrophobic and self-cleaning (Fang et al., 2015), thermally efficient for the animal's environment (Tsai et al., 2020), and flexible yet durable for flight (Johansson and Henningsson, 2021). Natural selection has favoured a solution that suits all these biological requirements, resulting in a wing structure that is a functional compromise for the animal's specific environmental conditions. Different species face different environmental challenges and will have varying adaptations to reflect these conditions. This is very relevant to bioinspired/biomimetic design challenges as most synthetic structures or materials also have multiple functional requirements. Identifying biological analogues to these requirements will therefore result in solutions that are better optimised for multiple conditions.

An awareness of phylogenetic constraints is also crucial. For example, while bats have evolved the capacity to fly, it is suggested that their aerodynamic efficiency is inferior to birds due to the phylogenetic constraints associated with their wing design (Muijres et al., 2012). Flexible membranes and elongated digits evolved in bats not because it was necessarily the optimal solution to flight, but because of its evolutionary context (Amador et al., 2019). Engineers also have access to structures and processes that are not readily available to natural selection. For example, the wheel is an energetically efficient invention to facilitate movement, but continuous rotation is rarely possible for animals constrained by musculoskeletal systems (Fish and Beneski, 2014). Biologists are well equipped to navigate these limitations and have the knowledge to properly abstract biological principles whilst avoiding their constraints.

Drawing From Diversity

Natural selection provides a diversity of solutions to life's design challenges; different species can represent distinct or sometimes

convergent solutions to similar problems. A focus on single study species provides only one answer to a design challenge, yet the diversity of life shows that there are multiple solutions which can be more or less optimal depending on environmental conditions. Therefore, a focus on the feature rather than species can be more rewarding and provides insights only possible when drawing from the full diversity of life. For example, adaptations for surface adhesion are widespread in the animal kingdom. An awareness of attachment strategies in animals of different sizes can provide insight into issues of scaling with size (Labonte and Federle, 2015), as well as possible solutions to the problem. Interactions between multiple solutions can also be observed when focusing on the feature rather than species. For instance, some animals have both adhesive pads and claws which can potentially be synergistic, or in other cases, redundant (Song et al., 2016; Naylor and Higham, 2019). Understanding the evolutionary contexts behind such interactions can inform the performance and necessity of multiple features in bioinspired/biomimetic designs. Another recent example is the insights drawn from the diversity of insect cuticles. Most insect exoskeletons feature gradual changes in stiffness across the cuticle and analysing this property has directly informed the development of functionally graded materials (Jafarpour et al., 2020). The uncommon, common feature of these examples are that they all draw insights from the *diversity* of life, rather than focussing on individual species.

In attempts to better appreciate biological diversity for use in art and design, tools such as AskNature have been developed to translate biological information to non-biologists (Deldin and Schuknecht, 2014). These tools serve as rich databases of biological strategies organised by function and can be extremely useful in the initial search for relevant solutions. However, the accessibility of these tools can ironically lead to the perpetuation of popular model species. Such databases do not represent the actual diversity of potential solutions in nature and are by no means an effective replacement for biologists who have expert knowledge on underappreciated systems or strategies (Graeff et al., 2019; Willocx et al., 2020). Therefore, the involvement of biologists continues to be crucial for diverse biological insights in bioinspired and biomimetic designs.

Embracing Bioinformed Design

A crucial component of biomimetic design is the abstraction process, as it is often unnecessary to entirely replicate a biological feature (Cutkosky, 2015; Whitesides, 2015). Nevertheless, a nuanced understanding of the biological system is required to abstract a feature effectively. For example, the micro-structure of shark skin needs to be understood in detail before it can be properly simplified into a synthetic riblet (Domel et al., 2018). Incorrectly translating such structures into the final design can result in a potential loss in performance. In addition, a holistic understanding of the system will prevent researchers from becoming too focused on a specific feature in isolation. For example, the Geckskin adhesive technology was developed by abandoning the conventional focus on gecko setae and instead developing a product inspired by the entire gecko foot (Patek, 2014). Here, the research team realised that the setae alone did not explain adhesive performance, but that effective attachment was the outcome of a system of synergistic features at different scales (Imburgia et al., 2019): specifically, the stiff tendons attached to their toepads also played a significant role in effective attachment (King et al., 2014).

It is important to note that gecko-inspired tapes have yet to match the performance of living geckos. Indeed, current gaps in the understanding of biological models remains a major obstacle in biomimetic design. For example, gecko-inspired adhesives have been designed to attach to smooth dry surfaces but are largely ineffective on non-ideal surfaces (Niewiarowski et al., 2016). To further approach the performance of the biological system, it is essential to study questions regarding the ecology of the animal: how are gecko toe pads tuned to specific environmental contexts? How do geckos move across irregular or wet surfaces? How do toe pads vary across species with different environmental challenges? There is considerable morphological variation in geckos, which is linked to habitat (Kulyomina et al., 2019; Norris et al., 2021). These insights from basic biological research are crucial to address current performance gaps and can only be achieved through the involvement of biologists (Higham et al., 2019).

Finally, we emphasise that a bioinspired/biomimetic approach to design is not a one directional relationship. Biologists also stand to gain valuable insights from the process: for example, engineers can provide a different approach toward problem-solving – whilst biologists may only arrive at a conceptual understanding of a trait, in many cases engineers can physically construct and test a structure or property. This direct approach is possible as engineers often have access to resources, technical expertise, and specialist equipment required for the testing and validation of functional hypotheses. Therefore, there is enormous potential for biologists to take advantage of the expertise and resources available to engineers to further explore biological questions in a physical and tangible context (Roberts et al., 2014). For example, biologists often have difficulty studying the functional morphology of extinct species due to the limitations of fossil evidence. Biomimetic tools have allowed for the structures of species such a fossil earwig (Saito et al., 2020) or remora (Gamel et al., 2019) to be replicated to study their evolution and function. In return, these findings provide insights for biomimetic designs, such as the improvement of underwater attachment (remora disc) or folding patterns (earwig wing). A move toward "bioinformation" is both synergistic and mutualistic, allowing biologists and engineers to produce insightful science and useful designs.

CONCLUDING REMARKS

The current state of bioinspired/biomimetic design suffers from a surprising paradox: effective bioinspiration or biomimetics requires intimate knowledge of biology, yet there is a lack of engagement from biologists in such projects. Here, we show that the output of bioinspired research seems to be characterised by limited collaboration with biologists and a very extensive

focus on a few representative species. This is problematic as significant insights from evolution and ecology are overlooked, and likewise, biologists are also missing unique opportunities to approach hypotheses from an engineering perspective. We therefore advocate for greater engagement between biologists and engineers – biologists benefit from a greater awareness of design challenges and methodological approaches in engineering, and engineers benefit from a greater awareness of the diversity of strategies forged by natural selection. There is no shortcut or secret method for success in interdisciplinary collaboration; both parties must actively seek opportunities to share and discuss ideas or challenges. Despite the well-known barriers to interdisciplinary engagement (Mazzocchi, 2019), we believe that such collaborations will not only promote the value of basic science but also generate rewarding opportunities for biologists to view their study system from a new perspective. There is evidently remarkable value and demand for biological expertise, and input from biologists will be key in overcoming current limitations of bioinspired/biomimetic technologies.

DATA AVAILABILITY STATEMENT

The raw data supporting the conclusions of this article will be made available by the authors, without undue reservation.

AUTHOR CONTRIBUTIONS

LN conducted the systematic assessment of the bioinspiration/biomimetic literature and analysed the findings. LN and ME drafted the manuscript. All authors contributed and edited the final manuscript and conceived of the work.

SUPPLEMENTARY MATERIAL

The Supplementary Material for this article can be found online at: https://www.frontiersin.org/articles/10.3389/fevo.2021.790270/full#supplementary-material

REFERENCES

Adriaens, D. (2019). "Evomimetics: the biomimetic design thinking 2.0," in *Proceedings of SPIE 10965: SPIE Smart Structures + Nondestructive Evaluation*, eds R. K. Martín-Palma, M. Knez, and A. Lakhtakia (Denver, CO: SPIE).

Agnarsson, I., Kuntner, M., and Blackledge, T. A. (2010). Bioprospecting finds the toughest biological material: extraordinary silk from a giant riverine orb spider. *PLoS One* 5:e11234. doi: 10.1371/journal.pone.0011234

Amador, L. I., Almeida, F. C., and Giannini, N. P. (2019). Evolution of traditional aerodynamic variables in bats (Mammalia: Chiroptera) within a comprehensive phylogenetic framework. *J. Mamm. Evol.* 27, 549–561. doi: 10.1007/s10914-019-09475-8

Blamires, S. J., Blackledge, T. A., and Tso, I.-M. (2017). Physicochemical property variation in spider silk: ecology, evolution, and synthetic production. *Annu. Rev. Entomol.* 62, 443–460. doi: 10.1146/annurev-ento-031616-035615

Clarivate (2021). *Web of Science* [Online]. Available online at: www.webofscience.com (accessed June 23, 2021)

Costello, M. J., May, R. M., and Stork, N. E. (2013). Can we name earth's species before they go extinct? *Science* 339, 413–416. doi: 10.1126/science.1230318

Cutkosky, M. R. (2015). Climbing with adhesion: from bioinspiration to biounderstanding. *Interface Focus* 5:20150015. doi: 10.1098/rsfs.2015.0015

Deldin, J.-M., and Schuknecht, M. (2014). "The asknature database: enabling solutions in biomimetic design," in *Biologically Inspired Design*, eds A. Goel, D. McAdams, and R. Stone (London: Springer), 17–27.

Domel, A. G., Domel, G., Weaver, J. C., Saadat, M., Bertoldi, K., and Lauder, G. V. (2018). Hydrodynamic properties of biomimetic shark skin: effect of denticle size and swimming speed. *Bioinspir. Biomim.* 13:056014. doi: 10.1088/1748-3190/aad418

Ehrlich, H. (2017). *Extreme Biomimetics*. Berlin: Springer.

Ehrlich, H., Simon, P., Motylenko, M., Wysokowski, M., Bazhenov, V. V., Galli, R., et al. (2013). Extreme biomimetics: formation of zirconium dioxide nanophase using chitinous scaffolds under hydrothermal conditions. *J. Mater. Chem. B* 1, 5092–5099. doi: 10.1039/C3TB20676A

Espeland, M., Breinholt, J., Willmott, K. R., Warren, A. D., Vila, R., Toussaint, E. F. A., et al. (2018). A comprehensive and dated phylogenomic analysis of butterflies. *Curr. Biol.* 28, 770–778.e5. doi: 10.1016/j.cub.2018.01.061

Fang, Y., Sun, G., Bi, Y., and Zhi, H. (2015). Multiple-dimensional micro/nano structural models for hydrophobicity of butterfly wing surfaces and coupling mechanism. *Sci. Bull.* 60, 256–263. doi: 10.1007/s11434-014-0653-3

Fish, F. E., and Beneski, J. T. (2014). "Evolution and bio-inspired design: natural limitations," in *Biologically Inspired Design*, eds A. Goel, D. McAdams, and R. Stone (London: Springer), 287–312.

Gamel, K. M., Garner, A. M., and Flammang, B. E. (2019). Bioinspired remora adhesive disc offers insight into evolution. *Bioinspir. Biomim.* 14:056014. doi: 10.1088/1748-3190/ab3895

Garb, J. E., Haney, R. A., Schwager, E. E., Gregoriè, M., Kuntner, M., Agnarsson, I., et al. (2019). The transcriptome of Darwin's bark spider silk glands predicts proteins contributing to dragline silk toughness. *Commun. Biol.* 2:275. doi: 10.1038/s42003-019-0496-1

Graeff, E., Maranzana, N., and Aoussat, A. (2019). Biomimetics, where are the biologists? *J. Eng. Des.* 30, 289–310. doi: 10.1080/09544828.2019.1642462

Haynl, C., Vongsvivut, J., Mayer, K. R. H., Bargel, H., Neubauer, V. J., Tobin, M. J., et al. (2020). Free-standing spider silk webs of the thomisid *Saccodomus formivorus* are made of composites comprising micro- and submicron fibers. *Sci. Rep.* 10:17624. doi: 10.1038/s41598-020-74469-z

Heppner, J. B. (2008). "Butterflies and moths (lepidoptera)," in *Encyclopedia of Entomology*, ed. J. L. Capinera (Dordrecht: Springer), 626–672.

Higham, T. E., Russell, A. P., Niewiarowski, P. H., Wright, A., and Speck, T. (2019). The ecomechanics of gecko adhesion: natural surface topography, evolution, and biomimetics. *Integr. Comp. Biol.* 59, 148–167. doi: 10.1093/icb/icz013

Imburgia, M. J., Kuo, C.-Y., Briggs, D. R., Irschick, D. J., and Crosby, A. J. (2019). Effects of digit orientation on gecko adhesive force capacity: synthetic and behavioral studies. *Integr. Comp. Biol.* 59, 182–192. doi: 10.1093/icb/icz024

ISO/TC266 (2015). *ISO 18458:2015-Biomimetics — Terminology, Concepts and Methodology*. Berlin: Beuth Verlag.

IUCN (2021). *The IUCN Red List of Threatened Species* [Online]. Available online at: https://www.iucnredlist.org/ (accessed September 21, 2021)

Jafarpour, M., Eshghi, S., Darvizeh, A., Gorb, S., and Rajabi, H. (2020). Functional significance of graded properties of insect cuticle supported by an evolutionary analysis. *J. R. Soc. Interface* 17:20200378. doi: 10.1098/rsif.2020.0378

Johansson, L. C., and Henningsson, P. (2021). Butterflies fly using efficient propulsive clap mechanism owing to flexible wings. *J. R. Soc. Interface* 18:20200854. doi: 10.1098/rsif.2020.0854

Kerr, G. G., Nahrung, H. F., Wiegand, A., Kristoffersen, J., Killen, P., Brown, C., et al. (2018). Mechanical properties of silk of the Australian golden orb weavers *Nephila pilipes* and *Nephila plumipes*. *Biol. Open* 7:bio029249. doi: 10.1242/bio.029249

King, D. R., Bartlett, M. D., Gilman, C. A., Irschick, D. J., and Crosby, A. J. (2014). Creating gecko-like adhesives for "real world" surfaces. *Adv. Mater.* 26, 4345–4351. doi: 10.1002/adma.201306259

Kulyomina, Y., Moen, D. S., and Irschick, D. J. (2019). The relationship between habitat use and body shape in geckos. *J. Morphol.* 280, 722–730. doi: 10.1002/jmor.20979

Labonte, D., and Federle, W. (2015). Scaling and biomechanics of surface attachment in climbing animals. *Philos. Trans. R. Soc. Lond. B* 370:20140027. doi: 10.1098/rstb.2014.0027

Lin, P. W., and Liu, C. H. (2019). Bio-inspired soft proboscis actuator driven by dielectric elastomer fluid transducers. *Polymers (Basel)* 11:142. doi: 10.3390/polym11010142

Locey, K. J., and Lennon, J. T. (2016). Scaling laws predict global microbial diversity. *Proc. Natl. Acad. Sci. U. S. A.* 113, 5970–5975. doi: 10.1073/pnas.1521291113

Maynard Smith, J. (1978). Optimization theory in evolution. *Annu. Rev. Ecol. Syst.* 9, 31–56. doi: 10.1146/annurev.es.09.110178.000335

Mazzocchi, F. (2019). Scientific research across and beyond disciplines: challenges and opportunities of interdisciplinarity. *EMBO Rep.* 20:e47682. doi: 10.15252/embr.201947682

Muijres, F. T., Johansson, L. C., Bowlin, M. S., Winter, Y., and Hedenstrom, A. (2012). Comparing aerodynamic efficiency in birds and bats suggests better flight performance in birds. *PLoS One* 7:e37335. doi: 10.1371/journal.pone.0037335

Naylor, E. R., and Higham, T. E. (2019). Attachment beyond the adhesive system: the contribution of claws to gecko clinging and locomotion. *Integr. Comp. Biol.* 59, 168–181. doi: 10.1093/icb/icz027

Niewiarowski, P. H., Stark, A. Y., and Dhinojwala, A. (2016). Sticking to the story: outstanding challenges in gecko-inspired adhesives. *J. Exp. Biol.* 219(Pt 7), 912–919. doi: 10.1242/jeb.080085

Norris, J., Tingley, R., Meiri, S., and Chapple, D. G. (2021). Environmental correlates of morphological diversity in Australian geckos. *Glob. Ecol. Biogeogr.* 30, 1086–1100. doi: 10.1111/geb.13284

Patek, S. N. (2014). Materials science. Biomimetics and evolution. *Science* 345, 1448–1449. doi: 10.1126/science.1256617

Petrenko, I., Summers, A. P., Simon, P., Żółtowska-Aksamitowska, S., Motylenko, M., Schimpf, C., et al. (2019). Extreme biomimetics: preservation of molecular detail in centimeter-scale samples of biological meshes laid down by sponges. *Sci. Adv.* 5:eaax2805. doi: 10.1126/sciadv.aax2805

Petroski, H. (2006). *Success Through Failure: The Paradox of Design*. Princeton, NJ: Princeton University Press.

Roberts, S. F., Hirokawa, J., Rosenblum, H. G., Sakhtah, H., Gutierrez, A. A., Porter, M. E., et al. (2014). Testing biological hypotheses with embodied robots: adaptations, accidents, and by-products in the evolution of vertebrates. *Front. Robot. AI* 1:12. doi: 10.3389/frobt.2014.00012

Saito, K., Perez-de la Fuente, R., Arimoto, K., Seong, Y. A., Aonuma, H., Niiyama, R., et al. (2020). Earwig fan designing: biomimetic and evolutionary biology applications. *Proc. Natl. Acad. Sci. U. S. A.* 117, 17622–17626. doi: 10.1073/pnas.2005769117

Schroeder, T. B. H., Houghtaling, J., Wilts, B. D., and Mayer, M. (2018). It's not a bug, it's a feature: functional materials in insects. *Adv. Mater.* 30:1705322. doi: 10.1002/adma.201705322

Selden, P. A. (2017). "Arachnids," in *Reference Module in Life Sciences*, ed. B. D. Roitberg (Amsterdam: Elsevier).

Snell-Rood, E. (2016). Interdisciplinarity: bring biologists into biomimetics. *Nature* 529, 277–278. doi: 10.1038/529277a

Song, Y., Dai, Z., Wang, Z., Ji, A., and Gorb, S. N. (2016). The synergy between the insect-inspired claws and adhesive pads increases the attachment ability on various rough surfaces. *Sci. Rep.* 6:26219. doi: 10.1038/srep26219

Tsai, C.-C., Childers, R. A., Nan Shi, N., Ren, C., Pelaez, J. N., Bernard, G. D., et al. (2020). Physical and behavioral adaptations to prevent overheating of the living wings of butterflies. *Nat. Commun.* 11:551. doi: 10.1038/s41467-020-14408-8

Unterlass, M. M. (2017). Geomimetics and extreme biomimetics inspired by hydrothermal systems—what can we learn from nature for materials synthesis? *Biomimetics* 2:8. doi: 10.3390/biomimetics2020008

Whitesides, G. M. (2015). Bioinspiration: something for everyone. *Interface Focus* 5:20150031. doi: 10.1098/rsfs.2015.0031

Willocx, M., Ayali, A., and Duflou, J. R. (2020). Where and how to find bio-inspiration? *CIRP J. Manuf. Sci. Technol.* 31, 61–67. doi: 10.1016/j.cirpj.2020.09.013

Wolff, J. O., Wells, D., Reid, C. R., and Blamires, S. J. (2017). Clarity of objectives and working principles enhances the success of biomimetic programs. *Bioinspir. Biomim.* 12:051001. doi: 10.1088/1748-3190/aa86ff

World Spider Catalog (2021). *World Spider Catalog* [Online]. Available online at: http://wsc.nmbe.ch (accessed September 16, 2021)

Xiang, H., Yang, X., Ke, L., and Hu, Y. (2020). The properties, biotechnologies, and applications of antifreeze proteins. *Int. J. Biol. Macromol.* 153, 661–675. doi: 10.1016/j.ijbiomac.2020.03.040

Yu, C., Liu, M., Zhang, C., Yan, H., Zhang, M., Wu, Q., et al. (2020). Bio-inspired drag reduction: from nature organisms to artificial functional surfaces. *Giant* 2:100017. doi: 10.1016/j.giant.2020.100017

Yu, X.-Q., Hu, X.-H., Zhu, L., Li, G., Guo, M., Li, Q., et al. (2021). Fabrication of magnetically driven photonic crystal fiber film *via* microfluidic blow-spinning towards dynamic biomimetic butterfly. *Mater. Lett.* 291:129450. doi: 10.1016/j.matlet.2021.129450

Zhou, Y., Robinson, A., Steiner, U., and Federle, W. (2014). Insect adhesion on rough surfaces: analysis of adhesive contact of smooth and hairy pads on transparent microstructured substrates. *J. R. Soc. Interface* 11:20140499. doi: 10.1098/rsif.2014.0499

Conflict of Interest: The authors declare that the research was conducted in the absence of any commercial or financial relationships that could be construed as a potential conflict of interest.

Publisher's Note: All claims expressed in this article are solely those of the authors and do not necessarily represent those of their affiliated organizations, or those of the publisher, the editors and the reviewers. Any product that may be evaluated in this article, or claim that may be made by its manufacturer, is not guaranteed or endorsed by the publisher.

frontiers in Ecology and Evolution

ORIGINAL RESEARCH
published: 17 March 2022
doi: 10.3389/fevo.2022.806453

An Artificial Intelligence Agent That Synthesises Visual Abstractions of Natural Forms to Support the Design of Human-Made Habitat Structures

Gabriele Mirra, Alexander Holland, Stanislav Roudavski, Jasper S. Wijnands and Alberto Pugnale*

Faculty of Architecture, Building and Planning, The University of Melbourne, Melbourne, VIC, Australia

Biodiversity is in a state of global collapse. Among the main drivers of this crisis is habitat degradation that destroys living spaces for animals, birds, and other species. Design and provision of human-made replacements for natural habitat structures can alleviate this situation. Can emerging knowledge in ecology, design, and artificial intelligence (AI) help? Current strategies to resolve this issue include designing objects that reproduce known features of natural forms. For instance, conservation practitioners seek to mimic the function of rapidly disappearing large old trees by augmenting utility poles with perch structures. Other approaches to restoring degraded ecosystems employ computational tools to capture information about natural forms and use such data to monitor remediation activities. At present, human-made replacements of habitat structures cannot reproduce significant features of complex natural forms while supporting efficient construction at large scales. We propose an AI agent that can synthesise simplified but ecologically meaningful representations of 3D forms that we define as visual abstractions. Previous research used AI to synthesise visual abstractions of 2D images. However, current applications of such techniques neither extend to 3D data nor engage with biological conservation or ecocentric design. This article investigates the potential of AI to support the design of artificial habitat structures and expand the scope of computation in this domain from data analysis to design synthesis. Our case study considers possible replacements of natural trees. The application implements a novel AI agent that designs by placing three-dimensional cubes – or voxels – in the digital space. The AI agent autonomously assesses the quality of the resulting visual abstractions by comparing them with three-dimensional representations of natural trees. We evaluate the forms produced by the AI agent by measuring relative complexity and features that are meaningful for arboreal wildlife. In conclusion, our study demonstrates that AI can generate design suggestions that are aligned with the preferences of arboreal wildlife and can support the development of artificial habitat structures. The bio-informed approach presented in this article can be useful in many situations where incomplete knowledge about complex natural forms can constrain the design and performance of human-made artefacts.

Keywords: artificial intelligence, reinforcement learning, human-made habitat structures, visual abstraction, computer-aided design, biological conservation, ecocentric design

OPEN ACCESS

Edited by:
Birgitta Dresp-Langley, Centre National de la Recherche Scientifique (CNRS), France

Reviewed by:
Laxmi Goparaju, Vindhyan Ecology and Natural History Foundation, India
Andreas Jedlitschka, Fraunhofer Institute for Experimental Software Engineering (IESE), Germany

****Correspondence:***
Gabriele Mirra
gabriele.mirra@unimelb.edu.edu

Specialty section:
This article was submitted to Models in Ecology and Evolution, a section of the journal Frontiers in Ecology and Evolution

Received: *31 October 2021*
Accepted: *01 February 2022*
Published: *17 March 2022*

Citation:
Mirra G, Holland A, Roudavski S, Wijnands JS and Pugnale A (2022) An Artificial Intelligence Agent That Synthesises Visual Abstractions of Natural Forms to Support the Design of Human-Made Habitat Structures. Front. Ecol. Evol. 10:806453. doi: 10.3389/fevo.2022.806453

INTRODUCTION: ARTIFICIAL INTELLIGENCE AND DESIGN OF HABITAT STRUCTURES

This article aims to investigate whether and how artificial intelligence can help in the urgent task of designing replacement habitat structures. We seek to demonstrate that an artificial intelligence agent can synthesise visual abstractions of natural forms and support the design of artificial habitat structures. The overarching purpose of our approach is to contribute to ecocentric design or design that seeks to benefit all forms of life and life-hosting abiotic environments.

Complex habitat structures are pervasive and tend to contain more organisms and species than simple habitats (Torres-Pulliza et al., 2020). Yet humans simplify habitats at an unprecedented rate (Díaz et al., 2015). For instance, large old trees are structurally complex organisms that provide critical habitats for many animals. Many human practices routinely remove old trees from urban and rural areas to satisfy economic, aesthetic and safety concerns (Le Roux et al., 2014). It is difficult to replace such organisms because large old trees take hundreds of years to mature (Banks, 1997). Ecologists predict that a massive reduction of the old-tree populations and the subsequent simplification of their local ecosystems are unavoidable in the near future worldwide, even if the planting of young trees increases significantly (Lindenmayer et al., 2012; Manning et al., 2012).

The global loss of large old trees and other complex natural structures calls for a remedial action. Artificial coral reefs (Baine, 2001) and wetlands (Mitsch, 2014) are instances where human-made habitat opportunities attempt to augment natural occurring structures. In these conditions, it is important to understand why complex natural habitat structures are more attractive to fauna and design artificial replacements that reproduce their key features. We do not aim to facilitate or be supportive of the alarming loss of natural habitats, such as large old trees or coral reefs. Preservation of such environments is the highest priority. Our work aims to contribute to situations where degradation has already occurred or is inevitable.

Restoration practitioners recognise that artificial structures will never fully match the geometries and functions of complex natural structures. Old trees that can live for many centuries provide a telling example. Here, a combination of growth processes and environmental factors occurring over extended timespans make highly differentiated shapes that typical construction methods cannot reproduce (Le Roux et al., 2015a) and the contemporary scholarship does not fully understand (Lindenmayer, 2017). As tens of millions of old trees will be lost within the next 50 years in south-eastern Australia alone (Fischer et al., 2009), designers seeking to replicate these complex forms must also consider rapid construction at scale and under conditions of uncertainty.

In such contexts, designers successfully use criteria such as the ease of construction and cost to judge the quality of artificial habitat structures. However, these approaches also introduce biases that result in simplified systems that do not occur in natural habitats. These biases include creating designs based on widely used artefacts and ignoring relationships and scales that are difficult to document. For instance, one emerging strategy for woodland restoration augments tree plantings with constructions including utility poles enriched with perch structures (Hannan et al., 2019) and nestboxes (Mänd et al., 2009). These structures can be successful in attracting wildlife. Yet their relatively homogenous forms do not replicate the number and diversity of naturally occurring branching structures of old trees. This means they are considerably less effective than their natural precedents (Le Roux et al., 2015a; Hannan et al., 2019). Therefore, designers of surrogate habitat structures need novel methods and tools that can emphasise, recognise, and replicate significant features of trees for artificial reproduction at high volumes.

Researchers, conservation managers and arborists are among human users who already use tools to sort, extract and visualise data to understand tree forms. However, these approaches rely on pre-existing parametrisation to describe and quantify tree structures. For instance, ecologists describe trees by measuring trunk diameters. This approach is simple but crude and can be significantly misleading. For example, large diameter young trees are not ecologically equivalent to old trees, in part because they have more simple shapes (Lindenmayer, 2017). Furthermore, there is no widely accepted definition or measure of a tree structure (McElhinny et al., 2005; Ehbrecht et al., 2017). Consequently, tree geometries do not easily reduce to discrete attributes without significant artefacts and the loss of meaningful information (Parker and Brown, 2000; Ehbrecht et al., 2017).

As an alternative to such parameter-based approaches, we propose to achieve bio-informed designs through an AI-driven synthesis of visual abstractions. This process reduces the amount of information in visual data to produce simplified representations that heighten semantically relevant features of such data (for a review, see Arnheim, 2010; Viola et al., 2020). For our objective, relevant data includes three-dimensional scans of natural habitat structures. In this context, human design objectives seek to express the needs and preferences of nonhuman animals and other lifeforms (Roudavski, 2021). An ability to express needs and preferences is particularly important for nonhuman users such as arboreal fauna. These users have needs that are not fully understood by humans. The process of abstraction is beneficial in such cases because it can focus on relevant features of a source object without the need to pre-specify parameters or types.

We acknowledge an increasing interest in AI systems dealing with visual information. These systems include applications in medicine, geographical information systems, design and other domains (Soffer et al., 2019; Reimers and Requena-Mesa, 2020; Mirra and Pugnale, 2021). We propose that such emerging techniques can significantly contribute to environmental conservation and regeneration through the design of artificial habitat structures. Exploiting this opportunity, we ask whether and how an artificial intelligence agent can synthesise simplified surrogates of natural forms. Consequently, this article seeks to demonstrate the ability of AI to capture and reproduce characteristic features of complex geometries.

The article is structured as follows. Section "Materials and Methods: An Autonomous Agent for Visual Abstraction of Complex Natural Forms" discusses AI techniques for visual information processing, including data generation, reconstruction, and synthesis of visual abstractions. In this section, we also introduce our AI agent, explain the use case, describe the training procedures and discuss the evaluation methods. Section "Results: Demonstration of Autonomous Visual Abstraction and Verification" demonstrates the capability of the AI agent to synthesise visual abstractions of tree forms. Our output analysis indicates that the visual abstractions generated by the AI agent are verifiable and meaningful. Section "Discussion: Proposed Advancements and the Future Development of the Artificial Intelligence Toolkit" compares our findings with previous studies, highlighting our innovations in three areas: AI for the synthesis of visual abstractions in 3D, resistance to human biases, and design innovation. This section also presents this work's current limitations and prospects for future research.

MATERIALS AND METHODS: AN AUTONOMOUS AGENT FOR VISUAL ABSTRACTION OF COMPLEX NATURAL FORMS

The steps we followed to answer the research question and test the hypothesis include:

- Step 1: Select an AI model that can synthesise visual abstractions of 3D forms. In our case, a reinforcement learning agent.
- Step 2: Define an appropriate case study. We use large old trees.
- Step 3: Adapt the AI model to the case study.
- Step 4: Develop measurement and analysis routines to compare human-reduced artificial habitat structures, trees represented as simplified 3D models, and AI-synthesised forms.
- Step 5: Evaluate visual abstractions produced by the AI agent.

Artificial Intelligence Model Selection

This section justifies our choice of an AI model to synthesise visual abstractions and describes its main features. We aim to use AI to extract visual features from complex natural forms that are three-dimensional and synthesise visual abstractions of these forms. We provide a brief overview existing AI techniques that can be trained on 3D visual data to perform similar tasks and describe their limitations. We focus on strategies to represent 3D data and applications for 3D data generation and reconstruction.

Our overview includes applications of generative models for 3D data generation and explains their unsuitability for the case study presented in this article, we then describe applications of AI agents that interact with a modelling environment to reconstruct forms. These agents can reduce the representation accuracy of target 3D forms but are trained only to reconstruct samples that are stored in the training dataset. Finally, we describe how generative models and AI agents can be combined to synthesise visual abstractions of habitat structures. We identify an existing technique that can achieve this goal in 2D and outline our plan to extend it for 3D applications.

Artificial Intelligence for 3D Data Generation

Artificial Intelligence comprises a broad range of techniques that can simulate how humans process visual information, including 2D images and 3D forms. Among these techniques, Convolutional Neural Networks (CNNs) (Krizhevsky et al., 2012) have become mainstream in AI due to their success in image classification.

The convolution operation can extract features from spatially organised data, such as a grid of pixels – i.e., images – which the AI model combines into low-dimensional representations useful for data classification. The reverse of the convolution operation – named deconvolution can synthesise features from low-dimensional representations. An AI model can be trained to aggregate these features and generate or reconstruct data. Convolution and deconvolutions natively process 2D data but can work in 3D if the representation format of the 3D data is discrete and regular.

Generative models, such as generative adversarial networks (GAN) (Goodfellow et al., 2014) and variational autoencoders (VAE) (Kingma and Welling, 2014), exploits deconvolutional layers to synthesise images at high fidelities and resolutions (Brock et al., 2019; Karras et al., 2019). They also can perform a variety of image translation tasks, including translation from photographs to sketches (Isola et al., 2017) and from low-resolution to high-resolution images (Ledig et al., 2017).

Previous studies used generative models featuring 3D deconvolutions for 3D data generation. AI researchers had to develop strategies to represent 3D data in a format that complied with the requirements of the deconvolution operations. The most straightforward approach converts a 3D model into a voxel grid, or occupancy grid, which is a data format originally proposed for 3D-model classification tasks (Maturana and Scherer, 2015; Wu et al., 2015). AI researchers used voxel grids to train AI models to generate new forms (Brock et al., 2016; Wu et al., 2016) and to translate text or 2D sketches into 3D models (Chen et al., 2018; Delanoy et al., 2018).

Alternative representation strategies developed for classification tasks – including unordered point clouds (Qi et al., 2017; Wang et al., 2019) or heterogeneous meshes (Feng et al., 2019; Hanocka et al., 2019) – cannot work for data generation tasks because the output of an AI model consists of a finite and ordered set of numbers. One strategy that extends the application of generative models beyond voxel grids involves representing the 3D models that populate the dataset as isomorphic meshes and training a model to synthesise new topologically equivalent meshes (Tan et al., 2018). This approach can also work with point clouds by ensuring one-to-one point correspondences between every data sample (Gadelha et al., 2017; Nash and Williams, 2017). Besides data generation, these strategies proved effective for 3D data reconstruction from partial 3D input (Litany et al., 2018) or 2D images (Yan et al., 2016; Fan et al., 2017).

These applications demonstrate that generative models can effectively learn to synthesise 3D data, but not all representation formats are suitable for this task. Furthermore, 3D deconvolution operations produce very accurate data, making the AI-generated forms too detailed to be considered visual abstractions. In application to the design of habitat structures, this is not helpful as preserving the complexity of existing structures is not practicable.

Artificial Intelligence for Inverse Graphics

A different approach to the problem of 3D data generation involves training an AI agent to perform modelling actions within modelling software. This approach does not rely on deconvolution operations to produce 3D forms and thus can produce less detailed forms. Therefore, it has a greater potential for synthesising visual abstractions of natural habitat structures.

The main differences with the generative models described in section "Artificial Intelligence for 3D Data Generation" are that:

- *The learning task is dynamic*: the agent must learn to perform a set of modelling actions rather than synthesising a form in one shot.
- *Forms can be generated through any external modelling environment*: The choice of a representation format that is suitable for AI training is less relevant for the quality of the generated forms because, after training, the 3D modelling actions can be rendered by any modelling environment to produce forms at high resolutions.

The application of this approach focused on inverse graphics, i.e., the problem of predicting modelling actions necessary to reconstruct 3D forms. Solving this problem involves: (1) deciding on a representation that supports comparisons between target and generated forms; (2) defining a similarity metric; and (3) designing how the AI agent interacts with the modelling environment, which includes defining the typology of modelling actions and the effect of each action on the generated form.

Generally, inverse graphics aims to reconstruct an exact replica of target forms. The modelling environment is not constrained, and the agent can perform all the actions necessary to reconstruct the form. For instance, Willis et al. (2021) developed a reinforcement learning agent that selects modelling actions such as *extrude* and *Boolean union* to reconstruct a target CAD model procedurally. They used a domain-specific language (DSL) to formalise sequences of actions in a symbolic way. Their implementation represented 3D models as graphs, whereas the agent assessed the quality of the reconstructions by measuring the similarity between the actions necessary to produce the target form and the actions performed by the agent. Sharma et al. (2018) also used a DSL and trained an agent to reconstruct 3D forms. Their agent performed comparisons in the voxel space and assessed similarity by a set of geometric metrics, including the chamfer distance.

Other studies used a constrained modelling environment, such that the agent could only approximate the target form. Kim et al. (2020) developed an agent that reconstructed 3D forms through the aggregation of primitives. The model placed 3D components in a voxel grid to reconstruct target geometries that were also represented as voxels. Besides formal similarity, the model considered the stability of generated forms by getting feedback from a physics simulator. Liu et al. (2017) and Zou et al. (2017) applied a similar approach to construct simplified representations of target meshes through the aggregation of multiple primitives.

Overall, approaches based on AI agents can either produce an accurate reconstruction of target forms or simplified representations of them. The representation accuracy of the generated forms depends on how the agent interacts with the modelling environment and assesses the similarity between generated and target forms. However, most applications address data reconstruction, which in our case study would preclude the necessary innovation, for example, to support the production of the AI-generated forms via artificial means and their adaptation to novel ecosystems.

Artificial Intelligence-Driven Synthesis of Visual Abstractions

Through the analysis of literature on AI, we found that there are no models that are specifically designed to synthesise visual abstractions in 3D. Despite this, existing models do show some of the features that are necessary to perform this task. For instance, the AI agent developed by Zou et al. (2017) can generate simplified representations of target meshes by assembling solid primitives. However, their AI agent could not generate forms other than those contained in the training dataset. Conversely, generative models like GANs can learn the underlying distribution of a dataset of 3D forms and sample new regions of such distribution to generate new data (Wu et al., 2016). Yet, the GAN generator has infinite representation capabilities. Consequently, a well-trained model can produce synthetic forms that are very accurate. The generator does not try to reduce the number or complexity of the extracted features and, therefore, does not produce visual abstractions.

A model that can synthesise visual abstractions should be able to extract visual features from a dataset of forms in the same way GANs do. It should also be able to produce synthetic data through interaction with a constrained modelling environment, which is what an AI agent trained for inverse graphics does.

Computer scientists achieved these objectives for 2D images applications by integrating an AI agent with a GAN discriminator. Ganin et al. (2018) used this approach to train an AI model named "Synthesising Programs for Images using Reinforced Adversarial Learning" – SPIRAL – to generate visual abstractions of 2D images. This application tasked the AI agent with learning a set of drawing actions to reproduce the key features of an image dataset within a drawing software.

Unlike previous applications of AI for inverse graphics (see section "Artificial Intelligence for Inverse Graphics"), in SPIRAL, humans do not supply the agent with information about human drawings, and the agent must develop a strategy by trial and error. An additional component – a GAN discriminator – produces a similarity metric that informs the agent about the quality of the synthesised images.

The SPIRAL model and its upgrade SPIRAL++ (Mellor et al., 2019) demonstrated that the agent could learn to extract

meaningful visual features from samples and reproduce such features while drawing on an empty canvas, even without examples of drawing actions. The implementation controlled the accuracy of the synthesised images by (1) number of actions; and (2) action typology. In this case, a lower number of actions produced less realistic images but forced the agent to focus more efficiently on the most relevant features. For instance, an agent trained to generate human faces in 17 drawing actions attempted to maximise the efficiency of the actions by exploiting a single stroke to produce every facial feature. The action typology affected the character of the representation. For instance, if the agent had used straight lines instead of curves, it would have produced abstract shapes that could only crudely approximate the features of a human face. Yet, humans might still easily recognise such arrangements as sketches of faces.

To date, studies applied SPIRAL and SPIRAL++ to generate human faces, handwritten digits, and images representing 3D scenes. There are no current implementations of SPIRAL for 3D data to our knowledge. Despite that, we selected this SPIRAL model for further development because, unlike GANs, it can autonomously decide the number and characteristics of the features to reproduce in a synthetic visual abstraction. Furthermore, unlike current applications for inverse graphics, it does not require a dataset of drawing instructions and supports fine control of the abstraction process through the specification of constraints. Later in the article, we describe how our version of SPIRAL can extract visual features from a 3D dataset of tree forms and synthesise visual abstractions of such forms.

Use-Case Selection

Our second step defines a relevant use case for the AI agent that defines a scenario where abstraction is possible and beneficial.

We first establish a domain of complex forms suitable for simplification through a process of abstraction. We then select an example known to contain relevant features. As described in the introduction, we focus on characteristics of large old trees. Below, we define four groups of characteristics, from general to specific, and explain why trees can serve as a useful case study.

Large Old Trees Within Ecosystem Dynamics

Our first group relates to patterns of energy and material flows. We acknowledge that recent research describes trees as complex and highly social organisms. At the level of whole landscapes, large old trees mediate critical physical, chemical, and biological roles at varying spatial and temporal scales. They regulate hydrological, nitrogen and carbon regimes; alter micro- and meso-climatic conditions; act as key connectivity nodes in modified landscapes such as paddocks and cities; contribute to vertical and horizontal habitat heterogeneity; and serve as local hotspots of biodiversity (Lindenmayer and Laurance, 2016). Underground, systems of roots and mycorrhizal fungi form communicatory networks that connect trees (Beiler et al., 2010). In such networks, large old trees act as hub nodes with high connectivity to other plants. Highly-connected large old trees improve responsiveness to threats, maximise resource utilisation and build forest resilience by sharing nutrients (Gorzelak et al., 2015) and supporting long-term succession (Ibarra et al., 2020). These characteristics provide ample scope for future work but remain beyond the scope of this study.

Large Old Trees as Habitat Structures

Our second group narrows our focus to the composition and arrangement of physical matter. In doing so, we consider the trees' capability to support dwelling. Ecologists describe large old trees as keystone habitat structures because they support far more reptiles, insects, birds and other taxa than other landscape elements (Manning et al., 2006; Stagoll et al., 2012). Large old trees support more diverse animal and plant communities than smaller and younger trees because they have unique structures with many different attributes. Hollows and cavities afford breeding sites; foliage offers shelter; fissured bark offers invertebrate food resources, and large complex canopies with an abundance of diverse branches serve as sites for resting and social activities (Lindenmayer and Laurance, 2016). These important characteristics provide a broad selection of definable features for potential artificial replication.

Large Old Trees as Structures Supporting Specific Bird Activities

Our third group relates to bird sheltering and perching. To demonstrate the potential for our AI agent to synthesise visual abstractions of tree habitat structures, we select two significant and interrelated activities supported by trees. Many birds, including passerines – representing 60% of all bird species – spend most of their time perching. Large tree crowns provide a variety of sheltered and exposed perch sites, creating opportunities for habitation (Hannan et al., 2019). For instance, one study observed a quarter of all bird species exclusively used perched in structures provided by large trees (Le Roux et al., 2018). Canopies of large old trees have significantly more branches and branch types and so support more birds than small trees (Stagoll et al., 2012; Barth et al., 2015). We use existing ecological evidence in combination with our own statistical estimates of branch types to generate baselines for the artificial replication of branch types and distributions.

Large Old Trees Through the Three-Dimensional Distributions and Shapes of Perch Sites

Our fourth and final group relates to how the geometrical characteristics of canopies affect bird preferences, wellbeing, and survival. Birds rely on their physiological, sensory, and cognitive abilities to make use of tree canopies. Tall old trees are visually prominent and can serve as landmarks that link landscapes (Fischer and Lindenmayer, 2002; Manning et al., 2009). In the canopies of old trees, dieback creates vertical structural heterogeneity (Lindenmayer and Laurance, 2016), resulting in diverse and segmented branch distributions (Sillett et al., 2015). These complex canopy shapes provide a broad range of geometric conditions supporting birds, including significant quantities of exposed and near-horizontal branches (Le Roux et al., 2018). Studies of large old trees show that many individual birds and bird species prefer to perch on horizontal branches and branches lacking foliation (Le Roux et al., 2015a; Zielewska-Büttner et al., 2018). The existence of such evidence makes it possible to

consider geometric properties of branch distributions in isolation from other essential characteristics of trees.

Despite having many key attributes and functions, these steps show that it is possible to isolate important characteristics of large old trees for use in our case study. We focus on branch distributions within the canopy structure of old trees as a test case for AI-driven visual abstraction of complex habitat structures. Our approach can accommodate and layer additional measurements for other characteristics.

The next step in our method establishes base datasets of canopy structures for use within our AI model.

Data Collection and Training Dataset Preparation

We establish base datasets (Dataset 1: Natural habitat-structures and Dataset 2: Artificial habitat-structures) representing the tree canopy features identified previously as our focus (**Figure 1**). These datasets allow our AI agent to be exposed to branch features and distributions occurring in natural trees. They also enable us to evaluate the resulting AI-generated forms. We briefly outline these datasets below. For technical details about the workflow and the equipment and software used, refer to Appendix D: Habitat Structure Dataset Construction.

To create an appropriate training dataset of branch features (Dataset 1: Natural habitat-structures), we first acquired geometries of three natural trees in a format that captures large volumes of structural information in three dimensions. Given the technical constraints of the modelling environment discussed below, we selected younger trees to test our approach. Although these trees have simpler canopy shapes than the canopy of older trees, they still represent a significant increase in structural complexity and perch diversity relative to current artificial habitat structures (refer to section "Measurement and Comparison" for a comparison between the artificial habitat structures and tree samples in our datasets).

We use LiDAR (Light Detecting and Ranging), as it does not require pre-existing categorisation of geometrical features. Instead, this technology creates 3D points representing locations where the tree surfaces reflect the laser beams (Atkins et al., 2018). We then isolate points representing branches from the resulting point clouds, and fit geometric primitives that approximate individual branches. From this, we extract the 3D centroids and radii of all branches in each sample tree. Refer to Appendix D: Habitat Structure Dataset Construction for technical details of the workflow.

To enable an evaluation of the forms synthesised by our AI agent in comparison to existing artificial habitat structures (Dataset 2: Artificial habitat structures), we select a range of artefacts representing existing artificial habitat structures of increasing geometric complexity. These structures provided benchmark states of complexity for comparison with our AI-synthesised forms. They also represented meaningful reductions of complexity performed by humans with existing conservation techniques for artificial habitat construction (Hannan et al., 2019). This set of sample structures includes – from simple to more structurally complex – a non-habitat vertical structure representing a non-enriched utility pole (I), a two (T) and three (Y) prong habitat-structure representing utility poles enriched with perches, and a more complex 9-prong artificial structure (X) analogous to a translocated dead snag with major tree limbs retained (**Figure 2**).

We then pre-processed our dataset to make it suitable for AI training. Current technical constraints require AI to work with input data at relatively coarse resolutions. We describe in detail the modelling environment that we constructed for the AI agent in the next section. Here, we briefly outline how we create a simplified dataset of tree forms appropriate for the limited resolution of the modelling environment.

Figure 3 shows the data preparation process. To simplify the tree representations, we first discard all branch centroids with a radius smaller than 5 cm. We then convert these centroids into $32 \times 32 \times 32$ voxel representations to comply with the maximum resolution set for the 3D modelling environment. To do so, we assign zeros to the voxels that contain one or more branch centroid points. We then normalise the data by centring and scaling the voxel representations so that their largest dimension does not exceed the size of the voxel grid. These measures discourage AI agents from differentiation based on size at the expense of more relevant characteristics such as branching structures.

This process results in a set of $32 \times 32 \times 32$ voxel grids representing natural trees (Dataset 1: Natural habitat structures). We apply a similar strategy to represent current artificial habitat structures as voxel grids (Dataset 2: Artificial habitat structures).

The steps outlined in this section establish a useable case for training and testing our AI agent. Despite simplifications, this case is characteristic of many habitat structures and their geometries. The proposed technique supports future scaling and customisation.

Model and Environment

This step of the process implements an artificial agent that can ingest and learn from the dataset described above, making it suitable for the use case.

The application presented in this article required several adaptations of the SPIRAL architecture. We use the implementation by Mellor et al. (2019) – SPIRAL++ – as a baseline because it features upgrades that stabilise training and simplify the learning task for the agent. In the article, we use the acronym SPIRAL to refer to both implementations by Ganin et al. (2018) and Mellor et al. (2019), as the agent's policy architecture is the same.

Our model had to be able to observe 3D representations of trees described in the previous section and synthesise visual abstractions of such trees within a 3D modelling environment. Currently, SPIRAL works with 2D images. Although Ganin et al. describe an application for 3D modelling, the agent always observes 2D projections, and the existing design limits its actions to translations of geometric primitives already placed in the 3D canvas.

Following previous applications of AI for 3D data generation (Wu et al., 2016), we define the observation, or the visual input for the model, as a 3D array of numbers that we represent as a

FIGURE 1 | Natural and artificial habitat structures of differing complexity: an old tree; a translocated dead tree (complex artificial habitat structure); an enriched utility pole (simple artificial habitat structure).

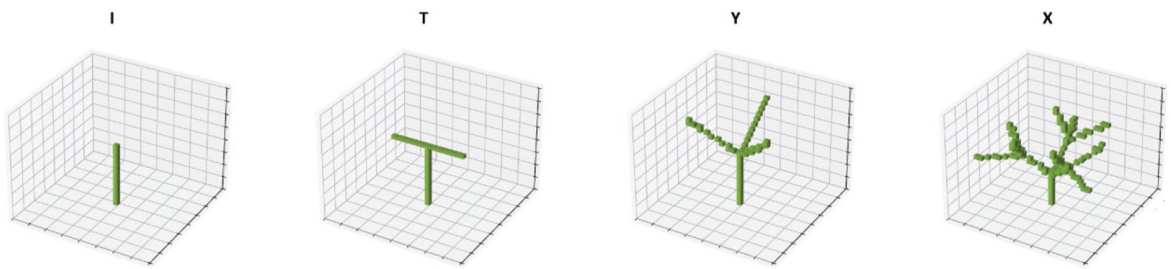

FIGURE 2 | Artificial habitat-structure dataset. Voxel representations of current artificial structures (Dataset 2): a non-habitat utility pole (I), two forms of utility poles enriched with perches (T and Y), and a 9-prong artificial structure analogous to a translocated dead tree (X).

voxel grid. We set the size of the grid to be 32 × 32 × 32, due to hardware constraints, and assign each location of the grid values of 0 or 1. According to this definition, a 3D form is a discrete array of binary values, where 0 corresponds to the coordinate of each point and 1 to the empty space.

We prepare a 3D modelling environment to allow the SPIRAL agent to perform observable actions in three dimensions. In Ganin et al. (2018), the agent interacts with an external drawing software that allows a wide variety of drawing actions, including the selection of brushes, pressure, and colour. Our implementation runs in a custom 3D modelling environment with a limited number of actions but has future potential to integrate with common CAD software and exploit a full range of modelling actions.

The environment consists of a 3D canvas, which initialises as empty space – a 32 × 32 × 32 array of ones – and a set of modelling actions. The agent can interact with the environment by moving the cursor within a sub-voxel grid of size 16 × 16 × 16 contained in the main 32 × 32 × 32 voxel grid. The cursor can switch the state of one or multiple voxels. The environment renders the actions performed by the agent as groups of visible voxels.

Since we aim to train AI agents to emphasise features of a tree canopy structure without copying its geometry, we limited

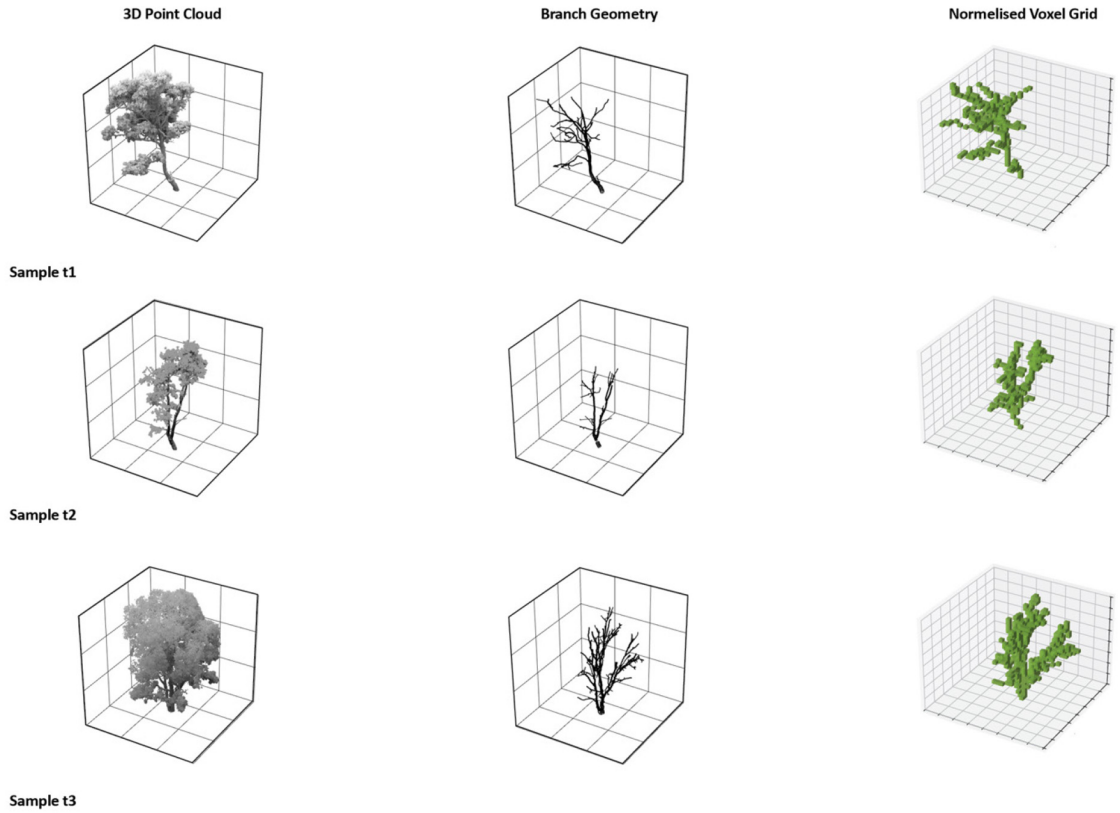

FIGURE 3 | Conversion of the 3D scans of existing trees into 32 × 32 × 32 normalised voxel representations to create the natural habitat-structure dataset.

the action space to the placement of lines in the 3D modelling environment. We choose lines because existing state-of-the-art ecological research uses lines to define cylinders that describe three-dimensional branching structures of trees (Malhi et al., 2018). Spatial configurations of lines can also readily translate into full-scale construction techniques.

Our custom agent places lines by specifying start and end points. The modelling environment renders such lines as sequences of voxels with a value of 0. Formally, we describe the placement of a line as a modelling action defined by two elements: end point (P'') and placement flag (f). Given an initial start point (P'), the agent decides the location of the endpoint within the voxel grid boundaries. Then, it controls the variable f to either place a line between P' and P'' or jump directly to P'' without placing any object in the canvas. P'' becomes the start point for the next modelling iteration.

It is worth mentioning that we could provide 3D visual input in any other format, including point clouds and meshes. As discussed in section "Artificial Intelligence Model Selection", many AI techniques can process such formats with limited computational power. We opt for voxel representations because the translation of the 2D convolutional layers of the SPIRAL architecture to 3D convolutional layers – necessary to extract visual features from 3D data – is straightforward and does not require extensive fine-tuning of network parameters other than layers sizes. Moreover, since the agent is trained to perform sequences of 3D modelling actions – by selecting voxel coordinates within a discrete 3D grid – our implementation generates forms that can be rendered in any CAD software and at any resolution. For these reasons, we considered the use of voxel representations as the best approach to test the hypothesis of this research work.

To process the voxel grids and let the agent perform actions in the 3D modelling environment, we reimplemented the SPIRAL model using the Tensorflow open-source machine learning platform (v 2.6.0). We modified the architectures of the agent's policy and the discriminator as follows:

- We turned all the 2D convolutional and deconvolutional layers of policy and discriminator into 3D convolutional and deconvolutional layers. We preserved all original kernel and stride sizes but halved the number of filters for the residual blocks and kept the same for the remaining layers.
- We upscaled the embedding layer by 2, due to the increased size of the action-space locations.
- We included a new term in the conditioning vector to account for the extra dimension in the action space locations.

We provide additional details of our reimplementation of the SPIRAL architecture in Appendix B: Network Architecture, and a description of our training procedure in Appendix A: Training

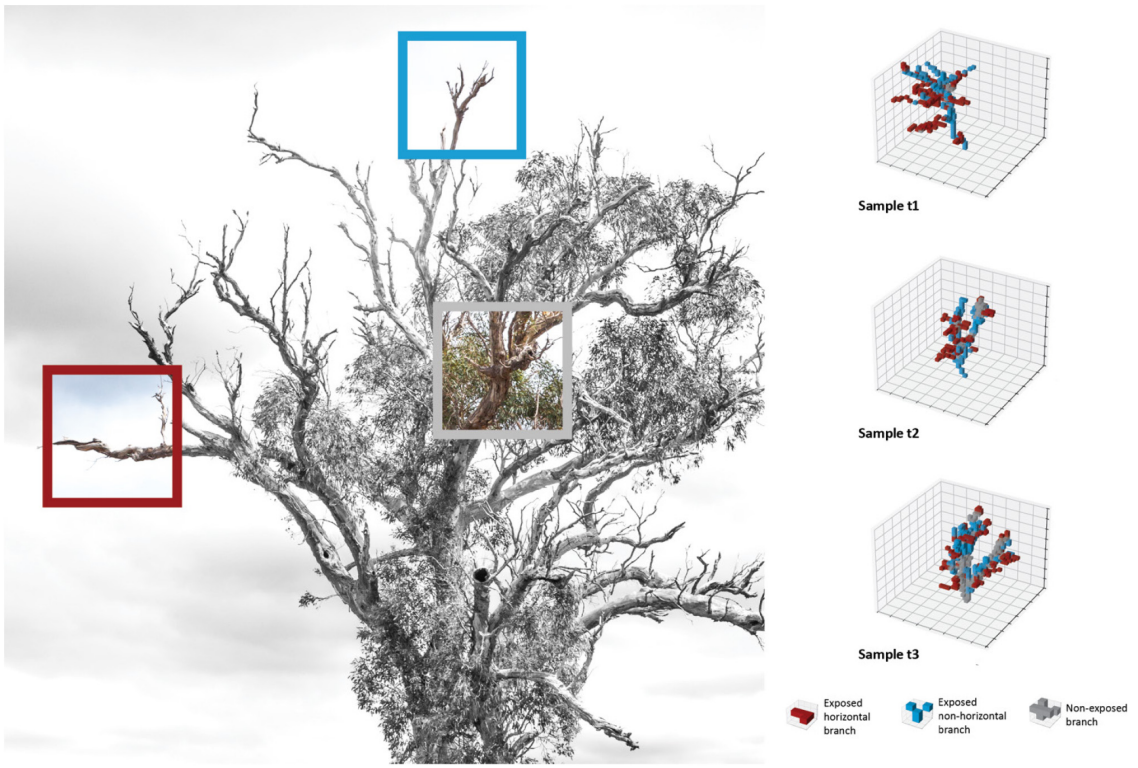

FIGURE 4 | Segmentation of 32 × 32 × 32 voxel representations. **(Left)** Select branch types in a large old tree. **(Right)** 3D segmentation of the sample tree dataset.

Procedure and Hyperparameters. To validate the adaptations described above, we tested the model on a benchmark, which we describe in detail in Appendix C: Model Calibration.

Measurement and Comparison

Having prepared a training dataset and developed an AI agent trained to produce 3D forms, we evaluate the outcomes. These steps aim to confirm that resulting AI-synthesised visual abstractions of natural structures are verifiable, meaningful and can serve as a base for future scaling.

For this purpose, we developed a measurement and assessment routine that can compare trees represented as voxels (Dataset 1), human-reduced sets of habitat structures (Dataset 2), and AI-synthesised forms. Since our focus is on the branch distributions of old trees as outlined in section "Use-Case Selection", we base our assessment on two quantitative indexes:

- *Complexity index:* Our first measure is an overall estimation of geometric complexity. We focus on complexity as a measure of the geometry-habitat relationship based on the evidence that it positively correlates with biodiversity. More diverse geometries of branches in a tree canopy allow species to use a greater number of structures as their habitat.
- *Perch index:* Our second measure quantifies specific geometric features we identified as relevant for birds for perching. These features are branches that are elevated, horizontal and exposed. Such branch conditions represent perch sites chosen by birds to rest for periods of time and have relatively unobstructed views with clear access.

This two-prong assessment strategy combines a broad but generic measure (the complexity index) with a measure that focuses on an important but narrow activity of a key habitat user (the perch index). For further justification of each measure, refer to Appendix E: Measurement Supporting Information.

There is also an additional, implicit measure that is automatically learnt by the AI discriminator during the training process: the similarity index. We do not use the similarity index to compare forms. Instead, the AI agent uses this measure to evaluate how many features of the voxelised trees observed during the training process are preserved in the visual abstractions it generates. This internal similarity index ensures that the voxel forms evaluated by our comparison routine are not random aggregations but are already statistically congruent to the source data of voxelised trees.

To generate the complexity index, we use the fractal dimension, which is a ratio that measures how the detail of geometry changes at different scales (Godin et al., 2005). We used box-counting in three-dimensional arrays (Chatzigeorgiou Group, 2019) as the method for our measurement, which is a standard procedure for calculating the fractal dimension of 3D objects.

To generate the perch index, we developed an automatic procedure that finds all horizontal and exposed branches in

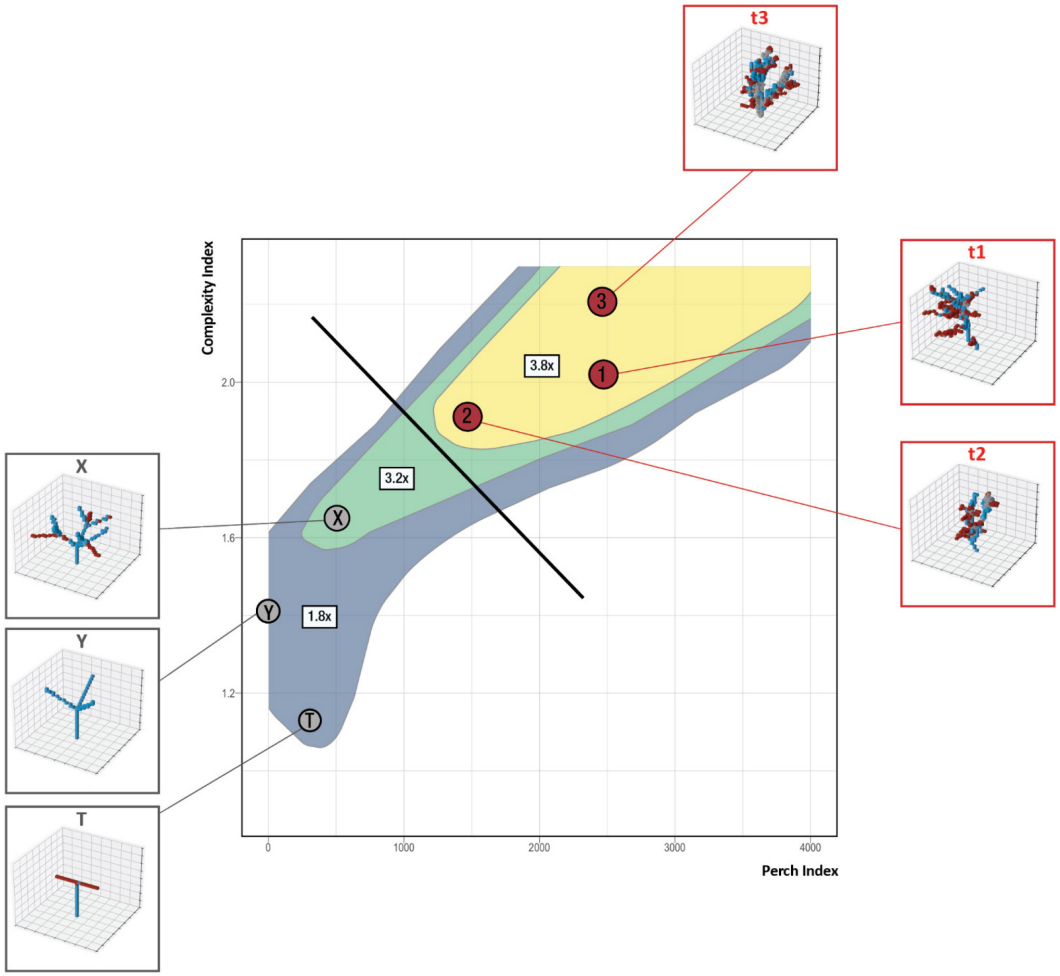

FIGURE 5 | Validation of measurement workflow through a comparison of the assessment routine outcomes and field observations of bird response to the same structural types.

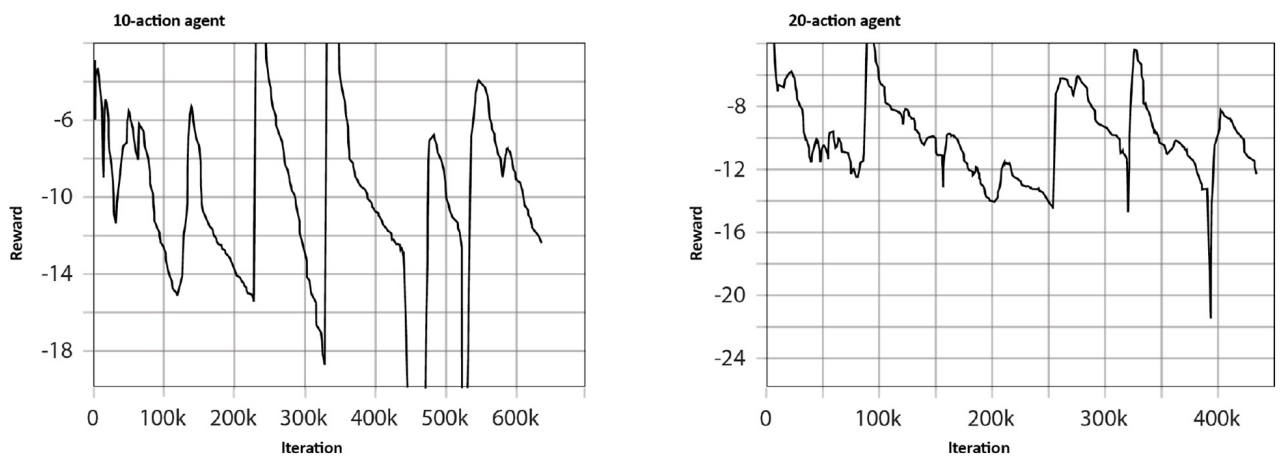

FIGURE 6 | Trend of the reward achieved by the 10-action and 20-action agents over consecutive training iterations.

the voxelised forms. To find these branches, we first segment the voxel representations according to three classes of branch conditions. Our branch classes are exposed horizontal branches (red), exposed non-horizontal branches (blue), and non-exposed branches (grey) (**Figure 4**).

Our branch classification procedure works as follows. We first define a branch as a $3 \times 3 \times 3$ window centred at the voxel location. For every voxel, we assign a label to the voxels included in the window by verifying the occurrence of the following geometric conditions:

- If the number of voxels within the window exceeds a threshold *T*, we label the voxels as a non-exposed branch.
- If the number of voxels within the window is less than or equal to *T*, we label the voxels as a non-horizontal exposed branch.
- If the number of voxels within the window is less or equal than *T* and either the top or the bottom plane of the window is empty, we label the voxels as a horizontal exposed branch.

Finally, to convert this segmentation routine into a perch index, we sum the z co- ordinate of all voxels classified as horizontal- exposed.

Following a set of experiments, we defined a value of 5 for the threshold *T*. The legend in **Figure 4**, bottom right, visualises the results obtained by segmenting randomly populated $3 \times 3 \times 3$ windows.

We validated our routines by segmenting the voxel representations of the training dataset and visually inspecting the quality of the resulting segmentations (**Figure 4**, right). The analysis revealed that, despite the coarse resolution, the routine could extract semantic information that matches the three branch categories.

As a final step, we also validated our measurement workflow by comparing the assessment of structures in our training and comparison datasets with empirical observations of bird behaviour.

The 2D graph in **Figure 5** shows the comparison space defined by our measurements. We define the assessment space by our complexity and perch indexes and plot voxel representations of natural trees (red) and artificial habitat structures (grey) in this space. Bubbles represent the three types of habitat structures in our datasets that have also been experimentally observed for their bird species response: enriched habitat pole (T and Y), translocated dead snag (X) and remnant trees (T1, T2, and T3).

The contours under this assessment space represent the observed mean native species gain when a structure type is installed compared to a site with no habitat structures. Contour levels include bird response values for enriched utility poles (blue, with the lowest species response), translocated dead trees (green) and natural trees (yellow, with the highest species response).

We use data collected by Hannan et al. (2019) to populate our species response contours. Compared to a site with no habitat structures, Hannan et al. (2019) found that enriched utility poles, translocated dead trees and living natural trees increased native bird species richness by multiples of 1.8, 3.2, and 3.8, respectively (**Figure 5**, blue, green and yellow contours).

We found that the positions of the structural types in our assessment space align with the species response multipliers derived from bird observations. Furthermore, Hannan et al. (2019) observed that 38% of all bird species only visit natural trees. The diagonal line (**Figure 5**, black) shows that we can express this gap in bird response between trees (red) and artificial structures (grey) in our assessment space.

These validation processes show that the assessment space defined by our complexity and perch indexes expresses aspects of birds' response to structures even if other important features are not quantified. This space also suggests that, even when old trees are excluded, it is possible to design artificial habitat structures to better match birds' preferences. Finally, this assessment space shows that there is still a significant gap between best-in-class artificial habitat structures and the performance of natural trees.

The outcome of this step is a set of validated metrics for assessing spatial complexity and features of forms generated by the AI agent.

RESULTS: DEMONSTRATION OF AUTONOMOUS VISUAL ABSTRACTION AND VERIFICATION

Our results show that an AI agent can synthesise visual abstractions of complex natural shapes. In particular, they show that: (1) the agent can use the incoming data in 3D to learn design strategies; and (2) the resulting abstractions are verifiable and meaningful.

We first illustrate how the AI agent can synthesise artificial forms by learning design strategies that simplify the structures of natural trees.

The Effectiveness of the Training Procedure

We tested the ability of the agent to synthesise visual abstractions of tree forms through two applications: (1) synthesis of forms with 10 actions; and (2) 20 actions.

We select 20 actions for two reasons. First, in the original SPIRAL implementation (Ganin et al., 2018), the agent could only be trained to perform sequences of 20 actions. Although in SPIRAL++ Mellor et al. (2019) were able to increase the number of actions to 1,000 – in which case the agents could reproduce very detailed features of the given image dataset – they also managed to generate recognisable visual abstractions of human faces with 20 actions. Second, in our 3D implementation, a number of actions higher than 20 would increase the computing time and cause out-of-memory issues. Therefore, we chose 20 actions as the upper bound. We also describe a second application where the agent can perform 10 actions. This version aims to assess the abstraction capabilities of our model further.

The two tasks involved extracting visual features from voxel representations of trees from Dataset 1: Natural Trees. We considered the representations in the dataset as a distribution of trees. In practice, such a limited number of 3D models is insufficient to represent the properties of tree populations.

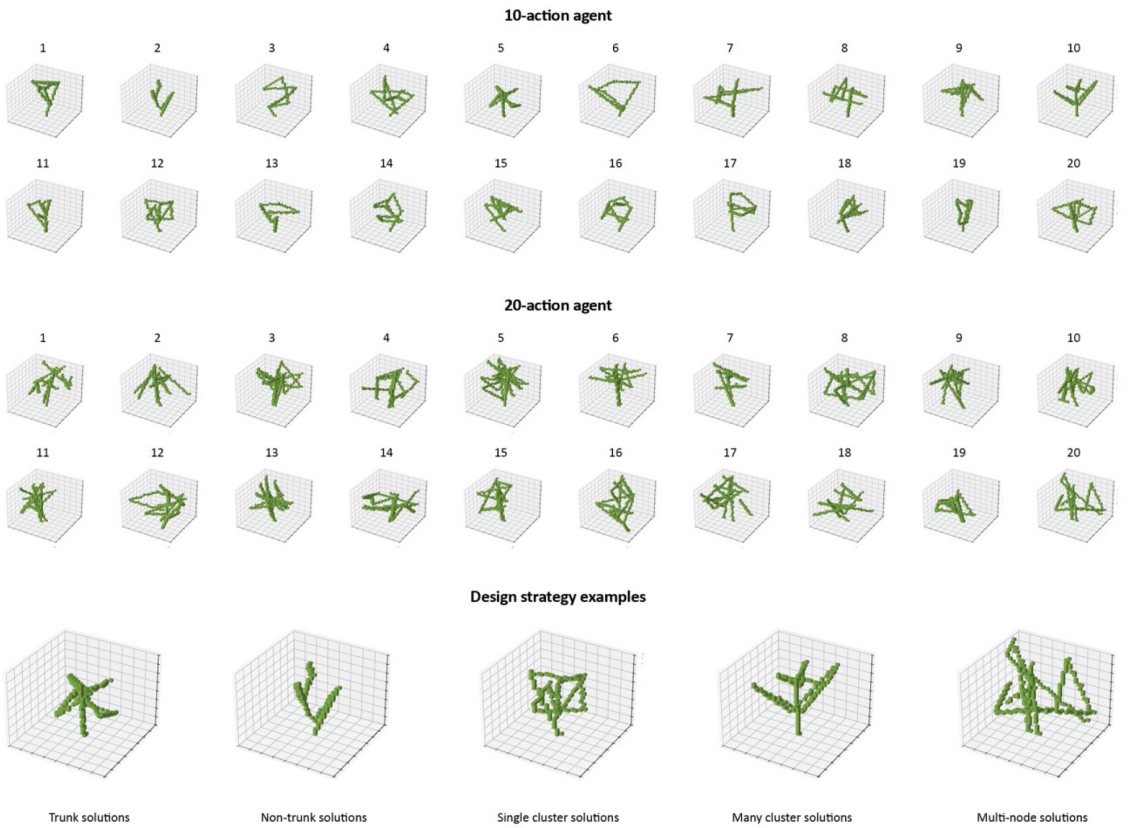

FIGURE 7 | Visual abstractions produced by the 10-actions agent and the 20-actions agent during the last training iterations.

Furthermore, a dataset that contains only three samples has high variance, which causes instability during the training process.

To alleviate these issues, we implemented a strategy based on data augmentation. We augmented the dataset using rigid transformations to ensure that the agent focused on the structural features of the trees. Similar to Maturana and Scherer (2015), we rotated every 3D form about the z-axis located at the centre of the ground plane by consecutive intervals of 10°. We populated the resulting dataset with 35 extra samples per tree structure for a total of 108 voxel representations. This data augmentation strategy produced a distribution of samples characterised by an independent variable of rotation.

To simplify the learning task in both applications, we set the starting location of the cursor at the centre of the ground plane. This forced the agent to start modelling forms from a location aligned with the base of the dataset samples.

Figure 6 shows the results of the training process for the two applications. The graphs represent the trends of the reward collected by the agents over consecutive training iterations. We smoothed the curves using an exponential moving average with 0.8 as the smoothing factor.

We observed that the rewards fluctuated erratically throughout the process, as visible in the graph spikes. These fluctuations, which do not appear in the reward curves described by Mellor et al. (2019), are due to the increased difficulty of exploring a 3D environment. The agents must select the end point of a line among a grid of 16^3 locations and an extra value for the placement flag for every time step. This results in a $2 \times 16^{3 \times 10}$ number of permutations for the 10-action agent and $2 \times 16^{3 \times 20}$ for the 20-action agent.

To guarantee appropriate exploration of the action space, we increased the weight of the entropy loss term – which is a term included in the learning function to prevent early convergence – by a factor of 10. Furthermore, since every observation consists in an array of 32^3 numbers, the specification of an appropriate batch size was computationally impractical. We used batch sizes of 32 and 16 – instead of 64, as recommended by Ganin et al. (2018) – to train the 10-action agent and the 20-action agent, respectively. Appendix A: Training Procedure and Hyperparameters provides further details on the hyperparameters used to train the two agents.

Although these modifications were a major source of instability of the training processes, we found that each spike corresponded to a tentative local convergence. The agents could successfully find a design strategy to trick the discriminator several times, but due to the increased entropy cost, they had to resort to a random exploration of other actions to find a different design strategy. Because of the peculiarity of the training curves – which share similarities with conventional GAN training – we stopped the training processes once they reached a time limit,

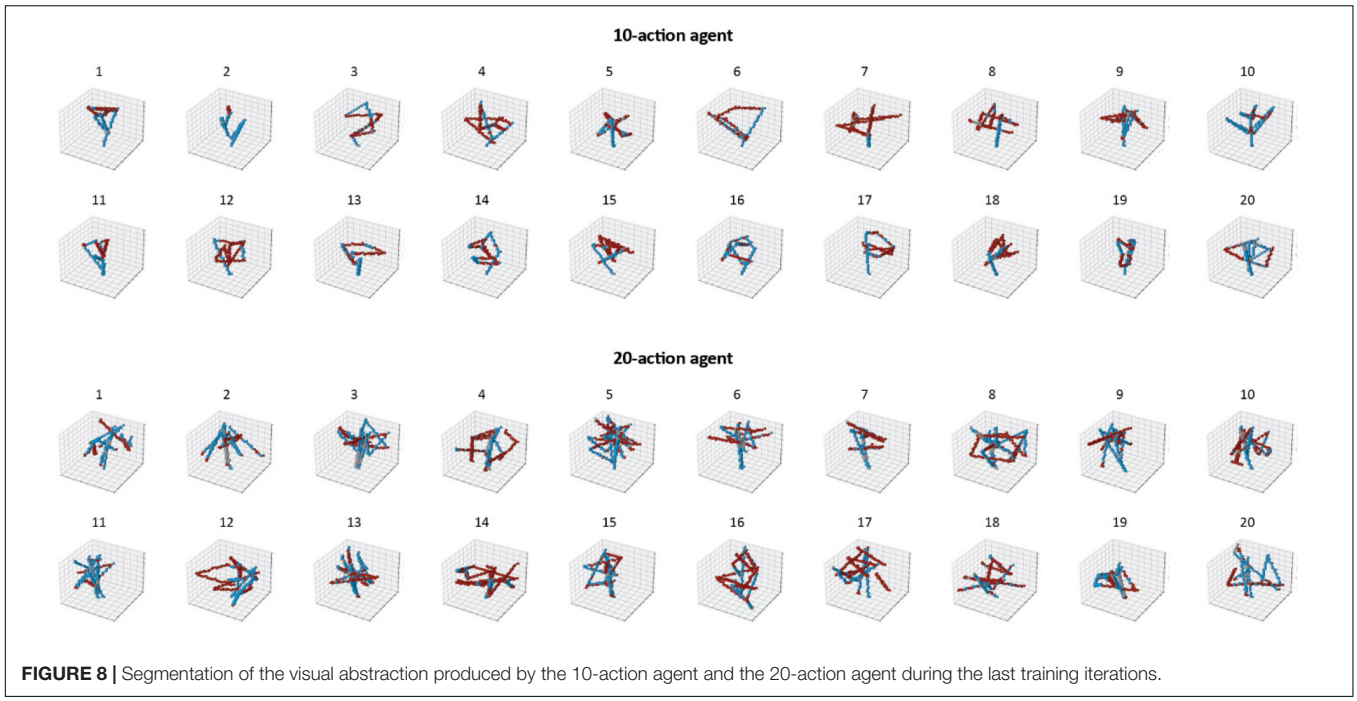

FIGURE 8 | Segmentation of the visual abstraction produced by the 10-action agent and the 20-action agent during the last training iterations.

rather than checking for convergence. In the following sections, we validate the success of the training process by analysing the forms produced by the agents.

Qualitative Analysis: Demonstrating That Abstraction Is Possible

We extracted 20 forms generated by the two agents during the last training iterations to assess the success of the training process qualitatively. Our results confirm that we can describe the AI-synthesised forms in terms of the characteristics of trees and human-simplified artificial structures.

Figure 7 shows the selected forms sorted per training iterations. Through inspection, we found that the agents learnt different design strategies. In the 10-action agent, these were:

- *Trunk solutions*: forms with clear canopy-trunk segmentation (e.g., samples 5, 9, 10, 11, 12, and 17).
- *Non-trunk solutions:* forms without a clear trunk (e.g., samples 2, 3, 14, 16, and 16).

Within each of these broader categories, we also identified:

- *Single cluster solutions:* forms with a single elevated aggregation of lines resembling an intact tree canopy (e.g., samples 12, 17, and 20 in the trunk category; and 6 in the no-trunk category).
- *Many cluster solutions*: forms characterised by multiple sub-clusters. Such distributions resemble vertically heterogenous trees with multiple sub-canopies (e.g., samples 9 and 10 in the trunk category, samples 2 and 3 in the no-trunk category).

Clearly defined canopy structures occurred most often in conditions where agents had a scarce supply of lines, as in the 10-action agent. This suggested that confining the number of lines forced agents to place lines that maximised the reward for each line, resulting in a design strategy that produced forms most closely resembling trees.

The 20-action agent had to search within a larger space of possibilities. This agent exploited the larger number of actions to place as many horizontal lines as possible to approximate the input tree branches. This resulted in more erratic forms. However, it also resulted in an additional strategy that we did not see in the 10-action agent. This category was:

- *Multi-node solutions:* synthesised forms attached to the ground plane with multiple points (e.g., samples 10, 13, and 20).

Our qualitative analysis confirmed that the AI agents were able to simplify tree structures in a way that created forms that had relevant features (understood as *many cluster solutions)*. They also produced forms that were different to trees and tree-like artificial habitat structures (understood as *multi-nodal solutions)*.

The next step is to verify that the AI-synthesised visual abstractions were meaningful. We ensured that by comparing their performance with natural trees and human-made structures. We discuss the performance of these AI-generated forms in our previously established evaluation space below.

Quantitative Analysis: Verification of Abstraction and Comparison to Other Structures

To confirm that AI-driven synthesis of visual abstractions is possible and verifiable, we performed a quantitative analysis that compared the synthesised forms with natural trees and human-made structures.

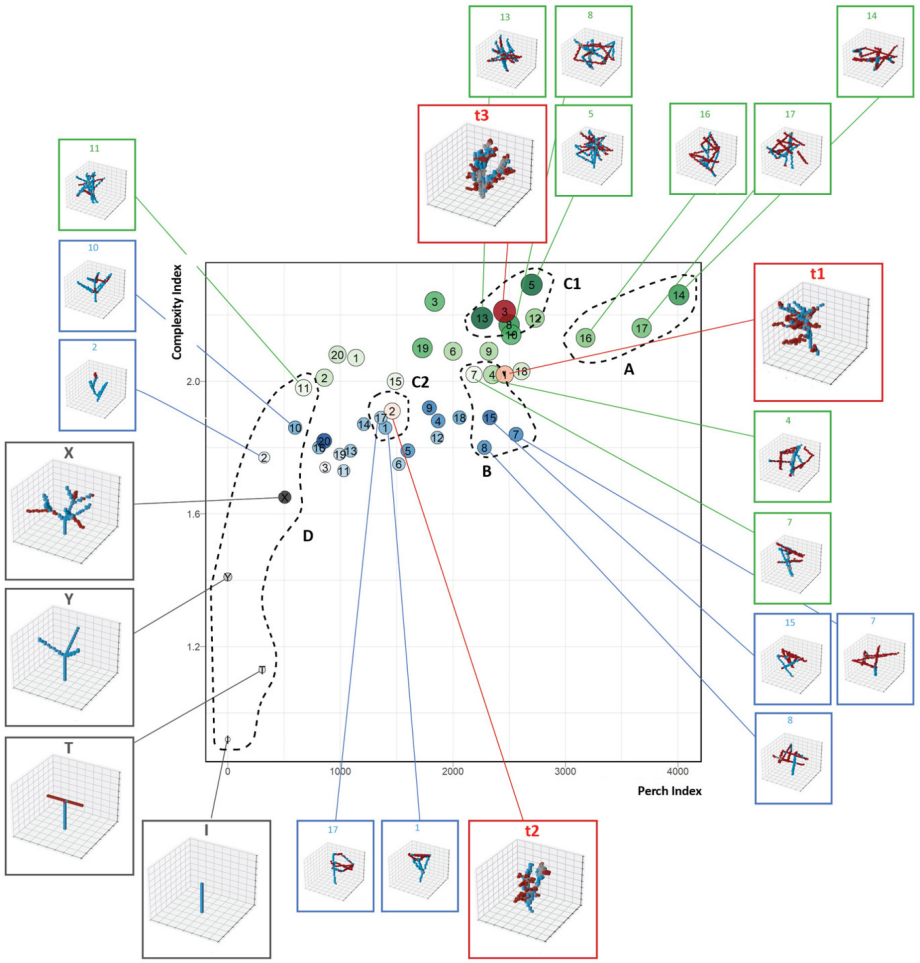

FIGURE 9 | Comparison between 3D representations of natural trees (red), human-defined simplified trees (grey), and forms synthesised by the 10-action agent (blue) and 20-action agent (green).

Using the comparison space described in section "Measurement and Comparison," we compared the AI-synthesised forms with the voxel representations of human-defined structures and natural trees. **Figure 8** visualises the outputs of the segmentation process that identifies exposed horizontal branches (red).

The 2D graph in **Figure 9** visualises the forms as bubbles in the comparison space. The x and y axes correspond to the perch and complexity indexes. We also considered a third metric – material cost – which we computed as the sum of the visible voxels. This cost maps to the scale and colour transparency of the bubbles. We colour coded the bubbles according to our four dataset types: voxel representations of human-defined habitat structures (black), voxel representations of natural trees (red), forms synthesised by the 20-actions agent (green) and forms synthesised by the 10-actions agent (blue).

We first examined the location of the representations of natural trees. The three samples showed a high complexity index and occurred at the centre of the perch index axis. High geometric complexity indicated a level of diversity of branch distributions that representations of human-defined artificial structures did not have. We assumed that natural physical constraints, such as the maximum number and length of horizontal elements that a tree can have, limited the maximum perch index of these samples.

Overall, we observed a correlation between the perch index and the size of the blobs, which represented the material cost. Generally, canopy structures represented by many voxels – and a greater material cost – also had a higher number of horizontal exposed voxels.

By observing the distributions of the four dataset types, we found a clear separation between representations of human-defined habitat structures and the AI-synthesised forms. Our samples of human-defined structures were distributed evenly along the complexity index axis and had a low perch index. In contrast, the AI-synthesised forms were distributed across the graph and concentrated around our voxel representation of natural trees. We found that the distribution of the AI-synthesised forms defined two main "bands" of complexity. These two bands partially overlapped along the perch index dimension and expanded from left to right. Occurring in the topmost

band were the forms synthesised by the 20-action agent, which achieved the highest complexity.

We analysed the graph more deeply by describing and comparing the samples from the different datasets grouped into five distinct clusters: A, B, C1, C2, and D. We acknowledge that these clusters are not derived statistically. Instead, we defined them by delimiting regions in the graph we deemed relevant to the design challenge.

Cluster A included the most performing forms synthesised by the 20-action agent as per our comparison space. These canopy structures were defined by patterns of lines that filled a large portion of the voxel grid and did not resemble trees. Form 14 returned the highest fractal dimension and perch index. However, unlike forms 16 and 17, this structure was short: it did not include enough vertical elements. Consequently, we considered form 14 a poor candidate for further design iterations.

Cluster B included AI-generated forms distributed at the centre of the graph. We highlighted these representations as they achieved a perch index comparable to natural forms while maintaining a moderate level of complexity and cost. The forms synthesised by the 10-action agent occupied the lowest part of the cluster and were all less complex than the simplest natural form (2, red). These forms had a distinct trunk and several horizontal lines that maximised space-filling while creating large voids. The cluster also included two forms synthesised by the 20-action agent, which shared similar features but had a higher fractal dimension.

Clusters C1 and C2 included AI-synthesised forms that were closer to the highest scoring natural form (3, red) and the lowest scoring one (2, red). By analysing these clusters, we found an alignment between the similarity metric considered by the agents and the metrics used for this evaluation. We used the 20-action agent to synthesise the forms in cluster C1. Forms 13 and 5 were tree-looking structures with multiple lines. Form 8 included a horizontal ring that increased the perch index. We used the 10-action agent to synthesise the forms in cluster C2. These forms consisted of simple looped and branched distributions.

Cluster D included representations of human-defined habitat structures and the AI-generated forms that had a low perch index. We chose this cluster so we could analyse features that characterised AI-synthesised forms that were closer to examples of current artificial habitat structures. Forms 2 and 10 were branched structures synthesised by the 10-action agent. These forms had a higher complexity index than the human-defined artificial habitat structures. This was due to the increased thickness of the branches containing multiple overlapping lines. These overlapping lines create a varied surface. In contrast, the representations of artificial structures were modelled to mimic simple poles. The more pronounced local diversity within individual branch shapes of the synthesised forms meant the AI solutions had a higher structural complexity than the human-defined artificial habitat structures, even if their overall appearance was similar. We note that, in reality, the translocated dead snag would also have a varied surface – and thus score higher on our complexity index – on its surface than Sample X, which is its voxelised representation.

In summary, our analysis demonstrates that – within the limits of the chosen voxel representation format – the AI agents produced forms that were more similar to the natural canopy structures than the examples of human-defined canopy structures used for the comparison. We assessed this similarity by combining a visual inspection and interpretation strategy with our comparison space. The analysis also showed that the agents produced a varied set of forms with differing levels of complexity and perch indexes. Many of the solutions contained diverse and relevant canopy shapes and branch distributions. We identified in the AI-synthesised forms a subset that balanced geometric complexity with material cost and perch index. This subset corresponds to Cluster B and includes the best candidates for future exploration.

DISCUSSION: PROPOSED ADVANCEMENTS AND THE FUTURE DEVELOPMENT OF THE ARTIFICIAL INTELLIGENCE TOOLKIT

Benefits for the Design of Artificial Habitat Structures

We see the results presented in this article as the first step toward AI-supported design of artificial habitat structures. In this approach, AI can support human designers from idea generation to decision-making. Our results improve on previous studies in three areas, as described in **Table 1**.

Extending "Synthesising Programs for Images Using Reinforced Adversarial Learning" to 3D on a Domain-Specific Challenge

Our first improvement relates to meaning extraction. Ecologists struggle to define large old trees because they represent ecosystem-specific phenomena that have many important ecosystem roles. We responded to this challenge by conceptualising large old trees as layers of characteristics from ecosystem dynamics to specific branch distributions. For further details, see section "Use-Case Selection".

This study focused on branch distributions within tree canopies. These characteristics present a non-trivial challenge for meaning extraction. Branching structures in trees form highly heterogenous patterns and tightly packed patterns. Many of their features are unknown (Ozanne et al., 2003; Lindenmayer and Laurance, 2016) and remain difficult to quantify (Parker and Brown, 2000).

To tackle this challenge, we extended previous applications of SPIRAL by making it operational in 3D. Our implementation demonstrates that the two AI agents can reduce the complexity of branch distributions and synthesise their visual abstractions. Although the agents had no information about features meaningful to tree-dwelling organisms or artificial habitat designs, they produced forms that retained ecologically meaningful features suggesting their usefulness for the design of artificial habitat structures. Our segmentation and comparison procedures showed that even in relatively simple modelling

TABLE 1 | Results overview, meaning, and potential.

Challenges	***State-of-the-art***	***Proposed advancements***
Capability. Develop tools to work with 3D complex natural structures and their surrogates	Current AI applications for the synthesis of visual abstractions, such as SPIRAL, work with two-dimensional data	*Meaning extraction*. Our AI agent works on three-dimensional data about tree canopies and branches. Future work can extend this to other characteristics such as hollows, peeling parks, clusters of trees, and other complex habitat structures
Accountability. Intervene in complex situations characterised by the conditions of uncertainty and incomplete knowledge	Current designs produce forms of low-fidelity, such as utility poles and pre-determined parametrisation of incompletely understood natural habitat structures	*Bias Identification.* Our process considers how trees work for birds. It resists biases of pre-existing parametrisations and designs. This approach allows us to assess the retention of relevant features in possible designs
Innovation. Produce practical designs that work for wildlife as well as for human procurement and production systems	Existing designs of habitat structures either do not look like trees and do not perform well, or look like trees, but are prohibitively difficult, slow, and expensive to produce	*Abstraction and reproduction.* Our designs can retain ecologically relevant features of trees while being more amenable for fabrication, installation, maintenance, and multi-purpose use

environments, these agents could synthesise features that are relevant to arboreal organisms.

We briefly describe one extraction process that focused on elevated perches. Reflecting the input dataset of trees, the two agents adopted a strategy of concentrating lines at higher Z coordinates. Using this approach, the agents synthesised structures with a limited number of vertical elements closer to the ground and more lines higher up, mimicking an elevated canopy. The availability of such structures is important to tree-dwelling organisms who need to perch above certain heights. This means that artificial perch structures close to the ground will not be suitable. The process demonstrates that autonomous visual abstraction is possible in 3D, and a particular use case with complex geometries that escape typical description methods.

The AI agents discussed in this article learn from 3D coordinates of tree branches to construct visual abstractions. Future implementations can aim to consume other spatial data representing other layers of information within our conceptualisation of trees. Data about these structures and their users can be integrated in our training datasets as voxel representations. We also expect that non-spatial information, such as statistical information about bird behaviour, can further guide the agent in extracting features that are functionally relevant to the wildlife inhabitants.

Explicitly Identifying Biases

We are not yet ready to claim that the agents can produce suitable habitat designs. Instead, the benefit from our approach emerges from a combination of (1) developing forms by automatically synthesising natural structures described above; and (2) providing a numeric comparison between natural, existing artificial, and synthesised forms. Through (1) and (2), we created an approach that explicitly defines the biases in current designing strategies.

Identifying biases is crucial for improved designs because structures such as enriched habitat poles and translocated dead trees are reductions or abstractions of complex natural structures. In many instances, humans perform this abstraction with a limited understanding of the biases they can bring to the process. Such biases include a tendency to:

- Create designs based on widely used existing artefacts, such as utility poles, given that the final structures often result from efforts by domain experts who are not designers by profession.
- Focus on simplified forms that could be built using common structural systems, such as regularly spaced slats, or on discrete habitat features that are easy to identify, such as perches.
- Ignore scales and relationships that are difficult to document, such as representing complex and differentiated branching.

Our synthesised forms resist conditioning by existing examples of artificial habitats. Our comparison space showed that there is a large gap between the complexity of existing designs for artificial habitat structures and the unexplored design space indicated by natural structures and possible synthetic forms. This gap shows the clear need for bio-informed construction, manufacturing and design technologies that can better engage with non-standard and highly differentiated shapes.

Meaning Abstraction and Reproduction

The ambition of our process is to consider how artificial habitat-structures appear and work for birds. For this task, the third benefit of our approach relates to meaning abstraction and reproduction.

In our use case, traditional artificial habitat designs do not show the perch diversity and distributions observed in trees and do not perform well (Le Roux et al., 2015a; Lindenmayer, 2017). Recognising these limitations, recent ecological work has investigated the use of translocated dead snags as artificial habitats (Hannan et al., 2019). It has also studied the deliberate damaging of young trees to make them resemble old trees with their hollowing trunks and branches (Rueegger, 2017). There have been some notable improvements in performance through the use of these strategies (Hannan et al., 2019). However, the resulting structures closely resemble trees. This means they suffer from many of the same drawbacks as trees: they are heavy, require significant preparations, including footings and grading of terrain, and are difficult to implement at scale.

Our agents produced forms with perch distributions that are similar to trees. However, they also developed solutions that were distinct from the structures as typical trees with their central stems and radial branch distributions. We could discount a high degree of these non-tree forms, including those

with many vertically oriented lines or those with many lines close to the ground plane. Our agents also learnt more useful strategies. For example, the multi-nodal forms created by the 20-action agent was an instance of load being distributed over multiple points rather than being concentrated in one trunk. Such strategies are useful in many restoration projects that occur in environments where large footings are impossible or destructive. Even though our agents had no knowledge of structural systems, their incentive to minimally describe the training dataset created a useful alternative structural strategy: maximising space-filling by distributing elements throughout 3D space using strategies not available to most tree species. These strategies suggest possibilities for expanding design options using AI-generated visual abstraction and will need to be further tested in future research.

Limitations and Future Development of the Artificial Intelligence Agent

In this section, we discuss the limitations of this work in relation to three themes: ecological knowledge, design, and artificial intelligence.

Limitations given by the state of ecological knowledge include its incompleteness. This applies to all aspects, from the number of known and described species to species behaviour. Field observation can be resource-intensive at large sites or with many individuals, difficult in the case of cryptic species, and slow when it must follow breeding cycles that take years.

These constraints impact potential human-made designs because they misalign with project-based work, brief periods of project-related research and the reliance on human expertise. In response to these limitations, this project aimed to take steps toward design processes that can accrue knowledge over time and be of use in the conditions of incomplete understandings of ecological interactions.

In regard to artificial intelligence, we recognise that future work will have to address several issues to improve the quality of the forms synthesised by the AI agent and turn the procedure into a useable design strategy.

First, we observed that the model was difficult to train. We related this to the complexity of the task in 3D. This task became more difficult because of the need to resort to a low-resolution voxel representation. Alternative strategies for 3D data representation are possible, and we shall test them in future work.

Second, our training dataset included only three samples. Training AI models on such a limited number of samples is a well-known issue, as the dataset does not represent an actual distribution and is characterised by high variance. All this causes instability in the training process. We partially addressed the problem by artificially expanding the dataset using a data augmentation strategy (section "The Effectiveness of the Training Procedure"). However, we consider developing larger datasets to be a priority to improve the model's capabilities.

Third, following the original SPIRAL implementation, we defined the learning task as maximising the similarity between the synthesised forms and the dataset samples with a limited number of modelling actions. The agent did that by maximising a reward computed from the similarity score. In future work, we will augment this reward definition with other metrics, such as structural stability, to synthesise forms that satisfy additional performance requirements.

Fourth, the SPIRAL agent learned to perform sequences of actions: at each step, the agent observed a partially designed form, got a partial reward, and decided what to design next. This feature opens several possibilities in terms of human-machine interaction that we did not explore in this article. For instance, the designer can provide SPIRAL with any partially defined form and ask the agent to complete the design based on its acquired experience. We plan to integrate this feature in a Graphical User Interface (GUI) to explore the implications of a human-AI partnership in the design of artificial habitat structures.

Last, we limited the action space to the placement of lines in the canvas, making the agent produce forms with limited variations. We will include other modelling actions to increase the expressive capabilities of the agent and synthesise more diverse, and potentially more performative forms for artificial habitat structures.

As we already mentioned in section "Extending Synthesising Programs for Images Using Reinforced Adversarial Learning to 3D on a Domain-Specific Challenge," this work serves as a basis for future scaling for trees. It also has the potential to be extended toward other domains of complex natural structures, such as rock formations or coral reefs. We expect further experimentation in this domain to continue in parallel with increasing computing power. Future input datasets can be rich, with multiple layers of information. It is already possible to create high resolution, feature-rich classifications for training in many instances. To give one example, **Figure 10** illustrates an extended version of our tree sample data. This dataset has multiple layers of information, including branch centroids (bubbles), key habitat structures (colours), predictions of faunal use (colour intensity) and species richness (size of bubble). We have included this figure in the manuscript to show that such datasets already exist and represent key targets for our future research on AI.

Our AI-synthesised forms are not better than human-made artificial habitat structures or natural trees. Our approach instead complements other innovations in artificial habitat design. Wildlife response to novel artificial habitat structures such as translocated dead trees is encouraging. However, stakeholders for this infrastructure, including birds, bats, insects, and other life forms, have preferences only partially known to human ecologists, conservation managers, and designers.

More generally, the work on artificial intelligence and ecocentric design can contribute to ecological research by supplying requirements for data acquisition, novel analytical techniques for numerical analysis, and generative procedures for field testing. Future implementations of AI agents can work with additional meaningful constraints and targets, including constructability, thermal performance, materiality, modularity, and species-related requirements. These AI agents can suggest unexpected solutions that will be combinable with other design approaches such as expert-driven development or performance-oriented modelling.

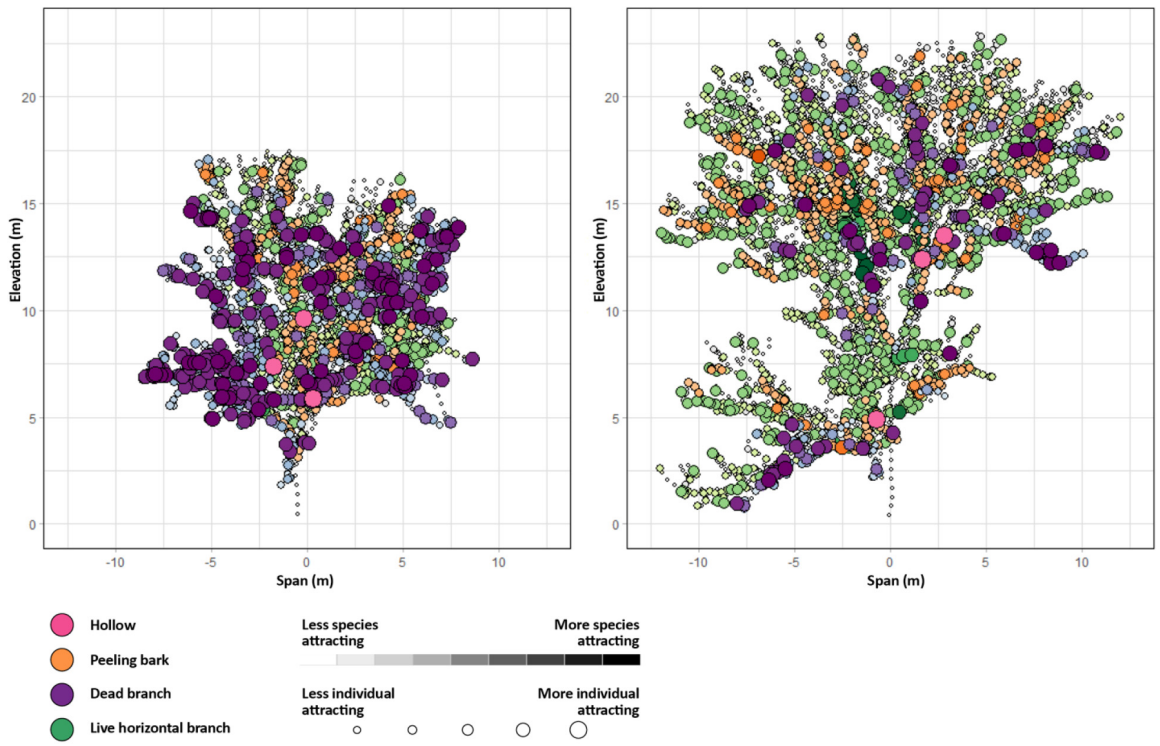

FIGURE 10 | Two large old trees from the full version of our dataset.

CONCLUSION: TOWARD ARTIFICIAL INTELLIGENCE-ASSISTED DESIGN

In this study, we demonstrate that an artificial intelligence agent can synthesise simplified surrogates of natural forms through a process of abstraction. We show that the forms generated by the agent can be ecologically meaningful and thus contribute to the design of artificial habitat structures. Human-driven degradation of natural habitats makes such work necessary and urgent. The process of habitat simplification accelerates extinctions and loss of health because less diverse habitats can support fewer forms of life. It is difficult to create suitable artificial habitat designs because the reproduction of key features of natural habitat structures is complex and resource-intensive. In response, our study extends existing work in ecological restoration and AI. We interpret the design of artificial habitat structures as a bio-informed process that relates to the cognitive mechanism of abstraction. Our innovative AI agent can synthesise visual abstraction of 3D forms by recombining features extracted from datasets of natural forms, such as trees. The assessment routines that compared geometries of natural trees, artificial habitat structures and synthesised objects confirmed that the outcomes of the process preserve meaningful features.

Our design strategy offers novel methods for reconstructing trees and other complex natural structures as they are seen by nonhuman habitat users, such as birds and other wildlife. The forms produced by our agent can be beneficial because they avoid biases common to existing strategies for artificial habitat design. Strategies developed by our AI agent can produce structures that resemble trees but can also deviate from natural structural forms, while preserving some of their meaning. This research creates an opportunity for future work that can include objectives to satisfy additional criteria in habitat provision, such as material use and constructability, to apply our approach to other sites and species and implement the outcomes at large scales and numbers. This work will depend on further development and – in particular – on the construction and field-testing of physical prototypes. To conclude, this work offers innovative applications in ecology, design and computer science, demonstrating the potential for AI-assisted design that seeks to benefit all forms of life and life-hosting environments.

DATA AVAILABILITY STATEMENT

The raw data supporting the conclusions of this article will be made available by the authors, without undue reservation.

AUTHOR CONTRIBUTIONS

GM developed, trained, tested the AI model, and implemented the verification workflow. AH generated datasets of trees and implemented the procedure for assessing the results. JW provided

technical support to the AI development and contributed to the literature review. GM and AH contributed to the literature review, research design, and drafting and editing the manuscript. SR and AP directed the conception and design of the project and contributed to the writing and editing. All authors worked on the conclusions and approved the final version of the manuscript.

FUNDING

The project was supported by research funding from the Australian Research Council Discovery Project DP170104010 and the funding from the Australian Capital Territory Parks and Conservation Service.

ACKNOWLEDGMENTS

We respectfully acknowledge the Wurundjeri and Ngunnawal peoples who are the traditional custodians of the lands on which this research took place. We thank Philip Gibbons and Darren Le Roux for their contributions to the ecological aspects of this project.

SUPPLEMENTARY MATERIAL

The Supplementary Material for this article can be found online at: https://www.frontiersin.org/articles/10.3389/fevo.2022.806453/full#supplementary-material

REFERENCES

Arnheim, R. (2010). *Toward a Psychology of Art: Collected Essays*. Berkeley: University of California Press.

Atkins, J. W., Bohrer, G., Fahey, R. T., Hardiman, B. S., Morin, T. H., Stovall, A. E. L., et al. (2018). Quantifying Vegetation and Canopy Structural Complexity from Terrestrial Lidar Data Using the Forestr R Package. *Methods Ecol. Evolut.* 9, 2057–2066. doi: 10.1111/2041-210x.13061

Baine, M. (2001). Artificial Reefs: A Review of Their Design, Application, Management and Performance. *Ocean Coastal Manag.* 44, 241–259. doi: 10.1016/s0964-5691(01)00048-5

Banks, J. C. G. (1997). "Tree Ages and Ageing in Yellow Box," in *The Coming of Age. Forest Age and Heritage Values*, ed. J. Dargavel (Canberra: Environment Australia), 17–28.

Barth, B. J., FitzGibbon, S. I., and Wilson, R. S. (2015). New Urban Developments That Retain More Remnant Trees Have Greater Bird Diversity. *Landsc. Urban Plan.* 136, 122–129. doi: 10.1016/j.landurbplan.2014.11.003

Beiler, K. J., Durall, D. M., Simard, S. W., Maxwell, S. A., and Kretzer, A. M. (2010). Architecture of the Wood-Wide Web: Rhizopogon Spp. Genets Link Multiple Douglas-Fir Cohorts. *New Phytol.* 185, 543–553. doi: 10.1111/j.1469-8137.2009.03069.x

Belton, D., Moncrieff, S., and Chapman, J. (2013). Processing Tree Point Clouds Using Gaussian Mixture Models. *ISPRS Anna. Photogr.* 2, 43–48.

Brock, A., Donahue, J., and Simonyan, K. (2019). *Large Scale GAN Training for High Fidelity Natural Image Synthesis*. arXiv:1809.11096 [cs, stat] [preprint].

Brock, A., Lim, T., Ritchie, J. M., and Weston, N. (2016). *Generative and Discriminative Voxel Modeling with Convolutional Neural Networks*. arXiv:1608.04236 [cs, stat] [preprint].

Bütler, R., Lachat, T., Larrieu, L., and Paillet, Y. (2013). "Habitat Trees: Key Elements for Forest Biodiversity," in *Integrative Approaches as an Opportunity for the Conservation of Forest Biodiversity*, eds D. Kraus and F. Krumm (Erfurt: European Forest Institute), 84–91.

Calders, K., Newnham, G., Burt, A., Murphy, S., Raumonen, P., Herold, M., et al. (2015). Nondestructive Estimates of Above-Ground Biomass Using Terrestrial Laser Scanning. *Methods Ecol. Evolut.* 6, 198–208. doi: 10.1111/2041-210x.12301

Chen, K., Choy, C. B., Savva, M., Chang, A. X., Funkhouser, T., and Savarese, S. (2018). "Text2Shape: Generating Shapes from Natural Language by Learning Joint Embeddings," in *Lecture Notes in Computer Science*, (Perth: Springer Verlag), 100–116. doi: 10.1007/978-3-030-20893-6_7

Delanoy, J., Aubry, M., Isola, P., Efros, A. A., and Bousseau, A. (2018). 3D Sketching using Multi-View Deep Volumetric Prediction. *Proc. ACM Comput. Graph. Interact. Tech.* 1, 1–22. doi: 10.1145/3203197

Díaz, S., Demissew, S., Carabias, J., Joly, C., Lonsdale, M., Ash, N., et al. (2015). The IPBES Conceptual Framework: Connecting Nature and People. *Curr. Opin. Environ. Sustainabil.* 14, 1–16. doi: 10.1016/j.scitotenv.2020.144492

Ehbrecht, M., Schall, P., Ammer, C., and Seidel, D. (2017). Quantifying Stand Structural Complexity and Its Relationship with Forest Management, Tree Species Diversity and Microclimate. *Agricult. Forest Meteorol.* 242, 1–9.

Fan, H., Su, H., and Guibas, L. (2017). "A Point Set Generation Network for 3D Object Reconstruction from a Single Image," in *2017 IEEE Conference on Computer Vision and Pattern Recognition (CVPR)*, (Honolulu: IEEE), 2463–2471.

Feng, Y., Feng, Y., You, H., Zhao, X., and Gao, Y. (2019). "MeshNet: Mesh Neural Network for 3D Shape Representation," in *Proceedings of the 33rd AAAI Conference on Artificial Intelligence*, (Honolulu: AAAI Press), 8279–8286. doi: 10.1609/aaai.v33i01.33018279

Fischer, J., and Lindenmayer, D. B. (2002). The Conservation Value of Paddock Trees for Birds in a Variegated Landscape in Southern New South Wales. 2. Paddock Trees as Stepping Stones. *Biodiv. Conserv.* 11, 833–849.

Fischer, J., Stott, J., Zerger, A., Warren, G., Sherren, K., and Forrester, R. I. (2009). Reversing a Tree Regeneration Crisis in an Endangered Ecoregion. *PNAS* 106, 10386–10391. doi: 10.1073/pnas.0900110106

Frey, J., Asbeck, T., and Bauhus, J. (2020). Predicting Tree-Related Microhabitats by Multisensor Close-Range Remote Sensing Structural Parameters for the Selection of Retention Elements. *Remote Sens.* 12:867. doi: 10.3390/rs12050867

Gadelha, M., Maji, S., and Wang, R. (2017). "Shape Generation using Spatially Partitioned Point Clouds," in *Proceedings of the British Machine Vision Conference 2017, BMVC 2017*, (London: BMVA Press), 1–12. doi: 10.3390/s20247117

Ganin, Y., Kulkarni, T., Babuschkin, I., Eslami, S. M. A., and Vinyals, O. (2018). *Synthesizing Programs for Images using Reinforced Adversarial Learning*. arXiv:1804.01118 [preprint].

Godin, C., Sinoquet, H., and Costes, E. (2005). "Plant Architecture Modelling: Virtual Plants and Complex Systems," in *Plant Architecture and Its Manipulation*, ed. C. Turnbull (Oxford: Blackwell), 238–287.

Goodfellow, I. J., Pouget-Abadie, J., Mirza, M., Xu, B., Warde-Farley, D., Ozair, S., et al. (2014). "Generative Adversarial Nets," in *Proceedings of the 27th International Conference on Neural Information Processing Systems - Volume 2 NIPS'14*, (Cambridge: MIT Press), 2672–2680.

Gorzelak, M. A., Asay, A. K., Pickles, B. J., and Simard, S. W. (2015). Inter-Plant Communication Through Mycorrhizal Networks Mediates Complex Adaptive Behaviour in Plant Communities. *AoB Plants* 7:lv050. doi: 10.1093/aobpla/plv050

Hackenberg, J., Spiecker, H., Calders, K., Disney, M., and Raumonen, P. (2015). SimpleTree: An Efficient Open Source Tool to Build Tree Models from TLS Clouds. *Forests* 6, 4245–4294.

Hannan, L., Le Roux, D. S., Milner, R. N. C., and Gibbons, P. (2019). Erecting Dead Trees and Utility Poles to Offset the Loss of Mature Trees. *Biol. Conserv.* 236, 340–346. doi: 10.1016/j.biocon.2019.06.001

Hanocka, R., Hertz, A., Fish, N., Giryes, R., Fleishman, S., and Cohen-Or, D. (2019). MeshCNN: A Network with an Edge. *ACM Trans. Graph.* 38, 1–12. doi: 10.1145/3306346.3322959

Ibarra, J. T., Cockle, K., Altamirano, T., van der Hoek, Y., Simard, S., Bonacic, C., et al. (2020). Nurturing Resilient Forest Biodiversity: Nest Webs as Complex Adaptive Systems. *Ecol. Soc.* 25:27. doi: 10.1201/b17131-7

Isola, P., Zhu, J.-Y., Zhou, T., and Efros, A. A. (2017). "Image-to-Image Translation with Conditional Adversarial Networks," in *2017 IEEE Conference on Computer Vision and Pattern Recognition (CVPR)*, (Honolulu: IEEE), 5967–5976.

Karras, T., Laine, S., and Aila, T. (2019). *A Style-Based Generator Architecture for Generative Adversarial Networks*. arXiv:1812.04948 [cs, stat] [Preprint].

Kim, J., Chung, H., Lee, J., Cho, M., and Park, J. (2020). *Combinatorial 3D Shape Generation via Sequential Assembly*. arXiv:2004.07414 [cs, stat] [preprint]

Kingma, D. P., and Welling, M. (2014). "Auto-Encoding Variational Bayes," in *ICLR 2014 - Conference Track Proceedings (Banff)*, (Vienna: ICLR). doi: 10.1093/bioinformatics/btaa169

Krizhevsky, A., Sutskever, I., and Hinton, G. E. (2012). "ImageNet Classification with Deep Convolutional Neural Networks," in *Advances in Neural Information Processing Systems 25*, eds F. Pereira, C. J. C. Burges, L. Bottou, and K. Q. Weinberger (New York, NY: Curran Associates Inc), 1097–1105.

Lafayette, L., Sauter, G., Vu, L., and Meade, B. (2016). *Spartan performance and flexibility: An hpc-cloud chimera*. Barcelona: OpenStack Summit.

Le Roux, D. S., Ikin, K., Lindenmayer, D. B., Bistricer, G., Manning, A. D., and Gibbons, P. (2015a). Enriching Small Trees with Artificial Nest Boxes Cannot Mimic the Value of Large Trees for Hollow-Nesting Birds. *Restorat. Ecol.* 24, 252–258. doi: 10.1111/rec.12303

Le Roux, D. S., Ikin, K., Lindenmayer, D. B., Manning, A. D., and Gibbons, P. (2015b). Single Large or Several Small? Applying Biogeographic Principles to Tree-Level Conservation and Biodiversity Offsets. *Biol. Conserv.* 191, 558–566. doi: 10.1016/j.biocon.2015.08.011

Le Roux, D. S., Ikin, K., Lindenmayer, D. B., Manning, A. D., and Gibbons, P. (2014). The Future of Large Old Trees in Urban Landscapes. *PLoS One* 9:e99403. doi: 10.1371/journal.pone.0099403

Le Roux, D. S., Ikin, K., Lindenmayer, D. B., Manning, A. D., and Gibbons, P. (2018). The Value of Scattered Trees for Wildlife: Contrasting Effects of Landscape Context and Tree Size. *Div. Distribut.* 24, 69–81. doi: 10.1111/ddi.12658

Ledig, C., Theis, L., Huszar, F., Caballero, J., Cunningham, A., Acosta, A., et al. (2017). *Photo-Realistic Single Image Super-Resolution Using a Generative Adversarial Network*. arXiv:1609.04802 [cs, stat] [preprint]

Lewandowski, P., Przepióra, F., and Ciach, M. (2021). Single Dead Trees Matter: Small-Scale Canopy Gaps Increase the Species Richness, Diversity and Abundance of Birds Breeding in a Temperate Deciduous Forest. *Forest Ecol. Manag.* 481:118693. doi: 10.1016/j.foreco.2020.118693

Lindenmayer, D. B. (2017). Conserving Large Old Trees as Small Natural Features. *Biol. Conserv.* 211, 51–59. doi: 10.1016/j.biocon.2016.11.012

Lindenmayer, D. B., and Laurance, W. F. (2016). The Ecology, Distribution, Conservation and Management of Large Old Trees. *Biol. Rev.* 92, 1434–1458. doi: 10.1111/brv.12290

Lindenmayer, D. B., Laurance, W. F., and Franklin, J. F. (2012). Global Decline in Large Old Trees. *Science* 338, 1305–1306. doi: 10.1126/science.1231070

Litany, O., Bronstein, A., Bronstein, M., and Makadia, A. (2018). "Deformable Shape Completion with Graph Convolutional Autoencoders," in *Proceedings of the IEEE Computer Society Conference on Computer Vision and Pattern Recognition*, (Salt Lake City: IEEE), 1886–1895.

Liu, F., Li, S., Zhang, L., Zhou, C., Ye, R., Wang, Y., et al. (2017). "3DCNN-DQN-RNN: A Deep Reinforcement Learning Framework for Semantic Parsing of Large-scale 3D Point Clouds," in *Proceedings of the IEEE International Conference on Computer Vision*, (Venice: IEEE), 5679–5688.

Malhi, Y., Jackson, T., Bentley, L. P., Lau, A., Shenkin, A., Herold, M., et al. (2018). New Perspectives on the Ecology of Tree Structure and Tree Communities Through Terrestrial Laser Scanning. *Interf. Focus* 8:20170052. doi: 10.1098/rsfs.2017.0052

Mänd, R., Leivits, A., Leivits, M., and Rodenhouse, N. (2009). Provision of Nestboxes Raises the Breeding Density of Great Tits Parus major Equally in Coniferous and Deciduous Woodland. *IBIS* 151, 487–492.

Manning, A. D., Fischer, J., and Lindenmayer, D. B. (2006). Scattered Trees Are Keystone Structures - Implications for Conservation. *Biol. Conserv.* 132, 311–321. doi: 10.1016/j.biocon.2006.04.023

Manning, A. D., Gibbons, P., Fischer, J., Oliver, D., and Lindenmayer, D. B. (2012). Hollow Futures? Tree Decline, Lag Effects and Hollow-Dependent Species. *Anim. Conserv.* 16, 395–405. doi: 10.1111/acv.12006

Manning, A. D., Gibbons, P., and Lindenmayer, D. B. (2009). Scattered Trees: A Complementary Strategy for Facilitating Adaptive Responses to Climate Change in Modified Landscapes? *J. Appl. Ecol.* 46, 915–919. doi: 10.1111/j.1365-2664.2009.01657.x

Maturana, D., and Scherer, S. (2015). "VoxNet: A 3D Convolutional Neural Network for real-time object recognition," in *2015 IEEE/RSJ International Conference on Intelligent Robots and Systems (IROS)*, (Hamburg: IEEE), 922–928.

McElhinny, C., Gibbons, P., Brack, C., and Bauhus, J. (2005). Forest and Woodland Stand Structural Complexity: Its Definition and Measurement. *Forest Ecol. Manag.* 218, 1–24.

Mellor, J. F. J., Park, E., Ganin, Y., Babuschkin, I., Kulkarni, T., Rosenbaum, D., et al. (2019). *Unsupervised Doodling and Painting with Improved SPIRAL*. arXiv:1910.01007 [preprint].

Mirra, G., and Pugnale, A. (2021). Comparison Between Human-Defined and AI-Generated Design Spaces for the Optimisation of Shell Structures. *Structures* 34, 2950–2961.

Mitsch, W. J. (2014). When Will Ecologists Learn Engineering and Engineers Learn Ecology? *Ecol. Engin.* 65, 9–14.

Nash, C., and Williams, C. K. I. (2017). The Shape Variational Autoencoder: A Deep Generative Model of Part-Segmented 3d Objects. *Comput. Graphics Forum* 36, 1–12. doi: 10.1111/cgf.13240

Ozanne, C. M. P., Anhuf, D., Boulter, S. L., Keller, M., Kitching, R. L., Körner, C., et al. (2003). Biodiversity Meets the Atmosphere: A Global View of Forest Canopies. *Science* 301, 183–186. doi: 10.1126/science.1084507

Parker, G. G., and Brown, M. J. (2000). Forest Canopy Stratification: Is It Useful? *Am. Natural.* 155, 473–484. doi: 10.1086/303340

Qi, C. R., Su, H., Mo, K., and Guibas, L. J. (2017). "PointNet: Deep Learning on Point Sets for 3D Classification and Segmentation," in *Proceedings of the 30th IEEE Conference on Computer Vision and Pattern Recognition, CVPR 2017*, (Honolulu: IEEE), 77–85.

Reimers, C., and Requena-Mesa, C. (2020). "Deep Learning – an Opportunity and a Challenge for Geo- and Astrophysics," in *Knowledge Discovery in Big Data from Astronomy and Earth Observation*, eds P. Škoda and F. Adam (Netherland: Elsevier), 251–265.

Roudavski, S. (2021). "Interspecies Design," in *Cambridge Companion to Literature and the Anthropocene*, ed. J. Parham (Cambridge: Cambridge University Press), 147–162.

Rueegger, N. N. (2017). Artificial Tree Hollow Creation for Cavity-Using Wildlife – Trialling an Alternative Method to That of Nest Boxes. *Forest Ecol. Manag.* 405, 404–412.

Seidel, D. (2018). A Holistic Approach to Determine Tree Structural Complexity Based on Laser Scanning Data and Fractal Analysis. *Ecol. Evol.* 8, 128–134. doi: 10.1002/ece3.3661

Sharma, G., Goyal, R., Liu, D., Kalogerakis, E., and Maji, S. (2018). "CSGNet: Neural Shape Parser for Constructive Solid Geometry," in *Proceedings of the IEEE Computer Society Conference on Computer Vision and Pattern Recognition*, (Salt Lake City: IEEE), 5515–5523. doi: 10.1109/TPAMI.2020.3044749

Sillett, S. C., Van Pelt, R., Kramer, R. D., Carroll, A. L., and Koch, G. W. (2015). Biomass and Growth Potential of Eucalyptus Regnans up to 100m Tall. *Forest Ecol. Manag.* 348, 78–91. doi: 10.1016/j.foreco.2015.03.046

Soffer, S., Ben-Cohen, A., Shimon, O., Amitai, M. M., Greenspan, H., and Klang, E. (2019). Convolutional Neural Networks for Radiologic Images: A Radiologist's Guide. *Radiology* 290, 590–606. doi: 10.1148/radiol.2018180547

Stagoll, K., Lindenmayer, D. B., Knight, E., Fischer, J., and Manning, A. D. (2012). Large Trees are Keystone Structures in Urban Parks. *Conserv. Lett.* 5, 115–122.

Tan, Q., Gao, L., Lai, Y.-K., and Xia, S. (2018). "Variational Autoencoders for Deforming 3D Mesh Models," in *Proceedings of the IEEE Computer Society Conference on Computer Vision and Pattern Recognition*, (Salt Lake City: IEEE), 5841–5850.

Torres-Pulliza, D., Dornelas, M. A., Pizarro, O., Bewley, M., Blowes, S. A., Boutros, N., et al. (2020). A Geometric Basis for Surface Habitat Complexity and Biodiversity. *Nat. Ecol. Evol.* 4, 1495–1501. doi: 10.1038/s41559-020-1281-8

Viola, I., Chen, M., and Isenberg, T. (2020). "Visual Abstraction," in *Foundations of Data Visualization*, eds M. Chen, H. Hauser, P. Rheingans, and G. Scheuermann (Cham: Springer), 15–37.

Wang, Y., Sun, Y., Liu, Z., Sarma, S. E., Bronstein, M. M., and Solomon, J. M. (2019). Dynamic Graph CNN for Learning on Point Clouds. *J. Image Graph.* 26, 2691–2702.

Willis, K. D. D., Pu, Y., Luo, J., Chu, H., Du, T., Lambourne, J. G., et al. (2021). Fusion 360 Gallery: A Dataset and Environment for Programmatic CAD Construction from Human Design Sequences. *ACM Transact. Graph.* 40, 1–24.

Wu, J., Zhang, C., Xue, T., Freeman, W. T., and Tenenbaum, J. B. (2016). "Learning a Probabilistic Latent Space of Object Shapes via 3D Generative-Adversarial Modeling," in *Papers presented at NIPS, the flagship meeting on neural computation, held in December 2004 in Vancouver*, (Barcelona: Neural Information Processing Systems Foundation), 82–90.

Wu, Z., Song, S., Khosla, A., Yu, F., Zhang, L., Tang, X., et al. (2015). "3D ShapeNets: A Deep Representation for Volumetric Shapes," in *Proceedings of the IEEE Computer Society Conference on Computer Vision and Pattern Recognition*, (Boston: IEEE), 1912–1920.

Yan, X., Yang, J., Yumer, E., Guo, Y., and Lee, H. (2016). "Perspective Transformer Nets: Learning Single-View 3D Object Reconstruction without 3D Supervision," in *NIPS'16: Proceedings of the 30th International Conference on Neural Information Processing Systems*, (Boston: IEEE), 1704–1712.

Zielewska-Büttner, K., Heurich, M., Müller, J., and Braunisch, V. (2018). Remotely Sensed Single Tree Data Enable the Determination of Habitat Thresholds for the Three-Toed Woodpecker (*Picoides tridactylus*). *Remote Sens.* 10:1972.

Zou, C., Yumer, E., Yang, J., Ceylan, D., and Hoiem, D. (2017). "3D-PRNN: Generating Shape Primitives with Recurrent Neural Networks," in *Proceedings of the IEEE International Conference on Computer Vision*, (Venice: IEEE), 900–909.

Conflict of Interest: The authors declare that the research was conducted in the absence of any commercial or financial relationships that could be construed as a potential conflict of interest.

frontiers | Frontiers in Ecology and Evolution

ORIGINAL RESEARCH
published: 29 April 2022
doi: 10.3389/fevo.2022.805385

Numerosity Categorization by Parity in an Insect and Simple Neural Network

Scarlett R. Howard[1,2], Julian Greentree[3], Aurore Avarguès-Weber[4], Jair E. Garcia[5], Andrew D. Greentree[6] and Adrian G. Dyer[5,7]*

[1] Centre for Integrative Ecology, School of Life and Environmental Sciences, Deakin University, Burwood, VIC, Australia, [2] School of Biological Sciences, Monash University, Clayton, VIC, Australia, [3] School of Science, Royal Melbourne Institute of Technology (RMIT) University, Melbourne, VIC, Australia, [4] Centre de Recherches sur la Cognition Animale (CRCA), Centre de Biologie Intégrative (CBI), Université de Toulouse, CNRS, UPS, Toulouse, France, [5] Bio-Inspired Digital Sensing Lab, School of Media and Communication, Royal Melbourne Institute of Technology (RMIT) University, Melbourne, VIC, Australia, [6] Australian Research Council (ARC) Centre of Excellence for Nanoscale BioPhotonics, School of Science, Royal Melbourne Institute of Technology (RMIT) University, Melbourne, VIC, Australia, [7] Department of Physiology, Monash University, Clayton, VIC, Australia

A frequent question as technology improves and becomes increasingly complex, is how we enable technological solutions and models inspired by biological systems. Creating technology based on humans is challenging and costly as human brains and cognition are complex. The honeybee has emerged as a valuable comparative model which exhibits some cognitive-like behaviors. The relative simplicity of the bee brain compared to large mammalian brains enables learning tasks, such as categorization, that can be mimicked by simple neural networks. Categorization of abstract concepts can be essential to how we understand complex information. Odd and even numerical processing is known as a parity task in human mathematical representations, but there appears to be a complete absence of research exploring parity processing in non-human animals. We show that free-flying honeybees can visually acquire the capacity to differentiate between odd and even quantities of 1–10 geometric elements and extrapolate this categorization to the novel numerosities of 11 and 12, revealing that such categorization is accessible to a comparatively simple system. We use this information to construct a neural network consisting of five neurons that can reliably categorize odd and even numerosities up to 40 elements. While the simple neural network is not directly based on the biology of the honeybee brain, it was created to determine if simple systems can replicate the parity categorization results we observed in honeybees. This study thus demonstrates that a task, previously only shown in humans, is accessible to a brain with a comparatively small numbers of neurons. We discuss the possible mechanisms or learning processes allowing bees to perform this categorization task, which range from numeric explanations, such as counting, to pairing elements and memorization of stimuli or patterns. The findings should encourage further testing of parity processing in a wider variety of animals to inform on its potential biological roots, evolutionary drivers, and potential technology innovations for concept processing.

Keywords: even, honeybee (*Apis mellifera*), neuromorphic, numerical cognition, simple artificial neural network, odd

OPEN ACCESS

Edited by:
Guy Gilles Beauchamp, Concordia University, Canada

Reviewed by:
Giorgio Vallortigara, University of Trento, Italy
Vera Vasas, Queen Mary University of London, United Kingdom
Eirik Søvik, Volda University College, Norway

****Correspondence:***
Scarlett R. Howard
scarlett.howard@monash.edu

Specialty section:
This article was submitted to Behavioral and Evolutionary Ecology, a section of the journal Frontiers in Ecology and Evolution

Received: *30 October 2021*
Accepted: *02 March 2022*
Published: *29 April 2022*

Citation:
Howard SR, Greentree J, Avarguès-Weber A, Garcia JE, Greentree AD and Dyer AG (2022) Numerosity Categorization by Parity in an Insect and Simple Neural Network. Front. Ecol. Evol. 10:805385. doi: 10.3389/fevo.2022.805385

INTRODUCTION

Categorization is the ability to group certain objects or elements together on the basis of similar perceptual or functional properties while the objects are still distinguishable from each other (Zentall et al., 2002; Zhang et al., 2004; Benard et al., 2006). Categorization enables an efficient mechanism to group objects or events by shared properties (Troje et al., 1999; Zentall et al., 2002). For example, non-human animals can categorize visual stimuli such as photographs of humans (Herrnstein and Loveland, 1964), animals (Freedman et al., 2001), or food (Bovet and Vauclair, 1998).

Parity (odd/even grouping) is typically considered a relatively abstract mathematical property (Krueger and Hallford, 1984; Krueger, 1986; Clark and Campbell, 1991; Dehaene et al., 1993) which can be described as a form of number categorization. The task of classifying a numerosity as odd or even is defined and presumably determined by numerical calculations, for example, being able to determine whether a number is a multiple of two or not (Clark and Campbell, 1991), although other potential mechanisms are described in the "Discussion" section. Parity has been considered by some authors as a more demanding task than magnitude comparison (Dehaene and Cohen, 1991; Dehaene et al., 1993) in terms of the complexity of numerical calculations needed to determine whether a number is even or odd (Clark and Campbell, 1991). Studies of parity tasks in humans have revealed differences in physical spatial relationships (e.g., handedness) (Berch et al., 1999; Reynvoet and Brysbaert, 1999; Nuerk et al., 2004), accuracy, and reaction times between odd and even numbers (Hines, 1990; Nuerk et al., 2005; Alards-Tomalin et al., 2016). For example, when Arabic numerals were presented to participants on a computer screen and participants were required to respond using keys with their left or right hand, even numbers were responded to faster with the right hand than with the left hand. Similarly, odd numbers were responded to more quickly with the left hand than the right (Reynvoet and Brysbaert, 1999). Even numbers are also categorized more quickly and accurately than odd numbers in humans (Hines, 1990; Nuerk et al., 2005; Alards-Tomalin et al., 2016). There are linguistic effects on parity categorization; children aged between about 8–15 years old typically associate the word "even" with "right" and the word "odd" with "left" (Berch et al., 1999). These findings suggest that odd and even processing tasks potentially have a biological grounding in how numbers are processed beyond cultural transmission. However, no study to our knowledge has previously assessed the ability of non-human animals to perform a parity task.

The honeybee is an appealing comparative model species for testing visual and cognitive tasks (Zhang, 2006; Srinivasan, 2010; Avarguès-Weber et al., 2011a,b; Dyer, 2012). Honeybees can be trained to complete tasks and learn concepts including size discrimination (Avarguès-Weber et al., 2014; Howard et al., 2017a,b), same/different rules (Giurfa et al., 2001), and maze navigation (Collett et al., 1993; Zhang et al., 1996, 2000). Bees can also categorize natural visual stimuli (Zhang et al., 2004), abstract stimuli (Benard et al., 2006), and even human face-like stimuli (Avarguès-Weber et al., 2010b). For example, while human face-like stimuli are seemingly biologically irrelevant to honeybees, individuals can group either face-like or non-face-like stimuli, thereby demonstrating a capacity to categorize complex abstract stimuli using configural type processing (Avarguès-Weber et al., 2010b).

Invertebrates, including honeybees, have demonstrated widespread non-symbolic numerical abilities (Bortot et al., 2021). Free-flying honeybees have demonstrated a limited numerical ability to count and discriminate quantities of one to four (Chittka and Geiger, 1995; Dacke and Srinivasan, 2008; Gross et al., 2009) with classical appetitive conditioning methods. This limit of four is known as a "subitizing" number processing limit that appears common across species from very different taxonomic backgrounds (Jevons, 1871; Kaufman et al., 1949; Miller, 1956; Simons and Langheinrich, 1982; Trick and Pylyshyn, 1994; Chittka and Geiger, 1995; Piazza et al., 2002; Tomonaga and Matsuzawa, 2002; Saaty and Ozdemir, 2003; Agrillo et al., 2008; Dacke and Srinivasan, 2008; Gross et al., 2009; Cowan, 2010; Gómez-Laplaza and Gerlai, 2011; Rugani et al., 2013; Seguin and Gerlai, 2017), although for some species it is higher or lower than four (Hassmann, 1952; Miller, 1956; Simons and Langheinrich, 1982; Davis and Pérusse, 1988; Saaty and Ozdemir, 2003; Nieder, 2005; Cowan, 2010; Carazo et al., 2012). The existence of a numerical processing limit at about four objects/elements, suggests the underlying neural mechanism may be evolutionarily conserved (Giurfa, 2019). Using appetitive-aversive conditioning procedures, where correct choices result in a reward while errors result in an aversive outcome and thus promote visual attention (Avarguès-Weber et al., 2010a), honeybees can acquire the capacity to discriminate between quantities above the subitizing limit of four (Howard et al., 2018a, 2019c). Honeybees have become an important comparative model for understanding numerical cognition and have demonstrated an ability to order zero numerosity at the lower end of the positive number line (Howard et al., 2018b,a), perform simple addition and subtraction (Howard et al., 2019a,b), match abstract characters to small quantities (Howard et al., 2019d), relate size and number concepts (Bortot et al., 2019b), and perform quantity discrimination (Howard et al., 2018a, 2019c, 2020a; Bortot et al., 2019a).

Due to the demonstration of efficient learning of cognitive-like problems in honeybees (Zhang and Srinivasan, 2004; Srinivasan, 2010; Avarguès-Weber and Giurfa, 2013), they are also becoming a popular insect model for bio-inspired technology. Insects, such as honeybees, demonstrate many goal-directed and plastic behaviors that are currently beyond the capacity of today's artificial systems (Helgadóttir et al., 2013). This ability makes them useful in a range of bio-inspired technologies and designs including computing, sensory processing in robots, and concept learning in machines (Helgadóttir et al., 2013; Sandin et al., 2014; Kleyko et al., 2015). The examination of honeybee flight strategies, cognition, and vision have been useful in developing artificial intelligence, flight control, aerial machine navigation, accurate distance estimation, successful landing procedures, and the regulation of flying height (Srinivasan et al., 1999; Srinivasan, 2006, 2011; Bukovac et al., 2013). Honeybee processing has also been used in the creation of computational models of biological systems, known as neuromorphic systems.

Neuromorphic systems are designed for processing real-world problems by being able to cope with uncertainty and use brain-like computations. Honeybees live in complex environments and can learn concepts to solve problems, thus they are considered an ideal model for neuromorphic systems (Helgadóttir et al., 2013; Sandin et al., 2014; Kleyko et al., 2015). More recently, some authors have shown that simple artificial neural networks consisting of a small number of neurons are able to perform some of the complex numerical tasks which honeybees have successfully learnt. For example, Vasas and Chittka (2019) were able to demonstrate that a neural network consisting of just four neurons could distinguish between numerosities up to six elements. Similarly, MaBouDi et al. (2021) created a simple neural network of nine neurons which could solve a numerosity task using spatial frequency as a cue. This recent work suggests that honeybees may be useful in designing more efficient neuromorphic computing systems which use less computational power than many current solutions. The advantage of bio-inspired neural models is that Darwinian evolution has likely enabled efficient solutions as biological brains need to be highly efficient with energy (Niven et al., 2007). For example, an integrated circuit based on the biological principle of spiking neurons is capable of operating on significantly lower energy requirements (Merolla et al., 2014), and neuromorphic computing solutions may avoid the complexity and cost of traditional computer architectures (Sandin et al., 2014).

Given the ability of honeybees to learn abstract numerical tasks, we decided to investigate whether bees may be able to learn to discriminate between odd vs. even numerosities. We employed appetitive-aversive conditioning as has previously been shown to promote visual attention and learning (Chittka et al., 2003; Avarguès-Weber et al., 2010a; Howard et al., 2019c). To elicit mechanistic solutions, it is possible to construct artificial neural networks that simulate how a low number of neurons can learn seemingly complex mathematical problems. Such work reveals that as few as four neurons are capable of processing quantities and also enable concept processing like empty sets (zero) being quantitatively less than positive integers (Vasas and Chittka, 2019).

Here we test and demonstrate the capacity of honeybees to learn to categorize odd and even numerosities of elements between one and ten, and extrapolate that acquired knowledge to categorize novel numbers in terms of parity. We then constructed a simple neural network to understand if a miniature artificial brain can have access to processing the concepts of odd and even. We discuss how such simple neural mechanisms can benefit neuromorphic computing by enabling alternative architectures that can be implemented which save time, energy, and money.

MATERIALS AND METHODS

Experiment 1: Odd vs. Even Categorization by Honeybees

Study Species and Recruitment

Experiments were conducted with free-flying honeybees (*Apis mellifera*) in Toulouse, France during summer in 2017. Foragers (n = 26) were recruited from a gravity feeder providing ca. 10–20 % (by volume) sucrose solution, and each marked with a different color on the thorax to identify individual bees used in the experiments. Honeybees were recruited from over 25 hives maintained at Paul Sabatier University in Toulouse, France.

Apparatus

Individual honeybees were trained to visit a vertical rotating screen, 50 cm in diameter (Dyer et al., 2005). The screen allowed the spatial arrangement of stimuli to be randomly changed throughout the experiment, thus excluding positional cues. Stimuli were presented vertically on 6 × 8 cm moveable hangers with a landing platform attached below the presentation area. Hangers and surrounding screen areas were washed with 30% ethanol and then water between choices, foraging bouts, and before each test to prevent the use of olfactory cues (Zhang et al., 1996; Howard et al., 2017a,b). One bee was tested at a time during training and testing phases, which typically lasted 2–4 h per bee.

Four stimuli (two stimuli with an identical even number of elements; two stimuli with an identical odd number of elements) were presented simultaneously above landing platforms on the respective hangers. During training a 10 μL drop of either 50% sucrose solution (CS+) or 60 mM quinine solution (CS-) were placed on the platforms and used as rewarding and punishing outcomes for correct and incorrect choices, respectively, during the training phase, as this promotes enhanced visual discrimination performance (Avarguès-Weber et al., 2010a) and quantity discrimination (Howard et al., 2019c).

Stimuli

All stimuli were covered with 80 μm Lowell laminate. Stimuli were 6 × 6 cm white card squares presenting multiple black geometrical elements varying in size (**Figure 1** and **Supplementary Figure 1**). Each stimulus was composed of elements of a single shape out of four options: circle, square, diamond, or triangle. The stimuli were changed following a pseudo-random order between bouts (return of bee to the hive), therefore a bee could make multiple choices (up to six) on the same set of stimuli in a single bout, although this was uncommon (generally 2–3 choices). During the preference test and training phase, the number of elements presented to bees ranged from 1 to 10 and only three of the four possible element shapes (circle, square, diamond, triangle) were used (**Supplementary Figure 1**). During the transfer test stimuli consisted of 11 or 12 elements of the same four possible element shapes (**Supplementary Figure 1**). The cumulated surface area of the black elements was 10 ± 0.3 cm^2 regardless of shape, configuration, or number of elements. It is important to note that non-numerical cues correlating with magnitude, such as surface area, perimeter, edge length, spatial frequency, convex hull, density, or size of elements, do not predict the parity of a stimulus and thus bees were unable to use these cues to solve the task. There were 180 different stimuli available to be presented consisting of different element number, shape, and overall element configuration (**Supplementary Figure 1**) and additionally each stimulus could be presented at one of four rotational orientations (with the exception of symmetrical stimuli

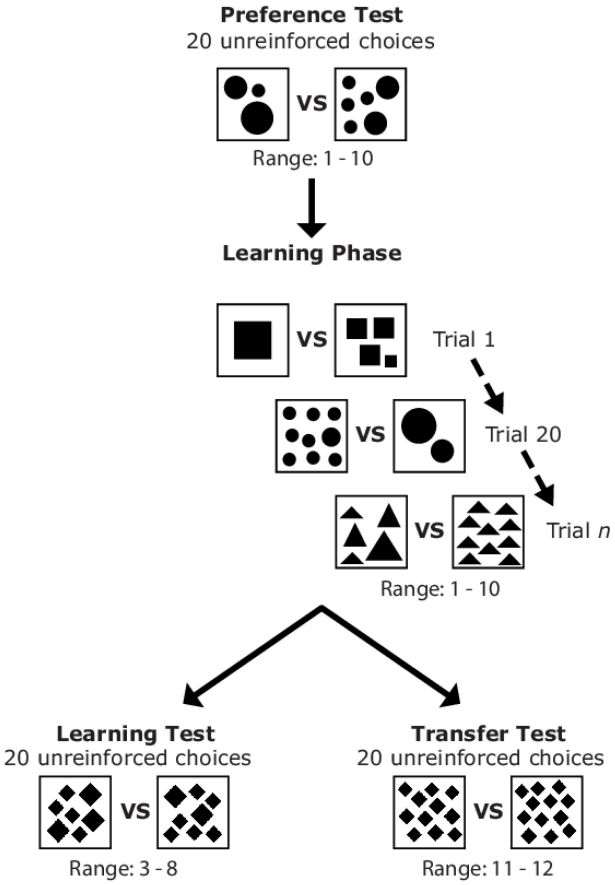

FIGURE 1 | Sequence of the different phases of Experiment 1 and examples of stimuli which could be presented to a bee during the preference test, learning phase, learning test, and transfer test.

such as those containing one element). In addition, odd and even numbers were presented in a pseudo-random order, within subject, to ensure ∼50% of even numbers were higher than the odd number and ∼50% were lower than the odd number, thereby excluding bees from learning a magnitude task. Stimuli were analyzed for symmetry to determine if this could be a possible cue for bees to learn to classify numerosities as odd or even (Giurfa et al., 1996). We compared the horizontal and vertical bisections of all stimuli for symmetry scores and compared these between odd and even stimuli. There were no significant differences in symmetry between odd and even stimuli (see **Supplementary Material** for full details), thus this could not be a cue driving bee choices.

Overview of Learning and Testing Phases

A counter-balanced design was used for this experiment, where one group of bees was trained to associate stimuli consisting of an even number of elements with a reward (n = 13), while a second group of independent bees were trained to associate stimuli containing an odd number of elements with a reward (n = 13). Group testing order was random. The experiment consisted of four parts: Preference Test, Learning Phase, Learning Test, and Transfer Test (**Figure 1**). Refresher training occurred between the learning and transfer tests to maintain bee motivation to revisit the apparatus and lasted for one foraging bout (Howard et al., 2017a,b). A choice was defined as a bee touching or landing on the hanger platform and tasting the drop of sucrose or quinine for learning trials. For the tests, a choice was considered as any touch of a hanger platform or the stimulus.

Preference Test

After bees had learnt to land on the hanger platforms without stimuli present (gray background) to receive a reward of sucrose, we conducted a preference test. The preference test involved recording 20 unreinforced choices (no reward or punishment for landings) for two numbers which were randomly selected to include one even and one odd number consisting of 1–10 elements (**Figure 1**) using one randomly selected element shape from the four options. In this test we thus determined if bees had any prior preferences to odd or even element numbers prior to the learning phase. A 10 μL drop of water was used as a neutral substance to motivate bees to land on the platforms.

Learning Phase

Learning phase stimuli were displayed on hangers and choices of bees were recorded until individuals reached a criterion of ≥ 80% for 10 consecutive choices (one trial block) after a minimum of 20 choices had been made (Howard et al., 2018a). A choice/trial during training was defined as a visit to the stimulus including drinking/tasting the substance on the hanger platform using the proboscis, antennae, or leg (Morawetz et al., 2013). Stimuli were randomly allocated for each bee and changed between bouts and landings. Two randomly selected numbers consisting of 3–8 elements (excluding boundary numbers; one randomly selected even number and one randomly selected odd number) were not presented to bees during the learning phase so these two numbers could be used as novel test stimuli during the learning test.

Bees generally made between 2 and 6 correct choices during each bout before they became satiated and returned to the hive. When a bee made an incorrect choice, it was allowed to continue making choices until a correct choice was made. Once a bee made a correct choice, it was collected onto a plexiglass spoon providing a 10 μL drop of 50% sucrose solution and placed behind an opaque barrier one meter away from the screen to drink while the stimulus element number and positions were randomly changed, and the platforms and surrounding areas were cleaned. After this, bees could either continue making choices or return to the hive if satiated. Bees generally returned from the hive within 5 min, during which time the apparatus was cleaned, new stimuli were placed on the hangers, and drops of sucrose and quinine were placed onto the hanger platforms. After bees had reached the learning criterion, they were collected onto a plexiglass spoon with sucrose, allowed to drink until satiated and then returned to the hive so the test stimuli could be introduced. Bees could then return to the experiment for the testing phases.

Learning Test

The learning and transfer tests were conducted in a pseudo-random order, balancing the number of times the learning or

transfer test occurred first. After bees had reached criterion in the learning phase, we presented a learning test using novel numbers, shape, and patterns to determine if bees had learnt to discriminate between "even" and "odd" numerosities. Numerosities used in this test were randomly chosen at the beginning of each experiment, excluding the two lowest or highest quantities in the training set (i.e., excluding 1, 2, 9, and 10; one randomly selected even number and one randomly selected odd number: 3, 5, or 7 and 4, 6, or 8). We recorded 20 unreinforced choices for this test. A 10 μL drop of water was placed on the platforms to motivate bees to land during the learning test.

Transfer Test

The transfer test to higher quantities outside of the original training set consisted of presenting bees with stimuli containing 11 and 12 elements of novel shape and pattern. This test aimed to determine if bees could differentiate between odd and even numerosities outside of the training set. We recorded 20 unreinforced choices per bee for this test. A 10 μL drop of water was placed on the platforms to motivate bees to land during the transfer test.

Time Recordings

Using a video camera, we were able to record the duration of both tests for seven of the bees (four trained to even; three trained to odd) to determine if there was a difference in the time taken to complete a test with lower numbers (learning test: 3–8 elements) and higher numbers (transfer test: 11 and 12 elements). The time was measured from the first choice to the last choice of the bee over the course of 20 choices.

Statistical Analysis

Did Bees Have an Innate Preference for Odd or Even Numerosities?

To determine whether bees had any prior preference to odd or even numerosities before training we estimated the mean of the "even number" choices, the intercept of a generalized linear mixed model (GLMM) with a binomial response, using individual bees as a random, categorical variable to account for the repeated measurements. Choice (even or odd number) was coded as a binary response (even or odd) modeled by a binomial distribution. The statistical tests and models were performed on the R environment for statistical analysis using the routine "glmer" available as part of the "lme4" package written for the R statistical language, run in R version 4.0.3 analysis (R Core Team, 2020).

Did Bees in Both Groups Learn Equally?

To determine if the bees in the two groups (trained to even; trained to odd) learnt equally, we statistically compared the number of trials required for bees to achieve criterion in both groups by means of a GLM model. The response variable included the number of trials taken to reach criteria by bees belonging to each group and stimuli group as a categorical predictor with two levels: even and odd. We initially assumed a Poisson distribution to model the response variable but the resulting model was overdispersed (overdispersion = 2.98). We thus assumed a negative binomial distribution for the response variable as usually done to alleviate overdispersion of Poisson models (Zuur et al., 2013). We used the routine "glm.nb" available in the package MASS (Venables and Ripley, 2002) for the R statistical program to fit the negative binomial model.

Could Bees Learn and Apply Odd and Even Number Categorization?

To determine whether bees could apply the concepts of odd and even in the learning and transfer tests with novel numbers, patterns, and shape, we analyzed the learning and transfer test data with the same statistic as described in section "Did Bees Have an Innate Preference for Odd or Even Numerosities?". We estimated the mean of the "correct" choices, the intercept of a GLMM with a binomial response, using individual bee ID as a random, categorical variable to account for the repeated measurements. Choice (correct or incorrect) was coded as a binary response modeled by a binomial distribution.

Were Results Consistent Across Groups and Tests?

We implemented a GLMM to determine if there were any asymmetries within the two tests (learning test; transfer test) and between the two groups trained to "even" and "odd" numbers. The model consisted of two fixed factors: test type and experimental group both with two levels, an interaction term between these two predictors, and a random term to account for the repeated measures collected from each individual bee. The response variable of the model consisted of the outcome of bee choices for each of the 20 trials coded as correct or incorrect. A binomial distribution was assumed for the response variable. The two levels of the test factor were learning test and transfer test. The two levels of the experimental group factor were bees trained to "even" numbers and bees trained to "odd" numbers. A total of 26 bees were divided across the two levels of the experimental group factor (13 in each group), and each bee was then tested under all levels of the test factor.

The model was fitted using the routine "glmer" available in the lme4 library (Bates et al., 2015) available for the R language. Statistical significance of the model terms was tested by means of Type III Wald Chi square test using routines available in the package car (Fox and Weisberg, 2019) for R.

Was There a Difference in Time Taken to Perform the Tests?

To determine if there was a difference in the time taken for bees to complete the learning test with lower numbers ranging from 3 to 8 compared to the transfer test of higher numbers 11 and 12, we used a Wilcoxon signed-rank test comparing the two related conditions (each bee participated in both tests). We compared seven bees for the time taken to complete the learning and transfer tests. This analysis was performed on the R environment for statistical analysis (Sokal and Rohlf, 1981; R Core Team, 2020).

Analysis of the Stimuli

To determine whether there was a significant difference in the spatial information content for the odd and even stimuli, we calculated the rotational average of the power spectrum of each image to produce a frequency spectrum for each image using the fast Fourier transform routine available in MATLAB

release 2016b. We then calculated the area under each spectrum corresponding to the stimuli of the odd and even sets, and compared them by means of a Wilcoxon rank-sum test.

Experiment 2: Discrimination of 11 vs. 12

Using a similar protocol as detailed above in Experiment 1, we trained and tested bees on their ability to discriminate between stimuli containing 11 and 12 elements. This experiment was performed in 2018, as their ability to categorize those numerosities during the transfer test in the Experiment 1 was unexpected considering the honeybee's previous limit of counting and discriminating numerosities. One group (n = 5) was trained to choose 11 elements while a second group was trained to choose 12 elements (n = 5). The learning test to determine if bees could differentiate between 11 vs. 12 was conducted with stimuli similar to the training set of novel patterns while the transfer test was conducted with multiple randomized, previously unseen element shapes (**Supplementary Figure 3**). We have provided video footage of an example of a bee completing this task (**Supplementary Video 1**).

Stimuli

Stimuli were 6 × 6 cm white card squares presenting multiple black elements. All stimuli were covered with 80 μm Lowell laminate. Elements were one of four shapes: circle, square, diamond, or triangle. The stimuli were changed following a random order between bouts (return of bee to the hive). During all phases of training and testing, bees were presented with stimuli containing either 11 or 12 elements, where one numerosity was rewarding and the other was punishing (counter-balanced). There were 66 different stimuli available to be presented consisting of different element number, shape, and overall element configuration (**Supplementary Figure 3**) and additionally each stimulus could be presented at one of four orientations. The training and learning test stimuli were varied between having equal overall black surface area for the pattern (set 1; equal black surface area of 10 cm^2) and elements all of equal surface area (set 2; each element was 1 cm^2). The transfer test stimuli were random shapes and objects not previously presented to bees (set 3).

Statistical Analysis

To determine whether bees could discriminate between the quantities 11 and 12 during testing, we estimated the mean of the "even number" choices, the intercept of a GLMM with a binomial response, using individual bees as a random, categorical variable to account for the repeated measurements. Choice (11 or 12) was defined as a fixed effect with a binary response. The statistical tests and models were performed on the R environment for statistical analysis (R Core Team, 2020).

Experiment 3: Odd vs. Even Categorization by a Simple Neural Network

To understand if a simple neural network is potentially able to perform odd and even categorizations of numerosities, we built and tested a model based on five neurons. The number of neurons employed was derived by a preliminary logic analyses of what type of network might plausibly enable processing (Vasas and Chittka, 2019). Our model was implemented in Python 3 and is schematically depicted in **Figure 2** by employing a simple propagation through the neural network that is iterated concurrently with the signal.

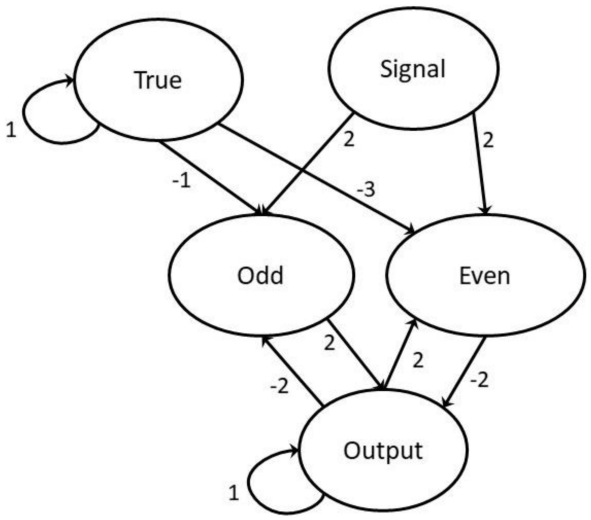

FIGURE 2 | The neural network with weightings marked with directed arrows.

The network comprises the following five neurons: Signal, True, two intermediary neurons, and Output. The Signal neuron receives a processed string of short excitations, modeled as a list of uniform strength signals (normalized to 1) separated by dormant regions of 0 magnitude of varying lengths. The two intermediary neurons model Even and Odd, respectively, filtering out the cases where the signal is even or odd and then affect the appropriate modification to the Output neuron. This is achieved using feedback from the state of the Output neuron. The Output neuron acts as both ongoing storage and the read-out value. The True neuron is activated at all points in time and is used for filtering the required strength of inputs to elicit a reaction from the activation function. Both the True and Output have strong weightings with themselves, meaning that without outside affects they hold their values indefinitely. In the modeling experiments a signal was entered concurrently with the propagation by setting the signal neuron's value according to a signal list. New neuron values [X_n (t + 1)] are obtained by summing the weighted values of all neurons ($w_m X_m(t)$) before passing them into the activation function.

$$X_n(t+1) = f\left(\sum_m w_m X_m(t)\right)$$

We used the linear activation/cleaning function from Vasas and Chittka (2019), which is motivated by neurons mirroring rapidity responses between a maximum and minimum value:

$$f(x) = \begin{cases} 0 & x \leq 0 \\ x & 0 < x < 1 \\ 1 & 1 \leq x \end{cases}$$

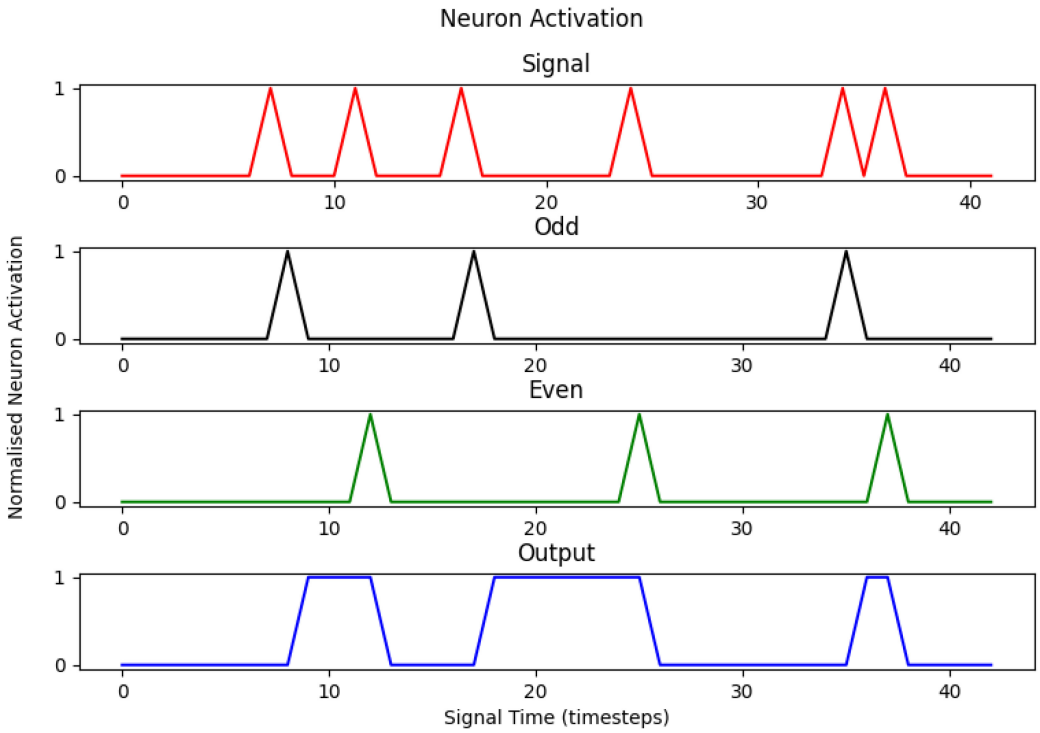

FIGURE 3 | The activation profiles of the neurons in the artificial neural network, for a sample signal of 6 pulses. The output is 1 for an odd signal and 0 for an even one.

The weighting values are specifically calculated to create the desired effect and not generated through a regression or optimization algorithm. The values of all neurons are initialized dormant (with a value of 0) except the True neuron which is initialized at 1.

An example of the implementation of the model can be seen in **Figure 3**, with the Signal (red) and complementary firings of the two intermediary neurons (Even—green, Odd—black) at a minor delay of one time step, with the Output neuron (blue) toggling states at another slight delay. The True neuron has been omitted for clarity but has a value of 1 at all times during the process.

Because of the concurrent signal feed into the neural network through the Signal neuron the computation time scales linearly with the length of the signal and is not directly affected by the size of the number being counted (except insofar as larger numbers will likely generate longer signals, and it must be possible for a sensory system to resolve such information). It is also not related to subitization thresholds nor explicitly related to counting and memory storage, only requiring the ability to separate all the objects being counted without repetition, a task which has been demonstrated to be possible for numbers larger than the subitization threshold (Howard et al., 2019c). The characteristics of the iterative method imply an ability to extrapolate accurate results for elements outside a learning set.

Whilst we cannot maintain this simple artificial neural network is indeed how an individual honeybee might actually learn to solve odd/even categorizations, the proposed neurons are consistent with how phasic or tonic neuron responses are processed in bee brains. For example, the flow of visual information in the bee eye begins at the retina level within each ommatidia, which subsequently project inputs to visual sequential processing areas including the lamina, the medulla, and the lobula before integration processing by the mushroom body (Menzel, 1973; Hertel and Maronde, 1987; Hertel et al., 1987; Yang and Maddess, 1997; Paulk et al., 2008). In the lobula of the bumblebee brain there are six anatomically distinct layers that display different levels of phasic–tonic, phasic, tonic, and/or on–off responses following visual stimulation including motion sensitivity (Paulk et al., 2008) as might be engaged in bee scanning of patterns (Vasas and Chittka, 2019). Our model is thus biologically plausible, and demonstrates that a parity categorization task might be possible using relatively few neurons.

RESULTS

Experiment 1: Odd vs. Even Categorization by Honeybees

Using appetitive-aversive differential (reward-aversion) conditioning (Avarguès-Weber et al., 2010a; Howard et al., 2019c), bees were trained to choose either "even" numerosities of elements (Group 1) or "odd" numerosities of elements (Group 2) as the correct option. Bees were trained to reach a criterion of $\geq$ 80% over 10 choices using the quantities of 1–10 (**Figure 1**). All bees reached criterion by 70 choices and none were discarded

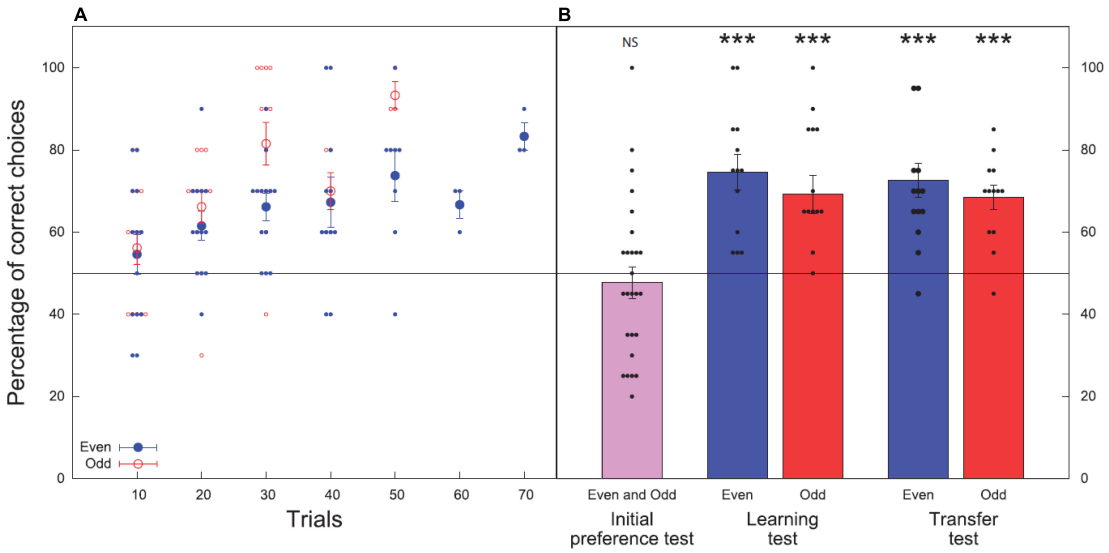

FIGURE 4 | Bee performance during the learning and test phases: initial preference test, learning test, and transfer test. Data shown are means ± standard error of the mean (SEM) for both treatment groups (even; odd). *N* = 13 bees were used in each group for each test, 26 bees were tested overall. Black line at 50% indicates the chance level performance. **(A)** Results of the learning phase (before reaching criterion). Closed blue circles show bees trained to even numbers while open red circles show results for bees trained to choose odd numbers. Larger circles show the mean ± SEM and smaller circles show the individual results of each bee. **(B)** Results of the preference, learning, and transfer tests for the respective groups (even; odd). Initial preference test shows the results of all 26 bees for their initial preference (before training) for even element numbers. Black circles show the individual results of each bee for all tests. Significance from chance level performance is indicated by *NS* > 0.05, *** ≥ 0.001. There was no significant difference between the learning and transfer tests.

from analysis. Before this learning phase was conducted, bees were tested for their potential preference for even or odd numerosities of elements for 20 choices (using quantities 1–10). After training, bees were tested on their ability to categorize novel numbers within the learning set (learning test; 20 choices; 3–8 elements), and novel numbers outside of the learning set (transfer test; 20 choices; 11 vs. 12 elements; **Figure 1**).

Preference Test

Overall bees chose even numbers in 47.7 ± 3.8% of choices [mean ± standard error of the mean (SEM)] and odd numbers in 52.3 ± 3.8% of choices. These choices were not significant from chance (H_0 = 50%, z = −0.396, P = 0.692, n = 26), therefore there was no evidence of a significant preference for odd or even numerosities among bees before training began.

Learning Phase

All bees in the group trained to even numbers (Group 1, n = 13) reached criterion within 70 choices, with an average of 49.0 ± 4.0 choices to reach criterion (**Figure 4A**). All bees in the group trained to odd numbers (Group 2, n = 13) reached criterion within 50 choices with an average of 36.0 ± 2.0 choices to reach criterion (**Figure 4A**). There was a significant difference in number of trials/choices taken to reach criteria between the two groups (z = −3.129, P = 0.002) with bees trained to associate odd numerosities with a reward reaching criterion in less choices.

Learning and Transfer Tests

In the learning test, bees trained to even numbers (Group 1) chose the correct stimulus with an accuracy of 74.6 ± 4.3%. The number of correct choices made during the unreinforced learning test was significantly higher than the chance expectation equivalent to 50% (z = 4.599, P < 0.001, n = 13). Bees trained to odd numbers (Group 2) chose correct stimulus with an accuracy of 69.2 ± 4.7% (z = 4.742, P < 0.001, n = 13; **Figure 4B**).

In the transfer test, where bees were presented with odd and even numbers of novel shape and pattern from outside of the learning set boundaries, the group trained to associate even numerosities with a reward (Group 1) chose the correct stimulus with an accuracy of 72.7 ± 4.1% (z = 4.627, P < 0.001, n = 13). Bees trained to associate odd numbers with a reward (Group 2) chose the correct stimulus with an accuracy of 68.5 ± 2.9% (z = 5.693, P < 0.001, n = 13; **Figure 4B**).

We found no significant effect of the interaction term in the GLMM fitted to test for consistency in the accuracy of the bees performance, evidencing that the proportion of correct choices was the same between tests and groups (test × groups: χ^2 = 0.010, df = 1, P = 0.920). Moreover, we found no significant difference in the proportion of correct choices obtained by bees in the learning and transfer tests (χ^2 = 2.99, df = 1, P = 0.083), nor in the proportion of correct choices obtained for the even and odd groups (χ^2 = 0.389, df = 1, P = 0.533). This shows that bees can learn and transfer the concepts of odd and even numbers to novel numbers within and beyond their training set with similar accuracy.

Count data from the learning test for bees trained to even [Shapiro-Wilk's test (W) = 0.840, df = 13, P = 0.021] or odd (W = 0.844, df = 13, P = 0.022) were not normally distributed. Count data for bees trained to even (W = 0.869, df = 13, P = 0.050) and odd (W = 0.952, df = 13, P = 0.632) in the transfer test

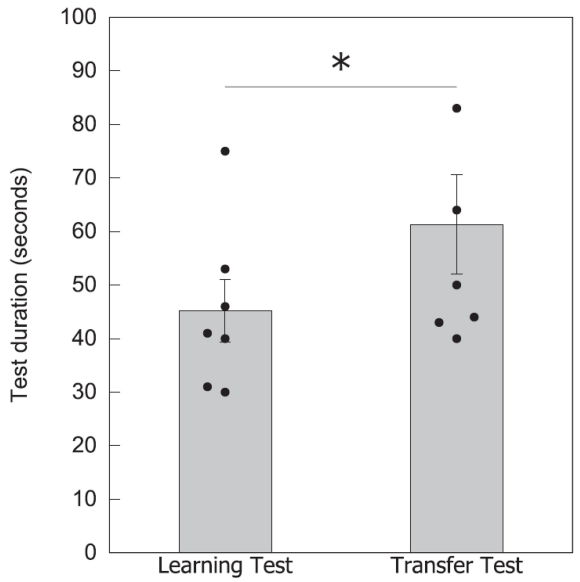

FIGURE 5 | Test duration for completing the learning and transfer tests. Data shown are means ± SEM for the learning and transfer tests. $N = 7$ bees were recorded for the time taken to complete each test. Black circles show individual data for each bee. Significantly different results are indicated by $^* \geq 0.05$.

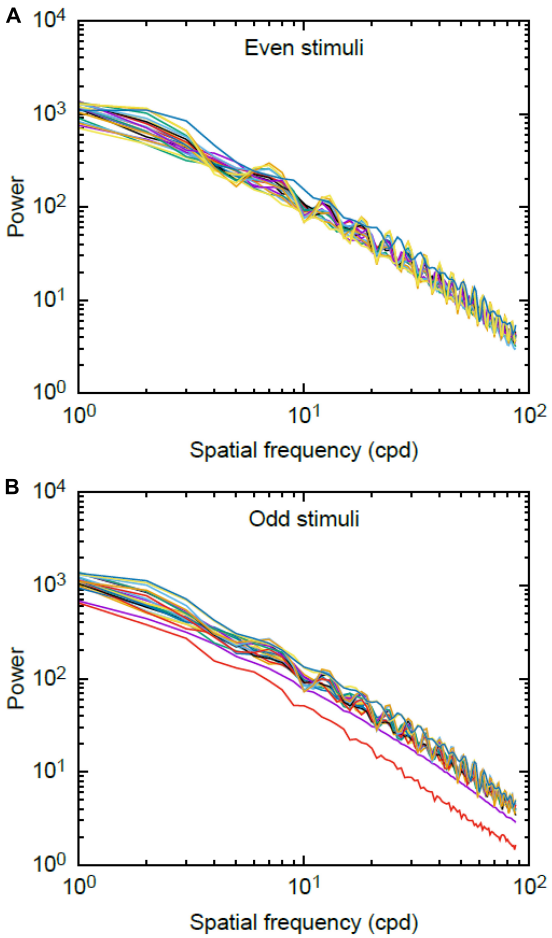

FIGURE 6 | Log-log plot of spatial frequency spectra for **(A)** even and **(B)** odd stimuli used during experiments. Data plotted are the 92 stimuli for the even set and the 88 stimuli for the odd set. There is no significant difference between mean value of the power spectra of the odd and even stimuli.

were normally distributed. We thus performed an additional robust split-plot ANOVA on 20% trimmed means (Q statistic) (Wilcox, 2011) to validate the results of the parametric test. Results supported the findings of the first analysis evidencing that there was no significant difference between the correct choices performed by bees trained to even or odd numerosities ($Q = 0.006$, $P = 0.942$), nor differences between the different tests ($Q = 1.69$, $P = 0.213$). The interaction term between the two factors was also non-significant at $\alpha = 0.05$ ($Q = 0.160$, $P = 0.695$). This shows bees reliably transferred the acquired concepts from the learning set to the novel numbers of 11 and 12.

Analysis of Time

To assist in understanding potential mechanisms that might enable parity categorization in bees, we additionally compared the time taken to complete each test for seven bees (recording from the first choice of a stimulus to the last choice in the test). In the learning test with a lower number of elements, bees took an average of 45.0 ± 5.8 s to complete the task ($n = 7$), while in the transfer test with a higher number of elements, bees took 61.0 ± 9.3 s to finish ($n = 7$; **Figure 5**). There was a significant difference between the two test times [Wilcoxon signed-rank test value (W) = 2.000, $P = 0.041$], which could be due to a number of reasons including the task complexity, discussed below in the "Discussion" section.

Analysis of Stimuli

The plots of the Fourier rotational values are shown in **Figure 6**. We found no significant difference between the total area of the power spectra corresponding to the even and odd stimuli [Wilcoxon-rank sum statistic (W) = 3836, $P = 0.545$].

Experiment 2: Discrimination of 11 vs. 12

As bees performed the transfer test in Experiment 1 at a level significant from chance, we tested their performance on learning and performing the numerical discrimination of 11 vs. 12 in a separate training and testing group. The results obtained in the transfer test of Experiment 1 were unexpected due to the bee's previous limit of differentiating between numerosities of three and four using appetitive differential conditioning (Gross et al., 2009) and 4 vs. 5 elements when appetitive-aversive differential conditioning was used (Howard et al., 2019c). Thus, we aimed to look more closely at whether they were able to discriminate these numbers in a second experiment.

As there were no significant differences between bees trained to quantities of 11 or 12 in either the learning test or transfer test (one-way ANOVA; $P > 0.05$), the two groups were combined for statistical analysis.

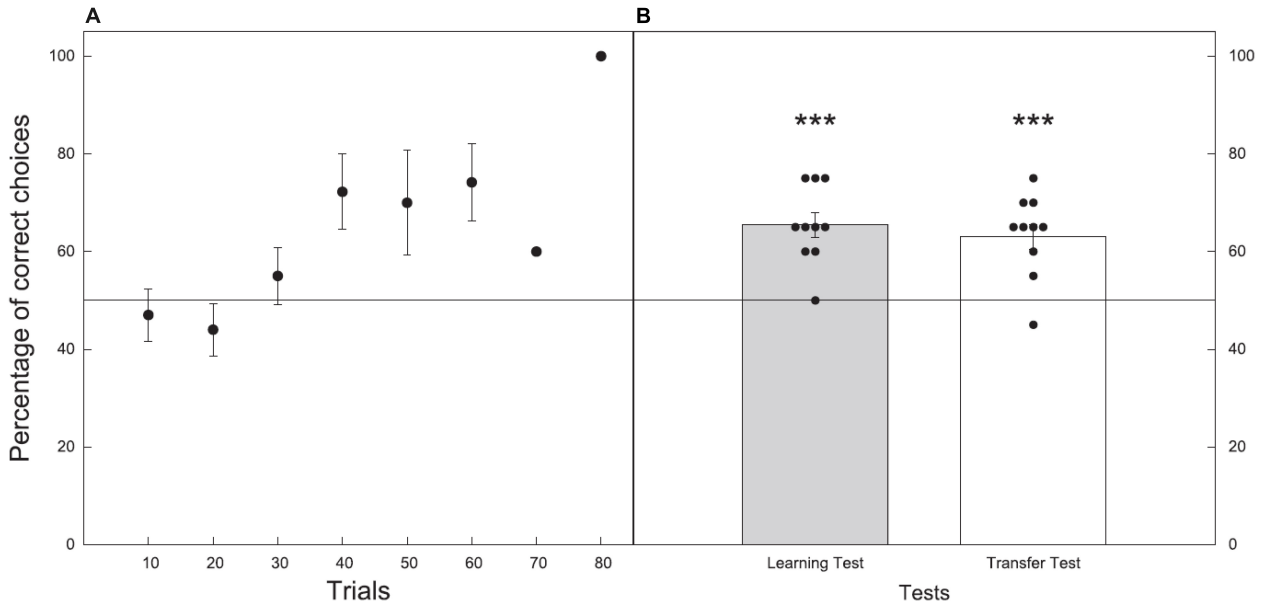

FIGURE 7 | Performance during the learning and test phases for Experiment 2 where bees were trained and tested on their discrimination of 11 vs. 12. Data shown are means ± (SEM). *N* = 10 bees were used. Black line at 50% indicates the chance level performance. **(A)** Results of the learning phase (before reaching criterion) with just one bee still learning in trial blocks 70 and 80. **(B)** Results of the learning (gray) and transfer (white) tests. Black circles show individual results of each bee in the tests. Significance from chance level performance is indicated by *** ≥ 0.001. There was no significant difference between the learning and transfer tests.

Learning Phase

All bees reached criterion within 72 choices, with an average of 43.3 ± 4.6 choices to reach criterion ($n = 10$; **Figure 7A**).

Learning Test

In the learning test, bees trained to either 11 or 12 chose the correct stimulus with an accuracy of 65.5 ± 2.5%. The number of correct choices made during the unreinforced learning test were significantly higher than the chance expectation equivalent to 50% ($Z = 4.300$, $P < 0.001$, $n = 10$; **Figure 7B**).

Transfer Test

In the transfer test, where bees were presented with numerosities of 11 vs. 12 of novel shape and pattern bees chose the correct stimulus with an accuracy of 63.0 ± 2.6% ($Z = 3.600$, $P < 0.001$, $n = 10$; **Figure 7B**).

Experiment 3: Odd vs. Even Categorization by a Simple Artificial Neural Network

We tested our neural network architecture on a large range of randomly generated stimuli both in terms of separation and numerosity of signal events, with the caveat that all events are spaced by more than 1 time step. The neural network is capable of classifying all inputs as odd or even with 100% accuracy from 0 to 40 elements and pulse separation 1–10. The method can be well understood to function for arbitrary length signals of arbitrary numerosity. Our network seems to be functioning at a significantly higher level of specificity than observed in bee experiments, which implies that the architecture present in the honeybees is not as well optimized as the model presented. The Odd and Even neurons function as conditional logic gates that will activate or deactivate the Output neuron, respectively, depending on its current state, whenever a new signal pulse is detected.

DISCUSSION

Odd and even categorization of numbers is considered an abstract and high-level numerical concept in humans (Hines, 1990; Dehaene et al., 1993; Berch et al., 1999; Reynvoet and Brysbaert, 1999; Nuerk et al., 2004, 2005; Alards-Tomalin et al., 2016), which builds upon diverse elements such as language, numerosity, symbolic representations of number, memory, and algorithms. We have shown that honeybees demonstrated an ability to learn the concepts of odd and even and were subsequently able to apply these concepts to categorize novel numbers by parity. Importantly, we also showed that honeybees were able to apply these concepts to numbers greater than the subitizing threshold. Appetitive-aversive conditioning is likely to be an important component of our finding (Chittka et al., 2003; Avarguès-Weber et al., 2010a; Howard et al., 2019c), suggesting that appropriate motivation and attention are likely to be important factors in observing numerical abilities in animals (Howard et al., 2019c, 2020a). We do not claim that honeybees were able to count all elements in the stimuli to categorize the quantities as even or odd, nor do we believe that honeybees employ the same complex mechanisms as used by humans. Below, we discuss several possibilities of how this task could potentially be

performed including mathematical calculations, pattern learning, and grouping of objects.

Studies of parity tasks in humans have often shown an asymmetry between categorizing odd and even numbers. Humans made significantly fewer errors and were faster when categorizing number sequences as even when compared to odd (Hines, 1990; Nuerk et al., 2005; Alards-Tomalin et al., 2016). Our results from the current experiment show a significant difference in the number of trials taken to reach criteria between the groups. Specifically, honeybees needed a significantly lower number of trials to reach criterion when learning to choose odd numbers as the correct alternative compared to the group trained to choose even numbers. This is in contrast to what is observed in humans, who are better at categorizing numbers as even compared to odd, and suggests that honeybees find odd categorization easier to learn. However, following the learning phase, we found no difference in performance level during tests between honeybees trained to either even or odd numbers as the correct alternative.

The bees' performance is consistent with the application of a rule-based type mechanism for problem solving (Perry and Barron, 2013; Howard et al., 2017a,b, 2018a), and would not be expected if bees were using an associative mechanism to solve the different visual problems (Howard et al., 2017a). This conclusion is evident when considering bees trained to even numbers, as an associative mechanism would predict they should choose the stimulus with 11 elements which is closest to simple predictors of the training set (i.e., 10 was the highest rewarding numerosity they encountered, thus 11 is closer to this numerosity than 12); whilst choices for the stimulus with 12 elements is consistent with the application of an "even" rule-based solution to the visual problem. Thus, we can rule out this simple associative mechanism allowing bees to successfully perform this task, and below we discuss the other potential mechanisms driving bee performance.

Interestingly, recent studies show that relatively complex cognitive-like learning demonstrated by honeybees can be achieved by simple neural networks in some cases (Cope et al., 2018; Vasas and Chittka, 2019; MaBouDi et al., 2021). We were similarly able to demonstrate that the categorization of odd or even numbers can be efficiently performed to 100% accuracy with a simple neural network, showing that it is biologically plausible that parity tasks are accessible to animals with comparatively small brains. A relatively complex numerical task, where bees must learn the concepts of "greater than vs. less than" and then value zero numerosity (Howard et al., 2018a), has been replicated by a simple artificial neural network containing four neurons (Vasas and Chittka, 2019). These studies suggest that complex cognitive-like behaviors may be accessible to assumed simple biological systems (such as the honeybee) as these tasks may demand less brain power than previously thought, or bees may be employing other mechanisms in order to solve the problem. In the current study, honeybees may be solving a task that appears relatively complex, parity categorization, in a way that does not demand a large and complex neural network (Cope et al., 2018; Vasas and Chittka, 2019; MaBouDi et al., 2021), suggesting that parity processing may potentially be learnt by other animals.

There is an important distinction that we draw between this neural network and more traditional machine learning approaches, especially in regard to its implications for biological systems. Neural network training is normally done from a naïve state to a specific state by some method based on stimulus/feedback. This implicitly draws parallels to biological states which, while not using the same training methods, still develop in response to feedback. Because this neural network was generated manually there is no evidence to suggest that similar results can be easily achievable via machine or deep learning algorithms, or actual biological processes. However, given that bees learnt odd and even categorization reasonably quickly and demonstrate an asymmetry in the number of choices to learn odd vs. even, it is reasonable to speculate that bees may have some innate neural mechanisms to help with parity processing. The asymmetry in learning suggests that bees may possess an innate processing advantage for odd quantities or have potentially previously encountered rewards linked with odd quantities, such as petal numbers on flowers. Innate neural mechanisms may recruit observed phasic–tonic, phasic, tonic, and/or on–off neural responses known to process complex visual stimulation including motion (Paulk et al., 2008) that could stimulate pre-existing neural processes that bees may have for efficiency in foraging tasks.

There are two principal mechanisms which have been suggested to potentially allow for the success in humans performing a parity task (Berch et al., 1999) and we can explore the possibility of both in relation to the current study on bees. The first is the use of a mental calculation strategy such as division by two (Clark and Campbell, 1991), and the second is the possibility of direct retrieval from semantic memory (Dehaene et al., 1993). For example, there is a possibility that humans can perform parity tasks based on memory which defines numbers ending in 0, 2, 4, 6, or 8 as an even number, and anything else as an odd number, thus bypassing the use of counting or mathematical calculations (Dehaene et al., 1993). As the numerosities used in the current study were non-symbolic, it seems unlikely that a similar mechanism could be used by honeybees to solve this task.

If success in a parity task was achieved by the use of a mental calculation, then the magnitude of the number should impact the response time, thus the greater the number, the greater the response time (Dehaene et al., 1993). In our experiment, bees did take a significantly longer time to categorize higher numbers (11 and 12) compared to lower numbers (3–8) in terms of parity, suggesting they found the transfer task more perceptually difficult in terms of cognitive processing or visual complexity. We can rule out an effect of novelty causing the difference in time between the tests as the numbers shown during both the learning and transfer tests were not previously shown to bees during training. While the time difference between tests could suggest that bees may have been counting the elements or even performing a division calculation as is observed in humans (Dehaene et al., 1993; Berch et al., 1999), we cannot discard the possibility of bees simply taking longer to process the more perceptually difficult stimuli, due to the presence of more objects to assess, before making a decision. In addition, there is no data available suggesting that honeybees may be able to perform division calculations making this hypothesis unlikely. Nevertheless, if bees are counting the

elements, they may not need to perform a division calculation if an existing brain mechanism for parity categorization is present in the brain. The asymmetry observed in the learning phase for the odd vs. even groups is suggestive of the bees using some combination of pre-existing mechanisms to solve the parity task.

Increased decision-making time with more perceptually difficult tasks has been observed in bumblebees (Spaethe et al., 2001; Dyer and Chittka, 2004; Dyer et al., 2007) as well as in humans (Pachella and Fisher, 1969), and honeybees do also make speed-accuracy trade-offs (Burns and Dyer, 2008). Thus, we are unable to determine if honeybees were using numerosity skills, such as counting or calculations, to successfully perform the categorization of numbers as odd or even, or, if they were using another perceptual mechanism not requiring activation of numerosity such as semantic memorization (discussed above), pattern learning (discussed below) or pairing elements (discussed below), which we consider a more likely scenario. In human parity tasks, number magnitude, although irrelevant to the task, has a strong effect on reaction time, therefore the reaction time of bees could also be impacted by the magnitude of the numbers used in the learning and transfer tests explaining the difference in time to complete each of the tests (Dehaene et al., 1993).

There are also possibilities for completing a parity task which are not discussed in studies on humans. For example, bees may learn to pair elements and remember that a leftover unpaired element may either reward or punish them. This theory would fit with our results and the difference in time to pair lower quantities of elements in the learning test compared to higher quantities in the transfer test. Alternatively, perhaps bees could learn the odd/even pattern; if a bee was trained to choose odd numerosities, 1 is correct, but 2 is incorrect, 3 is correct and so on, increasing in magnitude by one means a stimulus is either correct or incorrect. Interestingly, bees have been observed to processes some complex patterns in brief time frames suggesting auto processing mechanisms must exist for some types of stimuli (Srinivasan et al., 1993). Bees could potentially learn the pattern of odd and even numbers as differing by one additional element through the numerical continuum as resulting in a reward or aversive outcome. In any case, many of these hypotheses require bees to process each discrete element sequentially without re-inspecting any of them. While such accurate processing has been described for small quantities of items in bumblebees (MaBouDi et al., 2020), its application to arrays of 11 or 12 objects is definitively challenging. Further work would be necessary to explore how bees could potentially perform this challenging inspection task.

As bees are known to be able to categorize stimuli by symmetry (Giurfa et al., 1996), we analyzed our stimuli using horizontal and vertical bisections to measure symmetry between the odd and even numerosities presented. Our results (**Supplementary Material**) show that there were no significant differences in symmetry between odd and even stimuli, either along the horizontal or vertical planes of the images. This means that odd or even stimuli were unable to be categorized as "odd" or "even" by bees through the use of symmetry cues.

Finally, while there is recent debate about continuous low-level cues impacting numerosity tasks in honeybees (Howard et al., 2020b; Shaki and Fischer, 2020; MaBouDi et al., 2021), it is interesting to note that the current task does not allow honeybees use the low-level cues of surface area, perimeter, edge length, spatial frequency, convex hull, density, or size of elements. These cues generally correlate with increasing magnitude, however, as a parity categorization task does not require quantity discrimination (although magnitude can impact accuracy and time), these cues do not predict the correct or incorrect options. In a parity task, each quantity is correct or incorrect depending on whether it is odd or even and this changes with the addition of each new element, therefore bees cannot solve the task using cues which correlate with increasing magnitude. Despite this, the task may still be solved with other low-level cues not correlated with stimuli parameters, which we have yet to determine. Further research into parity tasks in honeybees and other animals are needed to determine the exact mechanisms and method by which this task can be performed by non-human animals.

Further experiments on other animal species would be valuable in determining the connections between number, space, processing time, and numerosity in parity tasks and additionally explore whether this abstract mathematical concept is accessible to other species. As there is an innate asymmetry in parity categorization in humans (Hines, 1990; Nuerk et al., 2005; Alards-Tomalin et al., 2016) and during training with honeybees, such a phenomenon could also be explored in other animals to determine whether odd and even recognition occurs as an innate preference in any other species. Further work would also be useful in determining exactly how honeybees are able to learn to categorize numerosities by parity and if it is cognitively complex, simple, or if pre-existing neural mechanism allow them to do it. In humans, we know the cortex plays a major role in both number processing (Dehaene et al., 1998; Hubbard et al., 2005; Tang et al., 2006; Piazza et al., 2007), for example the parietal cortex (Dastjerdi et al., 2013), and categorization (Peelen et al., 2009). However, we show here that honeybees are capable of number parity categorization without a cortex, strongly suggesting that alternative brain structures can facilitate such abilities. The current results, and other evidence that bees can reliably categorize stimuli (Zhang et al., 2004; Benard et al., 2006; Avarguès-Weber et al., 2010b), suggest that building neuromorphic computing solutions with very simplified mechanisms is possible. The advantage of such systems is that they require less information processing resulting in reducing both time and energy costs, thus enabling efficient deployment to operate in complex environments.

DATA AVAILABILITY STATEMENT

The original contributions presented in the study are included in the article/**Supplementary Material**, further inquiries can be directed to the corresponding author/s. The data sets analyzed in this study can be found in the **Supplementary Material**.

AUTHOR CONTRIBUTIONS

SRH, JG, and ADG collected the data. SRH, JG, AA-W, JEG, and ADG analyzed the data. All authors gave final approval for submission and contributed to experimental design, interpretation of the data and editing the manuscript.

FUNDING

SRH acknowledges the Australian Government Research Training Program (RTP) Scholarship, HDR Candidate Funding from the School of Media and Communication at RMIT University, the Fyssen Foundation, the L'Oréal-UNESCO for Women in Science Young Talents French Award, and the Alfred Deakin Postdoctoral Research Fellowship from Deakin University. AGD acknowledges financial support from the Australian Research Council (FT160100357).

ACKNOWLEDGMENTS

We thank Martin Giurfa for his comments on the study. We also thank the editor, Guy Gilles Beauchamp, and three reviewers for their constructive comments and suggestions, which improved the study.

SUPPLEMENTARY MATERIAL

The Supplementary Material for this article can be found online at: https://www.frontiersin.org/articles/10.3389/fevo.2022.805385/full#supplementary-material

REFERENCES

Agrillo, C., Dadda, M., Serena, G., and Bisazza, A. (2008). Do fish count? Spontaneous discrimination of quantity in female mosquitofish. *Anim. Cogn.* 11, 495–503. doi: 10.1007/s10071-008-0140-9

Alards-Tomalin, D., Walker, A. C., Nepon, H., and Leboe-Mcgowan, L. C. (2016). Dual-task interference effects on cross-modal numerical order and sound intensity judgments: the more the louder? *Q. J. Exp. Psychol.* 70, 1943–1963. doi: 10.1080/17470218.2016.1216139

Avarguès-Weber, A., and Giurfa, M. (2013). Conceptual learning by miniature brains. *Proc. R. Soc. B* 28:20131907. doi: 10.1098/rspb.2013.1907

Avarguès-Weber, A., D'amaro, D., Metzler, M., and Dyer, A. G. (2014). Conceptualization of relative size by honeybees. *Front. Behav. Neurosci.* 8:80. doi: 10.3389/fnbeh.2014.00080

Avarguès-Weber, A., Portelli, G., Benard, J., Dyer, A., and Giurfa, M. (2010b). Configural processing enables discrimination and categorization of face-like stimuli in honeybees. *J. Exp. Biol.* 213, 593–601. doi: 10.1242/jeb.039263

Avarguès-Weber, A., De Brito Sanchez, M. G., Giurfa, M., and Dyer, A. G. (2010a). Aversive reinforcement improves visual discrimination learning in free-flying honeybees. *PLoS One* 5:e15370. doi: 10.1371/journal.pone.0015370

Avarguès-Weber, A., Deisig, N., and Giurfa, M. (2011a). Visual cognition in social insects. *Annu. Rev. Entomol.* 56, 423–443. doi: 10.1146/annurev-ento-120709-144855

Avarguès-Weber, A., Dyer, A. G., and Giurfa, M. (2011b). Conceptualization of above and below relationships by an insect. *Proc. R. Soc. Lond. B* 278, 898–905. doi: 10.1098/rspb.2010.1891

Bates, D., Mächler, M., Bolker, B., and Walker, S. (2015). Fitting linear mixed-effects models using lme4. *J. Stat. Softw.* 67, 1–48. doi: 10.18637/jss.v067.i01

Benard, J., Stach, S., and Giurfa, M. (2006). Categorization of visual stimuli in the honeybee Apis mellifera. *Anim. Cogn.* 9, 257–270. doi: 10.1007/s10071-006-0032-9

Berch, D. B., Foley, E. J., Hill, R. J., and Ryan, P. M. (1999). Extracting parity and magnitude from Arabic numerals: developmental changes in number processing and mental representation. *J. Exp. Child Psychol.* 74, 286–308. doi: 10.1006/jecp.1999.2518

Bortot, M., Stancher, G., and Vallortigara, G. (2019b). Transfer from number to size reveals abstract coding of magnitude in honeybees. *Iscience* 23:101122. doi: 10.1016/j.isci.2020.101122

Bortot, M., Agrillo, C., Avarguès-Weber, A., Bisazza, A., Miletto Petrazzini, M. E., and Giurfa, M. (2019a). Honeybees use absolute rather than relative numerosity in number discrimination. *Biol. Lett.* 15:20190138. doi: 10.1098/rsbl.2019.0138

Bortot, M., Regolin, L., and Vallortigara, G. (2021). A sense of number in invertebrates. *Biochem. Biophys. Res. Commun.* 564, 37–42. doi: 10.1016/j.bbrc.2020.11.039

Bovet, D., and Vauclair, J. (1998). Functional categorization of objects and of their pictures in baboons. *Learn. Motiv.* 29, 309–322. doi: 10.1006/lmot.1998.1009

Bukovac, Z., Dorin, A., and Dyer, A. (2013). A-bees see: a simulation to assess social bee visual attention during complex search tasks. *Artificial Life Conf. Proc.* 13, 276–283.

Burns, J. G., and Dyer, A. G. (2008). Diversity of speed-accuracy strategies benefits social insects. *Curr. Biol.* 18, R953–R954. doi: 10.1016/j.cub.2008.08.028

Carazo, P., Fernández-Perea, R., and Font, E. (2012). Quantity estimation based on numerical cues in the mealworm beetle (*Tenebrio molitor*). *Front. Psychol.* 3:502. doi: 10.3389/fpsyg.2012.00502

Chittka, L., and Geiger, K. (1995). Can honey bees count landmarks? *Anim. Behav.* 49, 159–164. doi: 10.1016/0003-3472(95)80163-4

Chittka, L., Dyer, A. G., Bock, F., and Dornhaus, A. (2003). Psychophysics: bees trade off foraging speed for accuracy. *Nature* 424, 388–388. doi: 10.1038/424388a

Clark, J. M., and Campbell, J. I. (1991). Integrated versus modular theories of number skills and acalculia. *Brain Cogn.* 17, 204–239. doi: 10.1016/0278-2626(91)90075-j

Collett, T., Fry, S., and Wehner, R. (1993). Sequence learning by honeybees. *J. Comp. Physiol. A* 172, 693–706. doi: 10.1016/j.cub.2005.05.033

Cope, A. J., Vasilaki, E., Minors, D., Sabo, C., Marshall, J. A., and Barron, A. B. (2018). Abstract concept learning in a simple neural network inspired by the insect brain. *PLoS Comput. Biol.* 14:e1006435. doi: 10.1371/journal.pcbi.1006435

Cowan, N. (2010). The magical mystery four: how is working memory capacity limited, and why? *Curr. Dir. Psychol. Sci.* 19, 51–57. doi: 10.1177/0963721409359277

Dacke, M., and Srinivasan, M. V. (2008). Evidence for counting in insects. *Anim. Cogn.* 11, 683–689. doi: 10.1007/s10071-008-0159-y

Dastjerdi, M., Ozker, M., Foster, B. L., Rangarajan, V., and Parvizi, J. (2013). Numerical processing in the human parietal cortex during experimental and natural conditions. *Nat. Commun.* 4:2528. doi: 10.1038/ncomms3528

Davis, H., and Pérusse, R. (1988). Numerical competence in animals: definitional issues, current evidence, and a new research agenda. *Behav. Brain Sci.* 11, 561–579. doi: 10.1017/s0140525x00053437

Dehaene, S., and Cohen, L. (1991). Two mental calculation systems: a case study of severe acalculia with preserved approximation. *Neuropsychologia* 29, 1045–1074. doi: 10.1016/0028-3932(91)90076-k

Dehaene, S., Bossini, S., and Giraux, P. (1993). The mental representation of parity and number magnitude. *J. Exp. Psychol.* 122:371. doi: 10.1037/0096-3445.122.3.371

Dehaene, S., Dehaene-Lambertz, G., and Cohen, L. (1998). Abstract representations of numbers in the animal and human brain. *Trends Neurosci.* 21, 355–361. doi: 10.1016/s0166-2236(98)01263-6

Dyer, A. G. (2012). The mysterious cognitive abilities of bees: why models of visual processing need to consider experience and individual differences in animal performance. *J. Exp. Biol.* 215, 387–395. doi: 10.1242/jeb.038190

Dyer, A. G., and Chittka, L. (2004). Bumblebees (*Bombus terrestris*) sacrifice foraging speed to solve difficult colour discrimination tasks. *J. Comp. Physiol. A* 190, 759–763. doi: 10.1007/s00359-004-0547-y

Dyer, A. G., Neumeyer, C., and Chittka, L. (2005). Honeybee (*Apis mellifera*) vision can discriminate between and recognise images of human faces. *J. Exp. Biol.* 208, 4709–4714. doi: 10.1242/jeb.01929

Dyer, A. G., Whitney, H. M., Arnold, S. E., Glover, B. J., and Chittka, L. (2007). Mutations perturbing petal cell shape and anthocyanin synthesis influence bumblebee perception of *Antirrhinum majus* flower colour. *Arthropod Plant Interact.* 1, 45–55. doi: 10.1007/s11829-007-9002-7

Fox, J., and Weisberg, S. (2019). *An R Companion To Applied Regression*. Thousand Oaks, CA: Sage publications.

Freedman, D. J., Riesenhuber, M., Poggio, T., and Miller, E. K. (2001). Categorical representation of visual stimuli in the primate prefrontal cortex. *Science* 291, 312–316. doi: 10.1126/science.291.5502.312

Giurfa, M. (2019). An insect's sense of number. *Trends Cogn. Sci.* 23, 720–722. doi: 10.1016/j.tics.2019.06.010

Giurfa, M., Eichmann, B., and Menzel, R. (1996). Symmetry perception in an insect. *Nature* 382, 458–461. doi: 10.1038/382458a0

Giurfa, M., Zhang, S., Jenett, A., Menzel, R., and Srinivasan, M. V. (2001). The concepts of 'sameness' and 'difference' in an insect. *Nature* 410, 930–933. doi: 10.1038/35073582

Gómez-Laplaza, L. M., and Gerlai, R. (2011). Can angelfish (*Pterophyllum scalare*) count? Discrimination between different shoal sizes follows Weber's law. *Anim. Cogn.* 14, 1–9. doi: 10.1007/s10071-010-0337-6

Gross, H. J., Pahl, M., Si, A., Zhu, H., Tautz, J., and Zhang, S. (2009). Number-based visual generalisation in the honeybee. *PLoS One* 4:e4263. doi: 10.1371/journal.pone.0004263

Hassmann, M. (1952). Vom erlernen unbenannter anzahlen bei eichhörnchen (*Sciurus vulgaris*). *Z. Tierpsychol.* 9, 294–321. doi: 10.1111/j.1439-0310.1952.tb01855.x

Helgadóttir, L. I., Haenicke, J., Landgraf, T., Rojas, R., and Nawrot, M. P. (2013). "Conditioned behavior in a robot controlled by a spiking neural network," in *Proceedings of the 2013 6th International IEEE/EMBS Conference on Neural Engineering (NER)*, (Piscataway, NJ: IEEE), 891–894.

Herrnstein, R. J., and Loveland, D. H. (1964). Complex visual concept in the pigeon. *Science* 146, 549–551. doi: 10.1126/science.146.3643.549

Hertel, H., and Maronde, U. (1987). The physiology and morphology of centrally projecting visual interneurones in the honeybee brain. *J. Exp. Biol.* 133, 301–315. doi: 10.1186/s12868-016-0283-6

Hertel, H., Schäfer, S., and Maronde, U. (1987). The physiology and morphology of visual commissures in the honeybee brain. *J. Exp. Biol.* 133, 283–300. doi: 10.1002/cne.902460302

Hines, T. M. (1990). An odd effect: lengthened reaction times for judgments about odd digits. *Mem. Cogn.* 18, 40–46. doi: 10.3758/bf03202644

Howard, S. R., Avarguès-Weber, A., Garcia, J. E., Greentree, A. D., and Dyer, A. G. (2018a). Numerical ordering of zero in honey bees. *Science* 360, 1124–1126. doi: 10.1126/science.aar4975

Howard, S. R., Garcia, J., and Dyer, A. (2018b). Chasing the meaning of zero. *Australasian Sci.* 39:20.

Howard, S. R., Avarguès-Weber, A., Garcia, J. E., Greentree, A. D., and Dyer, A. G. (2019c). Surpassing the subitizing threshold: appetitive–aversive conditioning improves discrimination of numerosities in honeybees. *J. Exp. Biol.* 222:jeb205658. doi: 10.1242/jeb.205658

Howard, S. R., Avarguès-Weber, A., Garcia, J. E., Greentree, A. D., and Dyer, A. G. (2019b). Numerical cognition in honeybees enables addition and subtraction. *Sci. Adv.* 5:easv0961. doi: 10.1126/sciadv.aav0961

Howard, S. R., Avarguès-Weber, A., Garcia, J. E., Greentree, A. D., and Dyer, A. G. (2019a). Achieving arithmetic learning in honeybees and examining how individuals learn. *Commun. Integr. Biol.* 12, 166–170. doi: 10.1080/19420889.2019.1678452

Howard, S. R., Avarguès-Weber, A., Garcia, J. E., Greentree, A. D., and Dyer, A. G. (2019d). Symbolic representation of numerosity by honeybees (*Apis mellifera*): matching characters to small quantities. *Proc. R. Soc. B* 286:20190238. doi: 10.1098/rspb.2019.0238

Howard, S. R., Schramme, J., Garcia, J. E., Ng, L., Avarguès-Weber, A., Greentree, A. D., et al. (2020a). Spontaneous quantity discrimination of artificial flowers by foraging honeybees. *J. Exp. Biol.* 223:jeb223610. doi: 10.1242/jeb.223610

Howard, S. R., Avarguès-Weber, A., Garcia, J. E., Greentree, A. D., and Dyer, A. G. (2020b). Reply to comment on Howard et al. (2019): 'Nothing to dance about: unclear evidence for symbolic representations and numerical competence in honeybees'. *Proc. R. Soc. B* 287:20200095. doi: 10.1098/rspb.2020.0095

Howard, S. R., Avarguès-Weber, A., Garcia, J., and Dyer, A. G. (2017a). Free-flying honeybees extrapolate relational size rules to sort successively visited artificial flowers in a realistic foraging situation. *Anim. Cogn.* 20, 627–638. doi: 10.1007/s10071-017-1086-6

Howard, S. R., Avarguès-Weber, A., Garcia, J. E., Stuart-Fox, D., and Dyer, A. G. (2017b). Perception of contextual size illusions by honeybees in restricted and unrestricted viewing conditions. *Proc. R. Soc. B* 284:20172278. doi: 10.1098/rspb.2017.2278

Hubbard, E. M., Piazza, M., Pinel, P., and Dehaene, S. (2005). Interactions between number and space in parietal cortex. *Nat. Rev. Neurosci.* 6:435. doi: 10.1038/nrn1684

Jevons, W. S. (1871). The power of numerical discrimination. *Nature* 3, 281–282. doi: 10.1038/003281a0

Kaufman, E. L., Lord, M. W., Reese, T. W., and Volkmann, J. (1949). The discrimination of visual number. *Am. J. Psychol.* 62, 498–525.

Kleyko, D., Osipov, E., Gayler, R. W., Khan, A. I., and Dyer, A. G. (2015). Imitation of honey bees' concept learning processes using Vector Symbolic Architectures. *Biol. Inspired Cogn. Architectures* 14, 57–72. doi: 10.1016/j.bica.2015.09.002

Krueger, L. E. (1986). Why $2 \times 2 = 5$ looks so wrong: on the odd-even rule in product verification. *Mem. Cogn.* 14, 141–149. doi: 10.3758/bf03198374

Krueger, L. E., and Hallford, E. W. (1984). Why 2+ 2= 5 looks so wrong: on the odd-even rule in sum verification. *Mem. Cogn.* 12, 171–180. doi: 10.3758/bf03198431

MaBouDi, H., Barron, A. B., Li, S., Honkanen, M., Loukola, O. J., Peng, F., et al. (2021). Non-numerical strategies used by bees to solve numerical cognition tasks. *Proc. R. Soc. B* 288, 20202711. doi: 10.1098/rspb.2020.2711

MaBouDi, H., Galpayage Dona, H. S., Gatto, E., Loukola, O. J., Buckley, E., Onoufriou, P. D., et al. (2020). Bumblebees use sequential scanning of countable items in visual patterns to solve numerosity tasks. *Integr. Comp. Biol.* 60, 929–942. doi: 10.1093/icb/icaa025

Menzel, R. (1973). Spectral response of moving detecting and "sustaining" fibres in the optic lobe of the bee. *J. Comp. Physiol.* 82, 135–150. doi: 10.1007/bf00696149

Merolla, P. A., Arthur, J. V., Alvarez-Icaza, R., Cassidy, A. S., Sawada, J., Akopyan, F., et al. (2014). A million spiking-neuron integrated circuit with a scalable communication network and interface. *Science* 345, 668–673. doi: 10.1126/science.1254642

Miller, G. A. (1956). The magical number seven, plus or minus two: some limits on our capacity for processing information. *Psychol. Rev.* 63:81. doi: 10.1037/h0043158

Morawetz, L., Svoboda, A., Spaethe, J., and Dyer, A. G. (2013). Blue colour preference in honeybees distracts visual attention for learning closed shapes. *J. Comp. Physiol. A* 199, 817–827. doi: 10.1007/s00359-013-0843-5

Nieder, A. (2005). Counting on neurons: the neurobiology of numerical competence. *Nat. Rev. Neurosci.* 6, 177–190. doi: 10.1038/nrn1626

Niven, J. E., Anderson, J. C., and Laughlin, S. B. (2007). Fly photoreceptors demonstrate energy-information trade-offs in neural coding. *PLoS Biol.* 5:e116. doi: 10.1371/journal.pbio.0050116

Nuerk, H. C., Iversen, W., and Willmes, K. (2004). Notational modulation of the SNARC and the MARC (linguistic markedness of response codes) effect. *Q. J. Exp. Psychol. Sec. A* 57, 835–863. doi: 10.1080/02724980343000512

Nuerk, H.-C., Wood, G., and Willmes, K. (2005). The universal SNARC effect: the association between number magnitude and space is amodal. *Exp. Psychol.* 52, 187–194. doi: 10.1027/1618-3169.52.3.187

Pachella, R. G., and Fisher, D. F. (1969). Effect of stimulus degradation and similarity on the trade-off between speed and accuracy in absolute judgments. *J. Exp. Psychol.* 81:7. doi: 10.1037/h0027431

Paulk, A. C., Phillips-Portillo, J., Dacks, A. M., Fellous, J. M., and Gronenberg, W. (2008). The processing of color, motion, and stimulus timing are anatomically segregated in the bumblebee brain. *J. Neurosci.* 28, 6319–6332. doi: 10.1523/JNEUROSCI.1196-08.2008

Peelen, M. V., Fei-Fei, L., and Kastner, S. (2009). Neural mechanisms of rapid natural scene categorization in human visual cortex. *Nature* 460:94. doi: 10.1038/nature08103

Perry, C. J., and Barron, A. B. (2013). Honey bees selectively avoid difficult choices. *Proc. Natl. Acad. Sci. U.S.A.* 110, 19155–19159. doi: 10.1073/pnas.1314571110

Piazza, M., Mechelli, A., Butterworth, B., and Price, C. J. (2002). Are subitizing and counting implemented as separate or functionally overlapping processes? *Neuroimage* 15, 435–446. doi: 10.1006/nimg.2001.0980

Piazza, M., Pinel, P., Le Bihan, D., and Dehaene, S. (2007). A magnitude code common to numerosities and number symbols in human intraparietal cortex. *Neuron* 53, 293–305. doi: 10.1016/j.neuron.2006.11.022

R Core Team (2020). *R: A Language And Environment For Statistical Computing*. Vienna: R Foundation for Statistical Computing.

Reynvoet, B., and Brysbaert, M. (1999). Single-digit and two-digit Arabic numerals address the same semantic number line. *Cognition* 72, 191–201. doi: 10.1016/s0010-0277(99)00048-7

Rugani, R., Cavazzana, A., Vallortigara, G., and Regolin, L. (2013). One, two, three, four, or is there something more? Numerical discrimination in day-old domestic chicks. *Anim. Cogn.* 16, 557–564. doi: 10.1007/s10071-012-0593-8

Saaty, T. L., and Ozdemir, M. S. (2003). Why the magic number seven plus or minus two. *Math. Comput. Modelling* 38, 233–244. doi: 10.1016/s0895-7177(03)90083-5

Sandin, F., Khan, A. I., Dyer, A. G., Amin, A. H. M., Indiveri, G., Chicca, E., et al. (2014). Concept learning in neuromorphic vision systems: What can we learn from insects? *J. Softw. Eng. Appl.* 7, 387–395. doi: 10.4236/jsea.2014.75035

Seguin, D., and Gerlai, R. (2017). Zebrafish prefer larger to smaller shoals: analysis of quantity estimation in a genetically tractable model organism. *Anim. Cogn.* 20, 813–821. doi: 10.1007/s10071-017-1102-x

Shaki, S., and Fischer, M. H. (2020). Nothing to dance about: unclear evidence for symbolic representations and numerical competence in honeybees. a comment on: symbolic representation of numerosity by honeybees (*Apis mellifera*): matching characters to small quantities. *Proc. R. Soc. B* 287:20192840. doi: 10.1098/rspb.2019.2840

Simons, D., and Langheinrich, D. (1982). What is magic about the magical number four? *Psychol. Res.* 44, 283–294. doi: 10.2466/pms.2000.91.3.883

Sokal, R. R., and Rohlf, F. J. (1981). *Biometry*. San Francisco, CA: WH Freeman and Company.

Spaethe, J., Tautz, J., and Chittka, L. (2001). Visual constraints in foraging bumblebees: flower size and color affect search time and flight behavior. *Proc. Natl. Acad. Sci. U.S.A.* 98, 3898–3903. doi: 10.1073/pnas.071053098

Srinivasan, M. V. (2006). Small brains, smart computations: vision and navigation in honeybees, and applications to robotics. *Int. Congress Ser.* 1291, 30–37. doi: 10.1016/j.ics.2006.01.055

Srinivasan, M. V. (2010). Honey bees as a model for vision, perception, and cognition. *Annu. Rev. Entomol.* 55, 267–284. doi: 10.1146/annurev.ento.010908.164537

Srinivasan, M. V. (2011). Visual control of navigation in insects and its relevance for robotics. *Curr. Opin. Neurobiol.* 21, 535–543. doi: 10.1016/j.conb.2011.05.020

Srinivasan, M. V., Chahl, J. S., Weber, K., Venkatesh, S., Nagle, M. G., and Zhang, S.-W. (1999). Robot navigation inspired by principles of insect vision. *Robotics Autonomous Syst.* 26, 203–216. doi: 10.1016/s0921-8890(98)00069-4

Srinivasan, M. V., Zhang, S. W., and Rolfe, B. (1993). Is pattern vision in insects mediated by 'cortical' processing? *Nature* 362, 539–540. doi: 10.1038/362539a0

Tang, Y., Zhang, W., Chen, K., Feng, S., Ji, Y., Shen, J., et al. (2006). Arithmetic processing in the brain shaped by cultures. *Proc. Natl. Acad. Sci. U.S.A.* 103, 10775–10780. doi: 10.1073/pnas.0604416103

Tomonaga, M., and Matsuzawa, T. (2002). Enumeration of briefly presented items by the chimpanzee (*Pan troglodytes*) and humans (*Homo sapiens*). *Anim. Learn. Behav.* 30, 143–157. doi: 10.3758/bf03192916

Trick, L. M., and Pylyshyn, Z. W. (1994). Why are small and large numbers enumerated differently? A limited-capacity preattentive stage in vision. *Psychol. Rev.* 101:80. doi: 10.1037/0033-295x.101.1.80

Troje, N. F., Huber, L., Loidolt, M., Aust, U., and Fieder, M. (1999). Categorical learning in pigeons: the role of texture and shape in complex static stimuli. *Vis. Res.* 39, 353–366. doi: 10.1016/s0042-6989(98)00153-9

Vasas, V., and Chittka, L. (2019). Insect-inspired sequential inspection strategy enables an artificial network of four neurons to estimate numerosity. *IScience* 11, 85–92. doi: 10.1016/j.isci.2018.12.009

Venables, W. N., and Ripley, B. D. (2002). *Modern Applied Statistics with S*. New York, NY: Springer.

Wilcox, R. R. (2011). *Introduction To Robust Estimation And Hypothesis Testing*. Cambridge, MA: Academic Press.

Yang, E. C., and Maddess, T. (1997). Orientation-sensitive neurons in the brain of the honey bee (*Apis mellifera*). *J. Insect Physiol.* 43, 329–336. doi: 10.1016/s0022-1910(96)00111-4

Zentall, T. R., Galizio, M., and Critchfield, T. S. (2002). Categorization, concept learning, and behavior analysis: an introduction. *J. Exp. Anal. Behav.* 78, 237–248. doi: 10.1901/jeab.2002.78-237

Zhang, S. (2006). Learning of abstract concepts and rules by the honeybee. *Int. J. Comp. Psychol.* 19, 318–341.

Zhang, S. W., and Srinivasan, M. V. (2004). "Exploration of cognitive capacity in honeybees: higher functions emerge from a small brain," in *Complex Worlds From Simpler Nervous Systems*, ed. F. R. Prete (Cambridge, MA: MIT Press), 41–74.

Zhang, S., Bartsch, K., and Srinivasan, M. (1996). Maze learning by honeybees. *Neurobiol. Learn. Mem.* 66, 267–282. doi: 10.1006/nlme.1996.0069

Zhang, S., Mizutani, A., and Srinivasan, M. V. (2000). Maze navigation by honeybees: learning path regularity. *Learn. Mem.* 7, 363–374. doi: 10.1101/lm.32900

Zhang, S., Srinivasan, M. V., Zhu, H., and Wong, J. (2004). Grouping of visual objects by honeybees. *J. Exp. Biol.* 207, 3289–3298. doi: 10.1242/jeb.01155

Zuur, A. F., Hilbe, J. M., and Ieno, E. N. (2013). *A Beginner's Guide to GLM and GLMM with R: A Frequentist and Bayesian Perspective for Ecologists*. Newburgh, NY: Highland Statistics Limited.

Conflict of Interest: The authors declare that the research was conducted in the absence of any commercial or financial relationships that could be construed as a potential conflict of interest.

frontiers | Frontiers in Bioengineering and Biotechnology

ORIGINAL RESEARCH
published: 18 May 2022
doi: 10.3389/fbioe.2022.787220

Aerodynamic Performance of a Dragonfly-Inspired Tandem Wing System for a Biomimetic Micro Air Vehicle

Erfan Salami[1]*, *Elham Montazer*[2], *Thomas A Ward*[3], *Nik Nazri Nik Ghazali*[1]* and *Irfan Anjum Badruddin*[4,5]

[1]Department of Mechanical Engineering, Faculty of Engineering, University of Malaya, Kuala Lumpur, Malaysia, [2]Department of Mechanical Engineering, Sharif University of Technology, Tehran, Iran, [3]School of Engineering and Computer Science, Cedarville University, Cedarville, OH, United States, [4]Research Center for Advanced Materials Science (RCAMS), King Khalid University, Abha, Saudi Arabia, [5]Department of Mechanical Engineering, College of Engineering, King Khalid University, Abha, Saudi Arabia

The flying agility demonstrated by dragonflies is accomplished by means of complex aerodynamic forces produced by flapping their four wings arranged in a tandem configuration. The current study presents a novel tandem flapping wing mechanism for a biomimetic air vehicle that was designed and manufactured to experimentally investigate the aerodynamic forces. By optimizing the configuration and using spatial network analysis, it is shown that the designed structure can flap the wings in a linear up–down stroke motion and is capable of maintaining good consistency and aerodynamic performance. Such a mechanism could be used in a future biomimetic micro air vehicle (BMAV) design. The mechanism uses an electromagnetic actuator to flap the wings with a variable beat frequency (30–210 Hz) at various angles of attack (−10°–20°). The results show that the tandem wings generate approximately 50% higher lift than the forewing or hindwing pairs acting alone. Tandem wings also improve stability, which could potentially allow hovering.

Keywords: bioinspired, dragonfly, unsteady aerodynamics, biomimetic micro air vehicle, tandem flapping wings

OPEN ACCESS

Edited by:
Devi Stuart-Fox,
The University of Melbourne, Australia

Reviewed by:
Dengteng Ge,
Donghua University, China
Cecilia Laschi,
National University of Singapore, Singapore

***Correspondence:**
Erfan Salami
erfansalami@hotmail.com
Nik Nazri Nik Ghazali
nik_nazri@um.edu.my

Specialty section:
This article was submitted to Bionics and Biomimetics, a section of the journal Frontiers in Bioengineering and Biotechnology

Received: *30 September 2021*
Accepted: *04 March 2022*
Published: *18 May 2022*

Citation:
Salami E, Montazer E, Ward TA, Nik Ghazali NN and Anjum Badruddin I (2022) Aerodynamic Performance of a Dragonfly-Inspired Tandem Wing System for a Biomimetic Micro Air Vehicle. Front. Bioeng. Biotechnol. 10:787220. doi: 10.3389/fbioe.2022.787220

INTRODUCTION

Biomimetic micro air vehicles (BMAVs) are a group of microsized, unmanned aircraft that are bioinspired by the flapping wing motion of flying small birds or insects. Their microscaled size and ultra-light weight nature allow them to potentially fly inside buildings or compact spaces, making them the ideal urban drone. They can be used for remote surveillance of hazardous sites such as chemical spills, radiation leaks, high-voltage areas, active crime scenes, or other dangerous areas.

In order to understand the interest in BMAVs, it helps in having a better understanding of their aerodynamics (Salami et al., 2019). Insects use many unsteady and complex wing motions to generate lift. Ansari et al. were able to create models for the figure-of-eight motion that accounts for both the steady-state lift and unsteady lift component. The latter was broken down into leading-edge vortex (LEV) and trailing-edge wake (Ansari et al., 2006a; Ansari et al., 2006b). There are many types of lifts that insects use that can be mimicked by BMAVs (Li et al., 2021).

Dragonflies are quick flyers (Salami et al., 2016; Salami et al., 2017; Sivasankaran et al., 2017) that can change course quickly and move in a different direction. They can rapidly speed up from a hover

and vice versa. They have a high power-to-weight ratio because of the low aspect ratio of their wings. Rotating wings about several axes is another ability of dragonflies. This makes them among the quickest and most agile flying insects in the world (Li et al., 2018). The complex structure of dragonfly wings plays the main role in this capability (Rubentheren et al., 2016; Zhang et al., 2018; Salami et al., 2020).

Numerous scientists have studied the aerodynamics produced by various wing beat frequencies, wing motions, or interactions between the wings of dragonflies since they are very common and distributed almost around the world. Several studies have looked at the effects of subtle wing structural modifications on aerodynamics. The aforementioned topics are crucial in grasping when applying these features to future BMAV developments.

Flight with microscaled wing surface areas is possible because of the additional lift gained by flapping the wings. Lift and thrust are achieved due to vorticities generated by this flapping wing motion. One of the first types of flapping wing motion studied is clap-and-fling kinematics. These kinematics studies are typical of butterflies and hummingbirds (Weis-Fogh, 1972). Lift is generated as a wing pair flap and comes together at the end of a half stroke (clap) and then flings apart (similar to quickly flinging a hard-bound book open and closed) (Weis-Fogh, 1973). This motion generates a bound vortex on each wing that plays as the initial vortex of the opposite wing.

While the clap-and-fling was the first unsteady aerodynamic lift motion to be well-understood, further work by Lighthill, Maxworthy, and Ellington built upon this early study of insect flight (Lighthill, 1973; Maxworthy, 1979; Ellington, 1984). Ellington et al. discovered a wing motion known as the LEV (Ellington et al., 1996). Lift is generated by vortices attached to the wing as the wing pitches to an angle of attack (AOA) beyond the stall angle (for a conventional airfoil). This was further verified and quantified by several aerodynamicists by computational fluid dynamics (CFD) studies (Liu et al., 1998; Lan and Sun, 2001; Sun and Tang, 2002). Dickinson called the LEV generated by a translating wing "delayed stall" (Truong et al., 2011). Dickenson used a reduced order model to determine the role of the LEV and other wing kinematics in the total lift. By placing a large aphid wing model with six computer-controlled stepper motors used to flap the wing in mineral oil, it could be determined how the lift was generated by different wing motions (Dickinson et al., 1999). It was concluded that the primary contributor to the lift during hover is LEV-generated, but it was also found that more than 35% of the total lift generated was due to rotational effects (Dickinson et al., 1999).

Another significant component of the lift noted was wake capture. Wake capture is the lift generated when the wing changes direction and utilizes the wake from the previous flapping half stroke to generate lift. This is similar to the lift generated when an aircraft takes off into the wind, utilizing the flow of the wind over the wing to generate additional lift. Sun and Tang verified the additional lift generated at the end of each half stroke and the beginning of the next half stroke using CFD but offered different explanations for their occurrence (Sun and Tang, 2002).

Walker explained that since the Magnus force is independent of AOA and the rotational moment, it could not be the force Dickinson described (Walker, 2002). Walker also made a strong case for the inclusion of wake capture. After this, Dickinson stopped describing this as a Magnus force–like effect, revising his terminology to name it "rotational circulation" (Sane and Dickinson, 2002). More current research studies have identified the following sources of insect unsteady aerodynamic lift: clap-and-fling, LEV or delayed stall, added mass inertia (rotational inertia), rotational circulation, and wake capture (Sun and Xiong, 2005; Truong et al., 2011). Of these, added mass inertia is small and usually included as part of the rotational circulation and clap-and-fling is used by only a few flying insects or birds (Karásek, 2014). This leaves LEV, rotational circulation, and wake capture as the primary types of unsteady aerodynamic lift.

Early benchtop mechanisms focused on generating appropriate flight kinematics by flapping the wings in a figure-of-eight flapping translational motion while also variably rotating (or pitching) the wings (Conn et al., 2007; Galiński and Żbikowski, 2007). Many mechanisms were used to validate aerodynamic models of lift generation (Dickson and Dickinson, 2004; Galiński and Żbikowski, 2005). Based upon the hover model, turning using aerodynamic damping has also been studied (Cheng and Deng, 2011). Still, others have focused on generating flapping flight, but most of these BMAVs use a sail-like membrane to generate lift, which undulates rather than truly flaps (De Croon et al., 2009; Tsai and Fu, 2009; Hsu et al., 2010).

The wing structure is also very important. Wings must be able to manage the forces generated by flapping while remaining ultra-lightweight (Sivasankaran et al., 2016). The wings must be fabricated from advanced lightweight materials. Wings using chitin nanocomposite films, bioinspired from insect wing membranes, can be used to reduce the overall weight (Rubentheren et al., 2016).

Bomphrey and Nakata (Bomphrey et al., 2016) studied the aerodynamic performance of real dragonfly wings and its comparison with artificial wings by providing detailed 3D wing geometries of dragonflies and performing CFD and PIV analysis. They performed simulations at various speeds and angles of attack. They reported that the forewing sits in a region of positive pressure generated by the hindwing and, therefore, experiences reduced drag; conversely, the hindwing suffers higher drag owing to the forewing.

Accordingly, the aerodynamics comparison study among the selected BMAV wing configuration is still lacking. Therefore, the overall purpose of the present investigation is to compare the aerodynamic performances (lift, drag, and lift-to-drag ratio) between the symmetrical BMAV forewing, hindwing, and tandem wings at various wing beat frequencies and angles of attacks. Based on the experimental force measurements and high-speed imaging, the impact of wing configuration on the aerodynamic performance of the BMAV flapping flight is explained in the *Discussion*. In the time domain where cyclic averaging is being used to enhance the force profile, the stronger force peaks occur when the wing is generating lift at specific points during the flapping. Finally, the aerodynamic performance results obtained in this study are validated by real dragonfly data benchmarks taken from Bomphrey and Nakata (Bomphrey et al., 2016). Since future operational BMAV will likely be disposable due to their utility in conducting one-way missions into

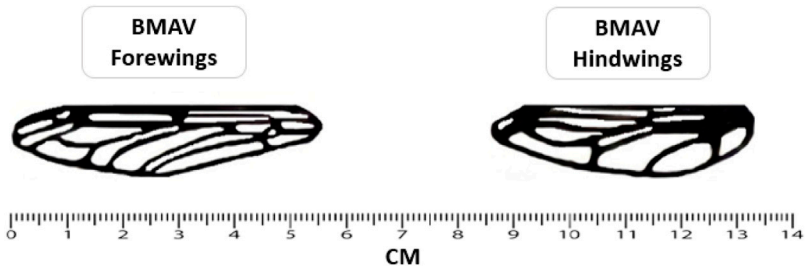

FIGURE 1 | Fabricated wings utilized in the present study.

TABLE 1 | BMAV wing structure specification.

Specification	Forewing	Hindwing
Base width	7.00 mm	8.5 mm
Center width	12.50 mm	14.4 mm
Tip width	7.23 mm	8.5 mm
Length	56.00 mm	48.00 mm
Mass	0.12 g	0.08 g

hazardous environments, minimizing cost and fabrication time is important. Therefore, utilizing lightweight disposable 3D printed plastic construction is a secondary goal of this research.

AERODYNAMIC MODEL

BMAV Wing

Since it is very complicated and expensive to manufacture the complex microstructures of a real dragonfly wing, the created wings are simplified duplications of the real wing set. The spatial network analysis technique has been used to perform the simplification. This method has performed the segmentation based on the pattern density value in order to bio-mimic the real dragonfly wing (Sivasankaran et al., 2016). An initial wire frame, 2D scaled model, was manufactured utilizing SolidWorks to build a 3D solid model by extruding the imported 2D wire frame.

The experimental results of the authors' previous research (Salami et al., 2020) regarding the nanomechanical properties of various BMAV wing materials demonstrated that the HIPS (high-impact polystyrene) and Ultrat fabricated wings approximately resembled a real dragonfly's nanoindentation results. While fabricating the BMAV with a 3D printer, it was found that HIPS had better final finishing and it is easier to take a more consistent melting temperature using the MakerBot machine. Accordingly, HIPS was chosen to fabricate the BMAV wings for the present study.

A synthesized, thin-film, nanocomposite membrane was then laid down over the wing frames. **Figure 1** and **Table 1** show the final BMAV fabricated wings and wing structure specifications.

Once the wing structure was printed out, the exposed top surface layer required sanding to remove the jagged material

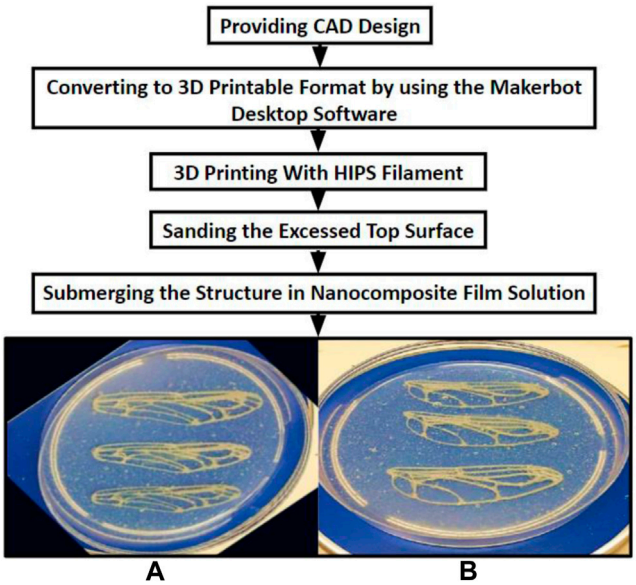

FIGURE 2 | Design process: **(A)** Forewing, **(B)** Hindwing.

remains on the structure. The structures were then submerged in the selected chitosan nanocomposite film solution in a petri dish, as illustrated in **Figure 2**. The chitosan nanocomposite suspension constituted a chitosan suspension reinforced with nanosized whiskers and crosslinked using tannic acid. The suspension was transformed into a thin 3-mm film using the casting evaporation method. A drying time of 48 h was required.

Flapping Mechanism and Experimental Setup

An electromagnetic flapping wing actuator has been utilized as a wing flapping mechanism in the current study. The power supply applied in this flapping wing mechanism was 12 V DC. For having a stable oscillation, an LM555 crystal clock oscillator integrated circuit, which has been displayed in **Figure 3**, was utilized. A capacitor and two resistors were used to accurately control the free-running frequency and

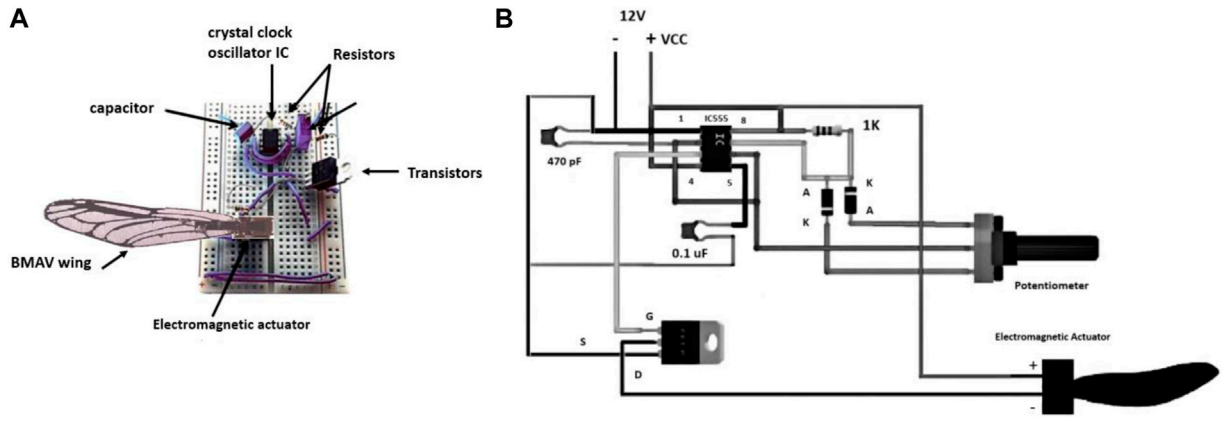

FIGURE 3 | Flapping mechanism: **(A)** Actual setup, **(B)** Electronic overview diagram.

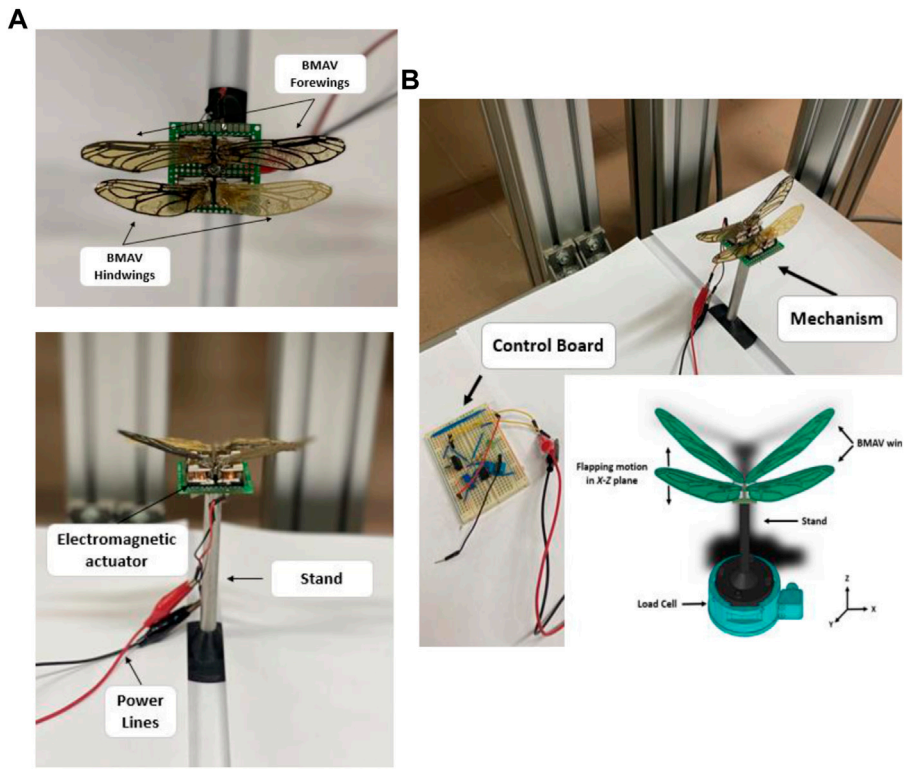

FIGURE 4 | (A) Wings and actuator formation, **(B)** Experimental setup.

duty cycle. The generated oscillation was fed to a Power MOSFET fast switch. The output of the Power MOSFET was utilized to actuate the miniature PC Board Relay. The frequency of the switch (corresponding to the wing beat frequency) can be adjusted by a 22-k potentiometer. A superglue was used to attach each of the BMAV wings to a flat iron plate (2 mm long and 2.75 mm thick) using. The iron plate was oscillated by an electromagnetic actuator (3–3 mm).

Figure 3 displays the flapping mechanism setup and electrical diagram of a wing structure attached to the actuator. For mimicking the joint of the real dragonfly, the plate was attached to the hinge of the BMAV wing. This flapping mechanism can make a linear up–down stroke motion at different wing beat frequencies, up to a maximum frequency of 250 Hz. Based on the real dragonfly wing flapping angle during hovering flight, the flapping degree was fixed to be 90°.

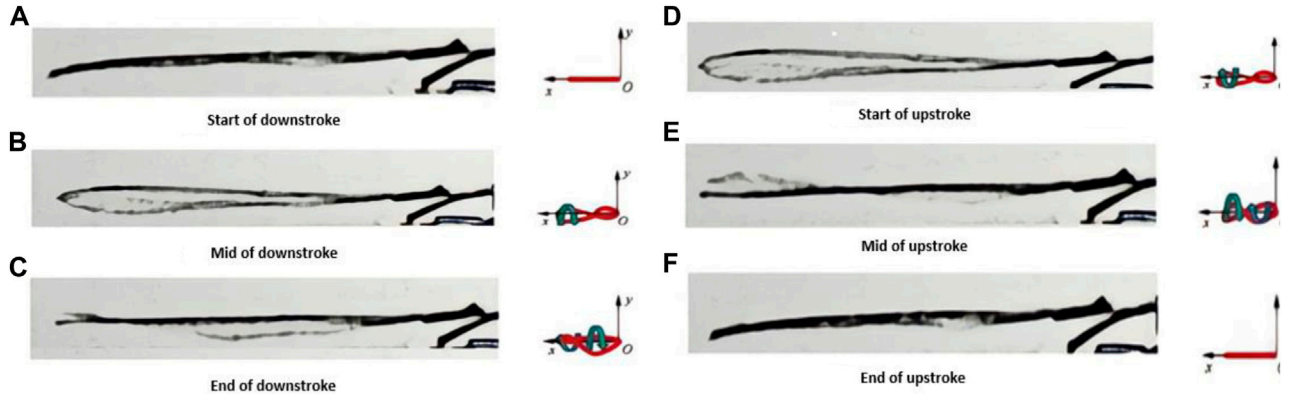

FIGURE 5 | Side view of the flapping wing captured by high speed camera during one flapping cycle at 30 Hz **(A)** Start of downstroke, **(B)** Mid of downstroke, **(C)** End of downstroke, **(D)** Start of upstroke, **(E)** Mid of upstroke, **(F)** End of upstroke.

BMAV FLAPPING AERODYNAMICS

Testing of the electromagnetic flapping mechanism was broken down into experiments and time-frequency domain analysis of the experimental data using cyclic averaging and fast Fourier transform (FFT). The frequency was varied by adjusting a power output voltage over the test run. Force data samples were collected at each frequency. Force data points were averaged to a single point. The only way to adjust the wing beat frequency was the DC voltage applied to the actuators. The wing beat frequency was then changed by adjusting the voltage applied by the power supply.

As **Figure 4** displays, to measure the forces, the electromagnetic mechanism was placed on a test stand attached to an ATI Gamma six-axis force/torque sensor. The FFT low-pass filter was used to filter the raw data which were obtained by the sensor. The net aerodynamic force was finally achieved by deducting the gravitational and inertial forces obtained in air from the total forces measured.

The *z*-axis force data (lift) and the *y*-axis force data (drag) are of primary importance and are looked upon for further analysis and understanding of the flapping mechanism. Torque data were deemed to add no additional information than that available from the force data. The torque data were useful early on in making sure that the sensor was aligned properly. Short duration data collection runs were used because of the large amount of data being collected. Each force data point plotted was the average of 10,000 samples over 10 s. Each test run was conducted over multiple frequencies to make a plot. Each experiment included five test runs.

The frequency is consistently monitored directly from the control board during the experiment as the digital output is directly proportional to the supplied voltage. The secondary method of calculating the flapping frequency from the high-speed camera data through its slow-motion capability and using a timer gives another way to verify the flapping frequency, as shown in **Figure 5**. The voltage supplied to the control board is directly proportional to the flapping frequency, and if the voltage is constant, the flapping frequency is also constant. So, if the digital readout stays constant, the flapping frequency is held constant. This also means that the more power (related to the voltage by $P = V^2/R$) delivered to the motor, the faster it flaps. The frequency can be increased proportionately by increasing the digital readout from one data collection to the next.

From a frequency-domain perspective, there will be peaks in the spectrum at each flapping wing cycle. The more consistent the flapping rate, the stronger the peak at that flapping rate or frequency. In the time domain where cyclic averaging is used to enhance the force profile, the stronger force peaks occur when the wing generates lift at specific points during flapping.

Since the data repeat at regular flapping intervals, the cyclical points of interest become more pronounced through cyclic averaging over multiple flapping periods, while more random data should be less pronounced. This means the vibrational noise data are random and can be reduced through averaging.

According to Dickinson, a baseline for the LEV effects could be generated. It became apparent that there were significant effects at the beginning and end of the stroke for which there explanations were needed. The peak at the beginning of the flapping wing half stroke is considered to be due to wake capture. The LEV is the greatest contributor to lift and wake capture, producing significant portions of the additional lift. **Figure 6** illustrates the averaged lift data for different periods of flapping cycles. There are also cyclical anomalies (vibrations) related to the flapping frequency that will become more pronounced and visible, especially as the frequency increases. Vibration anomalies can be seen in **Figure 6**, the smaller peaks in between LEV and wake capture peaks that are pointed by arrows. Reviewing the high-speed camera data shows that these readings are due to the wing going through mechanical oscillations.

The valley in between the two peaks that is pointed to by the arrows is the wing reversal for each half stroke, and the data between wake capture peaks in **Figure 6** have a positive average and correspond to the lift from the LEV. The first peak in each wing flapping cycle is due to stroke reversal, and the peak at the end of each cycle is due to wake capture. The data represent two forewings flapping symmetrically at a frequency of 30 Hz, which relates to a period of 0.03 s. The lift profiles show that the lift generated has components of both wake capture and LEV.

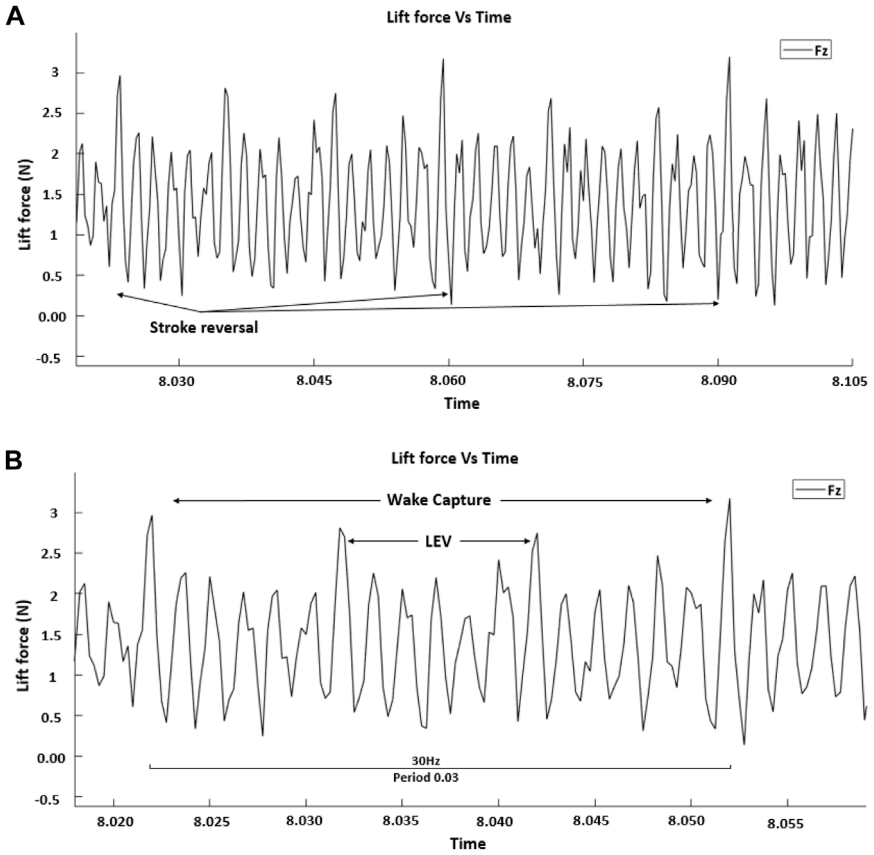

FIGURE 6 | Cyclic averaged data showing **(A)** multi periods and **(B)** a single period.

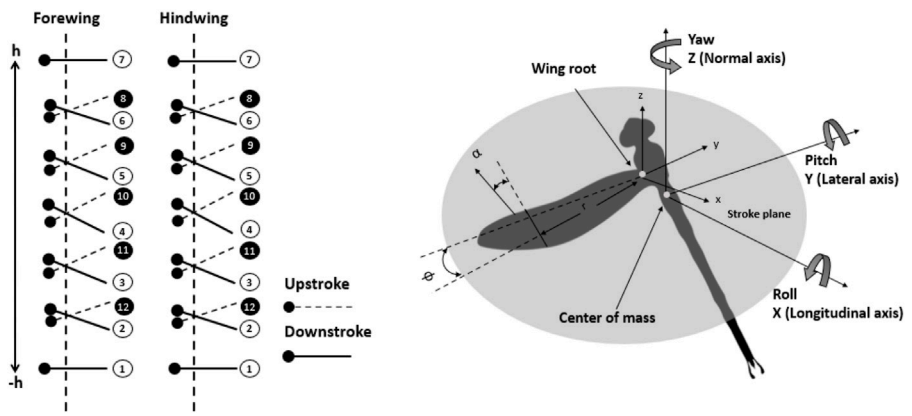

FIGURE 7 | Time history position and angles of attack of both forewing and hindwing trajectories at zero phase differences.

AERODYNAMICS PERFORMANCE

The experimental parameters are set on the basis of a comparison of the results obtained from previous researchers and the limitations of the experimental setup. The BMAV flight has been influenced by AOA, wing beat frequency, Reynolds number, and freestream velocity.

The aerodynamic forces and aerodynamics performance were evaluated for the flapping wing configuration from −10° to 20° AOA at various wing beat frequency ranges from 30 to 210 Hz. The chord Reynolds case relating to Rec = 0 was chosen to be the static case which means no incoming freestream velocity. Each test was repeated five times, and the results are the average

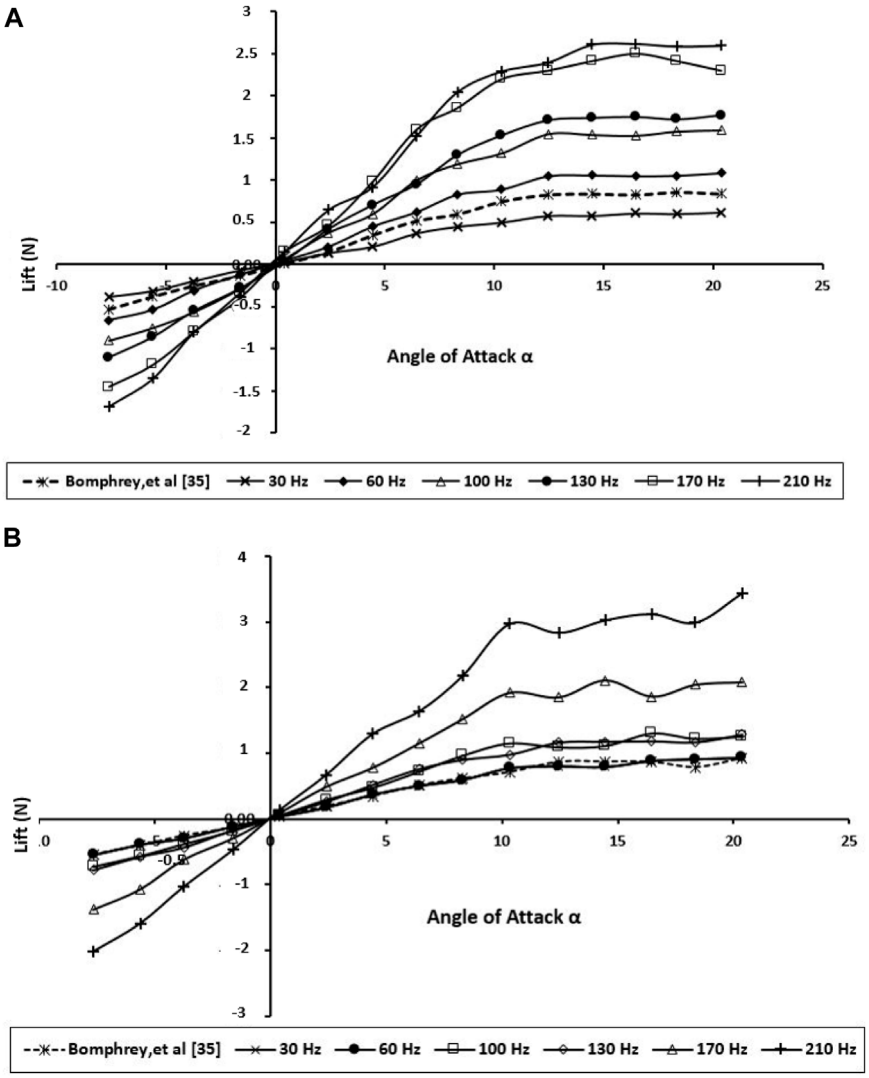

FIGURE 8 | Generated lift for the BMAV's wing at various angles of attack and wing beat frequencies; **(A)** forewing; **(B)** hindwing.

amounts of these five trials. The best way to adjust the wing beat frequency was the DC voltage applied to the actuators. The wing beat frequency was then varied by changing the voltage applied by the power supply. The voltage was increased by increments of 1.0 V from 5 to 12 V. Since the relationship between the wing beat frequency and corresponding applied voltage from the power supply is linear, the frequency changes slightly.

Figure 7 shows the time histories of the positions and angles of attack of both wings. The rotational axis was at the quarter chord from the leading edge of the wing model. The distance between the two wings was fixed at 1.5 chord length of the forewing, which has been demonstrated to be fitting (Maybury and Lehmann, 2004; Bomphrey et al., 2016). The dragonflies had been recorded by Wakeling and Ellington (Wakeling and Ellington, 1997) to examine their kinematics. They investigated that the average stroke of wing beat was around 90°. The average stroke amplitude can be predicted utilizing the stroke amplitude at midspan position $\frac{L}{2}\sin 45°$ as in flapping flight, where L is the wing length. In plunging movement, we selected the average stroke amplitude in flapping flight as our plunging amplitude. Consequently, $h = \frac{L_{fore}}{2}\sin 45°$ was set based on the length of forewing L_{fore}. The pitch amplitude was set at 30° according to the kinematics measured on the actual dragonflies by Chen et al. (Chen et al., 2013).

The aerodynamic performance of the dragonfly wings was examined experimentally by calculating the lift and drag forces for various angles of attacks and various wing beat frequencies as shown in **Figures 8**, **9**, respectively. More pressure differences in the surface of the dragonfly wing had been generated by higher AOA. Consequently, the lift increases with the angle of attack. In addition, for the positive AOA, the drag increases with the angle of attack. As shown in **Figures 8**, **9**, the current study's results are in good agreement with those of Bomphrey and Nakata (Bomphrey et al., 2016).

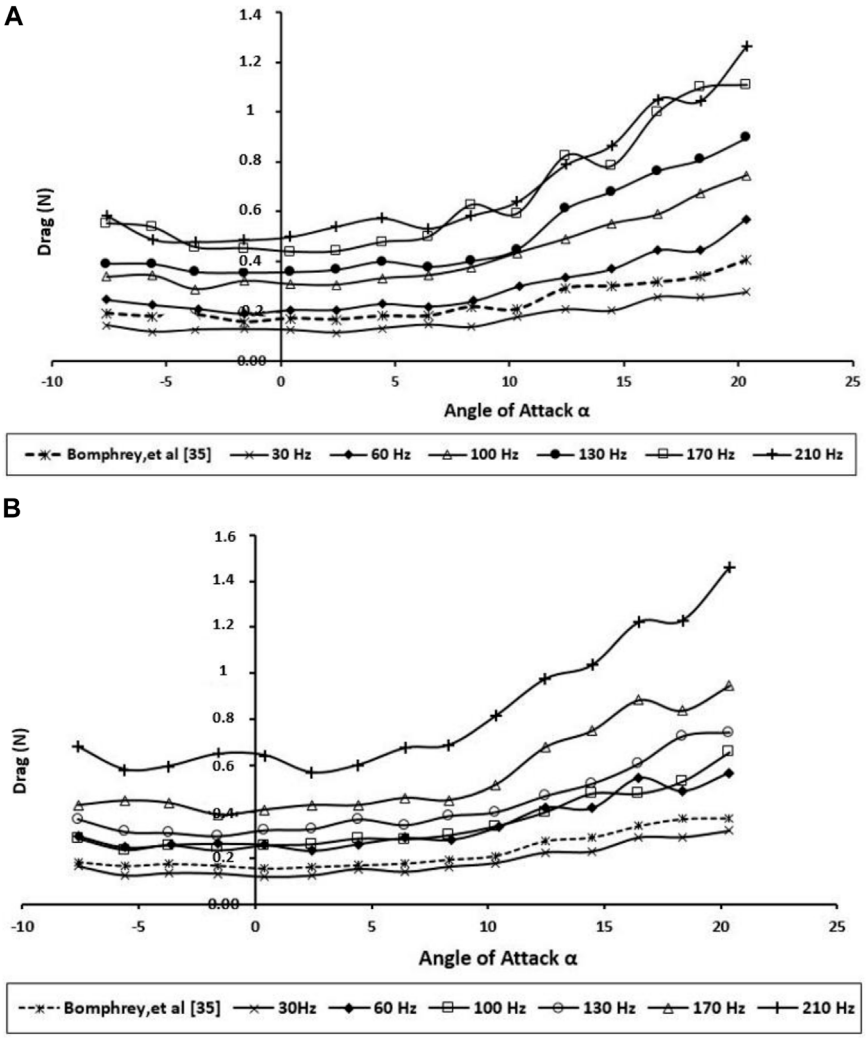

FIGURE 9 | Produced drag for the BMAV's wing at various angles of attack and wing beat frequencies; **(A)** forewing; **(B)** hindwing.

According to **Figure 8**, the higher frequency creates a slightly greater lift force than the lower frequency at all AOAs up to 10, so the bibliometric corrugated wing performs better due to more gradual stall characteristics. This AOA might be higher than what dragonflies naturally use when gliding; nevertheless, this specification could enhance the stability during flapping flight.

The experiments demonstrate that when the wings are about midway through its downstroke, the lift was mostly influenced. This is acceptable because a higher lift was generated during this period, as the wings achieved the maximum flapping velocity around midway through the downstroke. Unsurprisingly, **Figure 9** displays the hindwing lift was decreased by wing interaction at most wing beat frequencies. The reduction of the hindwing lift was not as remarkable as the one reported by Maybury and Lehmann (Maybury and Lehmann, 2004). This phenomenon can be explained as a downward flow is created in producing vertical force on the forewing, and the hindwing moves through the downwash-velocity field, which can cause a reduction in its aerodynamic forces.

The drag force (**Figure 9**) clearly shows that the drag performance of the BMAV wing at natural wing beat frequency is close to the real dragonfly wing even at a higher angle of attack (AOA ≥10.0°). Due to the flow separation on the lifting surface and stall, the drag force has increased dramatically. While the hindwing has its stall between 10.0° and 12.0° AOA, stall angles on flexible forewings were not found until between 15.0° and 17.0°. Compared with the various wing beat frequencies, the drag force acting on higher frequencies (170 and 210 Hz) was found to be the highest of all. By having flexible surface area, very high frequency causes the BMAV wing to have very poor resistance to adverse pressure gradient by flapping at higher AOA. This can also be found in the lift performance displayed in **Figure 9** (b). The lift performance of the BMAV hindwing at high frequency is also found to be very unstable. Accordingly,

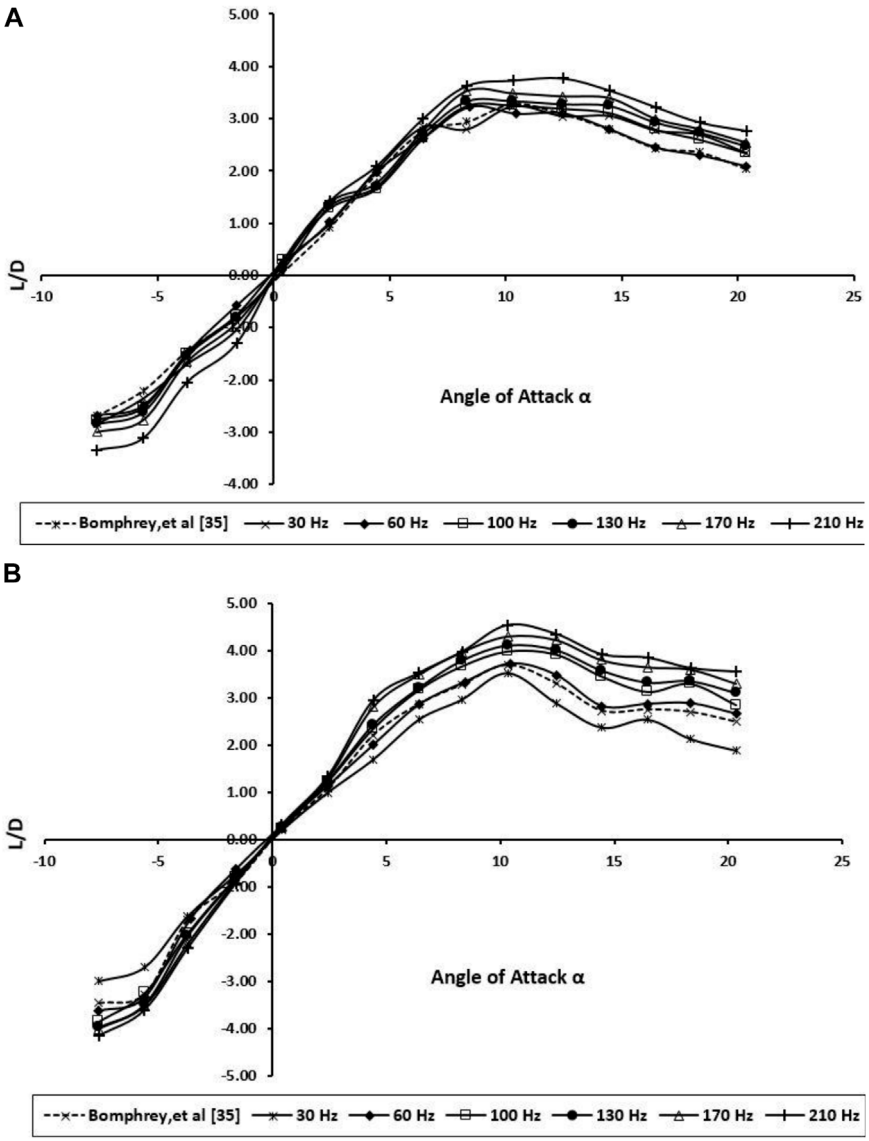

FIGURE 10 | Lift-to-drag ratio for the BMAV's wing at various angles of attack and wing beat frequencies; **(A)** forewing; **(B)** hindwing.

they would not be very practical frequencies for BMAV due to the very poor stability.

Drag, however, increases monotonically with increment in wing beat frequency (**Figure 9**). The result shows an enhancement in the lift-to-drag ratio with increasing wing beat frequency. Notably, based on **Figure 10**, the wing beat frequency does not have a significant effect on L/D improvement at low AOAs, which has been observed for high AOAs.

As mentioned in previous sections, actual scale BMAVs raises resistance to bending loads without significantly increasing compromising torsional stiffness or material volume, but as a conclusion, this is not offset by a substantial aerodynamic cost and may even lead to higher aerodynamic performance by enabling higher–aspect ratio geometries.

In dragonfly flight, the forewing and hindwings do not flap individually but interact with each other. The BMAV wings have been manually fitted in tandem configuration to run trials. The experiments were performed at various wing beat frequencies (30–210 Hz) with angles of attacks ranging from -10 to 20.

The forewing places in a positive pressure field created by the hindwing and consequently experiences reduced drag; on the other hand, the hindwing suffers greater drag due to the forewing. Combined aerodynamic performance is relatively good, especially in terms of the low drag owing to the wing high aspect ratios. Despite the fact that it is not acceptable to put the two BMAV wings excessively near one another (as the effective aspect ratio is reduced), a real dragonfly keeps the

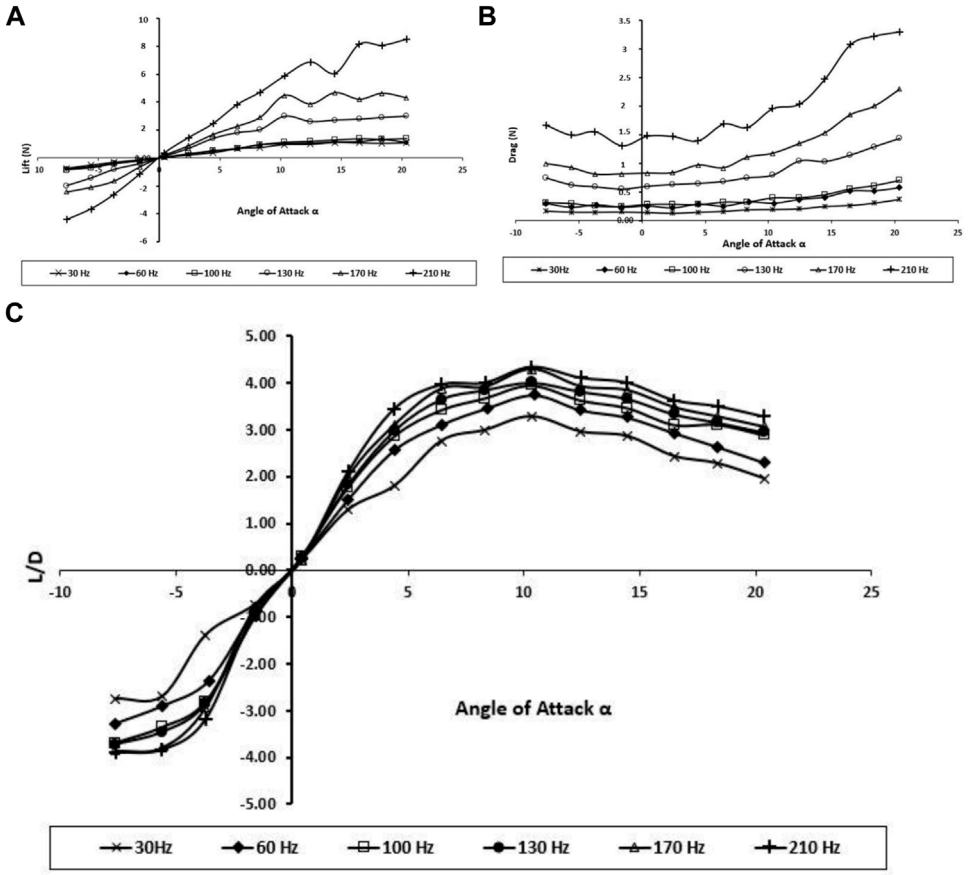

FIGURE 11 | Effect of tandem wings on **(A)** Lift force; **(B)** drag force; and **(C)** lift-to-drag ratio.

efficiency of each wing high by varying the wing angles to high efficiently (dashed line in **Figure 10**). In conventional, fixed-wing aircraft, high–aspect ratio wings reach better L/D at the cost of maneuverability.

Overall, the vortex interactions between the fore and hind wings can be considered either positive or negative. When the hindwing flaps with 0° of phase lag, constructive vortex interaction happens which strengthen the LEV generation of the hindwing, leading to large LEVs, and the resulting LEVs improve the peak lift and thrust production, as can be seen in **Figure 11**.

Furthermore, these experiments show that the tandem wings generate higher lift and drag forces than forewing and hindwing individually, and the aerodynamic performance of tandem wing results also shows improvement in the L/D and wing stability.

CONCLUSION

The advantages of using BMAV wings are clearly presented in this article. The mechanism presented in this article generates approximately 50% higher lift and drag forces than the forewing and hindwing individually; the aerodynamic performance of tandem wing results also show improvement in the L/D and wing stability. The aerodynamic forces and aerodynamics performance were measured for the flapping wing configuration from −10° to 20° AOA at various wing beat frequency ranges from 30 to 210 Hz. The wing movement produces two distinct force peaks at the beginning and end of each flapping cycle that are consistent and illustrates the wake capture. In summary, direct measurements of the forces generated by flapping wings propose that the aerodynamics of dragonflies may be described by an interactive mechanism and the interaction of the fore and hindwing. The experiments demonstrate that the lift was mostly influenced when the wings are almost midway through its downstroke. In addition, they show that higher AOA produces higher pressure differences in the surface of the dragonfly wing. Consequently, the lift rises with the AOA. In addition, for the positive AOA, the drag increases with the angle of attack. In dragonfly flight, the forewings and hindwings do not flap separately but interact with one another. The forewing places in an area of positive pressure created by the hindwing and, therefore, experiences reduced drag; conversely, the

hindwing suffers higher drag because of the forewing. Overall, the vortex interactions between the forewings and hindwings can be considered either positive or negative. When the hindwing flaps with 0° of phase lag, constructive vortex interaction happens, which strengthens the LEV generation of the hindwing, leading to large LEVs and the resulting improvement in the peak lift and thrust production.

DATA AVAILABILITY STATEMENT

The original contributions presented in the study are included in the article, further inquiries can be directed to the corresponding authors.

AUTHOR CONTRIBUTIONS

ES; Took the lead in planning and carrying out the experiments, data analysis and drafting the manuscript. EM; Data analysis and drafting the manuscript. TAW; Conceived the project idea and supervision. NNNG; Involved in project supervision. IAB Final revision and approval before publication.

ACKNOWLEDGMENTS

The authors gratefully acknowledge Faculty Grant GPF0.20A-2019, University of Malaya, Malaysia, for supporting to conduct this research work. The authors would also like to extend their appreciation to the Deanship of Scientific Research at King Khalid University for funding this work through the research groups program under the Grant Number R.G.P.2/63/43.

REFERENCES

Ansari, S. A., Żbikowski, R., and Knowles, K. (2006). Non-Linear Unsteady Aerodynamic Model for Insect-Like Flapping Wings in the Hover. Part 1: Methodology and Analysis. *Proc. Inst. Mech. Eng. G: J. Aerospace Eng.* 220 (2), 61–83. doi:10.1243/09544100jaero49

Ansari, S. A., Żbikowski, R., and Knowles, K. (2006). Non-Linear Unsteady Aerodynamic Model for Insect-Like Flapping Wings in the Hover. Part 2: Implementation and Validation. *Proc. Inst. Mech. Eng. Part G: J. Aerospace Eng.* 220 (3), 169–186. doi:10.1243/09544100jaero50

Bomphrey, R. J., Nakata, T., Henningsson, P., and Lin, H.-T. (2016). Flight of the Dragonflies and Damselflies. *Phil. Trans. R. Soc. B* 371 (1704), 20150389. doi:10.1098/rstb.2015.0389

Chen, Y. H., Skote, M., Zhao, Y., and Huang, W. M. (2013). Dragonfly (Sympetrum Flaveolum) Flight: Kinematic Measurement and Modelling. *J. Fluids Structures* 40, 115–126. doi:10.1016/j.jfluidstructs.2013.04.003

Cheng, B., and Deng, X. (2011). Translational and Rotational Damping of Flapping Flight and its Dynamics and Stability at Hovering. *IEEE Trans. Robot.* 27 (5), 849–864. doi:10.1109/tro.2011.2156170

Conn, A. T., Burgess, S. C., and Ling, C. S. (2007). Design of a Parallel Crank-Rocker Flapping Mechanism for Insect-Inspired Micro Air Vehicles. *Proc. Inst. Mech. Eng. C: J. Mech. Eng. Sci.* 221 (10), 1211–1222. doi:10.1243/09544062jmes517

De Croon, G. C. H. E., de Clercq, K. M. E., Ruijsink, R., Remes, B., and de Wagter, C. (2009). Design, Aerodynamics, and Vision-Based Control of the DelFly. *Int. J. Micro Air Vehicles* 1 (2), 71–97. doi:10.1260/175682909789498288

Dickinson, M. H., Lehmann, F.-O., and Sane, S. P. (1999). Wing Rotation and the Aerodynamic Basis of Insect Flight. *Science* 284 (5422), 1954–1960. doi:10.1126/science.284.5422.1954

Dickson, W. B., and Dickinson, M. H. (2004). The Effect of Advance Ratio on the Aerodynamics of Revolving Wings. *J. Exp. Biol.* 207 (24), 4269–4281. doi:10.1242/jeb.01266

Ellington, C. P. (1984). The Aerodynamics of Hovering Insect Flight. VI. Lift and Power Requirements. *Philosophical Trans. R. Soc. Lond. B, Biol. Sci.* 305 (1122), 145–181. doi:10.1098/rstb.1984.0054

Ellington, C. P., van den Berg, C., Willmott, A. P., and Thomas, A. L. R. (1996). Leading-Edge Vortices in Insect Flight. *Nature* 384 (6610), 626–630. doi:10.1038/384626a0

Galiński, C., and Żbikowski, R. (2005). Insect-Like Flapping Wing Mechanism Based on a Double Spherical Scotch Yoke. *J. R. Soc. Interf.* 2 (3), 223–235. doi:10.1098/rsif.2005.0031

Galiński, C., and Żbikowski, R. (2007). Materials Challenges in the Design of an Insect-Like Flapping Wing Mechanism Based on a Four-Bar Linkage. *Mater. Design* 28 (3), 783–796. doi:10.1016/j.matdes.2005.11.019

Hsu, C.-K., Evans, J, Veera, VSKV, and Huang, PG (2010). "Development of Flapping Wing Micro Air Vehicles-Design, CFD, Experiment and Actual Flight," in Proceeding of the 48th AIAA Aerospace Sciences Meeting Including the New Horizons Forum and Aerospace Exposition, Orlando, FL, January 04–07, 2010. doi:10.2514/6.2010-1018

Karásek, M. (2014). *Robotic Hummingbird: Design of a Control Mechanism for a Hovering Flapping Wing Micro Air Vehicle*. Bruxelles, Belgium: Universite libre de Bruxelles.

Lan, S., and Sun, M. (2001). Aerodynamic Properties of a Wing Performing Unsteady Rotational Motions at Low Reynolds Number. *Acta Mechanica* 149 (1-4), 135–147. doi:10.1007/bf01261668

Li, C., Gorb, S.N., and Rajabi, H. (2021). Biomechanical Strategies to Reach a Compromise Between Stiffness and Flexibility in Hind Femora of Desert Locusts. *Acta Biomaterialia* 134, 490–498. doi:10.1016/j.actbio.2021.07.030

Li, Q., Zheng, M., Pan, T., and Su, G. (2018). Experimental and Numerical Investigation on Dragonfly Wing and Body Motion During Voluntary Take-Off. *Sci. Rep.* 8 (1), 1011. doi:10.1038/s41598-018-19237-w

Lighthill, M. J. (1973). On the Weis-Fogh Mechanism of Lift Generation. *J. Fluid Mech.* 60 (1), 1–17. doi:10.1017/s0022112073000017

Liu, H., Ellington, C. P., Kawachi, K., van den Berg, C., and Willmott, A. P. (1998). A Computational Fluid Dynamic Study of Hawkmoth Hovering. *J. Exp. Biol.* 201 (4), 461–477. doi:10.1242/jeb.201.4.461

Maxworthy, T. (1979). Experiments on the Weis-Fogh Mechanism of Lift Generation by Insects in Hovering Flight. Part 1. Dynamics of the 'fling'. *J. Fluid Mech.* 93 (1), 47–63. doi:10.1017/s0022112079001774

Maybury, W. J., and Lehmann, F.-O. (2004). The Fluid Dynamics of Flight Control by Kinematic Phase Lag Variation between Two Robotic Insect Wings. *J. Exp. Biol.* 207 (26), 4707–4726. doi:10.1242/jeb.01319

Rubentheren, V., Ward, T. A., Chee, C. Y., Nair, P., Salami, E., and Fearday, C. (2016). Effects of Heat Treatment on Chitosan Nanocomposite Film Reinforced with Nanocrystalline Cellulose and Tannic Acid. *Carbohydr. Polym.* 140, 202–208. doi:10.1016/j.carbpol.2015.12.068

Salami, E., Ganesan, P. B., Ward, T., and Viyapuri, R. (2016). Design and Mechanical Analysis of a 3D-Printed Biodegradable Biomimetic Micro Air Vehicle wing. *IOP Conf. Ser. Mater. Sci. Eng.* 152, 012014. IOP Publishing. doi:10.1088/1757-899x/152/1/012014

Salami, E., Ganesan, P. B., Ward, T., and Viyapuri, R. (2017). Nano-mechanical Properties and Structural of a 3D-Printed Biodegradable Biomimetic Micro Air Vehicle Wing. *IOP Conf. Ser. Mater. Sci. Eng.* 210, 012073. IOP Publishing. doi:10.1088/1757-899x/210/1/012073

Salami, E., Ward, T. A., Montazer, E., and Ghazali, N. N. N. (2019). A Review of Aerodynamic Studies on Dragonfly Flight. *Proc. Inst. Mech. Eng. Part C: J. Mech. Eng. Sci.* 233 (18), 6519–6537. doi:10.1177/0954406219861133

Salami, E., Ward, T. A., Montazer, E., and Ghazali, N. N. N. (2020). Nanoindentation Analysis Comparing Dragonfly-Inspired Biomimetic

Micro-Aerial Vehicle (BMAV) Wings. *Ijbic* 16 (2), 111–120. doi:10.1504/ijbic.2020.109715

Sane, S. P., and Dickinson, M. H. (2002). The Aerodynamic Effects of Wing Rotation and a Revised Quasi-Steady Model of Flapping Flight. *J. Exp. Biol.* 205 (8), 1087–1096. doi:10.1242/jeb.205.8.1087

Sivasankaran, P. N., Ward, T. A., Salami, E., Viyapuri, R., Fearday, C. J., and Johan, M. R. (2017). An Experimental Study of Elastic Properties of Dragonfly-Like Flapping Wings for Use in Biomimetic Micro Air Vehicles (BMAVs). *Chin. J. Aeronautics* 30 (2), 726–737. doi:10.1016/j.cja.2017.02.011

Sivasankaran, P. N., Ward, T. A., Viyapuri, R., and Johan, M. R. (2016). Static Strength Analysis of Dragonfly Inspired Wings for Biomimetic Micro Aerial Vehicles. *Chin. J. Aeronautics* 29 (2), 411–423. doi:10.1016/j.cja.2016.02.007

Sun, M., and Tang, J. (2002). Lift and Power Requirements of Hovering Flight in Drosophila Virilis. *J. Exp. Biol.* 205 (16), 2413–2427. doi:10.1242/jeb.205.16.2413

Sun, M., and Xiong, Y. (2005). Dynamic Flight Stability of a Hovering Bumblebee. *J. Exp. Biol.* 208 (3), 447–459. doi:10.1242/jeb.01407

Truong, Q. T., Nguyen, Q. V., Park, H. C., Byun, D. Y., and Goo, N. S. (2011). Modification of a Four-Bar Linkage System for a Higher Optimal Flapping Frequency. *J. Intell. Mater. Syst. Structures* 22 (1), 59–66. doi:10.1177/1045389x10392611

Tsai, B.-J., and Fu, Y.-C. (2009). Design and Aerodynamic Analysis of a Flapping-Wing Micro Aerial Vehicle. *Aerospace Sci. Technology* 13 (7), 383–392. doi:10.1016/j.ast.2009.07.007

Wakeling, J., and Ellington, C. (1997). Dragonfly Flight. II. Velocities, Accelerations and Kinematics of Flapping Flight. *J. Exp. Biol.* 200 (3), 557–582. doi:10.1242/jeb.200.3.557

Walker, J. A. (2002). Rotational Lift: Something Different or More of the Same? *J. Exp. Biol.* 205 (24), 3783–3792. doi:10.1242/jeb.205.24.3783

Weis-Fogh, T. (1972). Energetics of Hovering Flight in Hummingbirds and in Drosophila. *J. Exp. Biol.* 56 (1), 79–104. doi:10.1242/jeb.56.1.79

Weis-Fogh, T. (1973). Quick Estimates of Flight Fitness in Hovering Animals, Including Novel Mechanisms for Lift Production. *J. Exp. Biol.* 59 (1), 169–230. doi:10.1242/jeb.59.1.169

Zhang, S., Sunami, Y., and Hashimoto, H. (2018). Deformation Behavior of Dragonfly-Inspired Nodus Structured Wing in Gliding Flight Through Experimental Visualization Approach. *Sci. Rep.* 8 (1), 5751. doi:10.1038/s41598-018-24237-x

Conflict of Interest: The authors declare that the research was conducted in the absence of any commercial or financial relationships that could be construed as a potential conflict of interest.

frontiers | Frontiers in Built Environment

MINI REVIEW
published: 27 May 2022
doi: 10.3389/fbuil.2022.805292

Tangled Tales of Mycelium and Architecture: Learning From Failure

Janet McGaw[1]*, *Alex Andrianopoulos*[2] *and Alessandro Liuti*[3]

[1]Faculty of Architecture Building and Planning, University of Melbourne, Melbourne, VIC, Australia, [2]School of Biosciences, Faculty of Science, University of Melbourne, Melbourne, VIC, Australia, [3]Research Manager, Arup University, Docklands, VIC, Australia

Architects, artists and engineers around the world have been experimenting with the potential of mycelium, the vegetative body of a fungus, as a future building material for the past 15 years. It shares many of the positive material attributes of polystyrene but unlike the synthetic material it is fully sustainable and completely biodegradable. Mycelium has also proved to be simple to grow at scale. Its capacity to rapidly grow its tangled hyphae in a multiplicity of directions, digesting nothing more than organic waste, has shown promise for the production of a variety of materials for the building industry. But despite this, mycelium has struggled to find a market within the building industry. Drawing on the literature, this article argues that the challenges have been psychological, aesthetic and economic, rather than technical. Western industrial systems have conditioned us to expect material cultures to be clean, precise and durable. Mycelium is messy and some fungi are known pathogens. Like any living creature it can be unpredictable. Further, while the materials for growing mycelium are cheap, initial production costs for mass production and distribution typical of industrial fabrication are high. The risk for investors in the absence of an assured market stymied early forays into production. But as the environmental crisis becomes more urgent, there is evidence of a growing interest in finding new avenues for production. Centralised large-scale production is only one way forward. Another, which learns from early failures, is mass production through a multiplicity of micro-scale, do-it-yourself systems.

Keywords: mycelium, architecture, fungus, bio-materials, building, sustainable construction

OPEN ACCESS

Edited by:
Cecilia Laschi,
National University of Singapore, Singapore

Reviewed by:
Asya Ilgün,
University of Graz, Austria
André Stephan,
Catholic University of Louvain, Belgium

***Correspondence:**
Janet McGaw
mcgawjk@unimelb.edu.au

Specialty section:
This article was submitted to Computational Methods in Structural Engineering, a section of the journal Frontiers in Built Environment

Received: *30 October 2021*
Accepted: *25 April 2022*
Published: *27 May 2022*

Citation:
McGaw J, Andrianopoulos A and Liuti A (2022) Tangled Tales of Mycelium and Architecture: Learning From Failure. Front. Built Environ. 8:805292. doi: 10.3389/fbuil.2022.805292

INTRODUCTION

The Intergovernmental Panel on Climate Change warns that there is unequivocal evidence of escalating global climate change and advises that developing better building systems is critical for a more resilient future (IPCC 1988; IPCC 2022; Sachs et al., 2021, World Resources Institute 2022). Intensifying concerns about environmental performance have led the building industry to broaden its approach beyond decreasing energy use through solar orientation, insulation, and low energy electrical fittings, to systemic concerns that take into account the materials from which buildings are constructed (Stephan, Crawford and De Myttenaere 2011; Mirabella et al., 2018; Moncaster et al., 2018). Research into novel bio-materials has grown in response (Jones and Brischke 2017; Pacheco-Torgal et al., 2020). While some research has translated into products for manufacture, there have been many failures along the way.

This article considers the successes and challenges for mycelium, a bio-polymer that has received significant attention globally. Although the innovations in the field have developed

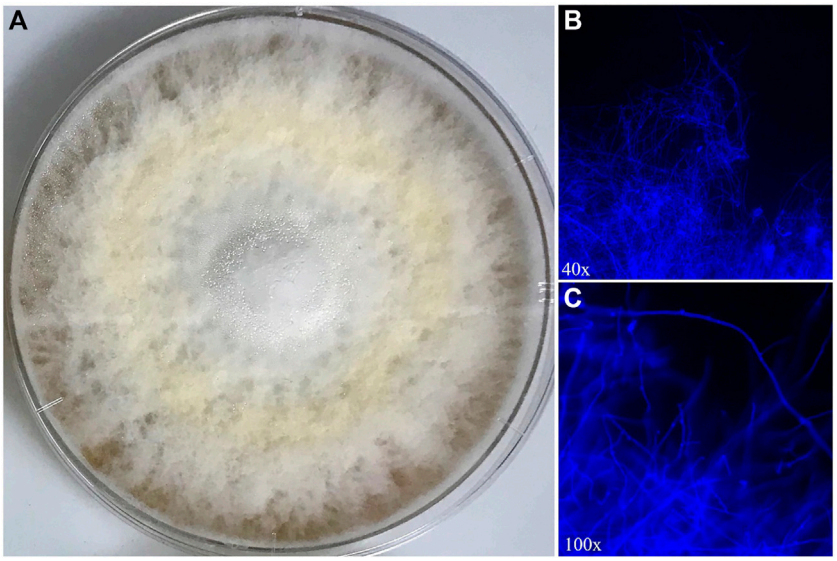

FIGURE 1 | *Pleurotus ostreatus*, commonly known as the oyster mushroom. *P. ostreatus* mycelial growth on a malt extract agar plate after 7 days incubation at 22°C **(A)**. The plate was inoculated in the centre and the fungus has grown to the edges and filled the entire plate. Microscopic images of mycelium from the plate on the left after staining cell walls with calcofluor white (fluorescent brightener 28). Images taken under fluorescent microscopy at 40 × **(B)** and 100 × **(C)** magnification. Image supplied by Alex Andrianopoulos.

through trans-disciplinary collaborations, most of the publications are narrowly focused along disciplinary silos—architectural design, biology, mechanical engineering, or agricultural engineering. Other literature reviews focus more comprehensively but narrowly on experimental scientific research and patents rather than those that have emerged in creative research or product development. This article, on the other hand, brings together varied interests. It draws selectively on scholarly literature from a range of pure and applied scientific disciplines—microbiology, engineering, bio-technology and agriculture—as well as grey literature, design industry websites, and the websites of material developers and producers.

POLYMERS IN THE BUILT ENVIRONMENT: SYNTHETIC AND NATURAL

Polymers are used in all facets of the building industry: paints, fillers, adhesives, flooring, cabinetry, electrical wiring, insulation and roofing (Harrison & Hester 2018). They are lightweight, versatile, impermeable and durable. While polymers are one of the most multiplicitous organic material types on earth (Seymour 1988; Rasmussen 2018), most of the polymers now in use in the built environment are synthetic. First developed in the early 19th century, they have multiplied and proliferated exponentially since the 1930s (Rasmussen 2018). Petroleum-based synthetic polymers present two significant problems: Firstly they perpetuate fossil fuel extraction, and secondly their durability renders them an enduring blight in landscapes long after their useful life in buildings is over. In an era facing twin challenges of global warming and plastic pollution, lessening the dependency on synthetics in the building industry is both a necessity and a challenge.

One of the most ancient and prolific natural polymers is found in fungi. Carbon-based polymers in the form of chitin and glucans constitute the cell walls of fungi, while their mycelium are akin to fibres. Fungi generally grow in two vegetative forms; single-celled yeast and multicellular hyphae. The budding yeast *Saccharomyces cerevisiae* is one of the most familiar domesticated species, used for bread, beer and wine making. But it is the multi-cellular filamentous fungi, which grow as long, tube-like cells joined end-to-end and form highly branched networks, that shares many characteristics with synthetic polymers and have recently been identified as a possible substitute in the building industry. Like synthetic polymers, mycelium can be lightweight, strong, and a good insulator. It is also similarly versatile. Through careful selection of appropriate species, adjusting the feeding stock and molds, mycelium can be made into a material as thin and flexible as leather, aggregated into blockwork, providing a substitute for thermal and acoustic insulation and even simulate mass concrete **Figure 1**.

Fungi are also key players in most ecosystems. They are major recyclers of organic material, transforming often inaccessible matter into available essential nutrients, as well as playing more direct and critical roles in the growth of numerous plant species. Across the fungal kingdom, mycelium displays many unique biological properties including a generic capacity to grow without light, to specialised activities such as the production of oxalic acids that have the strength to decompose rock, and peroxidase enzymes that break hydrocarbon bonds in complex carbohydrates such as lignin and turn them into simple sugars. These properties mean they can grow rapidly on carbon-based products we typically discard as waste materials such as husks,

sawdust, woodchip, and even coffee grounds. So, unlike artificial polymers which perpetuate the use of fossil fuels and, when discarded, endure for centuries as waste, fungi can grow on agricultural waste and are completely biodegradable. Despite these advantages, until a decade ago, fungi were a largely untapped resource as a building material.

DIFFERENT APPROACHES TO EXPERIMENTATION WITH MYCELIUM

Experimental research in mycelium for the built environment has branched and proliferated, much like mycelia itself. After a decade of largely invisible activity deep in the homes and minds of early developers in the 1990s and early 2000s, a first flush of experimental prototypes emerged between 2007 and 2014 in New York and California in the United States, and a few years later in Europe (focused in the Netherlands). Since then, a global network of researchers across creative and scientific disciplines, with and without manufacturers, has flowered. Most are working collaboratively in interdisciplinary teams: With artists, architects, interior designers, industrial designers and furniture makers engaging in creative research to explore the poetic and aesthetic possibilities of the material; scientific researchers, including engineers, microbiologists, bio-technologists and agricultural scientists testing mechanical, thermal and acoustic performance, morphology, optimal species and feeding regimes; and industry partners focussing on trials around repeatability, reproducibility and scalability. Outcomes have been disseminated through academic journals and conferences and exhibited in galleries and public and professional orientated design websites. Around 50 patents have been filed for numerous processes using fungal mycelium as a replacement for synthetic polymers since 2006 (Cerimi et al., 2019, Hüttner et al., 2020). The US-based companies Ecovative and MycoWorks were early leaders. Ecovative now dominates the US patents landscape (Cerimi et al., 2019). However, China dominates globally. Some products that hit the market early have disappeared. Others have found a niche and continued to grow. The field has developed as much by these failures as it has by the successes. Success in material performance is not the only requirement for viability for production.

Mycelium-based experimentation and prototyping has pursued four lines: Flat hardboard products for building panels; flexible leather substitutes; disposable packaging; architectural fittings and homewares. Architects, engineers, and building contractors, are increasingly aligning their strategies to sustainable development goals and net-zero targets which is translating into awareness of how design choices impact the carbon footprint of the built environment, and ultimately supply chain choices. The biggest advantage of mycelium is its biodegradability; where supply materials are sourced from waste material and renewable energy is used for production, bio-based materials promise considerable environmental performance in comparison to traditional counterparts. While the technology shows maturity in both low-risk disposable products and in industries with high turnovers, mycelium has struggled to find a niche within the construction industry. Markets need customers. Customers' desires and interests are driven to varying degrees by aesthetics, cost, and ethical concerns (Gagnier 2000). These in turn are shaped by bigger, often global, social, environmental and economic forces (Kompatsiaris and Chrysagis, 2020). As the climate crisis accelerates, economies are shifting (Miles 2014). So too is the willingness to embrace different aesthetics and pay higher premiums to satisfy ethical concerns. Consequently, there is an increasing appetite and interest in continuing the experimentation.

Panel Products

Mycelium's similarity to polystyrene and particle board led two groups to test and prototype biodegradable material substitutes for building products currently made from synthetic material from 2006 to 2009. In New York, engineering students Eben Bayer and Gavin McIntyre at Rensselaer Polytechnic developed a mycelium-based insulation material they thought could replace synthetic counterparts (Rensselaer 2007). They filed for a patent on the method they developed to grow the material in 2007 (US Patent no. 9485917) and set up a small company, Ecovative around the same time (Ecovative 2021a). Ecovative applied this technique to make an insulation board trademarked as 'Greensulate' the same year (Material District, 2022). Californian, artist and herbalist, Phil Ross, meanwhile, had spent the 1990s and early 2000s experimenting with cultivating mushrooms and testing similar material ideas. His small catenary shaped pavilion, assembled from blocks cast from the mycelium of *Ganoderma lucidum* (Reishi mushrooms), *Alpha Mycotectural teahouse,* was installed in an art gallery in Dusseldörf Germany in 2009 (Debatty et al., 2011). Ross filed for his first patent describing a method for producing fungus structures for construction and manufacturing in 2011 (US Patent no. 9410116). The patent describes methods for increasing the strength of the material through compression during the growth phase and methods for integrating structural support members. After teaming up with collaborator Sophie Wang to form the start-up MycoWorks, Ross and Wang spent 3 years applying these techniques into prototypes for the building industry. The suite of materials included panels and other flat moulded forms for interior linings, cabinets, furniture and structural systems. Both companies engaged in further exhibitions of their work: MycoWorks' collection was exhibited in the Design and Violence interactive at MoMA (Superflux 2014) and *Daring Growth* display at the 2016 Venice Biennale (MycoWorks 2021a); while Ecovative supplied mycelium blocks for a tower installation designed by architect David Benjamin from The Living, and Arups Engineering, at MoMA PSI *Hy-Fi* (Stott 2014).

Both MycoWorks and Ecovative developed long-term experimental research collaborations with engineers to test the mechanical, thermal and biological properties of mycelium. Ross worked with Travaglini et al (2013, 2014, 2015, 2016) while McIntyre collaborated with teams led by agricultural engineers Matthew Pelletier et al. (2013) and Alexander Zeigler et al. (2016), mechanical engineers Lai Jiang and Daniel Walczyk (Jiang et al.,

FIGURE 2 | Various mycelium-based panel product samples. Image supplied by Phil Ross.

2014a, 2014b, 2015, 2016, 2017a, 2017b, 2018) and Mohammed Islam et al. (2017). They found mycelium boards performed well enough on stability, strength and thermal insulation to compete with other comparable products on the market, which seemed to indicate that the products would be viable for use in the building industry. But from a business perspective, bio-based building materials could not compete with traditional materials based on cost-effectiveness **Figure 2**.

In theory mycelium panel products should be inexpensive to produce once systems are established. Growing media, like sawdust from softwood mills, organic waste from agribusiness or textiles from consumer goods, could be sourced from waste diverted from existing industries. Spores, meanwhile, are tiny and light to distribute. They could be engineered quickly at a relatively low cost *en masse* at research centres and distributed to cultivation and drying facilities. But there were a number of systemic challenges that needed to be addressed first to reduce risk for investors. Scaling up needed a degree of surety around demand. Production needed consistent and reliable supply chains for growing media, which in turn needed systems change within agriculture and industry. Demonstrating compliance to national building codes was costly. Fire testing, for example, costs tens of thousands of dollars. Large scale dedicated controlled spaces for growing were expensive but necessary and so to was large scale equipment for heat-treating. Consequently none of these panel products were developed into a viable product for the market.

Flexible Fabrics

Mycelium material manufacturers instead, responded to the failures in one market by tweaking their products for another. MycoWorks responded to their economic challenges by switching focus to a product line with a high turnover, but one for which consumers are willing to pay significant sums of money: Fashion. Partnering with Hermès, MycoWorks developed flexible mycelium fabrics with similar qualities to leather that are being used in their handbags (Hahn 2021). "Sylvania," also known as "Reishi Fine Mycelium," performs equally well or better than leather on measures of tensile strength, abrasion resistance and colourfastness (MycoWorks 2021b). Aligning with a luxury fashion house willing to pay for hand crafted materials allowed them to set a price that would turn a profit. US Biotech company Bolt Threads, launched an equivalent product, Mylo in 2017 (Hahn 2020). It is now being used by global sportswear manufacturers, Adidas and Lululemon, and the fashion house Stella McCartney and Kering, for "vegan" footwear and clothing lines (Hahn 2020). Ecovative has a similar product, marketed by the sheet, ready for "tanning" as well as a flexible, insulating foam for garments (Ecovative 2021b).

In developing a product that addressed economic imperatives, product developers discovered a new challenge. A number of familiar fungi are pathogens of animals, plants and other fungi which engenders a perception of threat in customers. Would mycelium fabrics bring molds and dry rots into wardrobes? Would people inhale dangerous spores? Some strains of fungi are known to cause significant yield losses in many crops such as wheat and rice and others of fruit. MycoWorks responded to such perceived fears by rehabilitating the reputation of fungi through sensorial design measures and customer education. These have included imprinting the material with a texture that mirrors leather, suffusing it with the fragrance of tanned leather, and visual marketing that creates an association of indulgence (MycoWorks 2021c). The process of both growing, but more importantly, killing mycelium through a drying process has also been communicated to customers.

Packaging

Ecovative, by contrast, responded to the failures in producing their panel insulation product for the market by exploiting mycelium's other great advantage—its capacity to grow to fit any container in which it is cultivated. They applied their know-how to disposable packaging. Packaging has an even higher turnover than the fashion industry. Indeed perishability is desirable. It also has a higher tolerance for irregularity and lower performance requirements than the building industry. Using a process that involves making a 3D virtual model of the form to be cradled, and producing custom designed thermoform growth trays, Ecovative has been able to grow packaging to suit any product. Their "mycelium foundry" in Green Island New York—a term that connotes fine craftsmanship and industry in one –is now capable of producing packaging at volume. Ecovative now has a contract to supply the multinational furniture giant, IKEA, with a bio-substitute for polystyrene packaging (Steffen 2019). IKEA, in turn, is leveraging the biodegradable packaging to appeal to a customer base increasingly concerned with the impacts of plastic waste on oceans, waterways and the ecosystems they support (Gosden 2016).

Other industries that tolerate, indeed embrace, materials that are part of a sustainable, circular economy include landscape design and gardening products. Grown.bio has licenced Ecovative's technology to market a line of planter boxes and other small pots (Grown.bio. 2022). An Australian collaboration between Swinburne University, Arup, the Royal Botanic Gardens and Studio Edward produced a floating sacrificial planter, "Mushi," that exploits mycelium's capacity to float and then biodegrade after extended contact with water (Melbourne

Design Week 2021). The waffle form is planted with wetland grasses that promote biodiversity. It builds on earlier work by one of the most influential mycologists, Paul Stamets, who explored interventions that exploit mycelium's dynamic capacities while it is alive to remediate contaminated soils and waterways (Miller 2013).

Architectural Fittings and Homewares

Mycelium's capacity to be cast into complex forms inspired much of the early creative experimentation by designers in Europe and subsequent application in furniture and other interior products and homewares. Maurizio Montalti of Officina Corpuscoli, in collaboration with Utrecht University, curated a series of exhibitions, including "The Future of Plastic" (2009), which focused on bowls and other vessels cast from mycelium, "Mycelium Design" (2014) and "Fungal Futures" (2016), which showcased a number of other European designers exploring the many shapes and textures that mycelium can morph into. Designers included Aniela Hoitink, who was an early developer of fine flexible mycelium for fashion; Jonas Edvard Neilson who was prototyping furniture; Kristel Peters, who exhibited concepts for footwear; and Phil Ross who displayed his interlocking blockwork. Many have continued to apply their knowledge in industrial design. Like fashion, these are building items that can attract a higher price than hidden lining boards and insulation. Edvard Neilson's MYX Lamps from 2014 (Chin 2014) and Danielle Trofe's Mushlume (Ecovative supply the mycelium) from 2011 are lighting products of note (Danielle Trofe Design 2020).

Montalti has also launched a company, Mogu, based in Italy. Mogu and Arup are working on a suite of mycelium-based products. One of them is "Foresta," an acoustic panel. This product has now been tested and certified for use and is now entering the European market (Arup 2021). It combines good technical properties (acoustic properties comparable to traditional panels; fire-resistance compliance; dimensional stability; safety; ease of assembly, disassembly and prospects for reconfiguring) with environmental performance and circular principles (the panel can be bio-degraded, unlike traditional composite panels that often end up in landfill). Like Ecovative's earlier Greensulate, Foresta is a sustainable alternative to similar synthetic products. But rather than a hidden filler, like the early thermal insulation, its selling point is that it is an office feature panel. Mogu and Arup are also developing further products for premium interior fit-outs. Compliances in the building industry are often less strict for temporary or non-structural elements, such as interior fitouts, so this market currently has the best applicability potential for bio-based material.

INTERFACE BETWEEN SCIENCE AND MANUFACTURING: PROSPECTS FOR THE FUTURE

A range of biological scientists have been working closely with these product designers to develop the best strains, growing media, and processes of cultivation to shape the performance of the product. Agricultural engineer, Alexander Zeigler (Ziegler et al., 2016) considered specific gravity, surface hardness, water absorption, coefficient of linear thermal expansion, and resistance to tension with different fungal strains and feed—hemp and cotton waste. Microbiologist Freek Appels, working with architect Maurizio Montalti and others from Utrecht and Maastricht Universities, has explored the relationship between moisture, feed, and heat on mechanical performance. They found that glycerol can change mycelium's density, hydrophilicity and mechanical properties from paper-like, to leather-like, to rubber-like, (Appels et al., 2019, 2020). Like plants, fungi have a wall that surrounds cells. The cell wall is composed of various carbohydrate types such as glucans and chitin and decorated by proteins such as mannans. The composition of the cell wall, that is the relative proportion of each of these components, varies between fungi and composition can also change depending on the growth conditions. Similarly, the architecture of cell walls—how each of these core components is layered relative to the underlying cell membrane and the way the components are chemically linked—also varies between fungi and growth conditions. Moreover, cell walls are continually remodelled by fungi to deal with changing environments and to allow for growth.

Mechanical engineers, on the other hand, have focused on aspects of structural performance. Since the pioneering work led by Travaligni for MycoWorks and Jiang and Islam (2017) for Ecovative, other collaborations have tested different mechanical limits. The recent wave of experimentation has tested more ambitious structural systems. Advancing on the earlier block systems which were modelled on masonry units, a research team led by Heisel has tested mycelium's capacity to replace cast concrete. The team, assembled from academics based at KIT Karlsruhe Germany, ETH Zürich, ETH Singapore and the Mycotech Lab Indonesia, has engineered a load-bearing branching structural system, dubbed the Mycotree (Heisel et al., 2017). Recognising mycelium's relative strength in compression but relative weakness in tension, the design uses funicular geometry much like those used in medieval stone vaults. The team has also developed neat timber brackets and connectors, supplemented with small sections of steel. Architecture students from Georgia Tech (Dessi-Olive 2019) have also tested casting monolithic mycelium *in situ*. Outcomes included arches and vaults, culminating with a 2.5 × 2.5 × 2.5 m cubic pavilion with a pointed Gothic style vaulted interior, grown from an inoculated base material supplied by Ecovative, within a removable plywood formwork. Finally, Eugene Soh's team, based in Singapore, is developing a technique for extruding mycelium paste that has applications for digital printing systems (Soh et al., 2020). This would enable an additive approach to making mycelium elements, eliminating the need for a mold, which the casting method requires.

There is also experimental work underway that capitalises on other material attributes shared by mycelium with synthetic polymers. Some polymers are particularly good at flowing into tiny voids in substrates while in their liquid form, interlocking with other particles to create a bond. They are the basis of many adhesives. A collaboration between plant biotechnology and

environmental science research units in China, Malaysia and Denmark, led by Nyuk Ling Ma and Christian Sonne, has tested mycelium as a possible "green" adhesive substitute for the toxic urea-formaldehyde commonly used in particle board (Khoo et al., 2020). Rather than focusing on feeding regimes for living mycelium, as other researchers and manufacturers have done, this team has explored the potential of dead mushrooms, a growing waste product from the food industry. Experiments show that heat compressing spent mushroom waste, at 160°C causes it to melt. Placing it under pressure (10 mPa for 20 min) with woody waste, like sawdust, forces it to penetrate and cohere to the particulate matter producing a particle board with higher internal bonding strength than building standards require, and high water and fire resistance too.

Finally, partnerships between computer scientists and mycologists are exploring the prospect of working collaboratively with mycelium whilst it is still alive. Unconventional computer scientists and mycologists are focussing on the patterns of electrical signals that mycelium produces (Adamatzky and Gandia 2021). Fungal Architectures consortium (Fungal Architectures 2020) is exploring how to enrich the functionality of mycelium to make it responsive to external stimuli (Beasley et al., 2020a; Adamatzky et al., 2020). These studies suggest that embedding nanoparticles and polymers into the fungal substrate would enable mycelium objects to become intelligent sensors that could respond to external environments (Olsson and Hansson, 1995; Adamatzky & Gandia 2021). This is opening further research into self-growing and self-repairing materials for the built environment. Metabolically inactive spores of certain fungi that biomineralize calcium carbonate when exposed to water and oxygen have been shown to be a successful concrete additive that can delay concrete degradation. Alkaliphilic fungi will remain viable for long periods of time despite the environmental conditions in concrete. When the concrete begins to crack, allowing air and water to penetrate, the spores germinate and the fungus precipitates calcium carbonate, repairing cracks (Van Wylick et al., 2021).

CONCLUSION

This article has offered a focused review of literature related to creative and scientific collaborations that have developed mycelium-based materials as an alternative to synthetic polymers. It shows that considerable advances have been made over the past 15 years. Early research revealed that the material held much promise. But creating a viable product for the market has met unexpected challenges. Interestingly creative responses to failures in one market have led to viable products for another. For mycelium to be used more broadly in the building industry, however, there remain three key challenges: Balancing biodegradability with an acceptable level of durability; demonstrating compliance with building standards through testing; and developing systems of production that are cost-effective. As research has both diversified and specialised, a range of composite materials that are fit-for-purpose are addressing the first challenge. The cost of testing for compliance with building codes remains high but the investment by some manufacturers, like Mogu, has paid off. Approvals have followed and markets are growing for their products. This is lowering the risk for others to do the same. Centralised large-scale production has been shown to work for packaging and textiles, but not yet for large-scaled building materials. Policy settings that support the status quo remain an impediment to investment. With an ever-broadening range of novel systems under development, these costs will continue to reduce. Micro-scale, do-it-yourself systems are another alternative. There are numerous products on the market and instructionals on the internet for mycelium-based products for gardening and food growing at home. These include Stamets' "Life Box," a corrugated cardboard impregnated with fungal spores and seeds, as well as mushroom growing kits. There are also some resources available for DIY builders, but these are still in their infancy. MycoWorks provides some resources (MycoWorks 2021d), as does Critical Concrete, a social initiative to educate on sustainable building generally and mycelium production for the building industry specifically (Criti.co 2022). Finally, novel research that is exploring the capabilities of fungus across its whole life cycle—as spores, while growing, and after it is dead—is revealing that there are many underexplored avenues for working with fungus in the built environment. As policies continue to evolve in light of the urgency of the climate crisis, zero-waste products such as these are likely to become increasingly viable.

AUTHOR CONTRIBUTIONS

JM, AA, and AL contributed to the conception and intellectual framing of the review. JM prepared the literature review and the first draft of the manuscript. AA and AL wrote sections of the manuscript. All authors contributed to the manuscript revision. All authors read and approved the submitted version.

ACKNOWLEDGMENTS

The authors would like to thank the University of Melbourne's Bio-Inspiration Hallmark Research Initiative for seed funding support: https://research.unimelb.edu.au/research-at-melbourne/multidisciplinary-research/hallmark-research-initiatives/bioinspiration.

REFERENCES

Adamatzky, A., and Gandia, A. (2021). On Electrical Spiking of Ganoderma Resinaceum. *Biophys. Rev. Lett.* 16, 133–141. doi:10.1142/S1793048021500089

Adamatzky, A., Tegelaar, M., Wosten, H. A. B., Powell, A. L., Beasley, A. E., and Mayne, R. (2020). On Boolean Gates in Fungal Colony. *Biosystems* 193-194, 104138. doi:10.1016/j.biosystems.2020.104138

Appels, F. V. W., van den Brandhof, J. G., Dijksterhuis, J., de Kort, G. W., and Wösten, H. A. B. (2020). Fungal Mycelium Classified in Different Material

Families Based on Glycerol Treatment. *Commun. Biol.* 3 (1), 334–335. doi:10.1038/s42003-020-1064-4

Appels, F. V. W., Camere, S., Montalti, M., Karana, E., Jansen, K. M. B., Dijksterhuis, J., et al. (2019). Fabrication Factors Influencing Mechanical, Moisture- and Water-Related Properties of Mycelium-Based Composites. *Mater. Des.* 161, 64–71. doi:10.1016/j.matdes.2018.11.027

Arup (2021). Acoustic Panel System Made from Fungi Offers Innovative Circular Design Solution for Workplaces. Available at: https://www.arup.com/projects/foresta-acoustic-panel-system (Accessed October 26, 2021).

Attias, N., Danai, O., Abitbol, T., Tarazi, E., Ezov, N., Pereman, I., et al. (2020). Mycelium Bio-Composites in Industrial Design and Architecture: Comparative Review and Experimental Analysis. *J. Clean. Prod.* 246, 119037. doi:10.1016/j.jclepro.2019.119037

Beasley, A. E., Powell, A. L., and Adamatzky, A. (2020a). *Fungal Photosensors*. arXiv 2003.07825. doi:10.48550/arXiv.2003.07825

Cerimi, K., Akkaya, K. C., Pohl, C., Schmidt, B., and Neubauer, P. (2019). Fungi as Source for New Bio-Based Materials: a Patent Review. *Fungal Biol. Biotechnol.* 6 (1), 1–10. doi:10.1186/s40694-019-0080-y

Chin, A. (2014). Jonas Edvard Nielsen Grows MYX Lamps from Mushroom-Mycelium, Designboom. Available at: https://www.designboom.com/design/jonas-edvard-myx-lamps-mushroom-mycelium-09-02-2014 (Accessed October 26, 2021).

Criti, co. (2022). Organic Materials in Architecture: Inside Mycelium, Porto: Critical Concrete. Available at: https://criti.co/course/view.php?id=61 (Accessed April 12, 2022).

Danielle Trofe Design (2020). A New Paradigm of Sustainability. Available at: https://danielletrofe.com (Accessed October 26, 2021).

Debatty, R., Evans, C., Garcia, P., and Grover, A. (2011). *New Art/Science Affinities*. Carnegie Mellon University, 84–87.

Ecovative (2021a). Ecovative. Available at: https://ecovative.com/our-story/>(Accessed October 16, 2021).

Ecovative (2021b). Ecovative. Available at: https://ecovative.com/foams/>(Accessed October 16, 2021).

Feldman, D. (2008). Polymer History. *Des. monomers Polym.* 11 (1), 1–15. doi:10.1163/156855508x292383

Fungal Architectures (2020). Fungal Architectures. Available at: https://www.fungar.eu (Accessed March 13, 2022).

Gagnier, R. (2000). *The Insatiability of Human Wants: Economics and Aesthetics in Market Society*. University of Chicago Press.

Girometta, C., Picco, A. M., Baiguera, R. M., Dondi, D., Babbini, S., Cartabia, M., et al. (2019). Physico-mechanical and Thermodynamic Properties of Mycelium-Based Biocomposites: a Review. *Sustainability* 11 (1), 281. doi:10.3390/su11010281

Gosden, E. (2016). Ikea Plans Mushroom-Based Packaging as Eco-Friendly Replacement for Polystyrene, the Sydney Morning Herald, 25 February. Available at: https://www.smh.com.au/business/companies/ikea-plans-mushroombased-packaging-as-ecofriendly-replacement-for-polystyrene-20160225-gn331e.html (Accessed October 16, 2017).

Grown.bio (2022). Grown.bio. Available at: https://www.grown.bio (AccessedApril 12, 2022).

Hahn, J. (2021). Hermès Creates Mycelium Version of its Classic Leather Victoria Handbag. Dezeen. Available at: https://www.dezeen.com/2021/03/18/hermes-mycelium-leather-victoria-bag-mycoworks (Accessed October 16, 2021).

Hahn, J. (2020). Major Fashion Houses Will Sell Products Made from Mushroom Leather by Next Year. Dezeen. Available at: https://www.dezeen.com/2020/10/08/mylo-consortium-adidas-stella-mccartney-lululemon-kering-mycelium (Accessed October 16, 2021).

Harrison, R. M., and Hester, R. E. (Editors) (2018). *Plastics and the Environment* (Cambridge: RSC Publishing).

Heisel, F., Schlesier, K., Lee, J., Rippmann, M., Saeidi, N., Javadian, A., et al. ((2017). "Design of a Load-Bearing Mycelium Structure through Informed Structural Engineering," in *World Congress on Sustainable Technologies*–49. WCST-2017) ss. 45 Available at: https://www.block.arch.ethz.ch/brg/files/HEISEL_2017_WCST_design-loadbearing-mycelium-structure_1546891598.pdf (Accessed March 13, 2022).

Hüttner, S., Johansson, A., Teixeira, P. G., Achterberg, P., and Nair, R. B. (2020). Recent Advances in the Intellectual Property Landscape of Filamentous Fungi. *Fungal Biol. Biotechnol.* 7 (16). doi:10.1186/s40694-020-00106-z

Islam, M. R., Tudryn, G., Bucinell, R., Schadler, L., and Picu, R. C. (2017). Morphology and Mechanics of Fungal Mycelium. *Sci. Rep.* 7, 13070. doi:10.1038/s41598-017-13295-2

Jiang, L. (2015). *A New Manufacturing Process for Biocomposite Sandwich Parts Using a Myceliated Core, Natural Reinforcement and Infused Bioresin*. USA: Rensselaer Polytechnic Institute. doi:10.13140/RG.2.1.4166.5528

Jiang, L., Bucinell, R., Li, B., Walczyk, D., and McIntyre, G. (2018). Bioresin Infused Then Cured Mycelium-Based Sandwich-Structure Biocomposites: Resin Transfer Molding (RTM) Process, Flexural Properties, and Simulation. *J. Clean. Prod.* 207, 123e135. doi:10.1016/j.jclepro.2018.09.255

Jiang, L., Walczyk, D. F., and McIntyre, G. (2014b). Vacuum Infusion of Mycelium-Bound Biocomposite Preforms with Natural Resins. *Adv. Compos. Mat. Expo. Comb. Strength Unsurpassed Innov.* Available at: https://www.researchgate.net/profile/Lai-Jiang-2/publication/274139042_Vaccum_Infusion_of_Mycelium-bound_Biocomposite_Preforms_with_Natural_Resins/links/55176c1e0cf2d70ee277bd5c/Vaccum-Infusion-of-Mycelium-bound-Biocomposite-Preforms-with-Natural-Resins.pdf (Accessed March 13, 2022).

Jiang, L., Walczyk, D., and McIntyre, G. (2017a). A New Approach to Manufacturing Biocomposite Sandwich Structures: Investigation of Preform Shell Behavior. *J. Manuf. Sci. Eng. Trans. ASME* 139, 021014. doi:10.1115/1.4034278

Jiang, L., Walczyk, D., and Mcintyre, G. (2014a). "A New Process for Manufacturing Biocomposite Laminate and Sandwich Parts Using Mycelium as a Binder," in American Society for Composites 29th Technical Conference. Available at: https://www.researchgate.net/profile/Lai-Jiang-2/publication/274138941_A_New_Process_for_Manufacturing_Biocomposite_Laminate_and_Sandwich_Parts_using_Mycelium_as_a_Binder/links/55176cb90cf2f7d80a3a7c32/A-New-Process-for-Manufacturing-Biocomposite-Laminate-and-Sandwich-Parts-using-Mycelium-as-a-Binder.pdf (Accessed March 13, 2022).

Jiang, L., Walczyk, D., McIntyre, G., and Bucinell, R. (2016). "A New Approach to Manufacturing Biocomposite Sandwich Structures: Mycelium-Based Cores," in ASME 2016 11th International Manufacturing Science and Engineering Conference (American Society of Mechanical Engineers). MSEC 2016. doi:10.1115/msec2016-8864

Jiang, L., Walczyk, D., McIntyre, G., Bucinell, R., and Tudryn, G. (2017b). Manufacturing of Biocomposite Sandwich Structures Using Mycelium-Bound Cores and Preforms. *J. Manuf. Process.* 28, 50–59. doi:10.1016/j.jmapro.2017.04.029

Jones, D., and Brischke, C. (2017). *Performance of Bio-Based Building Materials*. Sawston: Woodhead Publishing.

Khoo, S. C., Peng, W. X., Yang, Y., Ge, S. B., Soon, C. F., Ma, N. L., et al. (2020). Development of Formaldehyde-Free Bio-Board Produced From Mushroom Mycelium and Substrate Waste. *J. Hazard. Mater.* 400, 123296. doi:10.1016/j.jhazmat.2020.123296

Kompatsiaris, P., and Chrysagis, E. (2020). Crafting Values: Economies, Ethics and Aesthetics of Artistic Valuation. *J. Cult. Econ.* 13 (6), 663–671. doi:10.1080/17530350.2020.1798803

Material District (2022). Greensulate. Available at: https://materialdistrict.com/material/greensulate (Accessed March 13, 2022).

Melbourne Design Week (2021). Waterfront: 'Mushi' – Concept to Prototype. Available at: https://2021.designweek.melbourne/events/mycelium-wetland-an-organic-solution (Accessed October 18, 2021).

Miles, M. (2014). *Eco-aesthetics: Art, Literature and Architecture in a Period of Climate Change*. A&C Black, London: Bloomsbury Publishing.

Miller, K. (2013). How Mushrooms Can Save the World, Discover, Milwaukee: Kalmbach Media Co. Available at: https://www.discovermagazine.com/environment/how-mushrooms-can-save-the-world (Accessed October 27, 2021).

Mirabella, N., Röck, M., Ruschi Mendes Saade, M., Spirinckx, C., Bosmans, M., Allacker, K., et al. (2018). Strategies to Improve the Energy Performance of Buildings: A Review of Their Life Cycle Impact. *Buildings* 8 (8), 105. doi:10.3390/buildings8080105

Moncaster, A. M., Pomponi, F., Symons, K. E., and Guthrie, P. M. (2018). Why Method Matters: Temporal, Spatial and Physical Variations in LCA and Their Impact on Choice of Structural System. *Energy Build.* 173, 389–398. doi:10.1016/j.enbuild.2018.05.039

MycoWorks (2021c). An Advanced Materials Platform. Available at: https://www.mycoworks.com/our-products (Accessed February 24, 2022).

MycoWorks (2021a). Our Heritage: 2014-2016. Available at: https://www.mycoworks.com/ourOur Heritage: 2014-2016: Acceleration-heritage#acceleration (Accessed October 18, 2021).

MycoWorks, (2021b). Reishi Is Fine Mycelium. Available at: https://www.madewithreishi.com/products (Accessed October 18, 2021).

MycoWorks (2021d). Resources. Available at: https://www.mycoworks.com/resources (Accessed October 18, 2021).

Olsson, S., and Hansson, B. S. (1995). Action Potential-like Activity Found in Fungal Mycelia Is Sensitive to Stimulation. *Naturwissenschaften* 82, 30–31. doi:10.1007/bf01167867

F. Pacheco-Torgal, V. Ivanov, and D. C. Tsang (Editors) (2020). *Bio-based Materials and Biotechnologies for Eco-Efficient Construction* (Sawston: Woodhead Publishing).

Pelletier, M. G., Holt, G. A., Wanjura, J. D., Bayer, E., and McIntyre, G. (2013). An Evaluation Study of Mycelium Based Acoustic Absorbers Grown on Agricultural By-Product Substrates. *Industrial Crops Prod.* 51, 480–485. doi:10.1016/j.indcrop.2013.09.008

Rasmussen, S. C. (2018). Revisiting the Early History of Synthetic Polymers: Critiques and New Insights. *Ambix* 65 (4), 356–372. doi:10.1080/00026980.2018.1512775

Rensselaer (2007). Designs on the Future, Rensselaer Winter 2007-08. Available at: https://www.rpi.edu/magazine/winter2007-08/pdi-4.html (Accessed October 16, 2017).

Ross, P. (2017). "Your Rotten Future Will Be Great," in *Routledge Companion to Biology in Art and Architecture*. Editors C. N. Terranova and M. Tromble (Abingdon: Routledge), 370–403.

Sachs, J., Kroll, C., Lafortune, G., Fuller, G., and Woelm, F. (2021). *Sustainable Development Report: A Decade of Action of the Sustainable Development Goals*. Cambridge: Cambridge University Press. Available at: https://s3.amazonaws.com/sustainabledevelopment.report/2021/2021-sustainable-development-report.pdf (Accessed March 12, 2022).

Seymour, R. B. (1988). Polymers Are Everywhere. *J. Chem. Educ.* 65 (4), 327. doi:10.1021/ed065p327

Soh, E., Chew, Z. Y., Saeidi, N., Javadian, A., Hebel, D., and Le Ferrand, H. (2020). Development of an Extrudable Paste to Build Mycelium-Bound Composites. *Mater. Des.* 195, 109058. doi:10.1016/j.matdes.2020.109058

Steffen, A. (2019). IKEA Starts Using Compostable Mushroom-Based Packaging for its Products. Intelligent Living. Available at: https://www.intelligentliving.co/ikea-mushroom-based-packaging (Accessed October 16, 2021).

Stephan, A., Crawford, R. H., and De Myttenaere, K. (2011). Towards a More Holistic Approach to Reducing the Energy Demand of Dwellings. *Procedia Eng.* 21, 1033–1041. doi:10.1016/j.proeng.2011.11.2109

Stott, R. (2014). Hy-fio, the Organic Mushroom Brick Tower Opens at MoMA's PS1courtyard. ArchDaily. Available at: https://www.archdaily.com/521266/hy-fi-the-organic-mushroom-brick-tower-opens-at-moma-s-ps1-courtyard (Accessed October 16, 2017).

Superflux, 2014. *Mycotecture (Phil Ross) Design and Violence*. New York: MoMA Available at: https://www.moma.org/interactives/exhibitions/2013/designandviolence/mycotecture-phil-ross (Accessed October 18, 2021).

Travaglini, S., Dharan, C. K. H., and Ross, P. G. (2016). Manufacturing of Mycology Composites. Proc. Am. Soc. Compos. - 31st Tech. Conf. ASC.

Travaglini, S., Dharan, C. K. H., and Ross, P. G. (2015). "Thermal Properties of Mycology Materials," in Proceedings of the American Society for Composites - 30th Technical Conference.ACS.

Travaglini, S., Dharan, C., and Ross, P. G. (2014). "Mycology Matrix Sandwich Composites Flexural Characterization," in Proceedings of the American Society for Composites - 29th Technical Conference (ASTM-D30 Meeting), 16th., ASC US-Japan Conference on Composite Materials, La Jolla, CA.

Travaglini, S., Noble, J., Ross, P. P. G. P., and Dharan, C. C. K. H. C. (2013). Mycology Matrix Composites. *Annu. Tech. Conf. Am. Soc. Compos.ASC* 1, 517e535. doi:10.1017/CBO9781107415324.004

Van Wylick, A., Monclaro, A. V., Elsacker, E., Vandelook, S., Rahier, H., De Laet, L., et al. (2021). A Review on the Potential of Filamentous Fungi for Microbial Self-Healing of Concrete, *Fungal Biol. Biotechnol.* 8, 16. doi:10.1186/s40694-021-00122-7

Ziegler, A. R., Bajwa, S. G., Holt, G. A., McIntyre, G., and Bajwa, D. S. (2016). Evaluation of Physico-Mechanical Properties of Mycelium Reinforced Green Biocomposites Made from Cellulosic Fibers. *Appl. Eng. Agric.* 32 (6), 931–938. doi:10.13031/aea.32.11830

Conflict of Interest: AL is Research Manager, Arup University. Global parent company, Arup Group, was engaged as engineering consultants for the HyFi Tower, MoMA PS1, developed with architecture practice, The Living, and the Foresta acoustic panels, developed in collaboration with Mogu. Both are mentioned in the article.

The remaining authors declare that the research was conducted in the absence of any commercial or financial relationships that could be construed as a potential conflict of interest.

Publisher's Note: All claims expressed in this article are solely those of the authors and do not necessarily represent those of their affiliated organizations, or those of the publisher, the editors and the reviewers. Any product that may be evaluated in this article, or claim that may be made by its manufacturer, is not guaranteed or endorsed by the publisher.

frontiers | Frontiers in Ecology and Evolution

TYPE Original Research
PUBLISHED 08 September 2022
DOI 10.3389/fevo.2022.954838

OPEN ACCESS

EDITED BY
Devi Stuart-Fox,
The University of Melbourne, Australia

REVIEWED BY
Mingfeng Wang,
Brunel University London,
United Kingdom
Gilles Berillon,
UMR 7194 Histoire Naturelle
de l'Homme Préhistorique, France

*CORRESPONDENCE
William Irvin Sellers
william.sellers@manchester.ac.uk

SPECIALTY SECTION
This article was submitted to
Behavioral and Evolutionary Ecology,
a section of the journal
Frontiers in Ecology and Evolution

RECEIVED 27 May 2022
ACCEPTED 22 August 2022
PUBLISHED 08 September 2022

CITATION
Sellers WI, Cross CF, Fukuhara A,
Ishiguro A and Hirasaki E (2022)
Producing non-steady-state gaits
(starting, stopping, and turning) in a
biologically realistic quadrupedal
simulation.
Front. Ecol. Evol. 10:954838.
doi: 10.3389/fevo.2022.954838

Producing non-steady-state gaits (starting, stopping, and turning) in a biologically realistic quadrupedal simulation

William Irvin Sellers[1]*, Charlotte Francesca Cross[1], Akira Fukuhara[2], Akio Ishiguro[2] and Eishi Hirasaki[3]

[1]Department of Earth and Environmental Sciences, University of Manchester, Manchester, United Kingdom, [2]Research Institute of Electrical Communication, Tohoku University, Sendai, Japan, [3]Primate Research Institute, Kyoto University, Kyoto, Japan

Multibody dynamic analysis (MDA) has become part of the standard toolkit used to reconstruct the biomechanics of extinct animals. However, its use is currently almost exclusively limited to steady state activities such as walking and running at constant velocity. If we want to reconstruct the full range of activities that a given morphology can achieve then we must be able to reconstruct non-steady-state activities such as starting, stopping, and turning. In this paper we demonstrate how we can borrow techniques from the robotics literature to produce gait controllers that allow us to generate non-steady-state gaits in a biologically realistic quadrupedal simulation of a chimpanzee. We use a novel proportional-derivative (PD) reach controller that can accommodate both the non-linear contraction dynamics of Hill-type muscles and the large numbers of both single-joint and two-joint muscles to allow us to define the trajectory of the distal limb segment. With defined autopodial trajectories we can then use *tegotae* style locomotor controllers that use decentralized reaction force feedback to control the trajectory speed in order to produce quadrupedal gait. This combination of controllers can generate starting, stopping, and turning kinematics, something that we believe has never before been achieved in a simulation that uses both physiologically realistic muscles and a high level of anatomical fidelity. The gait quality is currently relatively low compared to the more commonly used feedforward control methods, but this can almost certainly be improved in future by using more biologically based foot trajectories and increasing the complexity of the underlying model and controllers. Understanding these more complex gaits is essential, particularly in fields such as paleoanthropology where the transition from an ancestral hominoid with a diversified repertoire to a bipedal hominin is of such fundamental importance, and this approach illustrates one possible avenue for further research in this area.

KEYWORDS

primate locomotion, biorobotics, biomechanics, simulation, quadrupedalism, chimpanzee

Introduction

Forward dynamic modeling, where muscle forces are used to drive the kinematics of a link-segment model, has a long history in locomotor biomechanics [e.g., (Hatze, 1977; Onyshko and Winter, 1980; Van den Bogart et al., 1989; Yamazaki et al., 1996)]. Its use in paleontology has grown over the last 25 years, particularly in paleoanthropology with the first models attempting to generate movements based on fossil morphology appearing in the late 1990s (Crompton et al., 1998; Kramer, 1999) followed by muscle driven models in the early 2000s (Sellers et al., 2004, 2005; Nagano et al., 2005; Ogihara and Yamazaki, 2006). Other vertebrates have also been simulated, starting with very simple 2D dinosaur models (Sellers and Manning, 2007) which were rapidly extended to 3D (Sellers et al., 2009), with increasing sophistication in terms of anatomical realism and including additional mechanical modalities to reduce the uncertainty of the predictions (Sellers et al., 2017). Whilst there are plenty of non-locomotor studies using MDA [for review see Lautenschlager (2020)], there are far fewer on locomotion. One particularly noteworthy example is a study on the early amniote *Orobates* that also included validation of the simulation by creating a physical robot (Nyakatura et al., 2019) and there a several examples of purely robotic studies of fossil vertebrates which attempt to understand mechanical and control features of the extinct organism [e.g., (Takita et al., 2000; Fukuoka and Akama, 2014; Zhao et al., 2022)].

Roboticists have been producing legged mobile robots inspired by animals for a much longer time. We can certainly find examples of mechanical legged automata dating back to the 15th century such as Leonardo Da Vinci's self-propelled mechanical lion (Rosheim, 2006) and the first autonomous, computer-controlled legged robot was probably the "Phony Pony" built by Frank and McGhee (McGhee, 1967; Frank, 1968). Since then, there have been a large number of bipedal and quadrupedal autonomous robots created both physically and as computer simulations. However, very few of these embrace the restrictions imposed by the physiology and anatomy of legged vertebrates. Skeletal muscle contracts in a highly non-linear fashion (Hill, 1938), usually acts in series with relatively compliant passive connective tissue (Hill, 1950), and has a relatively low power availability [maximum 390°Wkg^{-1} (Askew et al., 2001)] compared to modern actuators such as brushless DC motors which can easily exceed this by an order of magnitude (Larmine and Lowry, 2012). Similarly, vertebrates are highly redundant in terms of their actuation with a typical high quality quadrupedal musculoskeletal model having over 100 individual muscles (Larmine and Lowry, 2012; Sellers et al., 2013) operating over 12 or 16 joints. The real picture is even more extreme with vertebrate muscular control acting at the motor unit level and each skeletal muscle having 100–200 functional motor units (Gooch et al., 2014), although this level of complexity has yet to find its way into simulations.

This actuator complexity has made generating control patterns for anatomically and physiologically realistic models challenging. The number of actuators and their mixed functions means that the control problem has a high dimensionality and the common solution to this problem has been to rely on various machine learning algorithms to generate activation patterns. One approach is to use genetic algorithms to generate finite state feedforward controllers and this approach can results in spontaneous, high-quality gait (Sellers et al., 2003, 2004), but with the disadvantage that these simulations are computationally very expensive to generate. Alternative feedforward approaches include direct colocation (De Groote et al., 2016) and direct shooting (Anderson and Pandy, 2001) and whilst these are generally much quicker to calculate and excellent techniques when the overall pattern of locomotor kinematics are well-understood, they perform less well when the kinematics are complex or good models for the locomotor patterns do not exist. Instead, fully controlled solutions can be produced where the subsequent activation pattern is dependent entirely on the current state including feedback from sensory inputs. This can include black box solutions based on deep neural net reinforcement learning e.g., (Kidziński et al., 2018; Tsounis et al., 2020) or more transparent control solutions based on modulated central pattern generators e.g., (Aoi et al., 2010; Owaki et al., 2012). The advantage of controlled solutions is that they avoid the instability inherent in feedforward solutions and can potentially generalize to different environments, different gaits, and alterations in the actuators due to injury or fatigue. The disadvantage is that they generally cannot beat the locomotor performance metrics, whether top speed or energy economy, that can be achieved using highly optimized and highly specific feedforward solutions.

The goal of this paper is to extend current high bio-fidelity anatomical and physiological simulations so that they can produce non-steady-state gaits. Accelerating from a standstill to a steady speed, decelerating to stable standing, and being able to turn corners are the minimum competencies required by a legged animal and so these were set as the primary goals. The current work is simulation-based since part of the problem is coping with the challenges of physiologically realistic muscles and these are currently only possible to achieve in simulation although the use of freshly dissected vertebrate muscle as actuators might provide a physical solution in future (Shimizu et al., 2017). We chose our existing chimpanzee simulation framework both for its relevance to human evolution studies as well as representing one of the most detailed and

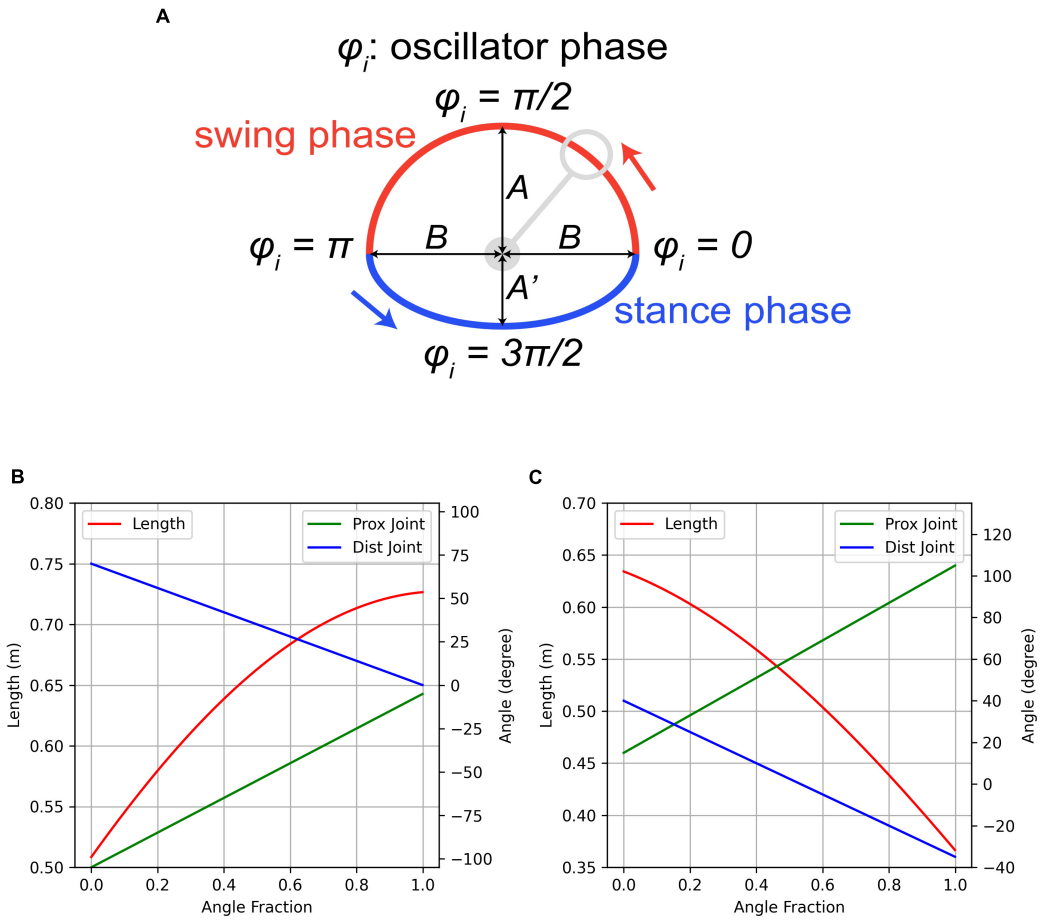

FIGURE 1
Diagram illustrating the control process. **(A)** Phase diagram for the *tegotae* controller illustrating the movement of the target point. **(B)** Forelimb joint angle controller illustrating how the angle fraction specifies the individual joint angles and the overall length. **(C)** Hindlimb joint angle controller illustrating how the angle fraction specifies the individual joint angles and the overall length.

well-tested quadrupedal models currently available (Sellers and Hirasaki, 2018).

Materials and methods

We wanted to provide a simple, transparent approach as an initial proof of concept and so this work is based on the *tegotae* central pattern generation with the individual oscillators entrained by reaction force feedback (Owaki et al., 2012; Fukuhara et al., 2016, 2018). In a quadrupedal robot this system drives the distal limb contact point in an approximately elliptical trajectory with the angular velocity (omega) modulated by the ground reaction force at the contact. The trajectory shape is controlled by three parameters that specify its horizontal (B) and vertical dimensions (A, Aprime), and there is fifth parameter that specifies the modulation gain from the ground reaction force (sigma), and the initial phase angle of the controller is also specified (phi). This process is illustrated in **Figure 1A**. This controller was implemented in the freely available open-source code GaitSym2019[1] in TegotaeDriver.cpp and the progression of the trajectory target is specified each time step by the following pseudocode (where *N* is the ground reaction force, *X* and *Y* are the coordinates of the trajectory, and deltaT is the time step of the simulation):

```
phi_dot = omega-sigma * N*cos(phi);
X = B * cos(phi);
if (phi < M_PI) Y = A * sin(phi);
else Y = Aprime * sin(phi);
phi = mod(phi + phi_dot * deltaT,
2 * M_PI);
```

This is a trajectory-based approach and so we needed to create lower-level controllers for the individual muscles

1 https://github.com/wol101/GaitSym2019

so that the contact point on the autopodia tries to follow the specified path. Reaching to a specified location in space is a completely standard robot arm activity and there are a very large number of algorithms that can achieve this [for review see Gasparetto et al. (2015)]. However, these suffer from exactly the same issues of redundant activators in the bio-realistic vertebrate context and so we developed a novel heuristic approach inspired by our previous work in leaping biomechanics (Sellers, 1996). In this work we needed to generate a specified trajectory for the whole-body center of mass by controlling the individual joint angles in the hindlimb which is an analogous problem to the one presented here. The *tegotae* controller specifies the desired position of the contact point relative to the proximal joint (the hip or shoulder) so we know the desired total length of the limb. If we allow the two distal joints (knee and ankle, or elbow and wrist) to increase from their minimum to maximum angles, and we have arranged the signs of the joint angles such that minimum angle corresponds to minimum length and maximum angle corresponds to maximum length then we can define a simple function that specifies the joint angles required for a specific limb length. We can also apply weighting factors so that we can prefer to activate a specific joint at different reach lengths. The only requirement is that the controlled change of angles leads to a monotonic change in overall length so that a unique angle fraction can be calculated from a desired length. The interaction between the angle fraction, individual joint angles and the limb length in the chimpanzee fore-and hind-limb are illustrated in **Figures 1B,C**. Once these angles are known, we can easily calculate the proximal joint angle required to achieve colocation of the distal contact point with the required trajectory. This approach requires certain assumptions about

TABLE 1 The ranges set for the *tegotae* controller values before optimization.

Value	Minimum	Maximum
Hand sigma	1.00E-05	1.00E-01
Hand A	0.05	0.1
Hand A prime	0.02	0.05
Hand B	0.1	0.25
Foot sigma	1.00E-05	1.00E-01
Foot A	0.05	0.1
Foot A prime	0.02	0.05
Foot B	0.1	0.25

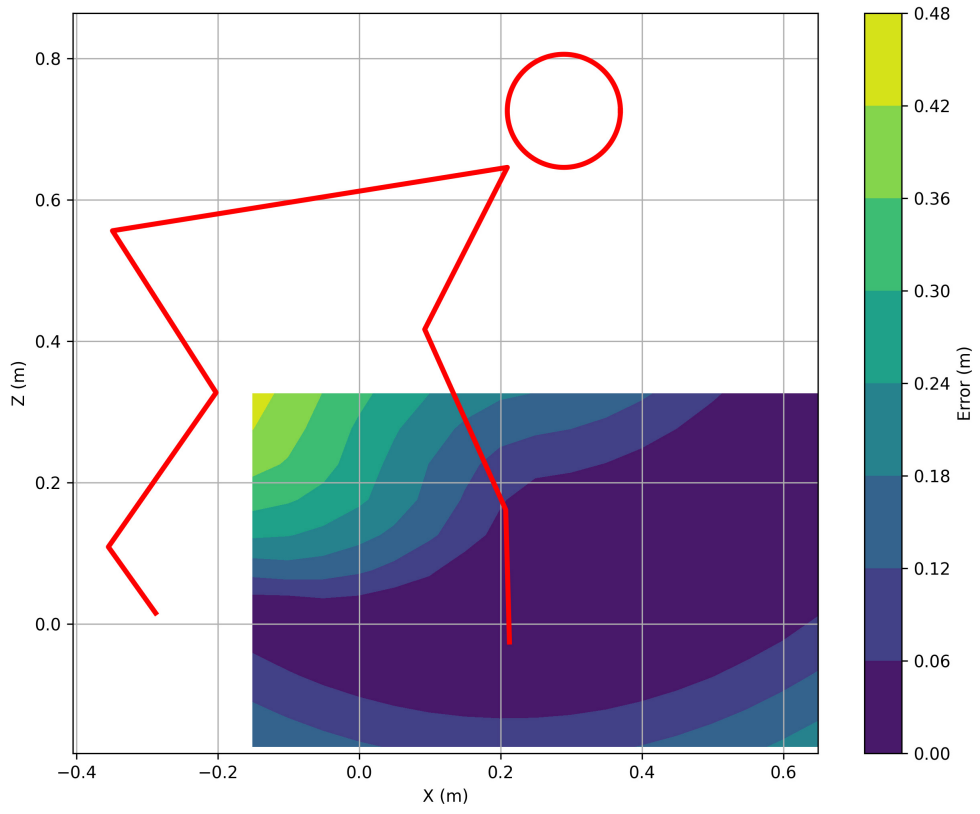

FIGURE 2
Contour plot of the colocation error magnitude for the forelimb tracking a target. The low error zone in dark blue shows the effective domain of the controller with the specified angular excursions, and the red line shows the initial pose of the model.

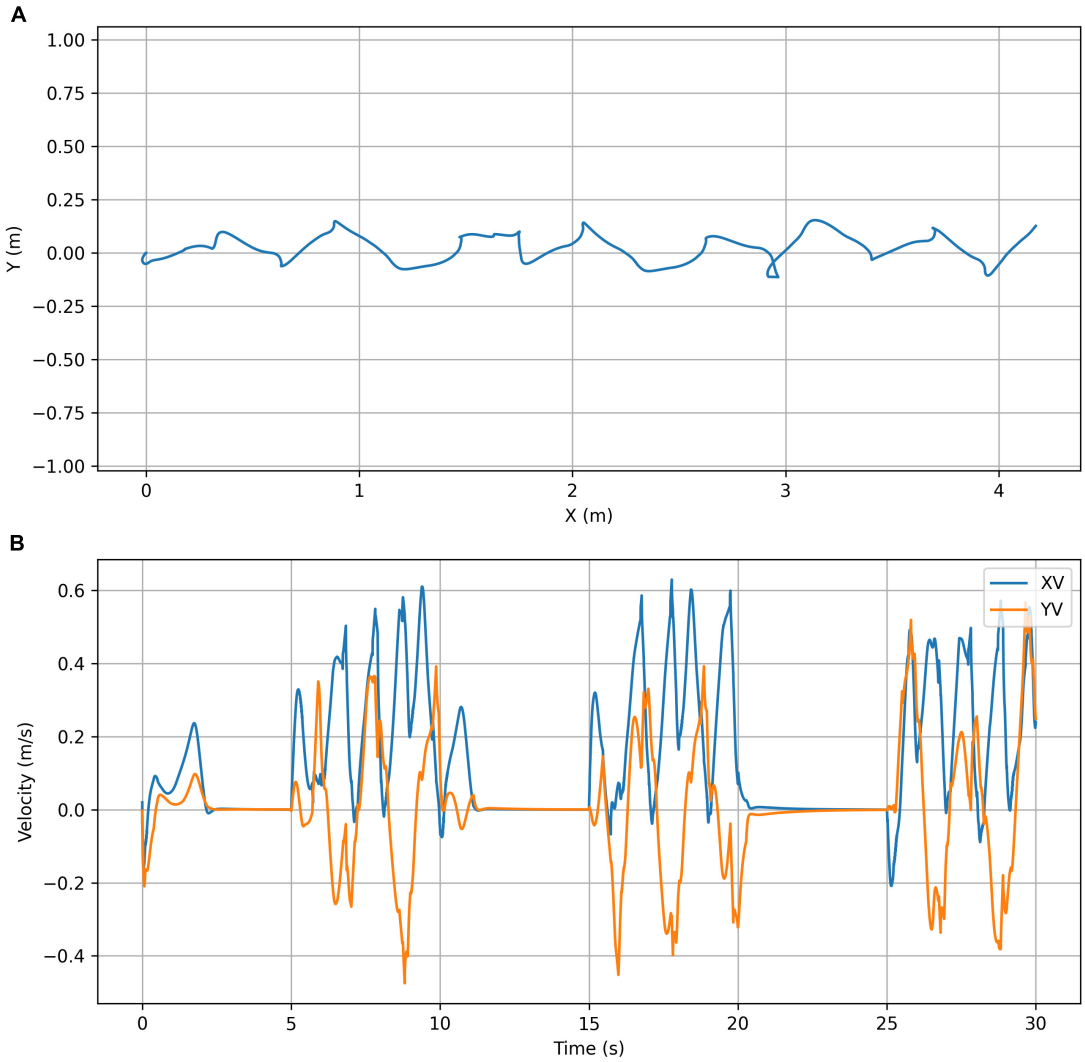

FIGURE 3
Start-stop simulation plots. **(A)** Trajectory plot showing the top view of the path taken by the center of mass of the chimpanzee's torso. **(B)** Velocity plot showing the X (forward) velocity and Y (lateral) velocity of the center of mass of the chimpanzee's torso.

the angular ranges available and will restrict the available positions for the contact point. Fortunately, whilst this might be a problem in the context of reaching for manipulation, it is not a problem for locomotor use since the desired locations are a small subset of all the possible places the autopodia can reach. Once all the desired joint angles are known then we can calculate the desired lengths for all the muscles in the limb including those that cross multiple joints, and we can achieve these desired lengths using simple PD length controllers on the individual muscles. There are issues with co-contraction that can cause problems in edge cases but in the restricted context of a limited reach target domain this approach works adequately and is extremely easy to both implement and calculate. It is implemented in GaitSym2019 as ThreeHingeJointDriver.cpp although the implementation only requires the two distal joints to be hinges, and the proximal joint can be a hinge joint, a universal joint, or a ball joint. The function of this driver can be defined by the following steps:

1. calculate the desired limb length,
2. calculate the angle fraction that generates the desired limb length at the distal two joints,
3. find the rotations about the local X and Y axes at the proximal joint (if this is a hinge joint then the X angle will be zero),
4. create a copy of the limb posed using the calculated angles,
5. read off the muscle lengths from the limb copy,
6. use these lengths as target lengths for the original limb muscles.

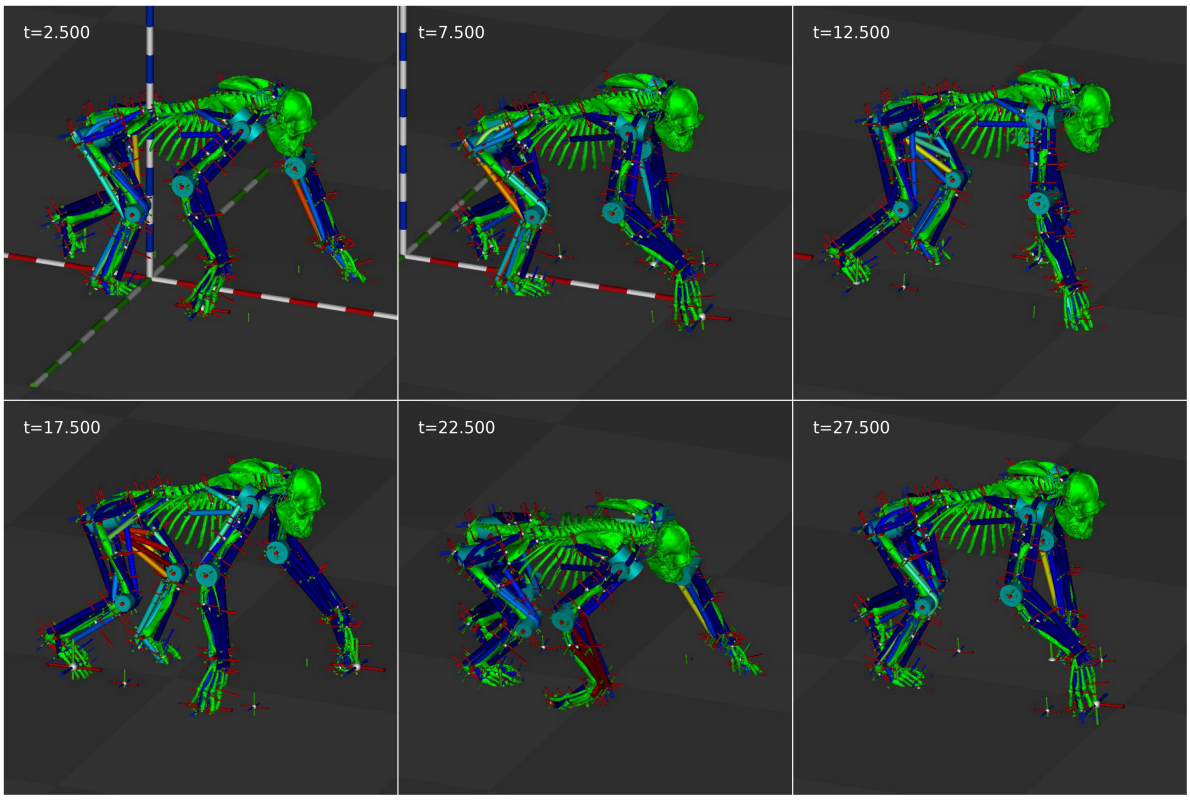

FIGURE 4
Still frames from the start-stop animation at 5 s intervals.

Step 5 hides a lot of complexity because the lengths of the various muscles can be quite difficult to calculate, especially if they wrap around objects in their paths. Fortunately, by building the limb copy in the desired pose, all of this calculation is handled by the GaitSym strap functions (TwoPointStrap.cpp, NPointStrap.cpp, CylinderWrapStrap.cpp, and TwoCylinderWrapStrap.cpp) and the required lengths can simply be read from the posed limb copy.

The chimpanzee musculoskeletal model is based on a CT scan of an adult male zoo specimen combined with dissection-based literature values for muscle parameters and has been detailed elsewhere (Sellers et al., 2013; Sellers and Hirasaki, 2018). The full specification of the model (dimensions, mass properties, muscle paths, and joint limits) is available in the human-readable **supplementary information** model data files. The extracted bone and skin meshes are also provided. The previous model used finite state feedforward drivers and these were removed before adding the additional specifications for the new drivers. This includes the PD length controllers for each muscle, the *tegotae* driver for each limb, and the three-hinge driver for each limb. The gain constants for the PD controllers were set by hand since the simulation proved not to be very sensitive to the specific values chosen (Kp = 200, Kd = 20). The angle limits for the three hinge drivers were set following the likely angular excursions seen in quadrupedal locomotion in chimpanzees (Watson et al., 2009). In the *tegotae* driver, omega was controlled directly to allow stopping and starting, and the initial value of phi was set to represent an appropriate phase difference between the limbs (Watson et al., 2011). The other values were set using a genetic algorithm optimizer, although since there are only eight independent values (see **Table 1**) the choice of optimization technique is not important. The optimizer fitness was set in different ways depending on the current goal. For the starting and stopping experiments it was the distance traveled forward. For the turning experiments it was the angle turned as well as the distance traveled in a circle. Omega was set to different values through the experiment to cause the simulation to accelerate from standing at the beginning and decelerate to standing at the end in all cases.

The simulation runs in almost real time on a standard desktop computer and each simulated locomotor bout is up to 30 s long. With only eight parameters to find, the optimization process is completed in a few hours since the genetic algorithm optimizer can take advantage of multiple cores on multiple networked computers using the local Condor Cluster at the University of Manchester. Genetic algorithm optimizers do not require any knowledge of gradients and can

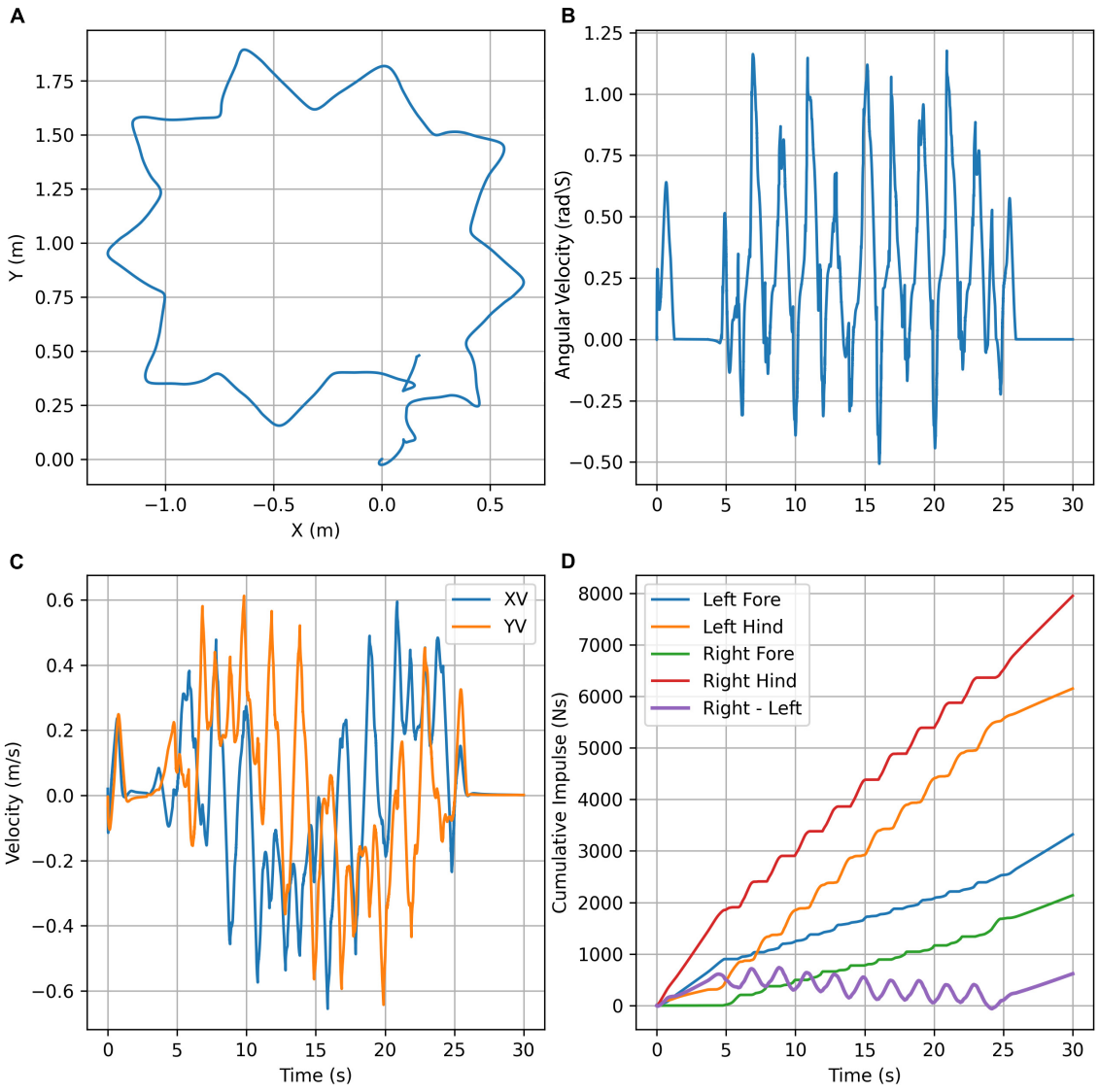

FIGURE 5
Turning simulation plots. **(A)** Trajectory plot showing the top view of the path taken by the center of mass of the chimpanzee's torso. **(B)** Angular velocity of the torso about the Z (vertical) axis. **(C)** Velocity plot showing the X (forward) velocity and Y (lateral) velocity of the center of mass of the chimpanzee's torso. **(D)** The vertical cumulative impulse at the contact points and the difference between the totals on the right-and left-hand sides.

cope with non-linear and discontinuous fitness functions so functioned well in this case although it is likely that other optimization algorithms could be considerably faster if that was an important consideration.

Results

The initial test was to check whether the reach controller could provide adequate positional control. This was done using a grid of target locations that needed to be lined up with the contact point on the distal limb segment. The target location is moved to the different locations on the grid and the controller then activates the muscles to achieve the required colocation. Figure 2 shows the results of this test for the forelimb controller and shows that the controller can drive a horizontal stride length of at least 0.7 m with a height range that varies depending on the limb position but is likely to be at least 0.2 m at mid stance. The actual range of movement of a chimpanzee hand is very much larger than this, but this range is more than adequate for quadrupedal locomotion. Supplementary Video 1 shows the process of tracking the moving target in action.

The second test was to see whether we could create controllers that could produce bouts of stable starting and

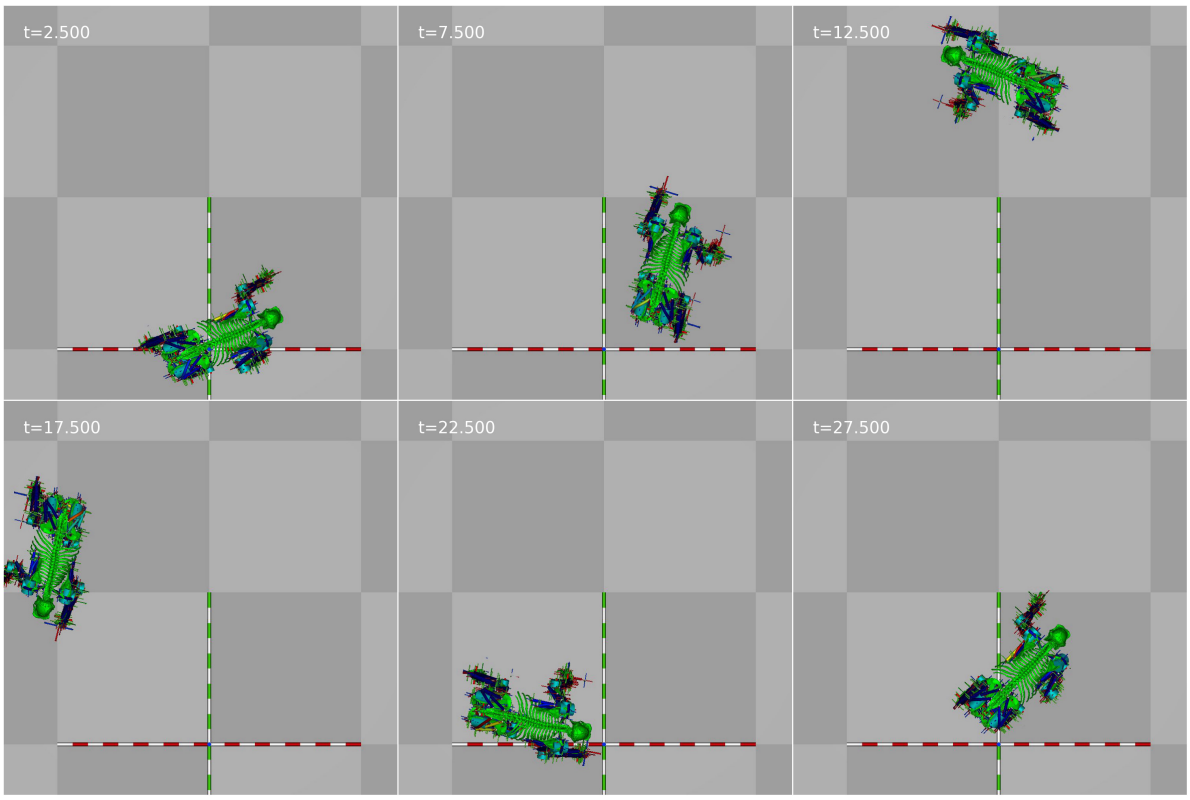

FIGURE 6
Still frames from the turning animation at 5 s intervals.

stopping. This used a fixed omega of zero for 5 s followed by πrad/s for 5 s, repeated three times for a 30 s start-stop sequence. **Figure 3** shows the position and velocity profile of the simulation and **Figure 4** shows its appearance at 5 s intervals. An animation of the gait achieved is shown in the **Supplementary Video 2**. It is clear that the controller is able to achieve the required start-stop locomotion with the simulation coming to rest for 5 s at 5 s intervals. However, the gait during the periods of movement has a very high variability in its forward velocity. There are also periods where the velocity is negative and this represents times when the *tegotae* driver is at rest and the PD controllers are finding stable muscle lengths.

The third test was to see whether we could achieve turning locomotion from a standing start. This test used a fixed omega of zero for 5 s, π rad/s for 20 s, and zero for the last 5 s. The values for B (effectively the stride length) on the left side were decreased by 5% whilst the values of B on the right side were increased by 5% so that the simulation would turn to the left. **Figures 5A,C,D** shows the position and velocity profile of the simulation as well as the vertical impulse under each contact and **Figure 6** shows its appearance at 5 s intervals. An animation of the gait achieved is shown in the **Supplementary VIdeo 3**. In this case, the controller is able to achieve the required turning locomotion relatively easily although falling over was much more common in turning than in traveling in a straight line which would suggest that the gait is less stable than that achieved in the start-stop experiments, and we can see from **Figure 5B** that the turning velocity is by no means constant.

It is hard to judge the quality of the achieved gait from the non-steady-state examples since there is very little to compare with. We do not have good performance criteria for non-steady animal gaits either experimentally or in simulation. The most that can be said is that qualitatively the appearance is reasonable but much less fluid than that observed from a living chimpanzee (although that is true for all simulated gaits using rigid torsos). However, it is possible to use the same controllers to generate continuous gaits by including omega as an optimisable parameter and following the gait morphing process where the mid-point of a previous simulation is used as the starting condition for the next simulation (Sellers et al., 2004). We can then use the distance traveled in a specified time as a fitness criterion for maximizing forward velocity, and the distance traveled for a specified metabolic energy cost as a fitness criterion for maximizing the energy efficiency. **Table 2** shows the maximum forward velocity and efficiency values achieved by the simulation using the new controllers as well as the values that were obtained with the same model but using feed forward controllers (Sellers and Hirasaki, 2018). Here we can

TABLE 2 Forward velocity and cost of transport values for the current controller optimized for either efficiency or forward velocity compared to values obtained using the same model but with a purely feedforward finite state controller (Sellers and Hirasaki, 2018).

Run	Distance (m)	Energy (J)	Time (s)	Velocity (m/s)	Cost of transport (J/kg.m)
tegotae efficiency	8.57	5000	9.10	0.94	8.77
tegotae velocity	6.01	4265	5.00	1.20	10.67
Feedforward $Fr = 0.25$	7.73	2203	8.88	0.87	4.29
Feedforward $Fr = 0.5$	5.28	2484	4.06	1.30	7.08

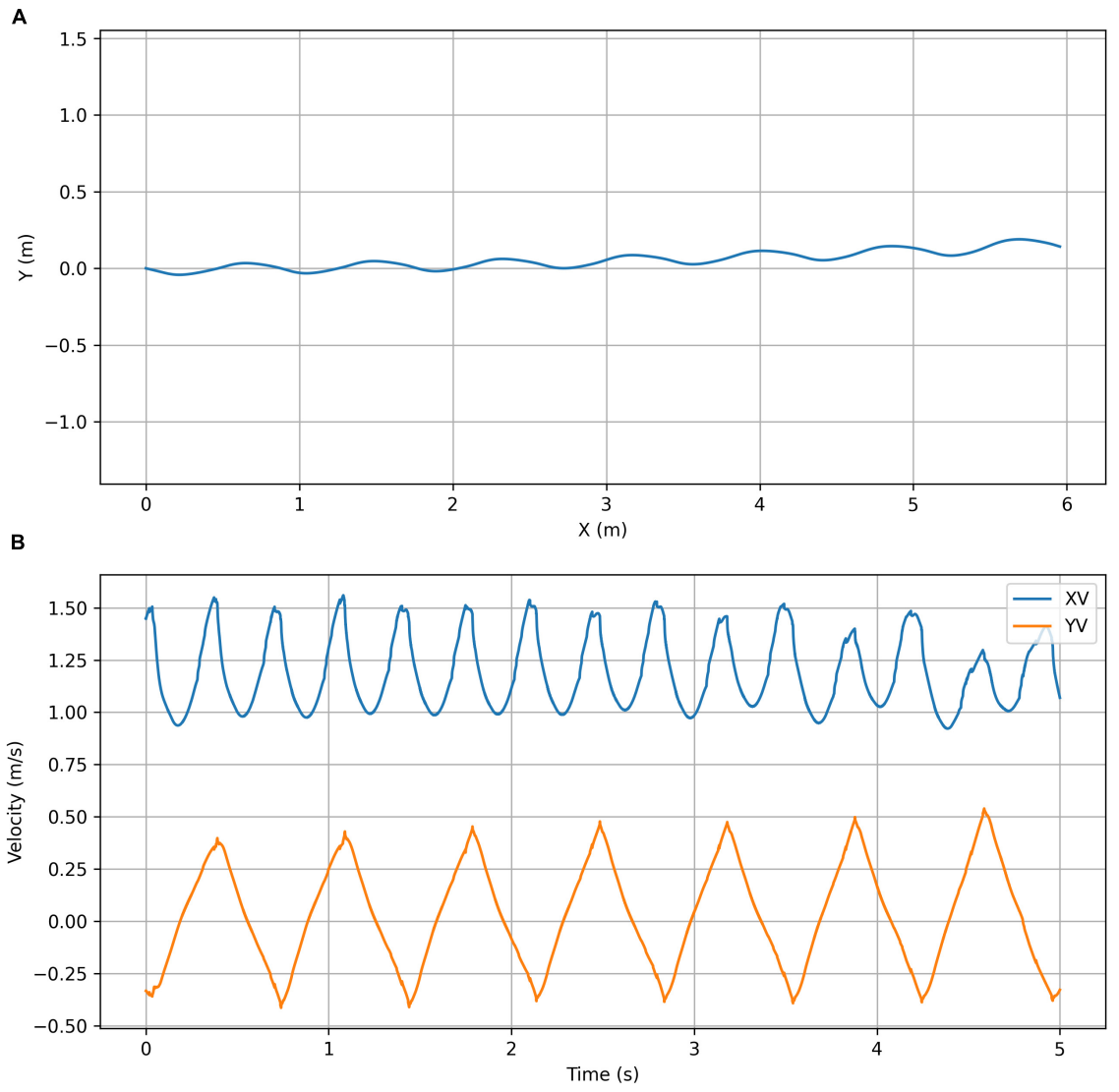

FIGURE 7
Optimized for forward velocity simulation plots. **(A)** Trajectory plot showing the top view of the path taken by the center of mass of the chimpanzee's torso. **(B)** Velocity plot showing the X (forward) velocity and Y (lateral) velocity of the center of mass of the chimpanzee's torso.

see that whilst the new controllers allow steady-state gait to be produced, their performance is worse than that achieved by highly tuned feedforward controllers, particularly for metabolic energy efficiency. Looking at the trajectory plots (Figures 6, 7) we can see that the continuous gaits still vary in forward velocity but never drop to zero as was found in non-steady-state examples. The montage frames (Figures 8, 9) and their respective animations (Supplementary Videos 4, 5) show much improved gaits compared to non-steady-state examples with much smoother movements. Unlike previous robotics work

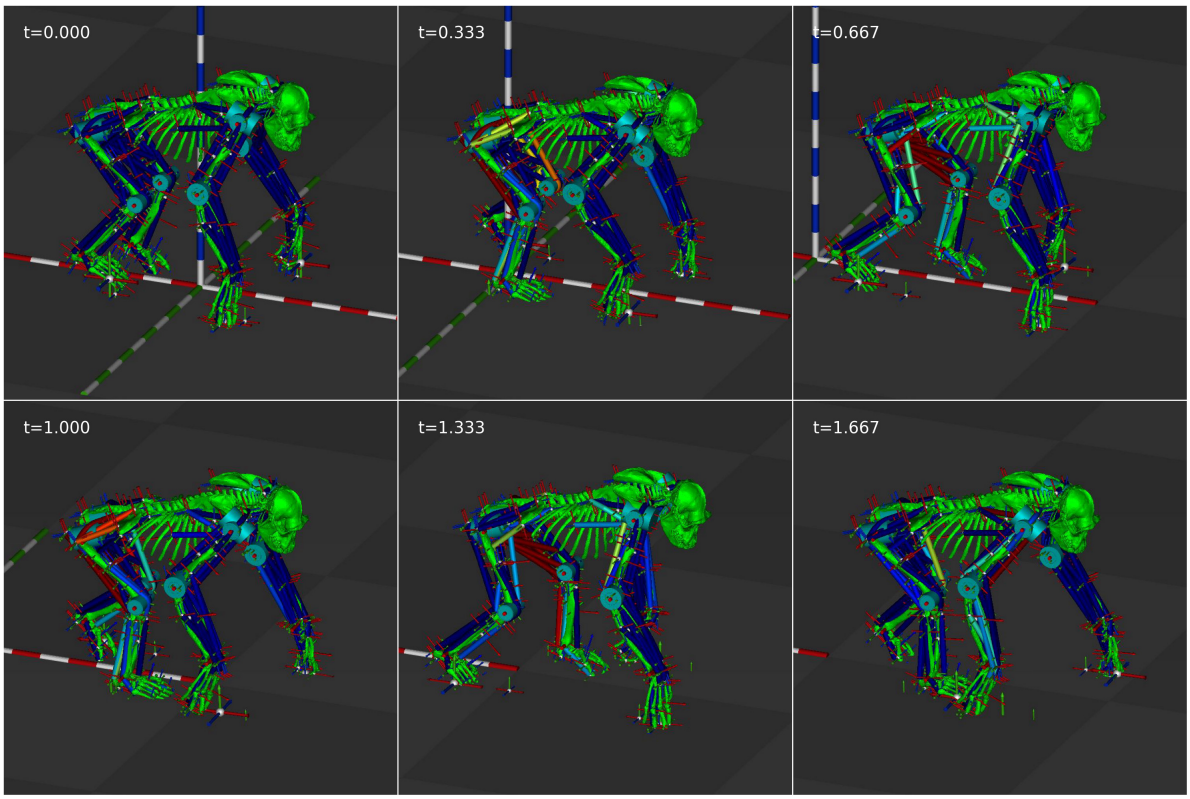

FIGURE 8
Still frames from the efficiency optimized animation at 0.333 s intervals.

using the same control system (Owaki and Ishiguro, 2017) we were unable to get spontaneous gait transitions to non-walking gaits. This has been achieved previously in feedforward simulations (Sellers et al., 2009) but was also not achieved with feedforward chimpanzee model (Sellers and Hirasaki, 2018).

Discussion

Our results demonstrate a novel way of achieving certain steady-state (walking at constant speed) and non-steady-state gaits (starting, stopping, and turning) in an anatomically and physiologically realistic quadrupedal vertebrate. The *tegotae* controller implementation, originally developed for legged robot control using biologically inspired ideas about central pattern generation (Owaki et al., 2012; Fukuhara et al., 2016), is therefore shown to generalize to a very different actuation and stability environment where the muscles are non-linear, the power availability is relatively low, and the aspect ratio of the body means that the risks of lateral tipping are high. We also demonstrate the utility of our simple heuristic reach controller as a way of coping with the large numbers of muscles that exist in anatomically realistic simulations, which is an essential part of allowing the contacts points in the simulation to follow the trajectories required for the gait controller. The implementation requires minimal computer power because there are relatively few global parameters to be optimized to produce effective locomotion. Starting and stopping are easy to generate (**Figures 2**, **3**) and this matches previous work with this control system (Fukuhara et al., 2016). Turning by changing the step length asymmetrically also works but it is somewhat less successful (**Figures 4**, **5**) probably because it is a considerable over-simplification of the process of turning gaits in quadrupeds [e.g., (Hase and Stein, 1999; Jindrich and Full, 1999; Walter, 2003; Demes et al., 2006)]. The vertical impulse (**Figure 5D**) illustrates how the turn is driven by increased reaction forces on the outer side with the largest contributions from the rear limbs matching the hind-limb drive model long associated with primate locomotion (Kimura et al., 1979) and highlighted as "hindlimb steering" in primate turning studies (Demes et al., 2006). Ideally the quality of these gaits could be compared to data obtained experimentally. There are excellent chimpanzee treadmill studies [e.g., (Taylor and Rowntree, 1973; Pontzer et al., 2014)] but these focus exclusively on straight line, constant speed locomotion. Kinematic studies on free-ranging chimpanzees [e.g., (Watson et al., 2009; Finestone et al., 2018)] could provide information on starting, stopping, and turning but to date they have also focused exclusively on

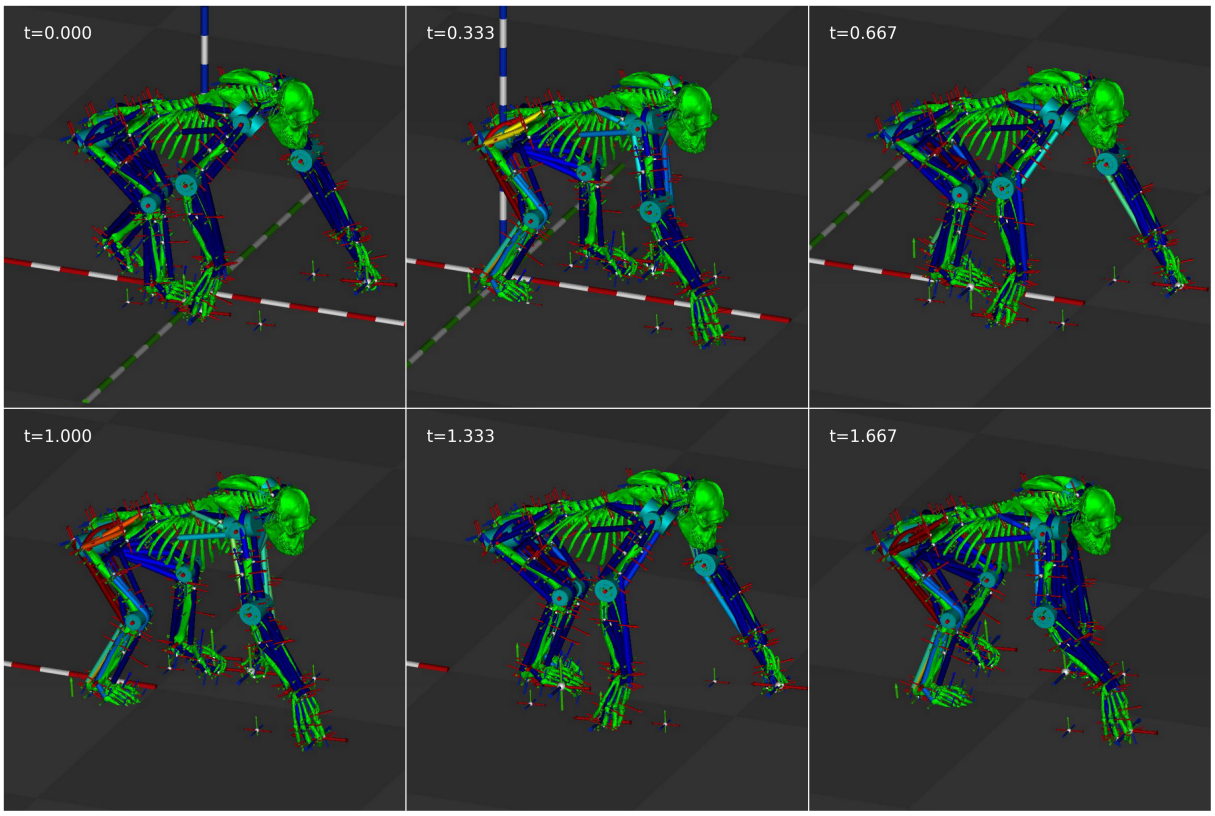

FIGURE 9
Still frames from the forward velocity optimized animation at 0.333 s intervals.

steady state locomotion. There is an interest in elucidating the role of non-steady state gaits in primate evolution [e.g., (Li et al., 2004)] but, with no formal studies as yet, this should prove a fruitful area for future research. Field researchers have long characterized the frequency of different gaits observed in free ranging chimpanzees [e.g., (Doran, 1992)] illustrating the appreciation that there is a need to understand the full range of locomotor capabilities seen in living and fossil primates. In addition, various forms of locomotion are recognized as a major selective factor in the context of human evolution [e.g., (Taylor and Rowntree, 1973; Pontzer and Wrangham, 2004; Crompton et al., 2010)]. However, getting kinematic information for an extended gait repertoire necessitates working with free-ranging animals and it is only recently that we have had good techniques for obtaining the necessary 3D information relatively easily from unmarked animals (Sellers and Hirasaki, 2014; Nath et al., 2019). We hope that providing a simulation framework that can accommodate some of these gaits will provide the necessary impetus for further work in this important area.

The controller can also produce continuous gaits (**Figures 6–8**, **10**) but these are considerably less accomplished than those produced by feedforward controllers using the same underlying model (**Table 2**). We would speculate that this is due to the magnitude of the speed changes of the simulation, and that this is probably caused by the variations in the speed of the contact point trajectory not exactly matching the natural pendular speeds of the system. This would mean that the individual limbs need to be driven actively by muscle contraction throughout the gait cycle, whereas in a highly tuned feedforward system, because the various pendular frequencies can be matched, the movement can be driven by a largely passive interchange of kinematic and potential energies within the body (McGeer, 1990).

It is very likely that steady-state legged locomotion is a largely feedforward controlled process, if only because the conduction time for neural signals means that direct feedback control is probably not possible and that any necessary error correction occurs at some temporal offset to the error detection (More et al., 2010). However, animals need to cope with non-steady-state activities such as those presented here and these are not currently easy to achieve using current simulation technology when the underlying model attempts to accurately reflect the physiology and anatomy of a cursorial vertebrate. Our current system therefore

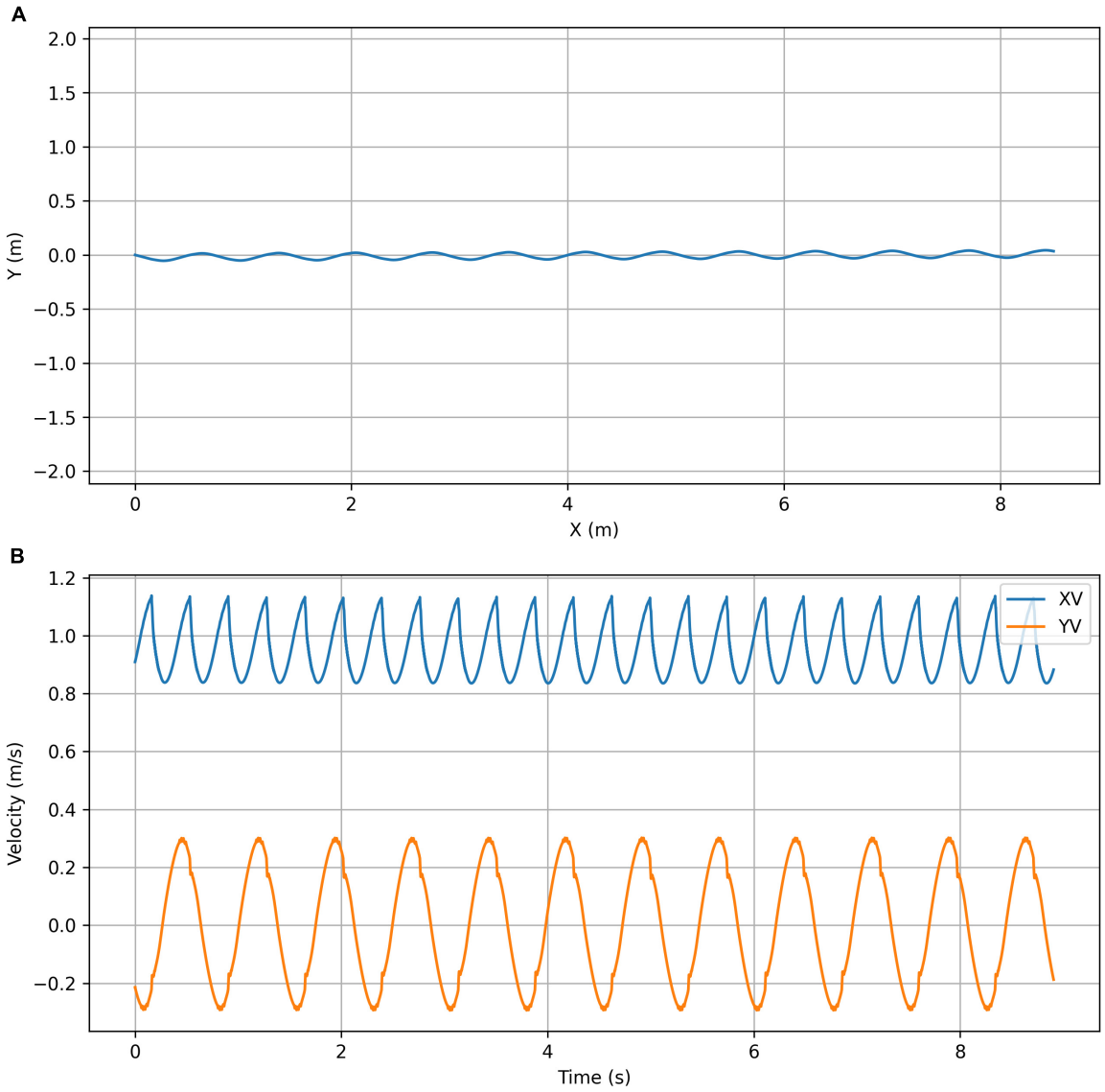

FIGURE 10
Optimized for efficiency simulation plots. **(A)** Trajectory plot showing the top view of the path taken by the center of mass of the chimpanzee's torso. **(B)** Velocity plot showing the X (forward) velocity and Y (lateral) velocity of the center of mass of the chimpanzee's torso.

provides a useful starting point for further work in this area. Our simulation is entirely forward dynamic, and could potentially be driven across a complex environment and have the option of choosing different routes, gaits and velocities as required. This would require a small library of control parameters that could be built up for the different requirements, and since there are only nine required in the current implementation, it should not be hard to transition between the required locomotor outcomes. Whilst this may not currently tell us very much about how animals achieve the precise levels of control they demonstrate, it means that we can expand locomotor reconstructions to consider the complete behavioral repertoire, and we can then analyses the form/function/environment interactions at a completely new level of complexity and brings us one step closer to the "Virtual World of Paleontology" (Cunningham et al., 2014).

To achieve this step change in locomotor simulation we clearly need to improve aspects of our controllers. The heuristic reach control system does not cope well with the problems of co-contraction and so is always likely to increase the energy requirement required for a movement whilst at the same time reducing the maximum power available. Fortunately, there are other more sophisticated reach control algorithms and it would certainly be possible to obtain the required reach behavior using an artificial neural network

approach (Vilaplana and Coronado, 2006). Indeed, the current controller could be used to generate training data where the current model state is used as an input, and the muscle activation pattern is used as an output, and the accuracy and speed of the location matching used as a performance indicator. The *tegotae* controller currently only uses a single reaction force feedback input, and the controlled trajectory is approximately elliptical. However, there are other sensory inputs that could be used to further modify the trajectory, and the trajectory itself can be modeled on generalized foot trajectories obtained from quadrupedal animals using some of the ideas from kinematic motion primitive studies (Spröwitz et al., 2014). Lateral stability could be improved by allowing the lateral location of the desired trajectory to move to compensate for sideways titling of the body and turning performance could be improved by allowing the desired foot trajectory to turn before the body itself. A feature of the physical quadrupeds that previously used this controller is a flexible torso (Fukuhara et al., 2016) and indeed adding extra degrees of freedom in the body and in the limb-girdles may be exactly what is required to improve the fluidity of the movement generated and improve turning performance. All of these changes increase the complexity of the simulations and the numbers of parameters in the controllers but the big advantage of the current approach is that the number of parameters is very small, particularly when compared to the number of controlled elements, so there is plenty of headroom for additional complexity without increasing the simulation or learning times too much.

Conclusion

We demonstrate a completely new approach to controlling high bio-fidelity vertebrate simulations that can cope with large numbers of muscles and non-steady-state locomotor patterns with minimal computational complexity. The current incarnation is a proof of concept and although it functions adequately it does not perform as well as dedicated feedforward controllers in steady-state locomotion. We suggest that the current system is a useful starting point for further work in this area and has the potential to allow us to create freely moving, biologically meaningful simulated legged animals for reconstructing synthetic paleontological worlds.

Data availability statement

The original contributions presented in this study are included in the article/**Supplementary material**, further inquiries can be directed to the corresponding author.

Author contributions

WS wrote the software and first draft of the manuscript. CC and WS performed the analysis simulations. EH and WS constructed and modified the chimpanzee model. AF, AI, and WS designed the control system. All authors contributed to conception and design of the study, manuscript revision, read, and approved the submitted version.

Funding

This work was supported by BBSRC grant number: BB/K006029/1 and JSPS Grant-in-Aid for Scientific Research (B) (grant number: 21H01269).

Acknowledgments

We would like to thank staff at the Primate Research Institute (PRI), Kyoto University for access to chimpanzee material, and we would like to acknowledge the assistance given by Research IT and the use of the Condor Cluster at the University of Manchester.

Conflict of interest

The authors declare that the research was conducted in the absence of any commercial or financial relationships that could be construed as a potential conflict of interest.

Publisher's note

Supplementary material

The Supplementary Material for this article can be found online at: https://www.frontiersin.org/articles/10.3389/fevo.2022.954838/full#supplementary-material

References

Anderson, F. C., and Pandy, M. G. (2001). Dynamic optimization of human walking. *J. Biomechan. Eng.* 123, 381–390. doi: 10.1115/1.1392310

Aoi, S., Ogihara, N., Funato, T., Sugimoto, Y., and Tsuchiya, K. (2010). Evaluating functional roles of phase resetting in generation of adaptive human bipedal walking with a physiologically based model of the spinal pattern generator. *Biol. Cybern.* 102, 373–387. doi: 10.1007/s00422-010-0373-y

Askew, G. N., Marsh, R. L., and Ellington, C. P. (2001). The mechanical power output of the flight muscles of blue-breasted quail (*Coturnix chinensis*) during take-off. *J. Exp. Biol.* 204, 3601–3619. doi: 10.1242/jeb.204.21.3601

Crompton, R. H., Li, Y., Wang, W., Günther, M. M., and Savage, R. (1998). The mechanical effectiveness of erect and "bent-hip, bent-knee" bipedal walking in *Australopithecus afarensis*. *J. Hum. Evol.* 35, 55–74. doi: 10.1006/jhev.1998.0222

Crompton, R. H., Sellers, W. I., and Thorpe, S. K. S. (2010). Arboreality, terrestriality and bipedalism. *Philos. Trans. R. Soc. B* 365, 3301–3314. doi: 10.1098/rstb.2010.0035

Cunningham, J. A., Rahman, I. A., Lautenschlager, S., Rayfield, E. J., and Donoghue, P. C. J. (2014). A virtual world of paleontology. *Trends Ecol. Evol.* 29, 347–357. doi: 10.1016/j.tree.2014.04.004

De Groote, F., Kinney, A. L., Rao, A. V., and Fregly, B. J. (2016). Evaluation of direct collocation optimal control problem formulations for solving the muscle redundancy problem. *Ann. Biomed. Eng.* 44, 2922–2936. doi: 10.1007/s10439-016-1591-9

Demes, B., Carlson, K. J., and Franz, T. M. (2006). Cutting corners: The dynamics of turning behaviors in two primate species. *J. Exp. Biol.* 209, 927–937. doi: 10.1242/jeb.02046

Doran, D. M. (1992). Comparison of instantaneous and locomotor bout sampling methods: A case study of adult male chimpanzee locomotor behavior and substrate use. *Am. J. Phys. Anthropol.* 89, 85–99. doi: 10.1002/ajpa.1330890108

Finestone, E. M., Brown, M. H., Ross, S. R., and Pontzer, H. (2018). Great ape walking kinematics: Implications for hominoid evolution. *Am. J. Phys. Anthropol.* 166, 43–55. doi: 10.1002/ajpa.23397

Frank, A. A. (1968). *Automatic Control Systems For Legged Locomotion Machines*, Ph.D. thesis. Los Angeles, CA: University of Southern California.

Fukuhara, A., Owaki, D., Kano, T., and Ishiguro, A. (2016). "Leg stiffness control based on "TEGOTAE" for quadruped locomotion," in *Living Machines*, eds N. F. Lepora, A. Mura, M. Mangan, P. F. M. J. Verschure, M. Desmulliez, and T. J. Prescott (Berlin: Springer), 79–84. doi: 10.1007/978-3-319-42417-0_8

Fukuhara, A., Owaki, D., Kano, T., Kobayashi, R., and Ishiguro, A. (2018). Spontaneous gait transition to high-speed galloping by reconciliation between body support and propulsion. *Adv. Robot.* 32, 794–808. doi: 10.1080/01691864.2018.1501277

Fukuoka, Y., and Akama, J. (2014). Dynamic bipedal walking of a dinosaur-like robot with an extant vertebrate's nervous system. *Robotica* 32, 851–865. doi: 10.1017/S0263574713001045

Gasparetto, A., Boscariol, P., Lanzutti, A., and Vidoni, R. (2015). "Path Planning and Trajectory Planning Algorithms: A General Overview," in *Motion and Operation Planning of Robotic Systems: Background and Practical Approaches*, eds G. Carbone and F. Gomez-Bravo (Cham: Springer International Publishing), 3–27. doi: 10.1007/978-3-319-14705-5_1

Gooch, C. L., Doherty, T. J., Chan, K. M., Bromberg, M. B., Lewis, R. A., Stashuk, D. W., et al. (2014). Motor unit number estimation: A technology and literature review. *Muscle Nerve* 50, 884–893. doi: 10.1002/mus.24442

Hase, K., and Stein, R. B. (1999). Turning strategies during human walking. *J. Neurophysiol.* 81, 2914–2922. doi: 10.1152/jn.1999.81.6.2914

Hatze, H. (1977). Complete set of control equations for human musculoskeletal system. *J. Biomech.* 10, 799–805. doi: 10.1016/0021-9290(77)90094-X

Hill, A. (1938). The heat of shortening and the dynamic constants of muscle. *Proc. R. Soc. Lond. B* 126, 136–195. doi: 10.1098/rspb.1938.0050

Hill, A. V. (1950). The series elastic component of muscle. *Proc. R. Soc. Lond. Ser. B* 137, 273–280. doi: 10.1098/rspb.1950.0035

Jindrich, D. L., and Full, R. J. (1999). Many-legged maneuverability: Dynamics of turning in hexapods. *J. Exp. Biol.* 202, 1603–1623. doi: 10.1242/jeb.202.12.1603

Kidziński, Ł, Mohanty, S. P., Ong, C. F., Hicks, J. L., Carroll, S. F., Levine, S., et al. (2018). "Learning to Run Challenge: Synthesizing Physiologically Accurate Motion Using Deep Reinforcement Learning," in *NIPS 2017 Competition Book*, eds S. Escalera and M. Weimer (Cham: Springer International Publishing), 101–120. doi: 10.1007/978-3-319-94042-7_6

Kimura, T., Okada, M., and Ishida, H. (1979). "Kinesiological characersitics of primate walking: its significance in human walking," in *Environment, Behavior, And Morphology: Dynamic Interactions In Primates*, eds M. E. Morbeck, H. Preuschoft, and N. Gomberg (New York, NY: Gustav Fischer), 297–311.

Kramer, P. A. (1999). Modelling the locomotor energetics of extinct hominids. *J. Exp. Biol.* 202, 2807–2818. doi: 10.1242/jeb.202.20.2807

Larmine, J., and Lowry, J. (2012). *Electric vehicle technology explained,* 2nd edn. Hoboken, NJ: John Wiley & Sons, Ltd. doi: 10.1002/9781118361146.ch7

Lautenschlager, S. (2020). Multibody dynamics analysis (MDA) as a numerical modelling tool to reconstruct the function and palaeobiology of extinct organisms. *Palaeontology* 63, 703–715. doi: 10.1111/pala.12501

Li, Y., Crompton, R. H., Wang, W., Savage, R., and GÜnther, M. M. (2004). Hind limb drive, hind limb steering? Functional differences between fore and hind limbs in chimpanzee quadrupedalism. *Camb. Stud. Biol. Evol. Anthropol.* 40, 258–277. doi: 10.1017/CBO9780511542336.016

McGeer, T. (1990). Passive dynamic walking. *Int. J. Robot. Res.* 9, 62–82. doi: 10.1177/027836499000900206

McGhee, R. B. (1967). Finite state control of quadruped locomotion. *Simulation* 9, 135–140. doi: 10.1177/003754976700900308

More, H. L., Hutchinson, J. R., Collins, D. F., Weber, D. J., Aung, S. K. H., and Donelan, J. M. (2010). Scaling of sensorimotor control in terrestrial mammals. *Proc. R. Soc. B Biol. Sci.* 277, 3563–3568. doi: 10.1098/rspb.2010.0898

Nagano, A., Umberger, B. R., Marzke, M. W., and Gerritsen, K. G. M. (2005). Neuromusculoskeletal computer modeling and simulation of upright, straight-legged, bipedal locomotion of Australopithecus afarensis (A.L. 288-1). *Am. J. Phys. Anthropol.* 126, 2–13. doi: 10.1002/ajpa.10408

Nath, T., Mathis, A., Chen, A. C., Patel, A., Bethge, M., and Mathis, M. W. (2019). Using DeepLabCut for 3D markerless pose estimation across species and behaviors. *Nat. Protoc.* 14, 2152–2176. doi: 10.1038/s41596-019-0176-0

Nyakatura, J. A., Melo, K., Horvat, T., Karakasiliotis, K., Allen, V. R., Andikfar, A., et al. (2019). Reverse-engineering the locomotion of a stem amniote. *Nature* 565, 351–355. doi: 10.1038/s41586-018-0851-2

Ogihara, N., and Yamazaki, N. (2006). "Computer Simulation of Bipedal Locomotion: Toward Elucidating Correlations among Musculoskeletal Morphology, Energetics, and the Origin of Bipedalism," in *Human Origins and Environmental Backgrounds*, eds H. Ishida, R. Tuttle, M. Pickford, and M. Nakatsukasa (New York, NY: Springer), 167–174. doi: 10.1007/0-387-29798-7_13

Onyshko, S., and Winter, D. A. (1980). A mathematical model for the dynamics of human locomotion. *J. Biomech.* 13, 361–368. doi: 10.1016/0021-9290(80)90016-0

Owaki, D., and Ishiguro, A. (2017). A quadruped robot exhibiting spontaneous gait transitions from walking to trotting to galloping. *Sci. Rep.* 7:277. doi: 10.1038/s41598-017-00348-9

Owaki, D., Kano, T., Nagasawa, K., Tero, A., and Ishiguro, A. (2012). Simple robot suggests physical interlimb communication is essential for quadruped walking. *J. R. Soc. Interface* 10:20120669. doi: 10.1098/rsif.2012.0669

Pontzer, H., and Wrangham, R. W. (2004). Climbing and the daily energy cost of locomotion in wild chimpanzees: Implications for hominoid locomotor evolution. *J. Hum. Evol.* 46, 317–335. doi: 10.1016/j.jhevol.2003.12.006

Pontzer, H., Raichlen, D. A., and Rodman, P. S. (2014). Bipedal and quadrupedal locomotion in chimpanzees. *J. Hum. Evol.* 66, 64–82. doi: 10.1016/j.jhevol.2013.10.002

Rosheim, M. E. (2006). *Leonardo's Lost Robots*. Berlin: Springer-Verlag.

Sellers, W. I. (1996). A biomechanical investigation into the absence of leaping in the locomotor repertoire of the Slender Loris (*Loris tardigradus*). *Folia Primatol.* 67, 1–14. doi: 10.1159/000157202

Sellers, W. I., and Hirasaki, E. (2014). Markerless 3D motion capture for animal locomotion studies. *Biol. Open* 3, 656–668. doi: 10.1242/bio.20148086

Sellers, W. I., and Hirasaki, E. (2018). Quadrupedal locomotor simulation: Producing more realistic gaits using dual-objective optimization. *R. Soc. Open Sci.* 5:171836. doi: 10.1098/rsos.171836

Sellers, W. I., and Manning, P. L. (2007). Estimating dinosaur maximum running speeds using evolutionary robotics. *Proc. R. Soc. B Biol. Sci.* 274, 2711–2716. doi: 10.1098/rspb.2007.0846

Sellers, W. I., Dennis, L. A., and Crompton, R. H. (2003). Predicting the metabolic energy costs of bipedalism using evolutionary robotics. *J. Exp. Biol.* 206, 1127–1136. doi: 10.1242/jeb.00205

Sellers, W. I., Dennis, L. A., Wang, W. J., and Crompton, R. H. (2004). Evaluating alternative gait strategies using evolutionary robotics. *J. Anat.* 204, 343–351. doi: 10.1111/j.0021-8782.2004.00294.x

Sellers, W. I., Manning, P. L., Lyson, T., Stevens, K., and Margetts, L. (2009). Virtual palaeontology: Gait reconstruction of extinct vertebrates using high performance computing. *Palaeontol. Electron.* 12:11A.

Sellers, W. I., Margetts, L., Bates, K. T., and Chamberlain, A. T. (2013). Exploring diagonal gait using a forward dynamic three-dimensional chimpanzee simulation. *Folia Primatol.* 84, 180–200. doi: 10.1159/000351562

Sellers, W. I., Pond, S. B., Brassey, C. A., and Manning, P. L. (2017). Investigating the running abilities of *Tyrannosaurus rex* using stress-constrained multibody dynamic analysis. *PeerJ* 5:e3420. doi: 10.7717/peerj.3420

Sellers, W. I., Wang, W., and Crompton, R. H. (2005). Stride lengths, speed and energy costs in walking of *Australopithecus afarensis*: Using evolutionary robotics to predict locomotion of early human ancestors. *J. R. Soc. Interface* 2, 431–441. doi: 10.1098/rsif.2005.0060

Shimizu, M., Ishii, D., Aonuma, H., and Hosoda, K. (2017). "Swimming frog cyborg which generates efficient hydrodynamic propulsion with webbed foot" in *2017 IEEE International Conference on Cyborg and Bionic Systems (CBS)*, (Piscataway, NJ: IEEE), 73–76. doi: 10.1109/CBS.2017.8266070

Spröwitz, A. T., Ajallooeian, M., Tuleu, A., and Ijspeert, A. J. (2014). Kinematic primitives for walking and trotting gaits of a quadruped robot with compliant legs. *Front. Comput. Neurosci.* 8:27. doi: 10.3389/fncom.2014.00027

Takita, K., Hodoshima, R., and Hirose, S. (2000). "Fundamental mechanism of dinosaur-like robot TITRUS-II utilizing coupled drive," in *Proceedings. 2000 IEEE/RSJ International Conference on Intelligent Robots and Systems (IROS 2000) (Cat. No.00CH37113), 1670-1675 vol.1673*, (Takamatsu: IEEE).

Taylor, C., and Rowntree, V. J. (1973). Running on two or on four Legs: Which consumes more energy? *Science* 179, 186–187. doi: 10.1126/science.179.4069.186

Tsounis, V., Alge, M., Lee, J., Farshidian, F., and Hutter, M. (2020). DeepGait: Planning and control of quadrupedal gaits using deep reinforcement learning. *IEEE Robot. Autom. Lett.* 5, 3699–3706. doi: 10.1109/LRA.2020.2979660

Van den Bogart, A. J., Schamhardt, H., and Crowe, A. (1989). Simulation of quadrupedal locomotion using a rigid body model. *J. Biomech.* 22, 33–41. doi: 10.1016/0021-9290(89)90182-6

Vilaplana, J. M., and Coronado, J. L. (2006). A neural network model for coordination of hand gesture during reach to grasp. *Neural Netw.* 19, 12–30. doi: 10.1016/j.neunet.2005.07.014

Walter, R. M. (2003). Kinematics of 90 degree running turns in wild mice. *J. Exp. Biol.* 206, 1739–1749. doi: 10.1242/jeb.00349

Watson, J. C., Payne, C. R., Chamberlain, A. T., Jones, R., and Sellers, W. I. (2011). "The influence of load carrying on gait parameters in humans and apes: implications for the evolution of human bipedalism," in *Primate Locomotion: Linking Field And Laboratory Research*, eds K. D'Août and E. E. Vereecke (New York, NY: Springer), 109–134. doi: 10.1007/978-1-4419-1420-0_7

Watson, J. C., Payne, R. C., Chamberlain, A. T., Jones, R. K., and Sellers, W. I. (2009). The kinematics of load carrying in humans and great apes: Implications for the evolution of human bipedalism. *Folia Primatol.* 80, 309–328. doi: 10.1159/000258646

Yamazaki, N., Hase, K., Ogihara, N., and Hayamizu, N. (1996). Biomechanical analysis of the development of human bipedal walking by a neuro-musculo-skeletal model. *Folia Primatol.* 66, 253–271. doi: 10.1159/000157199

Zhao, J.-S., Talori, Y. S., Song, H., Lu, W.-X., O'Connor, J. K., and Li, Z.-H. (2022). Reconstruction of *Caudipteryx* robot to identify the origin of avian flapping flight. *Proc. Inst. Mech. Eng. Part C J. Mech. Eng. Sci.* 236:09544062221086529. doi: 10.1177/09544062221086529

Frontiers in
Ecology and Evolution

Ecological and evolutionary research into our natural and anthropogenic world

This multidisciplinary journal covers the spectrum of ecological and evolutionary inquiry. It provides insights into our natural and anthropogenic world, and how it can best be managed.

Discover the latest Research Topics

See more →

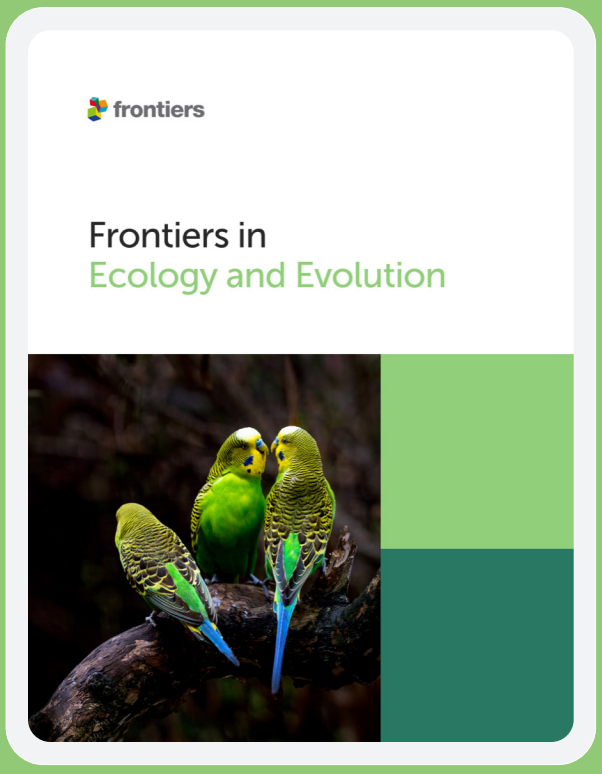

Frontiers

Avenue du Tribunal-Fédéral 34
1005 Lausanne, Switzerland
frontiersin.org

Contact us

+41 (0)21 510 17 00
frontiersin.org/about/contact